Dosimétrie par fibre optique pour la recherche spatiale et la physique des Hautes énergies

Nourdine Kerboub

To cite this version:

Nourdine Kerboub. Dosimétrie par fibre optique pour la recherche spatiale et la physique des Hautes énergies. Optique / photonique. Université Jean Monnet - Saint-Etienne, 2023. Français. NNT : 2023STET0029 . tel-04520557

HAL Id: tel-04520557

https://theses.hal.science/tel-04520557

Submitted on 25 Mar 2024

N°d'ordre NNT : **2023STET029**

THÈSE de DOCTORAT
DE L'UNIVERSITÉ JEAN MONNET SAINT-ÉTIENNE

Membre de l'Université de LYON

École Doctorale N° 488
Sciences, Ingénierie, Santé
Spécialité / discipline de doctorat : Optique

Soutenue publiquement/à huis clos le 04/10/2023, par :
Nourdine KERBOUB

Dosimétrie par fibre optique pour la recherche spatiale et la physique des Hautes énergies

---

Devant le jury composé de :

Mohamed BOUAZAOUI, Professor, Univ. Lille, Examinateur et Président du Jury

Sinead O'Keeffe, Doctor, University Of Limerick, Rapporteur & Examinatrice
Cornelia Hoehr, Doctor, TRIUMF, Rapporteur & Examinatrice
Mourad BENABDESSELAM, Professor, Univ. Nice Examinateur
Adriana Morana, Doctor, LabHC/UJM, Examinatrice
Diego Di Francesca, Doctor, CERN, Co-encadrant
Julien Mekki, Doctor, CNES, Co-encadrant
Sylvain Girard, Professor, LabHC/UJM, Directeur de thèse

THESE DE DOCTORAT

FIBER-BASED DOSIMETRY APPLIED TO SPACE RESEARCH AND HIGH ENERGY PHYSICS FACILITIES

Dosimétrie par fibre optique pour la recherche spatiale et la physique des hautes énergies

Thèse de doctorat de l'université Jean-Monnet de Saint-Etienne

École doctorale n° 488 – Sciences, Ingénierie, Santé
Spécialité de doctorat : Optique

Thèse préparée dans l'unité de recherche UMR5516 et au CERN, sous la direction de **Sylvain Girard**, Professeur des Universités, et la co-supervision de **Diego Di Francesca**, Docteur, et de **Julien Mekki,** Docteur

Thèse soutenue à Saint-Etienne, le 04 Octobre 2023, par

Nourdine KERBOUB

Composition du Jury

Sinead O'Keeffe Doctor, University Of Limerick	Rapporteur & Examinatrice
Cornelia Hoehr Doctor, TRIUMF	Rapporteur & Examinatrice
Mourad BENABDESSELAM Professor, Univ. Nice	Examinateur
Mohamed BOUAZAOUI Professor, Univ. Lille	Examinateur et Président du Jury
Adriana Morana Doctor, LabHC/UJM	Examinatrice
Diego Di Francesca Doctor, CERN	Co-encadrant
Julien Mekki Doctor, CNES	Co-encadrant
Sylvain Girard Professor, LabHC/UJM	Directeur de thèse

1 TABLE OF CONTENT

List of acronyms

FUT : Fibre Under Test
DUT : Device Under Test
RIA : Radiation Induced Attenuation
RL : Radiation Induced Luminescence
TIR : Total Internal Reflection
SI : Step Index
GI : Graded Index
RIRIC : Radiation Induced Refractive Index Change
NA : Numerical Aperture
SM : Single Mode
SMF Single Mode Fibre
MM : Multi-Mode
MMF : Multi-Mode Fibre
FMF : Few Mode Fibre
TID : Total Ionising Dose
CNRS : Centre national pour la recherche Scientifique
CNES : Centre National d’Etudes Spatiales
PhLAM : laboratoire de Physique des Lasers, Atomes et Molécules
TNID : Total Non-Ionizing Dose
DDD : Displacement Damage Dose
LET : Linear Energy Transfer
LEO : Low Earth Orbit
GEO : Geostationary Earth Orbit
GPS : Global Positioning System
MEO : Medium Earth Orbit
RHA : Radiation Hardness Assurance
SEE : Single Event Effect
SAA : South Atlantic Anomaly
RP : Radiation Protection
CERN : Conseil Européen pour la Recherche Nucléaire
OF : Optical Fibre
UV : Ultra-Violet
SNR : Signal to Noise Ratio
RIE : Radiation Induced Emission
BBE : Bright Burn Effect

2 INTRODUCTION

For the humanity, communication has been an extremely important asset that has defined the way our civilisations evolved and prospered. After centuries based on oral and hand written messages, more advanced means of communications were invented, that marked a turning point in the history. We can describe this turning point as the invention of Telecommunications : For the first time, the message could travel faster than its messenger.

One of the first remote telecommunication systems that was effectively exploited after centuries using pigeons and smoke signals, was the Chappe's optical telegraph in the 19th century [1] . Eventually appeared the electrical telegraph, with for instance the use of Morse signal as a protocol to transfer information through copper lines [2] and later the telephone which allowed to transfer the voice over the same media. These invention led to the installation of copper cables between oceans allowing messages to be sent from Europe to America within hours instead of weeks [3]. In addition to the development of wireless communication through electromagnetic signals via antennas, satellites opened a brand new horizon in terms of telecommunication. Indeed, Telstar 1 (1962) [4] was considered as the first active telecommunication satellite, even if the satellite's active repeater technology was first tested in the Courier 1B (1960) [5] satellite before. This happened after the launch of the first artificial satellite called Sputnik by the USSR in 1957 [6], [7]. This event triggered the race to space that rythmed the competition between the world most powerful countries for the next decades.

Around the same time, in 1966 a researcher called C.K. Kao investigated the potential offered by silica-based optical fibre as a medium for long distance telecommunication and concluded that this technology was a very promising candidate for such purpose [8]. Decades later, the extensive work performed around the world to tackle the challenge of the optimization of this technology succeeded since nowadays, optical fibre links transport nearly 99% of the internet data exchanges worldwide through inter-continental cables.

The optical fibre based communications have many advantages with respect to more traditional technologies that made them the preferred solution for intra- and inter-continental long-distance telecommunications : high speed transmission, higher data rate transmission, immunity to electromagnetic perturbations / interferences, reduced cost, as well as the fact that an optical fibre link is more difficult to spy than a copper link.

While telecommunications are by far the most important use of optical fibres, they are also today widely used in sensing applications. Indeed, researchers have discovered that some environmental parameters can be monitored via their impact on the optical fibre properties such as : Temperature , Strain , Humidity, Pressure [9], Gyroscopic changes [10], etc … This led to the deployment of optical fibre sensors in various environments, for instance to measure strain and leaks in the concrete structure of a dam or in big concrete foundation of a building [11]. The progress of the use of optical fibre based systems led to the installation of this technology in harsh radiation environments such as nuclear plants, satellites or accelerators where it was shown that radiation can have macroscopic observable effects on the fibres that arise from microscopic interactions of radiation with the silica. These effects limit in some cases the use of optical fibre based technology in such environments. However, scientists discovered that in some specific optical fibres, the relation between the amount of radiation deposited on an optical fibre and the observable effects is such that it can be used to measure radiation. This became an important topic in the optical fibre sensing community since the measure of radiation is an important research axis where many types of measurement devices co-exist for different uses. Several ways exist to use optical fibres as a radiation sensor, among which one is the use of radioluminescent optical fibres. This type of fibres emits light in the presence of radiation, with a proportional relation between the intensity of the emitted light and the radiation dose deposited per unit of time, or dose rate. This effect can be enhanced by the use of specific dopants and tuned to fulfill the need of the user. The features highlighted by this technique such as the ability to obtain an online and real-time radiation measurement, motivated this PhD work in collaboration between the CERN, UJM and CNES institutes.

The main goal of this work is to evaluate the potential of radioluminescent optical fibres for dosimetry in the framework of CERN’s accelerators and CNES space projects. Some potential use of such sensors for CERN could be for instance the measurement of the intensity and position of the beam during for radiation testing of electronics such as those taking place within the R2E project[1]. While in the case of CNES, one of the interests would be on-board satellite radiation levels measurement with the ability to identify increasing radiation levels announcing solar storms endangering astronauts.

In this PhD project, we choose to focus the work on a set of optical fibres developed in France by the University of Lille, which highlighted interesting detection performances. The aim of the research is to evaluate their potential use in the described intended projects, by characterizing their response under radiation in different conditions.

For this purpose, we will start by introducing the optical fibre technology, and the radiation effects on the matter in general as well as the main type of dosimeters used nowadays. Then, we will introduce the radiation effects on optical fibres, and describe how we can use them to measure radiation. After that, we will present the experimental techniques used in this work to characterize the optical fibre sensor considered for the application, and present the result of these characterizations. Finally, discussion of the obtained results will be accompanied by some analysis of the implication of the findings for the intended application.

3 GENERALITIES ON OPTICAL FIBRES

Silica-based optical fibres are a crucial technology in our current world, playing a vital role in continental and inter-continental telecommunications. These light waveguides consist of thin cylinders of amorphous glasses that are in most of the cases designed as a key element of high bandwidth data links even if there is a growing interest in exploiting them for sensing applications [12]. These fibres are made of a transparent dielectric, pure or doped amorphous silica, which is used to guide light over long distances by the total

---

[1] https://r2e.web.cern.ch

internal reflection (TIR) mechanism. It should be noted that other materials such as plastic, or light guidance mechanisms are used to produce optical fibres but those optical fibres are not considered in this PhD thesis work.

Figure 1 - Optical fibre cable for submarine inter-continental telecommunications (image found on Eurafibre.fr)

In the next part, we will introduce some of the properties and capabilities of silica-based optical fibres. After this introduction to the basics, we will review the main industrial techniques used to produce optical fibres and introduce how impurities and dopants impact the final performances of this photonic component.

3.1 SILICA-BASED OPTICAL FIBRES

3.1.1 Geometrical structure and light guiding properties

The architecture of a silica based optical fibre is shown in Figure 2a. The waveguide is composed of an inner cylindrical core in which the majority of the signal will be travelling. This core is surrounded by a material layer called cladding that should have a lower refractive-index than the one of the core. The refractive index of silica can be adjusted by doping it with some chemical elements allowing either to increase (Ge, N, P) or decrease (F, B) its refractive index. The principle of Total Internal Reflection (TIR) ensures the confinement of the light signal within the core of an optical fibre. This phenomenon occurs when light travels through a medium with a higher refractive index and strikes the interface with a medium of a lower refractive index at an angle greater than the critical angle . When this happens, the light is reflected back into the higher refractive index medium, here the core. To design an optical fibre, it is then crucial to conceive a refractive-index profile (RIP) adapted to the light guidance at the wavelength of interest.

In multimode fibres, we often refer to two main types of RIP: Step Index (SI) and Graded Index (GI). As shown in Figure 2b, while the change of refractive index in SI fibres is abrupt between the core and the cladding, it is smoothed out in GI fibres. This difference changes the way the light is propagated in the optical fibre.This feature has an effect on the modal dispersion, which is greatly reduced in GI fibre with respect to that in SI fibres. Indeed, the graded refractive index allows equalizing the celerity of the modes travelling in the core of the fibre. Due to the higher cost of production, GI fibres are usually used in medium-sized communication links (up to 10-20 km).

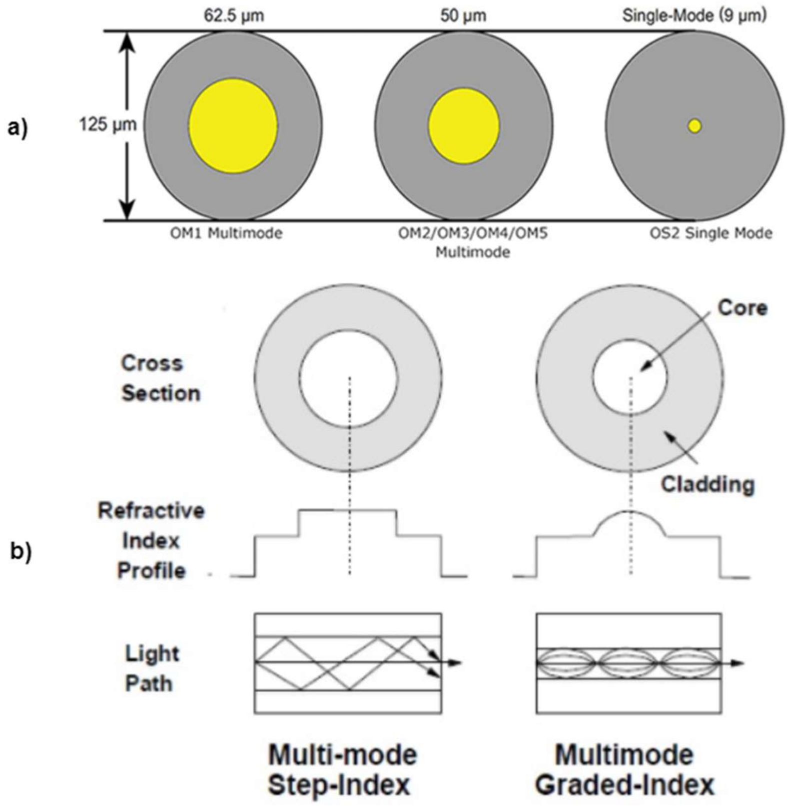

Figure 2 – a) Different core sizes of optical fibres, b) difference between SI and GI multimode fibres.. Image adapted from https://community.fs.com

The refractive index values of the core and the cladding will also define an important parameter of the fibre, called the Numerical Aperture, defined as follow in Step-Index fibres :

$$NA = \sqrt{n^2{}_{core} - n^2{}_{cladding}} = n_0 \times \sin \Theta_{max} \tag{1}$$

With n_{core} the refractive index of the core, $n_{cladding}$ the refractive index of the cladding and n_0 that of the surrounding material. Θ_{max} is defined as the maximum incidence angle below which an incident light ray will be guided in the optical fibre.

This parameter is the figure of merit of the fibre ability to collect light. The higher the NA value, the larger is the acceptance cone within which light will be guided in the fibre.

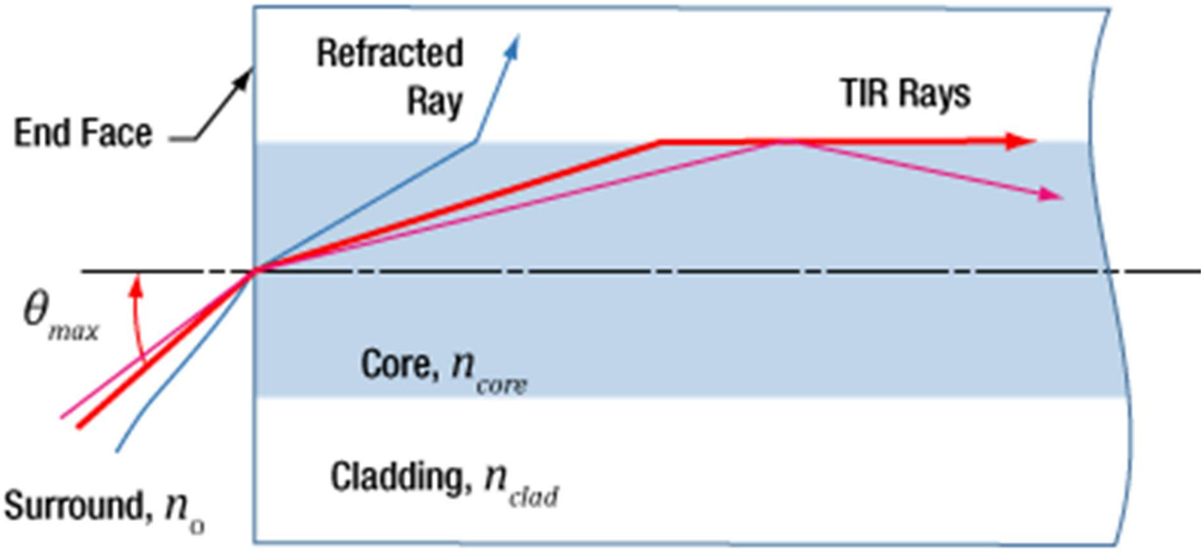

Figure 3 - Representation of TIR conditions and NA in optical fibres. Image Adapted from Thorlabs.com

Around the silica-based cladding, manufacturers usually use a mechanical coating made of plastic or polymer material to protect the fibre from mechanical strain which can induce a transmission performance degradation. Various coatings exist that differ by the temperature that they can widthstand before degrading the fibre mechanical or optical properties. In this PhD work, all the tested optical fibres have acrylate coatings, adapted to long-term operation at temperatures up to 80°C.

The geometrical optic approach for the description of the light guidance is quite incomplete. An optical fibre can be considered as an electromagnetic waveguide, therefore the small size of the core (with an order of magnitude comparable to the wavelength of the signal) has a major impact on the propagation properties of the fibre and leads to a discretization of the ways to guide the light and the appearance of the so-called optical modes. The RIP and the core size define the number of modes that can propagate within the targeted core at each wavelength. More precisely, we can distinguish two cases :

- Only one mode, called the fundamental mode, propagates into the core at the considered wavelength: the fibre is called as Single-Mode Fibre (SMF). This condition is obtained in the telecommunication Infrared (IR) domain (around 1550 nm) with core size in between of 8 and 12 µm. It should be noted that as the refractive index values depend on the wavelength, the fibre becomes multimodal at short wavelengths, typically below 1260 nm in telecommunication SMFs.
- Two or more modes propagate within the fibre core: this fibre is then called either Few Mode fibre (FMF) or Multi-Mode fibre (MMF). The standard diameter of a MMF for IR or Near-IR telecommunications is typically between 50 (OM2 to OM5 standards) to 62.5µm (OM1 standard) but it can be larger for specialized industrial applications, typically up to 200 µm.

For high-bandwidth telecommunications, SMFs are the most used technologies for long distances communications, while the MMFs are generally used for short distance telecoms due the lower costs of their associated optoelectronics.

<u>Optical attenuation</u>

The propagation of the light in the silica core of the optical fibre is affected by some light matter interactions which result in optical losses decreasing the transmitted signals. All these phenomena contribute to the optical attenuation which is defined by the following equation where $P_{Injected}$ is the optical power injected in the fibre and P_{Output} the power that is effectively transmitted up to the end of the fibre of a given length L. This parameter is usually reported in dB/km, which permits evaluating the optical losses across an optical link whose length is known.

$$Optical\ attenuation\ \left(\frac{dB}{km}\right) = -\frac{10}{L(km)} \times \log\left(\frac{P_{Output}}{P_{Injected}}\right) \qquad (2)$$

This attenuation is caused by different mechanisms, some are intrinsic to the fibre while other are extrinsic:

- Scattering : this mechanism refers to the interaction of light with microscopic density changes or surface irregularities which lead to fluctuations of the refractive index and alteration of the light guidance. This results in optical losses, due to non respect of TIR conditions. These losses are strongly wavelength-dependent. Rayleigh scattering mechanism is a phenomena, linear with propagation length, occurring at centers which are much smaller in sze than the light wavelength. Its intensity is proportional to the incoming optical intensity and to the fourth power of the inverse wavelength. Rayleigh scattering explains today most of the optical losses of SM fibres at telecommunication wavelengths. Brillouin scattering is a different type of scattering occurring in optical fibres, linked to the interaction between phonons and photons, than can induce additional losses.
- Absorption : Photons guided through the fibre can also interact with the fibre core and cladding materials, in particular the dopants and impurities (such as phosphorous or hydrogen for instance) present in the silica glass and be absorbed.
- Bending losses : Whereas the previous mechanisms are intrinsic, this latter is extrinsic to the fibre. This contribution to the attenuation is due to external stress applied to the fibre that induces localized change in its geometry, leading to a leak of light outside of the fibre. This effect can be limited by an adapted mechanical coating on the fibre or by an adapted RIP less sensitive to curvatures.

3.1.2 OF manufacturing

Silica-based optical fibre manufacturing processes have been extensively improved year after year, following the market growth over the last 50 years and the visionary work from C. K. Kao [8] in 1966 which identified the potential of optical fibres for telecommunications. The iterative improvements in terms of performances have been obtained by optimizing tens of chemical and geometrical parameters that define an optical fibre. Once a manufacturer finds an adapted design, fulfilling all his requirement, he needs to be able to produce this fibre without any significant change in the recipe over time. This is ensured by an important work carried out on the repeatability and control of the optical fibre characteristics, through a deep understanding and control of the manufacturing processes. The idea of this sub-chapter is to introduce the optical fibre manufacturing techniques used nowadays, and what is the impact of the variability in this process for OFs in radiation environment. We will focus mainly on the sol-gel process which is that used to produce the FUTs in the project. This process is not used for telecommunication fibres but is very interesting for the design of specialty optical fibres as it is more versatile in terms of the chemical compositions that can be achieved.

While all the processes used by the industry to produce optical fibres differ, they all rely on two main steps : The preform production, and the drawing of the fibre from the preform.

Preform production :

This first step of the manufacturing starts with the fabrication of a pure or doped silica glass rod, called the preform, that will be the starting material of the optical fibre. This rod is manufactured layer by layer in order that it can be doped with the ad hoc dopants to achieve the desired refractive index profile targeted for the optical fibre. This obtained preform has in the end, the exact same composition and RIP of the final optical fibre, with only a difference in terms of diameter. The fibre is obtained from the preform through the drawing process that consists in a homothetic reduction of this object.

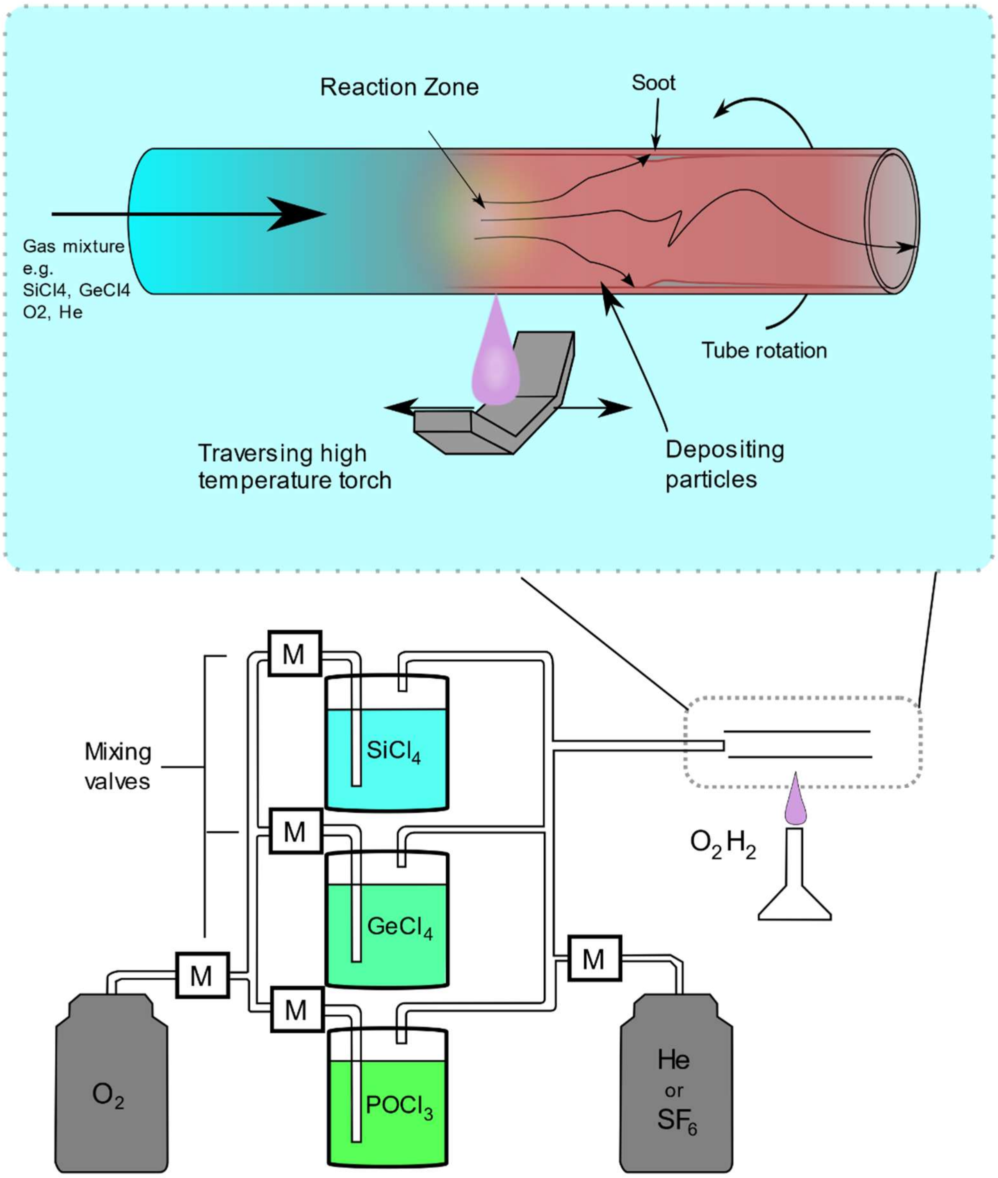

Figure 4 - Illustration of the MCVD process from [13]

Most of the different techniques of optical fibre manufacturing differ in the manufacturing process of the preforms. The main techniques used nowadays in Europe for commercial fibres are Modified Chemical Vapor Deposition (MCVD) and Plasma Chemical Vapor Deposition (PCVD). In both methods, the silica glass of the preforms is obtained by chemical reaction between gazes at high temperature (1400 - 1600° C) [14] and the glass is deposited layer by layer by vitrification on the inside of a high-purity silica tube. In the MCVD method, the high temperature is obtained by a furnace while the PCVD method exploits a microwave generated plasma [14].

While these two manufacturing processes are the most used, they are not always adapted to produce some exotic optical fibre with new classes of dopants, dedicated to non-standard application. For instance, the preforms of the optical fibres tested in this PhD work have been produced through the sol-gel method [15]. The basis of this method is to produce porous silica rods, and dope them by soaking them for hours in a solution containing ions of the dopants of choice. Additionnal steps such as high temperature drying to remove the solvent, are then performed to obtain a doped preform able to drawn with classical processes. This method will be further described in the chapter dedicated to the investigated optical fibres.

Drawing step:

The second step of the optical fibre manufacturing serves at transforming a several centimeters diameter preform into a much smaller diameter optical fibre. The actual standardarized optical fibre cladding diameter in telecom application is 125 µm.

To do so, the preform is placed on top of an industrial equipment called drawing tower, which can reach height above 10 m. A small furnace is placed on top to melt, at the desired rate, the preform at a temperature higher than its melting point (above 2000ºC). The obtained melted glass is attracted down by gravity, and pulled at a well-controlled tension by another device. This device ensures that the fibre is always drawn at the same speed and with the same tension. This bare fibre obtained is coated in-situ on the drawing tower with a protective layer (its coating) and wounded into a spool for storage and transportation.

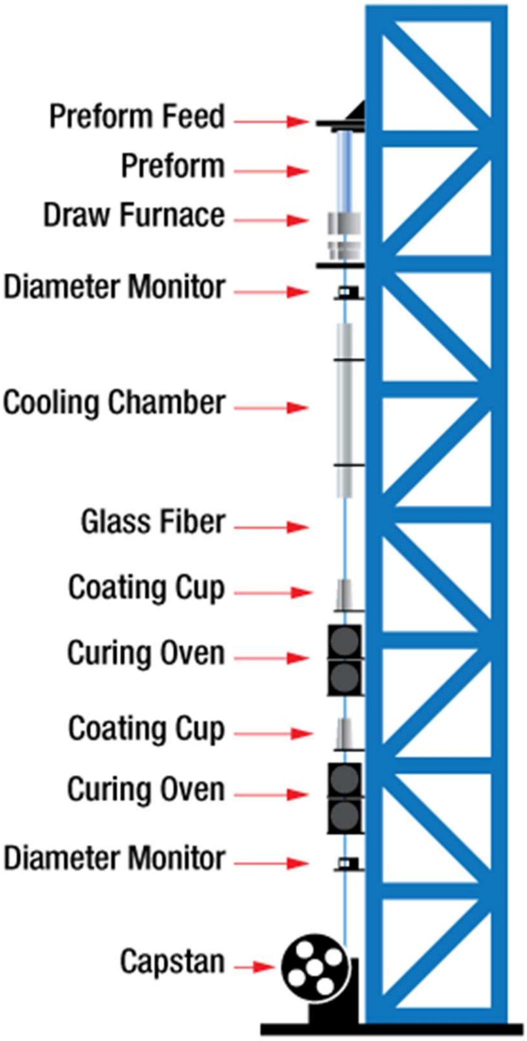

Figure 5 – Drawing tower used for optical fibre production adapted from [16]

Many studies have been carried out over the last 40 years to improve the repeatability of these processes and to control the parameters which could impact the final performance of the obtained optical fibre. Indeed, any change in the composition of the preform, the drawing conditions (speed, temperature, tension, …) can have a drastic impact either on the optical guiding performances or on the mechanical strength of the device. Furthermore as we will discuss later, these parameters can also greatly influence the fibre radiation responses. Additionnally, industry and final users need a well-controlled process to be able to apply batch qualification, on fibres obtained from different preforms. Once a preform is identified as a good candidate for the application, it is possible to obtain a very similar fibre by using the same production conditions.

However, this method has still some limitation. At least when it comes to radiation responses of exotic optical fibres. In this aspect, we can observe different behaviors from fibres produced following the same method [17]

3.2 RADIATION ENVIRONMENTS

When it comes to radiation effects or dosimetry, the knowledge of the targeted environment characteristics is very important. For this purpose, we use well-defined international units that allow the quantification of the radiation levels and their comparison across different environments. The main quantities used to characterize the radiation levels are :

- Total Ionization Dose (TID) : This quantity evaluate the energy deposited in the matter through ionization processes per unit of mass. It depends on the target material, since the energy deposited in the material by a given particle depends on the density and chemical composition of the matter. The usual unit used to define TID is the Gray (Gy) with 1 Gy = 1 J/kg. Other units exist such as the rad (100 rad = 1 Gy) which is still a commonly used unit, especially in the space industry.
- Dose rate : The dose rate is the TID deposited per unit of time in a given material. This is important for many applications because the effects on devices at a given dose are not the same depending on the dose rate. The unit is then the Gy/s.
- Total Non-Ionizing Dose (TNID) or Displacement Damage Dose (DDD): This parameter describes the amount of energy deposited in a given target material per unit og mass, through non-ionizing processes. This deposition of energy takes place via the interaction of the particle with the nucleus of the atoms of the target, leading to displacement damages in the atomic structure. The usual unit is the MeV.cm^2/g.
- Linear Energy Transfer (LET) : LET describes how much energy is deposited by a given particle when crossing a target material, through ionization processes [18]. It uses the same unit as DDD, the MeV.cm^2/g. The higher the LET, the shorter is the needed travel distance across a target material to absorb completely the energy of the incident particle.
- Fluence of particles: The number of particles emitted from or incident on a surface

in a given period of time, divided by the area of the surface. The usual unit is cm^{-2}.

- Flux of particle : Fluence per unit of time with units $cm^{-2}.s^{-1}$.

Additionnally, we usually classify a radiation environment by its particle type composition:

- Mono-energetic beam : One type of particles having all the same energy. This energy can in some cases be changed by tuning the accelerator settings and/or by using degraders to reduce the energy of a primary beam.
- Mixed field environment : Composed of different particle species having also different energies.

This distinction is made because the effects of radiation can be very different whetever an equipment is placed in a mono-energetic or mixed field, due to the combined effects of different particle species.

The main features describing the environments of interest for this work will now be introduced.

3.2.1 Space environment

Since the beginning of the space exploration era, and the discovery of the radiation belts by M. Van Allen in 1958 [19], the radiation environment around Earth and beyond has been extensively studied and characterized. The Earth magnetic field protects life on the ground by deflecting the ionizing particles coming from the Sun and outer space. However, a portion of the particles starts orbiting around the planet following the magnetic lines drawn by the Earth. The type of particles (protons or electrons), their energies, and their incidences with magnetic belt determine if they will be trapped or not in the belt. Finally, within a few days up to months, the trapped particles will be ejected from the belt, and later be replaced by new particles.

Numerous satellites [20]–[24] have been equipped with radiation monitors, providing enough data to produce models [25] that are nowadays exploited to give an approximation of the expected levels of radiation for a given mission. The near-Earth orbit radiation environment can be decomposed in different regions characterized by the compositions of their radiation fields:

- Low Earth Orbit (LEO) : This orbit region is characterized by a radiation field dominated by trapped protons with energies ranging up to 300 MeV. This area is composed by orbits with altitudes below 2000 km.
- Medium Earth Orbit (MEO) : In this region located at altitudes ranging from 2000 to 36000 km with respect to Earth, we observe an environment mainly characterized by a mix of protons and electrons.

- Geostationary Earth Orbit (GEO) : Located around 36000 km, this region is mainly used for Global Positionning Systems (GPS) or Satellite television because a satellite placed in this orbit always face the same area of the Earth's globe. This region is characterized by a radiation field mainly composed of high-energy electrons.

Table 1 summarizes the repartition of the protons and electrons across the Earth orbit, which are the main contributors to TID in spacecrafts. This table, extracted from [25], details the range of energy which can be found in the radiation belts.

	Particle Type	**Energy**	**Extension (Earth radii)**
Earth (Radius = 6 371 km)	electrons	1 keV-10 MeV	1-10
	protons	1 keV-300 MeV	1-7

Table 1 - Repartition of protons and electrons in the near-Earth orbit [25]

Whereas trapped protons and electrons are the most common particles in the Earth orbit, they are not the sole type of particles present in space. Indeed, the majority of the particles arriving on Earth originate from the Sun, which emits a large quantity of matter in all the directions. The ejected matter is composed of a mix of different particles such as protons, electrons, neutrons, gammas, x-rays and heavy ions *[26]*. Besides, the heavy ions do not contribute significantly to TID deposition on spacecraft. However, they play a role in the radiation hardness assurance (RHA) on electronic devices and more specifically in the Single Events Effects (SEE) studies due to their high probability to trigger events in electronic devices, and are therefore carefully evaluated by the models as well *[25]*. In the near-Earth orbit, they are concentrated towards the North and South magnetic poles due to the Earth magnetic field effect.

Additionnally, it is important to note that Earth is not a perfect sphere. If we had to describe its shape, it would more look like a apple or a potatoe to give an idea. This impacts its magnetic field and therefore has an effect on the radiation belts. Notably, there is a phenomenon called the South Atlantic Anomaly (SAA), located above the South America continent which is an area where the magnetic field is weaker than elsewhere at the same orbit. This area slowly drifts over time with the change of the magnetic field. The anomaly induces a “dive” of the radiation belt towards lower altitude in this area, leading to higher proton flux. This is for instance an issue for astronauts of the International Space Station (ISS) or LEO satellites, encountering higher radiation levels when crossing the SAA.

3.2.2 Accelerators environments

In the first part of the 20th century, particle accelerators were created in order to study the properties of subatomic particles. These machines use electro-magnets to increase the energy, and control the direction of propagation of charged particles. The energetic particle beams produced are then used to break down the atoms and observe smaller particles that are the building blocks of the matter. The particles circulate through the accelerator, to be stored for minutes or hours, before being used. Usually, the path followed by the particle beam is kept under vacuum. Indeed, during the circulation of the beam in the accelerator, any interaction of the high particle beam with some material, create a shower of secondary particles, impacting the whole experimental area around it. The material responsible of these interactions can be residual air, or related to beam optics such as collimators.

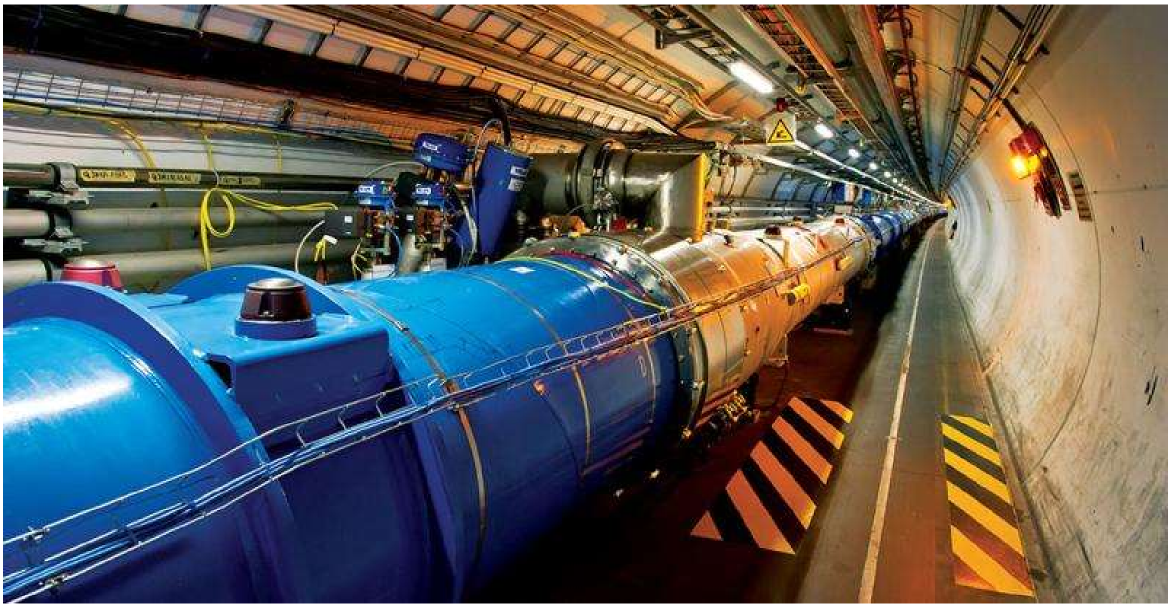

Figure 6 - Picture of the LHC tunnel from cern.ch

However, despite these precautions there is always a portion of the beam that get lost during the operation by entering in contact with the machine. This type of interaction is the main cause of the radiation levels observed around high energy particle accelerators. This explains why, physicists deport as much as possible the electronic and photonic equipments from the exposed areas surrounding the machine to shielded areas. The thickness and composition of the shielding depend on the the beam particle type, its energy, and the expected fluence per year. The shielding will be designed to keep the TID and fluences of particle in the specific area below certain limits according to RHA and Radiation Protection (RP) considerations. These designs result in very different radiation environments whether they are measured close to the accelerator or in those shielded areas. In these shielded areas, the environment is often dominated by neutrons that are resulting from the radiation interaction with shielding blocks made of concrete and steel.

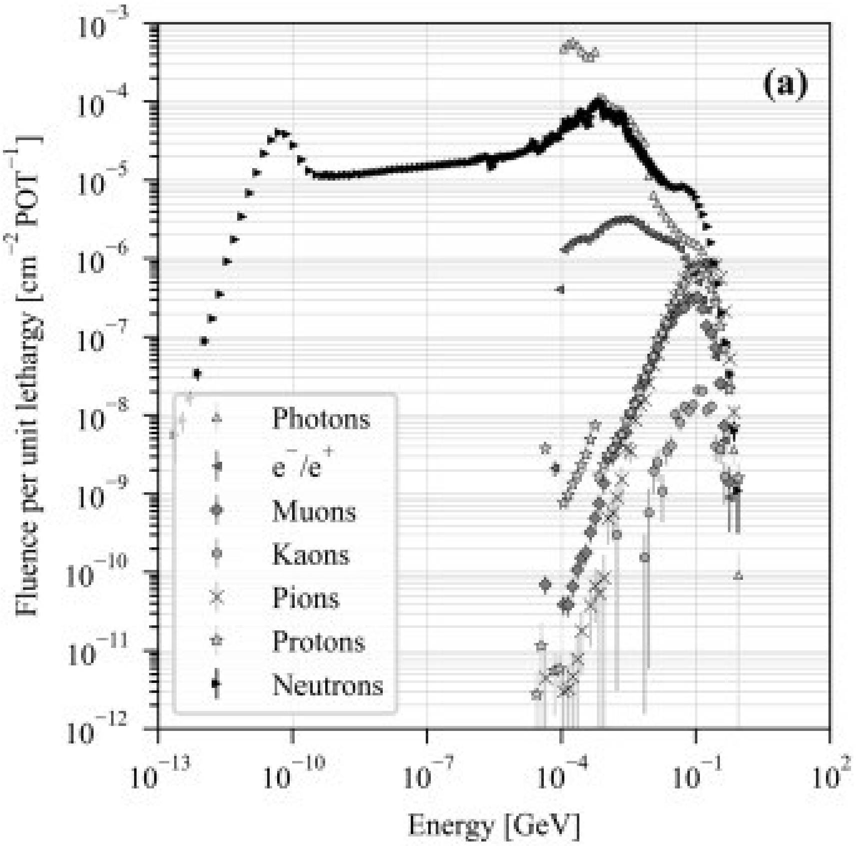

Figure 7 – Example of fluence spectra of the radiation field encountered in the CERN accelerator complex

To illustrate the radiation fields encountered in this complex environment, we can use the figure extracted from [27] which presents the fluence spectra of the different particle species as function of the energy, in one of the positions of the CHARM facility. This facility provides a radiation field which is considered as representative with respect to that observed in accelerators of the CERN accelerator complex. It is used to evaluate radiation effects on electronics, to be used in accelerator-like environments, and will be further presented in the next chapter.

3.2.3 Comparison of the two environments of interest

Since the project aims at developing dosimetry solutions for both accelerator and space applications, it is important to identify the similarities and differences between the two environments. Table 2 highlights their main characteristics :

Type of particle	Protons, Neutrons, Muons, Pions, Electrons …	Mainly Protons, Electrons and Heavy ions
Dose range (in SiO_2)	Up to 1 MGy	Up to 5 kGy, usually within 100-500 Gy
Dose rate range (in SiO_2)	Up to 10^{-1} Gy/s	10^{-9} to 10^{-7} Gy/s
Temperature range	Usually room temperature (RT)	-200°C to 300°C

Table 2 - Characteristics of the environments of interest in the study

It is important to note that the values of this table are extreme values, encountered in a small number of cases. However, we still choose to select these values as boundaries for the definition of the work. For instance, the mentionned temperature range in space corresponds to what can be encountered outside a satellite or spacecraft without thermal protection. This is useful to evaluate for instance, the possibility of performing low shielding environment dosimetry, to focus on very low energy particles, surface charging, etc. As a general comment, we can observe that the two environments differ on several points :

- Dose rate range : The dose rate in space is often smaller than that in accelerator environment. This can be more challenging for radioluminescence based dosimetry and will imply to optimize the sensitivity of the material and the detection chain.
- Dose range : the accelerator environment delivers higher doses which can impact the lifetime of the sensor whereas the levels reached in space are usually more limited. In this case, we'll have to ensure that the cumulated dose effects will not degrade too much the performances of the sensor.
- Temperature : Space is definitely a more challenging environment in terms of temperature. Strong variation can be expected whereas almost no variation is expected at CERN accelerators.

3.3 RADIATION EFFECTS ON OFS

Radiation effects in optical fibres refer to the changes of the macroscopic properties of optical fibres caused by exposure to ionizing or non-ionizing radiations. While optical fibre based communication and sensing systems performances are growing years after years, the implementation of such technologies in harsh environments such as space, accelerator, or nuclear industry increases. This makes the study of radiation effects on optical fibre, a strategic topic of research. To introduce the topic, we will describe the most critical radiation effects on optical fibres.

3.3.1 Basic mechanisms (Ionization processes, etc …)

Before looking into the specific macroscopic effects of radiation in optical fibres, it is important to introduce their effects at the atomic level on the silica material. The induced effect on the optical fibre material depends on the type and energy of the incident particle. As described schematically in the Figure 8 adapted from [28], the interaction of the particles can induce a multitude of processes that can mainly be distinguished in two categories : Knock-on and Radiolysis.

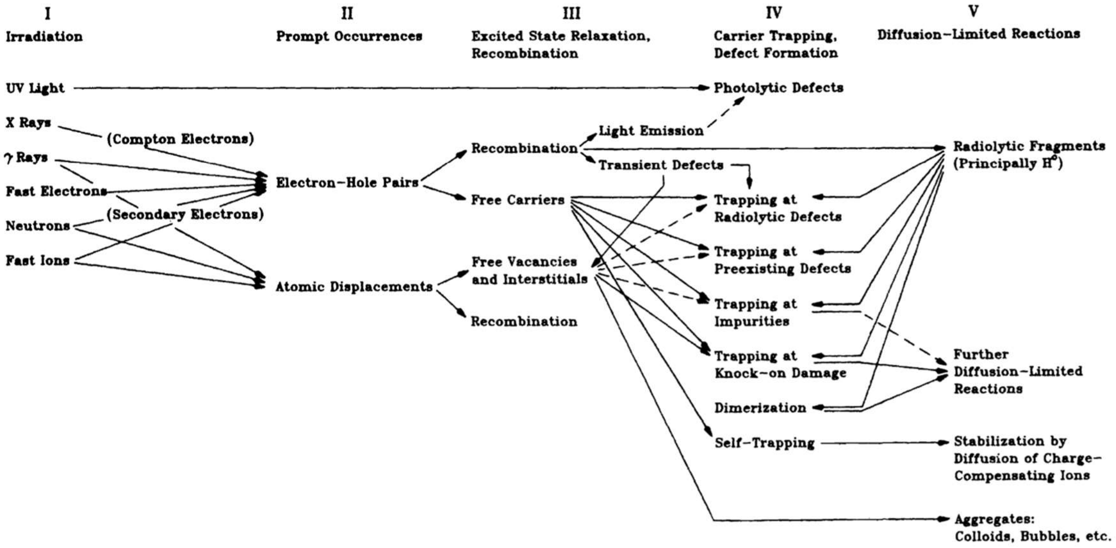

Figure 8 - Radiation effect processes depending on the type of particle, adapted from [28]

The knock-on process involves an interaction of the incident particle directly with the atoms of the target material leading to a modification of the atoms networks. Within this process, two routes are possible depending on the kinetic energy conservation conditions. If the total kinetic energy is conserved, we consider the interaction as elastic whereas if it is not, we therefore consider it as an inelastic collision.

On the other hand, radiolytic processes are induced through the interaction of the incident particle with the electrons of the target material atoms, leading to the creation of electron-hole pairs that can eventually produce atomic defects within the atoms matrix.

3.3.2 RIA (Radiation Induced Attenuation)

As described in the Chapter 3.1, one of the most important parameter of an optical fibre, is its attenuation at the wavelength of operation. In standard application, the attenuation is known during the selection of the fibre and will in most of the case not change significantly during the lifetime of the system. However, in harsh environment, the attenuation can increase catastrophically due to ionizing radiation and potentially cause the loss of functionality of an optical link.

The RIA is due to the interaction of the ionizing particles with the silica matrix, dopants and impurities, generating numerous point defects in the silica of the fibre core and cladding. These optically-active point defects, also called color centres, interacts with the photons travelling through the optical fibre, absorbing the photons then resulting in a increase of its attenuation.

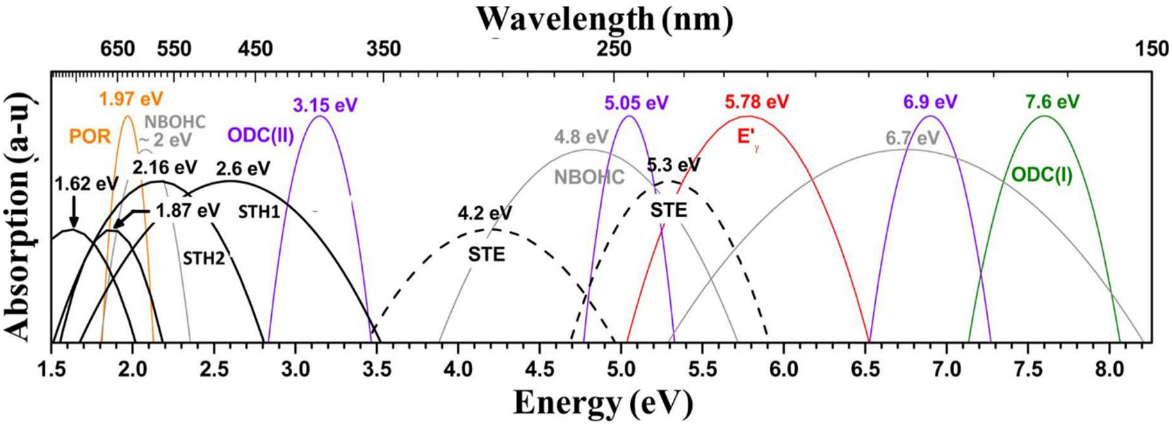

Figure 9 – Known defect related absorption bands in Silica glass in the UV-Visible region adapted from [29]. More information on the defects can be found in [30]–[34]

This phenomenon generally increases with the TID, and depends greatly on the composition of the fibre, and the environmental condition of the irradiation (mostly the dose rate, injected optical power and temperature) [29], [35]. Whereas some of the RIA effects disappear after the stop of the irradiation, through recovery processes, part of the initial RIA amplitude is stored in the fibre and impacts the transmission until the end of life of the optical link. This is an important issue for communication and sensing applications in harsh environment because it can drastically reduce the lifetime of the system. The RIA is expressed in dB/km or dB/m when the fibre exhibits very important radiation sensitivity. Additionnaly, a study of spectral measurements of the RIA or absorbance in an optical fibre can highlight characteristic absorption bands related to the presence of some known dopants and impurities. To illustrate this, in Figure 9 we display the main known defects with their optical absorption bands in the UV-Vis range in pure silica glass.

Whereas the RIA is a strong disadvantage for the use of optical fibres telecommunication based systems in radiaton harsh environment, it can become an asset for radiation sensing. Indeed, some very specific types of optical fibres have a linear RIA response versus TID, allowing measuring the TID along the fibre over long distance when coupled with distributed sensing techniques.

3.3.3 RIE (Radiation Induced Emission)

Another effect of ionizing radiation on silica glasses is the emission of parasitic photons from the optical fibre material, through different mechanisms. These emissions are named Radiation Induced Emission (RIE) among which we distinguish two different contributions:

- **Cerenkov Emission** : This process takes place when a charged particle travels in a material at a greater velocity than the phase velocity of light in the same medium. This emission is created during the travelling of the charged particle in the medium, generating electromagnetic shockwaves that result in the emission of a photon. It is to be noted that this process is quasi instantaneous and that the generated photon is emitted with an angle with respect to the propagation direction of the charged particle, depending on the target medium and speed of the charged particle. For instance, this angle is around 46° for silica when the charged particle travels at almost the speed of light in vacum. The emission spectrum of the Cerenkov contribution is very wide, and ranges usually from the UV-Vis up to the IR. This can be a problem for visible light telecommunication or sensing systems, especially under high flux of particle, inducing a degradation of the Signal to Noise Ratio (SNR). For instance, in Figure 11, we show the Cerenkov emission spectrum obtained in an optical fibre under an electron flux that illustrates how the spectrum can cover the whole visible spectrum range.

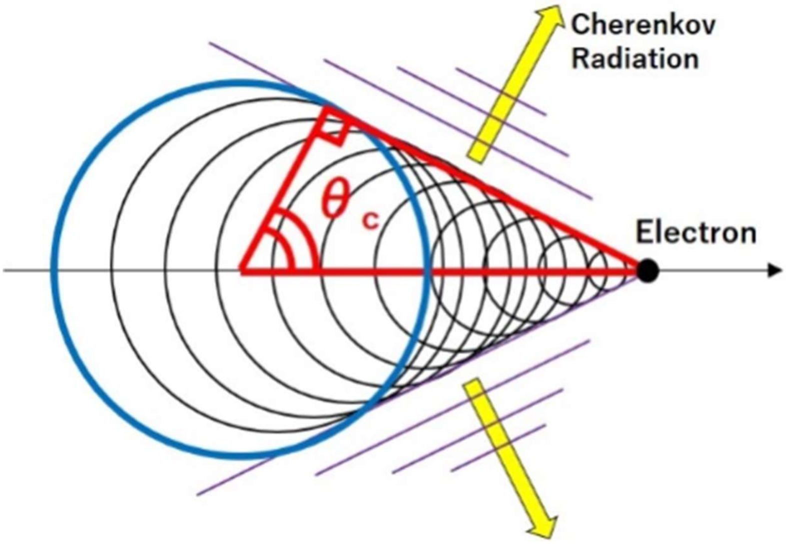

Figure 10 - Representation of the Cerenkov effect in the matter when a charged particle (here an electron) travels at speed greater than the celerity of the light in the same dielectric medium. The circles are the electromagnetic waves generated by the dipole formed by the charged particle, and the yellow arrow represents the direction of propagation of the emitted photons. Adapted from [36]

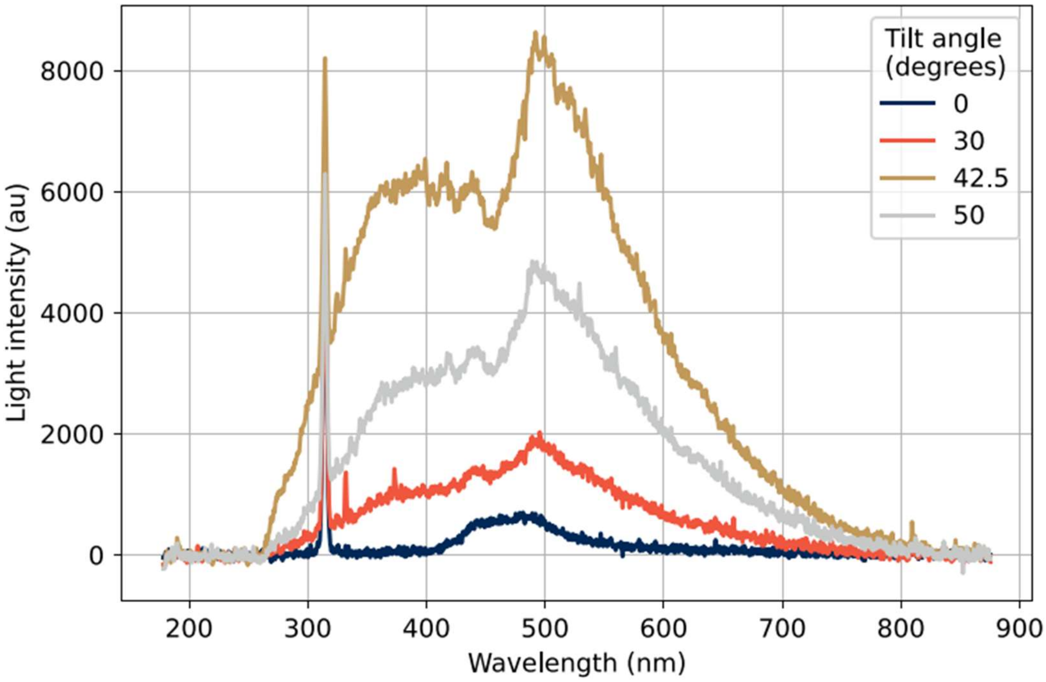

Figure 11 - Cerenkov spectrum in Gd^{3+} *doped fibre under electrons for different angles adapted from [37]. The sharp emission peak from the Gd*$^{3+}$ *centers is also visible at 314 nm.*

- **Radioluminescence** : This process occurs in optical fibres when ionizing radiation passes through the material. Some atomic defects can be excited and release a photon during the deexcitation process. These defects can be intrinsic or generated by the irradiation. In contrast of Cerenkov effect, the radioluminescence emission is not angle dependent. The photons are generated in all the directions by the colour centres. A part of these photons will be within the acceptance angle cone of the fibre and therefore guided along the fibre up to the optoelectronic equipment. As we will describe further in this work, this phenomenon can be used to perform radiation dosimetry because for some specialty fibres, the number of photons emitted by the fibre under irradiation is proportional to the dose rate. That means that measuring this radiation induced light from one end of the fibre with a detector, gives under certain conditions, an online monitoring of the radiation environment fluctuations.

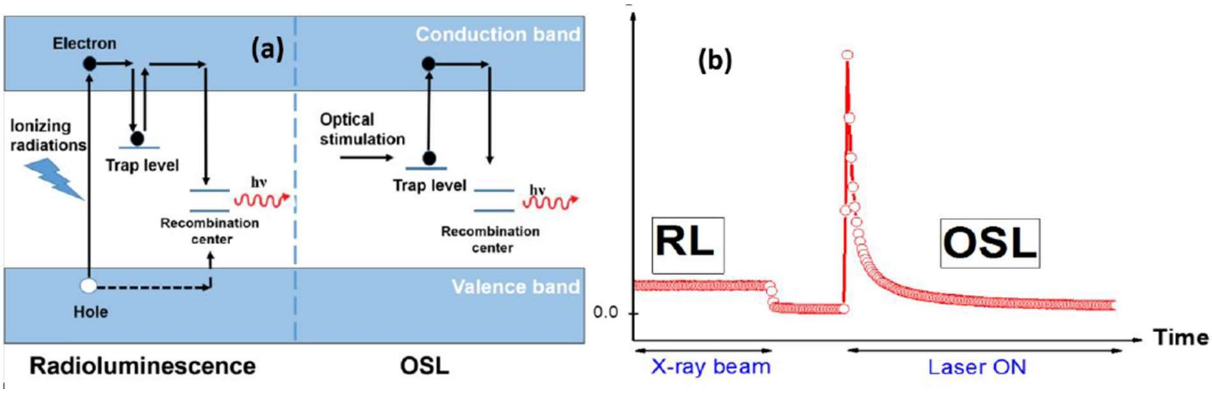

Figure 12 - Simplified Radioluminescence process adapted from [15]

- ***Optically Stimulated Luminescence (OSL)*** *:* This process occurs in certain optical fibres placed under irradiation, exposed to a laser excitation during or after the irradiation. When the particles travels through the fibre, it creates or excitate defect that can trigger the emission of a photon through RL as explained earlier. However, in some cases, the generated defects are more stable in time remain in this pseudo-stable state for long time. It is then possible, using a laser excitation, to trigger the recombination of these defects leading to the emission of photons. The number of photons relates to some extend to the number of generated defects and therefore to the deposited dose. This phenomena can be used to integrate the dose over a period time by exciting the defects at a specific wavelength at regular interval to determine the TID reached within the given period of time. In the best OSL sensors, the integration of the signal measured during the OSL is linear to the dose, within a limited dose range. Therefore, the interval of the reading of the OSL needs to be adapted depending on the expected dose rate.

3.3.4 RIRIC (Radiation Induced Refractive Index Change)

This phenomenon takes place in optical fibre when a very high fluence of particles damages sufficiently the silica matrix of the fibre to induce a change of its refractive index and therefore, of its guiding properties. This is an important problem for in-core nuclear instrumentation with optical fibre sensors.

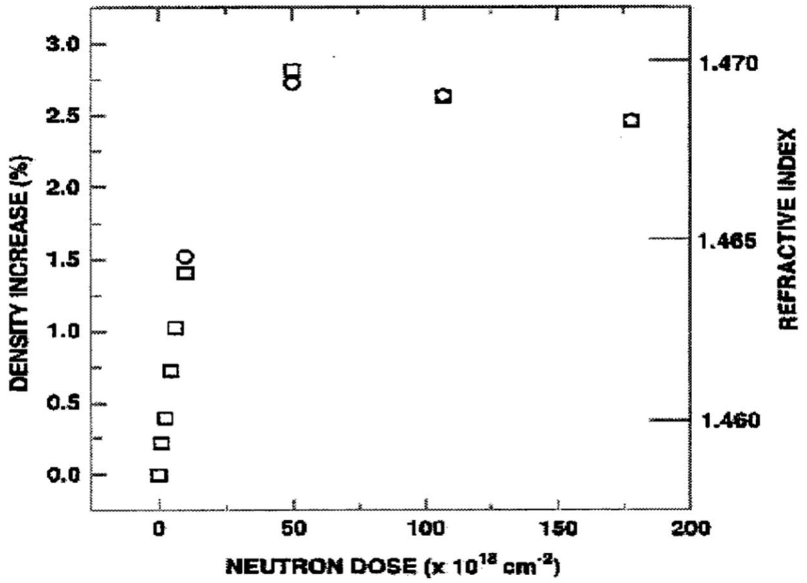

Figure 13 - Densification or change in refractive index vs neutron fluence in bulk amorphous silica glass from [38], [39].

This effect will not be considered in the rest of this manuscript as it is negligible in the environments of interest within the PhD project.

3.3.5 Environmental parameters impacting the radiation response of an optical fibre

The final response of an optical fibre under irradiation can be affected by many environmental parameters such as :

- **Dose levels** : The TID ranges have to be assessed for both regular optical fibre application in harsh environment or optical fibre based dosimetry. Indeed, the strategy adopted for the RHA (Radiation Hardness Assurance) or the sensor design depends often greatly on the expected TID. For instance, the RIA increases with dose. Meaning that the design of an RIA optical fibre based sensor needs to take into account the final expected RIA value, making sure the expected value is within the dose range of the sensor.
- **Dose rate** : The rate at which the radiation is deposited on a device (an OF for instance) has sometimes an important effect on the response of the equipment. For RHA or dosimetry purposes, the expected dose rate range needs to be estimated. Moreover, as a general rule, a good dosimeter needs to be as insensitive as possible to dose rate effects. With RL and Cerenkov it is different in the sense that the measure relies directly on dose rate.

- **Temperature** : This parameter can affect in different ways the radiation response of an optical fibre under irradiation. For instance, the RIA tends to be more important at lower temperature because the thermal annealing is less efficient at lower temperature but it has to be considered that the generation efficiencies, and not only the bleaching efficiencies, can be temperature dependent. It can also affect the efficiency of some RL processes as it will be further described in this work.

Depending on the environment, these different parameters can be estimated though experiments, simulations or approaches combining theoretical and experimental studies.

3.4 DOSIMETRY

3.4.1 Dosimetry techniques

To measure radiation, we need to rely on the measurement of its effects on a sensor. This effect can be of different forms such a change of tension or capacitance for instance. Nowadays, many different types of radiation sensors co-exist, with no perfect solution for all the applications : each domain of application requires one or several adapted sensor(s).

Ionization chamber

One of the most used and ancient radiation sensor is the ionization chamber, This devices used a closed enclosure, containing a well known gaz which is submitted to a strong electric field via electrodes placed across the chamber. When there is no radiation, there is no current travelling between the two electrodes. However, when a particle crosses the chamber, the ionized gaz will release electrons. These electrons, captured by the electric field will induce a current across the electrodes, and the dose deposited in the chamber can be therefore estimated by monitoring this current. This technique is for instance used in the LHC machine to detect beam losses.

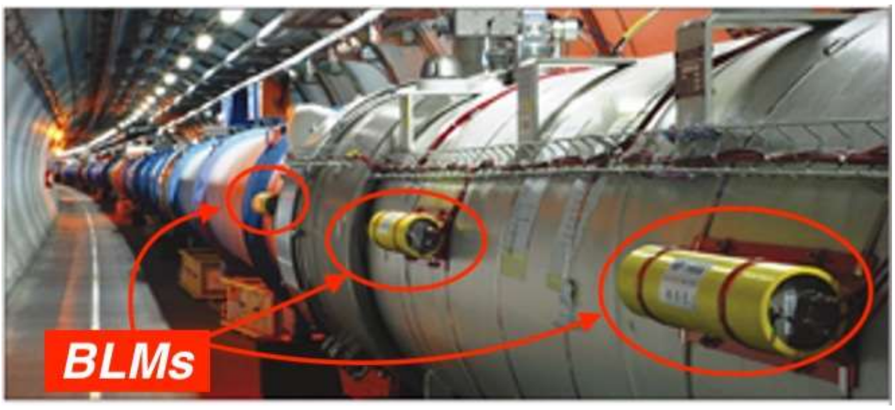

Figure 14 - Picture of the LHC machine, with a set of Beam Loss Monitors based on the ionization chamber technology [40]

Metal-Oxyde based dosimeters

Another form of radiation sensor, is based on the measurement of the radiation effect on an electronic component. The most widely used is the RadFET which is based on the voltage threshold shift (V_{th}) induced on a MosFET transistor, due to charge trapping in the oxide [41]. This device is for instance extensively used in the RadMON system performing radiation monitoring in the CERN accelerator complex [42] but also in space [43].

Figure 15 - RADMON system including RadFET for radiation monitoring in the CERN accelerator complex [44]

3.4.2 Active Optical fibre based dosimetry

Similarly to electronics, optical fibres suffers from radiation through different ways as described before. In some case, the radiation effects can be used to provide a measurement of the radiation environment surrounding the optical fibre. We can consider that this type of measurement use mainly three different effects : The RIA, the RL and the Cerenkov emission.

RIA :

RIA is at the basis of important dosimetry systems used nowadays. For some specific optical fibres, such as P-doped fibres, the relation between the RIA and the TID is simple (eg. linear over a given dose range) allowing to determine the TID by a measure of attenuation after an adapted calibration. One of the advantage of this technique is that one can perform recurrent reading without monitoring continuously the P-doped optical fibre without loosing information (if the saturation of the fibre is not reached).

Another advantage is that since the RIA occurs across the length of the optical fibre, depending on the localized TID, once can retrieve the TID deposited in portion of the fibre using time-of-flight reflectometry techniques. In other words, the RIA techniques allow distributed measurement with for instance the first implementation in an accelerator in DESY [45] followed more recently by an implementation at CERN [46].

RL :

While RIA allows either point or distributed measurements, RL only allow today a point measurement which can be limiting in certain application. However, RL usually allows measurement of dose rate/dose much lower than RIA based techniques, depending on the dosimeter architecture. Furthermore, the monitoring of the RL signal allows a real-time, online monitoring of the radiation which can be extremely important for some application such as pulsed beams. To summarize, we can see the RIA and RL based dosimetry systems as complementary in this mission, in the sense that RIA brings the distributed measurement, while RL allows point but more sensitive dosimetry.

Cerenkov :

This technique is similar to RL in the sense that the measure of the photons emitted by the fibre under irradiation allows the online monitoring of the radiation field. However, since the Cerenkov emission is angle dependent, this method is more adapted for beam line instrumentation for instance. On the other hand, Cerenkov emission has the advantage of its extremely fast response time. This can be an asset when monitoring pulsed beams with very short pulse durations or time between spills [47], [48].

3.4.3 Comparison of the performances and characteristics of dosimeters

As described in this chapter, the most used active dosimeters have different features, that can be compared to highlight the advantages or disadvantages of the different solutions depending on the planned application.

Table 3 - Comparison of the features of different active dosimeter technologies

	RADFET	**Ionisation Chamber**	**RL based dosimeter**	**Cerenkov Based dosimeter**	**RIA based dosimeter**
Distributed sensor or point sensor?	Point	Point	Point	Point*	Can be distributed or Point
Size	Medium	Large	Small	Small/medium	Small
Best Spatial resolution	Few centimeters	Few centimeters and above	Below 1 cm	Below 1 cm	Typically 1m , dependent on the interrogation techniques
Dose sensitive?	Yes	No	No	No	Yes
Direct dose rate Measurement?	No	Yes	Yes	Yes	No
Angle dependence	No	No	No	Yes	No
Types of particles	All	All	All	Charged	All

As shown in Table 3, the listed dosimeter technologies differ in their features which make them complementary. No dosimeter is perfect for all cases, but depending on the application, some of them will be more or less adapted to our needs.

4 EXPERIMENTAL SETUP, INVESTIGATED SAMPLES

In this chapter we first describe the optical fibre sensors considered in this project. We will then introduce the different techniques employed to characterize their performances as well as the developed experimental test benches.

4.1 OPTICAL FIBRE SENSORS UNDER STUDY

4.1.1 Manufacturing of the optical fibre sensors under study

In the framework of this PhD work, we included different types of optical fibres in our study, because of their interesting radiation detection capabilities which are described in the next sub-chapter. These materials are specifically designed for dosimetry applications by the PhLAM group [49], [50] from the University of Lille and the CNRS [51] (Centre National pour la Recherche Scientifique) in collaboration with UJM and other partners. Using their technological platform, they are able to produce differently doped optical fibres depending on the application. One of the interesting feature of this installation is the ability to produce exotic optical fibres via the sol-gel method with compositions that are not usually easily achievable with more conventional melt-quench and vapor phase methods manufacturing techniques [52]. This method starts from the preparation of nanoporous silica monoliths (shown in Figure 18) from tetraethylorthosilicate (TEOS) precursor [53], with are then stabilized at 1000 °C. After this step, the obtained xerogels are soaked in a solution containing salts of the choosen doping compound which will diffuse into the samples. Once the doping step finished, the samples are dried at 50 °C for several hours to remove the solvents, leaving the doping ions inside their nanopores.

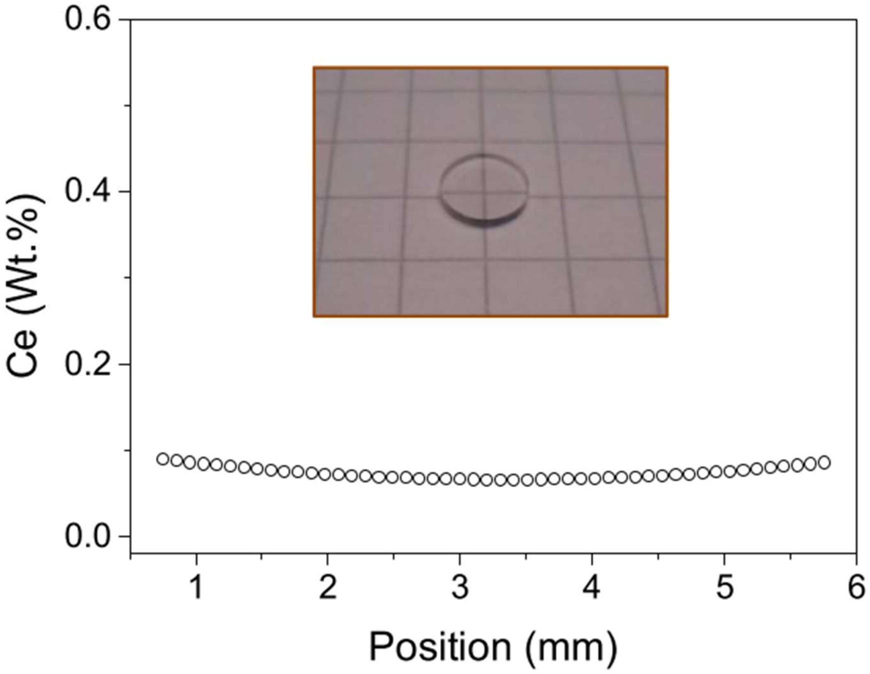

Figure 16 - Cerium element distribution profile in Ce-doped silica glass obtained by sol-gel route measured via EPMA adapted from [54]. In the inset is shown a picture of the cross section of the preform in which the measurement was performed.

Finally, the samples are densified in air or helium at 1200 °C to obtain transparent and cylindrical doped silica glasses [55]. As shown in Figure 16, the obtained silica glass is characterized by an almost uniform dopant distribution from across the rod. It is important to note that the atmosphere composition during the densification process impacts the RL efficiency of sensors as shown in [55]. For instance, in the silica matrix of Ce-doped fibres, cerium ions are found in the form of Ce^{4+} and Ce^{3+} ions with respective concentrations depending on the oxidizing-reducing conditions during the material fabrication [56]. However, while the Ce^{3+} ions have a very efficient radioluminescent and photoluminescent response, the Ce^{4+} ions do not present emission under irradiation or solarization. For this reason, it is important for the final sensitivity of the detector to increase as much as possible the concentration of Ce^{3+} ions in the silica glass and to limit the presence of Ce^{4+} ions. This is where the densification process plays a role (not only used for this reason). Figure 17 compares the optical absorption spectra of Ce-doped glasses produced and densified in two different atmospheres (Air and Helium). This data shows that the densification under helium atmosphere induces an increase of the concentration of Ce^{3+} ions. The same effect is observed in Cu-doped fibres, where the Cu^{+} concentration is promoted by the densification under inert atmosphere [55].

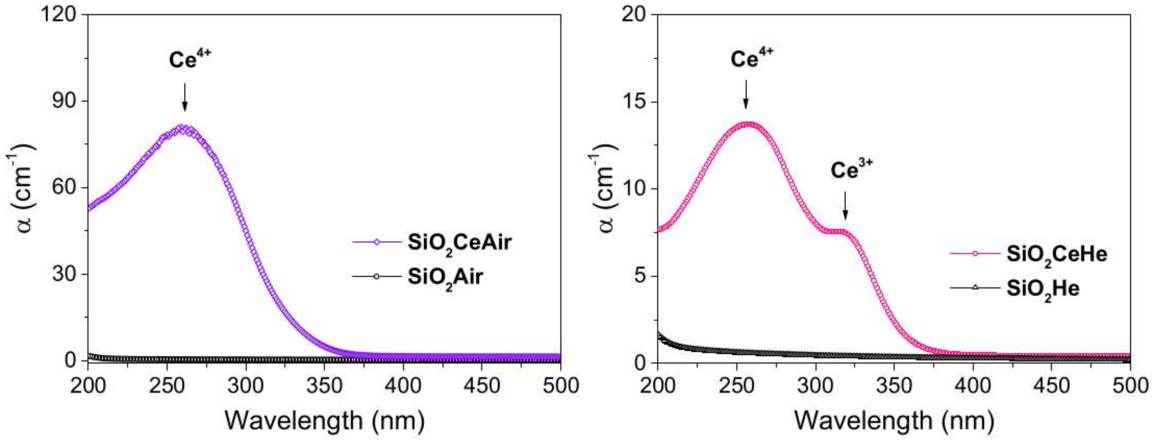

Figure 17 - Optical absorption spectra measured in Ce-doped silica glasses obtained by the sol-gel route technique using densification in Air and Helium. Adapted from [54]

The next step of the process is the drawing, which consist of "jacketing" the obtained doped cylinder with a pure silica tube and draw it under temperature of around 2000 °C into a millimeter sized cane [54]. In some cases, an Air-clad design is desired and therefore small silica capillaries are added around the millimeter sized doped silica cane, before stacking a pure silica tube around it [55].

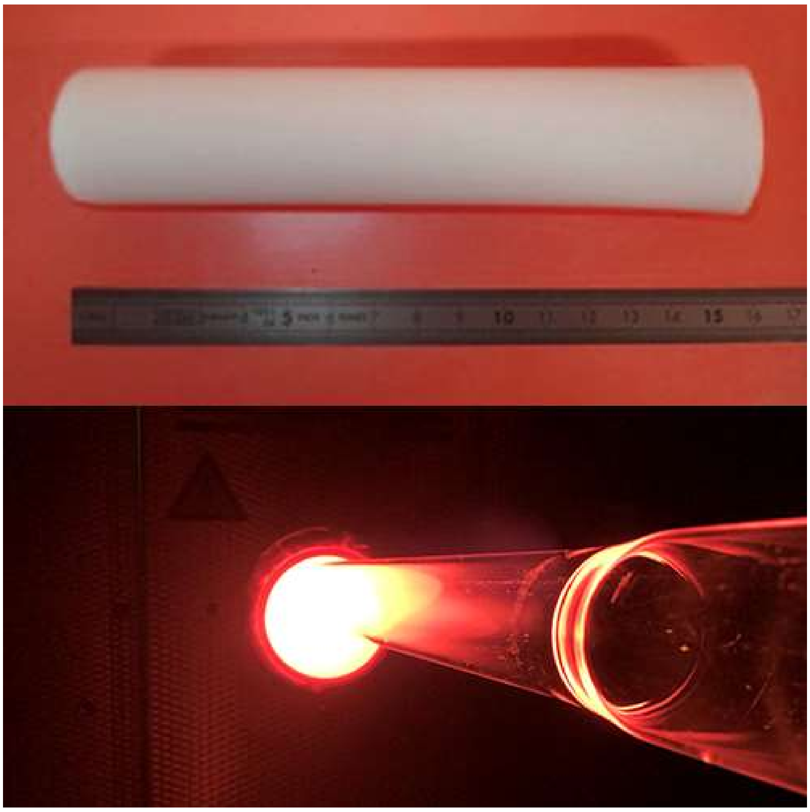

Figure 18 - Picture of a preform before densification next to a ruler and the oven used during for the densification process [50]

The obtained cane is called a rod that can be characterized as it is when optically coupled to a large (500-1000 µm) diameter silica optical fibre.

However, the drawing process can also be modified to obtain a 125 µm diameter optical fibre, allowing its splicing with conventional optical fibres. The drawing is performed using a drawing tower, visible in the picture shown in Figure 19. Once the fibre is drawn at the correct diameter, one or two coating is applied and the fibre spooled for storage and transportation.

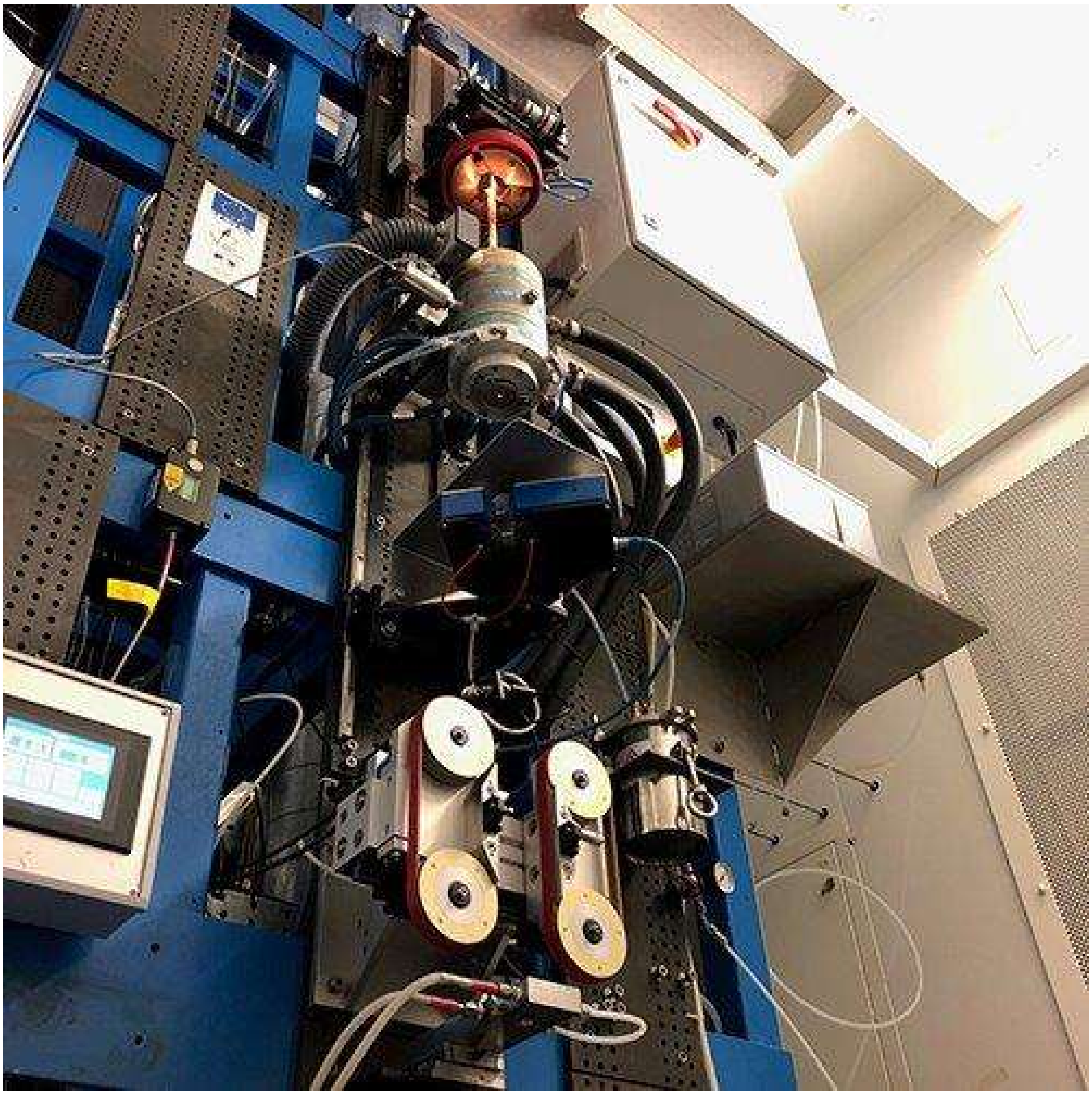

Figure 19 - 12 m high Drawing tower of the Fibertech technological plateforme, as part of the PhLAM Group installation. Extracted from [50].

Finally, at the end of this process we obtain an optical fibre composed of a doped silica core, surrounded by a pure silica cladding, and then by a lower refractive index coating. An important thing to note here is that the guiding of the light relies, for these fibres, on the difference of refractive index between the low index coating and the cladding. Indeed, the F300 Silica material used for the cladding has almost the same refractive index as the core, thus no total internal reflection occurs between the core and the cladding. An illustration of the mechanical structure of the optical fibre is presented in *Figure 20*.

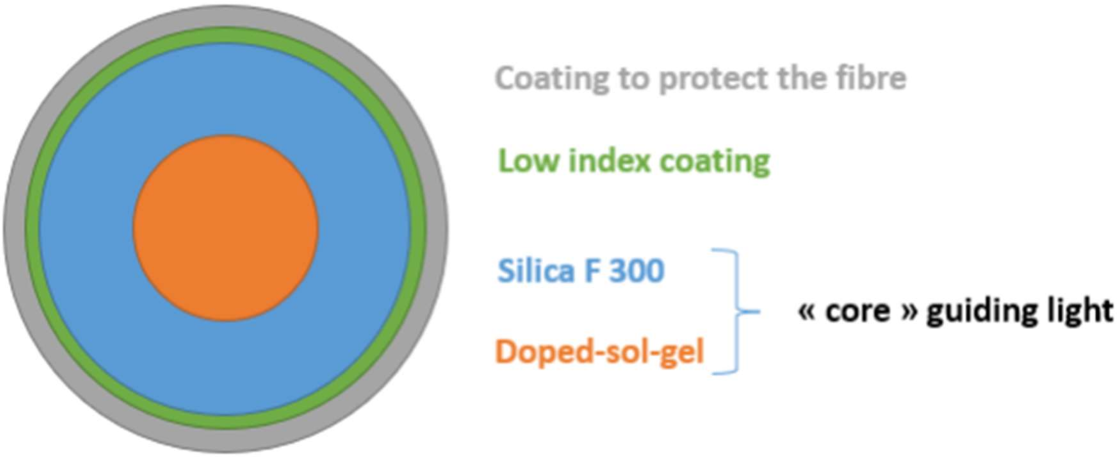

Figure 20 - Mechanical structure of the manufactured optical fibre via sol-gel technique.

4.1.2 Optical fibres considered in the study

During this PhD work, we decided to focus our research activities around the characterization of a selection of doped sol-gel glasses. Hereafter the list of the selected doped glasses and their respective doping mass concentration :

- Cerium (Ce) – 300 ppm [57]
- Copper (Cu) – 250 ppm [57]
- Co-doped with Cerium and Copper (CuCe) – Same concentration as in singly doped fibres [57]
- Gadolinium (Gd) – 1000 ppm [58]
- Co-doped with Cerium and Terbium (CeTb) – 0.07 wt.% for Cerium ions and 0.08 wt. % for Terbium ions.

We also have investigated the response of another type of optical fibre sensor, produced using a nitrogen doped preform from the FORC Group (Russia), and drawn into a MMF by the iXblue company. This fibre is also called ND2, and was already extensively studied in [26], [59]. Due to limited quantities available of this fibre, we only performed a partial characterization on it.

Table 4 reports information about the geometrical dimensions as well as the material used to produce these optical fibres. We can see that both the cladding and the low-index coating are commercial grade materials, from the DeSolite company. The size of the doped core is around 50 µm diameter, surrounded by a 125 µm cladding. The low-index coating thickness is between 25 and 40 µm, whereas the protective coating is between 160 and 200 µm thick.

Fiber sample + Reference	**Core size (doped region + silica around)**	**Core doped-region Size**	**Primary coating size (cladding material)**	**Secondary coating size (coating material)**	**Refractive index difference**	**cladding material**	**coating material**
Ce: T3276	125 µm	50 µm	180 µm	340 µm	~ 0	DeSolite® DF-0016	DeSolite® 3471-3-14
Cu: T3277	125 µm	50 µm	150 µm	350 µm	~ 0	DeSolite® DF-0016	DeSolite® 3471-3-14
CuCe: T3269	120 µm	50 µm	184 µm	322 µm	~ 0	DeSolite® DF-0016	DeSolite® 3471-3-14
CeTb: T4074	125 µm	54 µm	200 µm	325 µm	~ 0	DeSolite® DF-0016	DeSolite® 3471-3-14
Gd: T3274	125 µm	50 µm	177 µm	330 µm	~ 0	DeSolite® DF-0016	DeSolite® 3471-3-14

Table 4 - Informations about the optical fibres under study, produced by the PhLAM group

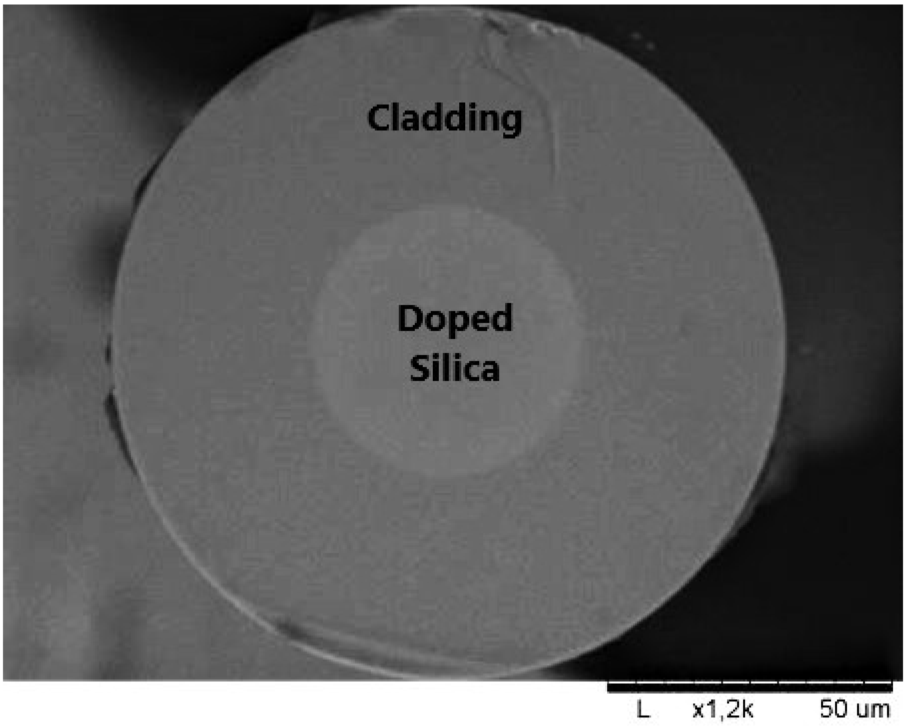

Figure 21 - Picture of the Ce-doped fibre under microscope with clear distinction between the core and cladding

For illustration, a picture under microscope of the core and cladding of a Ce-doped fibre is shown in Figure 21, where both regions are clearly observable due to their contrast.

Now that we have introduced all the investigated fibres and presented their manufacturing process, we will detail the previous studies available in the literature on these types of optical fibres for dosimetry applications. Some of the presented characterization that will be presented were performed from the same collaboration group (UJM, Phlam, Univ. Nice, Univ. Clermont Ferrand) that collaborate in the framework of several ANR projects such as SURFIN or FIDELIO. Other fibres have been already deeply investigated by other research team in Europe (mainly).

The presented studies are of different natures, and spans from studies of the material optical and structural properties, time-resolved and steady state photoluminescence emission, and optical responses when exposed to different kinds of ionizing radiation.

4.2 STATE-OF-THE-ART AND PREVIOUS KNOWLEDGE OF THE INVESTIGATED OPTICAL FIBRES

4.2.1 Ce-doped

The first fibre type to be presented in this chapter is the cerium-doped optical fibre which has been extensively studied by other research groups in the past. One of the first work presenting the potential of sol-gel Ce-doped optical fibres for dosimetry in high-energy physics and X-ray detection is found in [60], [61]. Their photoluminescence response as well as their emission under X-rays are characterized. In [61], the RL response is found to be linear under x-rays produced at 20 and 32 kV from 6×10^{-3} to 40 mGy/s. The main domains of utilization of this type of fibre, investigated by the authors from University of Milano-Bicocca, Milano Italy, are proton therapy dosimetry and x-rays measurements. For proton therapy, they showed that this fibre sensor has a good sensitivity under a 138 MeV proton beam with a reproducibility of the measurement within 0.5 %, and a good linearity in the 0.1 – 10 Gy range [62].

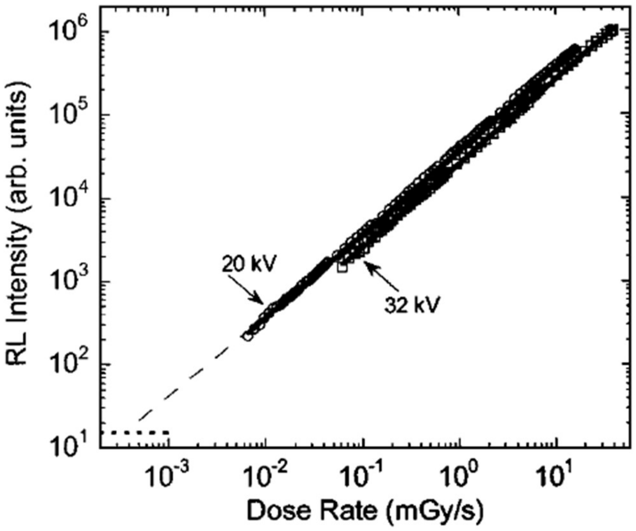

Figure 22 - Linearity of the RL response of Ce-doped silica glass under 20 and 32 kV X-rays. Adapted from [61]

However, in [63] the authors shows that during a radioluminescent measurement performed on a Ce-doped fibre, as shown in Figure 23, we can observe an increase of the RL emission during a redondant irradiation, at the fixed dose rate of 10 Gy/s. This is problematic for dosimetry application, since the response should remains as stable as possible over time and dose. The authors suggest that this is an effect related to intrinsic deep traps, possibly linked to oxygen deficient centers, that acts as electrons traps competing with the RL centers.

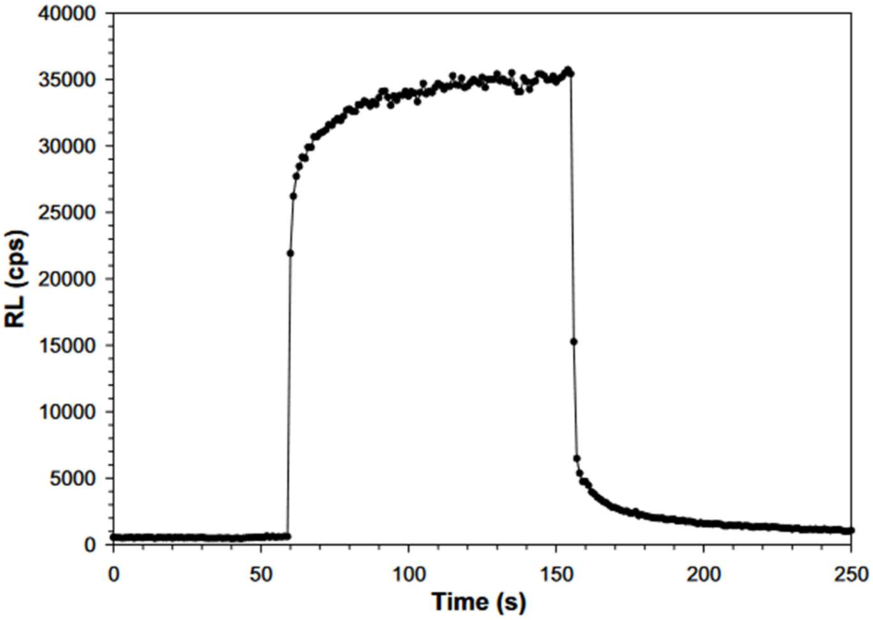

Figure 23 - RL response over time of a Ce-doped fibre under 12 MeV electrons, at 10 Gy/s. Adapted from [63] to highlight the detailed presence of deep traps expected to be inducing the observed increase of the signal during the irradiation.

More recently, UJM/ Univ. Lille and Nice started investigation this type of optical fibres sensors for potential application in X-rays detection, nuclear plants, medical applications. For instance, the response of such sensor under X-rays up to high dose rates was investigated and shown to be linear until at least 30 Gy/s [54] . This was to our best knowledge the first study on such inorganic sensor for high dose and dose rate. A study of the RL response under X-rays of a Ce-doped fibre based on an air-cladding configuration was performed in [64], confirming again the linearity of the RL response over dose rate. Furthermore, a study performed at the TRIUMF facility (Vancouver, Canada) showed that the RL response of the Ce-doped fibre under protons of energies from 35 to 65 MeV, provides a monitoring of the proton flux evolution during the irradiation [65]. The authors provided as well a spectrum of the RL emission in this fibre as shown in Figure 24. The emission is characterized by a broad band ranging from roughly 380 nm up to 750 nm with a maximum amplitude located at 460 nm. This emission is attributed to the allowed 5d →

4f optical transition of Ce^{3+} ions [54]. Additionnally, the decay time of this emission around 450 nm has been investigated via photoluminescence using a 322 nm laser excitation, and estimated to be around 84 ns [64]. This decay time means that we could potentially obtain a maximum time resolution of 500 to 1000 ns using such sensor for dosimetry in pulsed beams for instance.

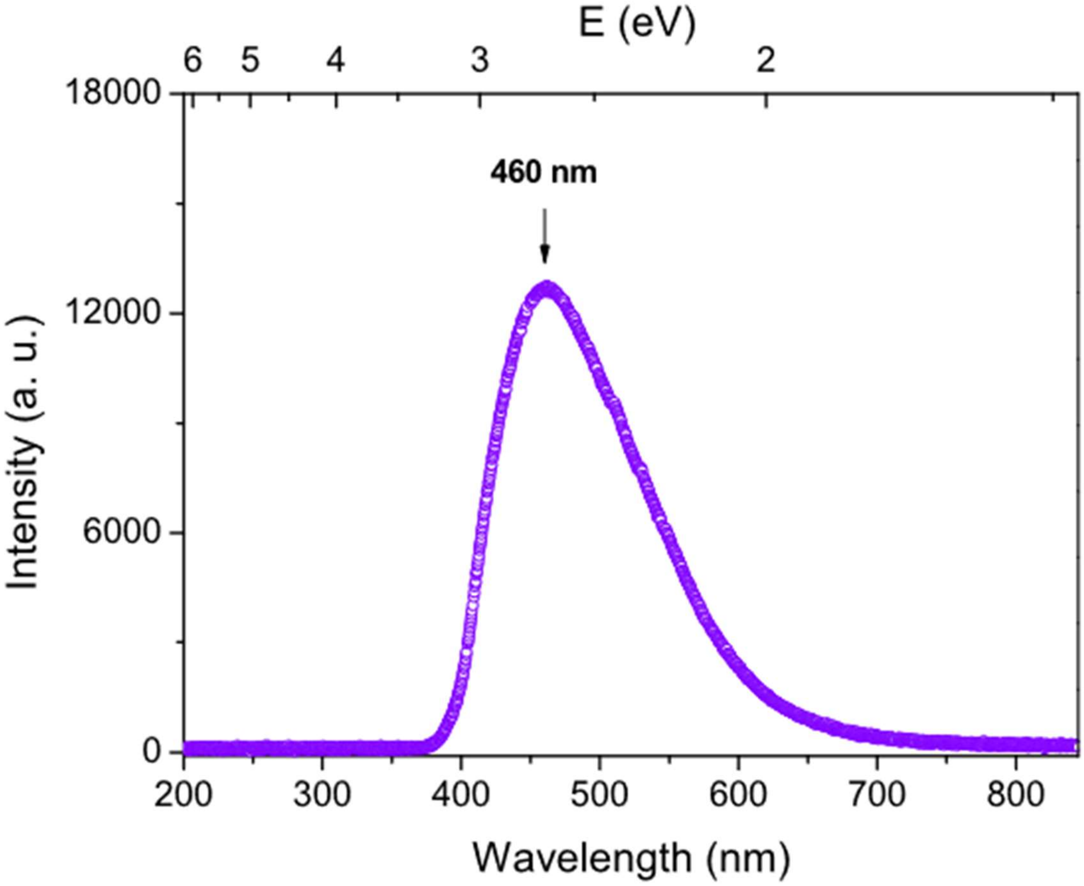

Figure 24 - RL emission spectrum of an Air-Clad Ce-doped optical fibre irradiated under 100 kV X-rays.

4.2.2 Cu-doped

This second type of doped fibre triggered interest of researchers for dosimetry application since the 1990’s, owing the strong emission in the blue green region exhibited under ionizing radiation or photoluminescence excitation. This emission is mostly due to the Cu^{+} ions, whose emission efficiency is increased by a factor 40 when the densification of the sol-gel glass is performed under helium [55]. This type of optical fibre sensor is characterized by a broad emission band centered around 550 nm as shown in the Figure 25

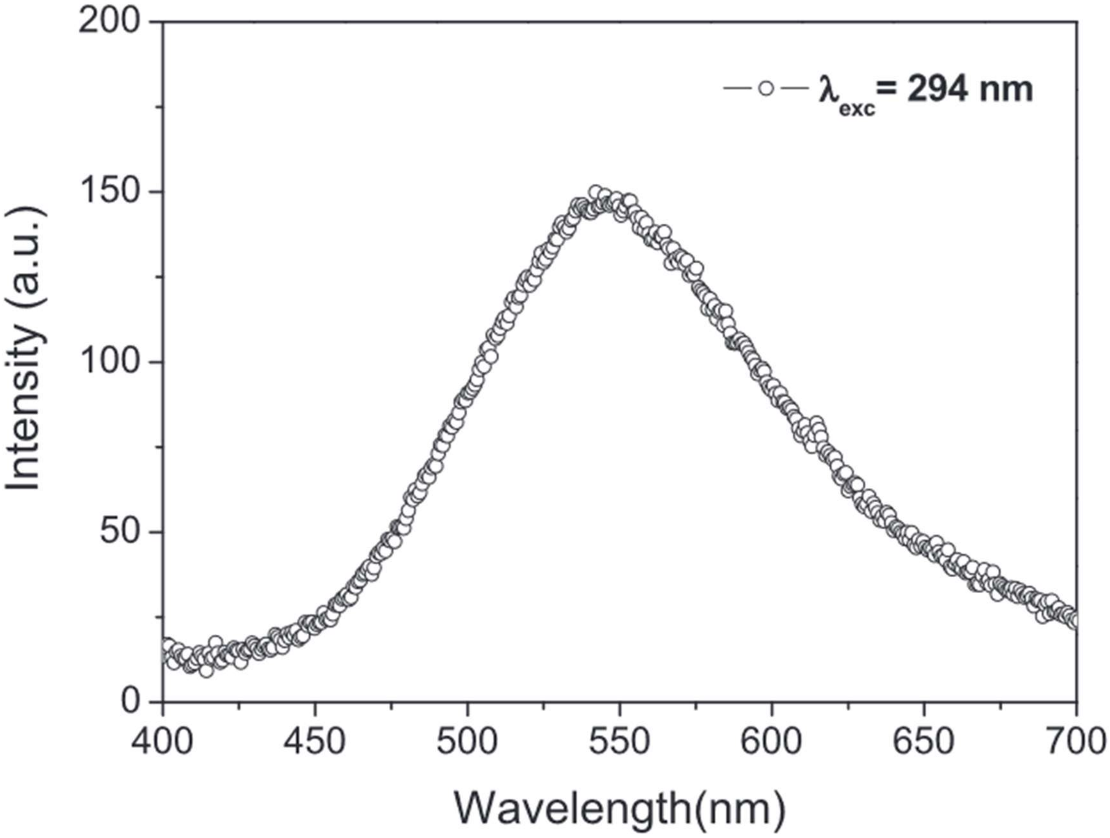

Figure 25 - Photoluminescence emission spectrum measured on a sol-gel copper doped optical fibre under 294 nm laser excitation. Adapted from [55]

Along with Ce-doped fibre, this fibre has been tested under protons in *[65]* exhibiting promising detection capabilities for protons therapy application. In addition, during a study focused on low-dose/low dose-rate conditions, this fibre has been tested under X-rays and has shown a linear RL response with the dose rate from 260 µGy/s to 800 mGy/s *[66]* as shown in *Figure 26*.

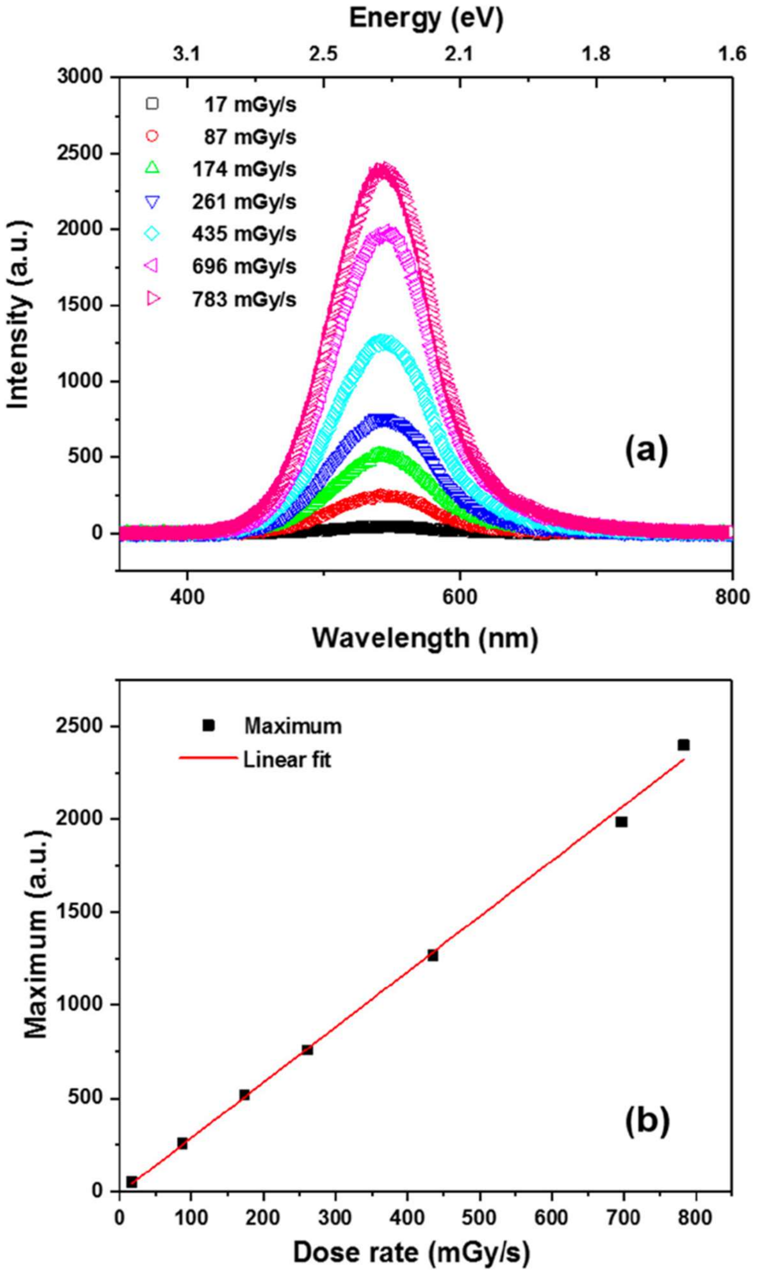

Figure 26 - a) RL emission spectra of Cu-doped fibre under X-ray excitation at different dose rates and b) Linearity of the RL emission versus dose rate. Adapted from [66].

4.2.3 CuCe-codoped

Combining the same techniques employed to develop the singly Cerium and Copper doped fibres, the PhLAM group designed the co-doped CuCe fibre. This fibre contains doping concentration of Cerium and copper ions in the same proportions as in the singly doped sensors. The idea behind this design is to profit at the same time from the highly efficient

RL emissions of both Copper and Cerium ions.

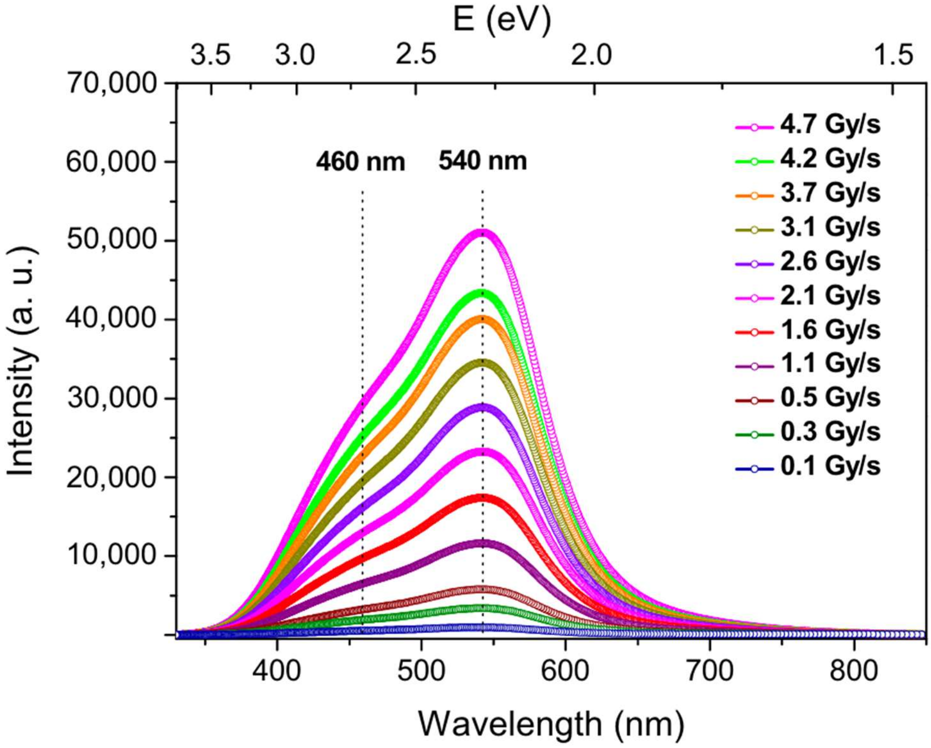

Figure 27 - RL spectra obtained on CuCe co-doped optical fibre sensor under X-rays at different dose rates measured at the LabHC laboratory. Adapted from [57].

As shown in *Figure 27*, the RL spectra obtained from this sample fibre extends from roughly 380 nm up to 700 nm, covering both previously presented Cerium and Copper emission ranges. When measuring the RL emission at different dose rates with a PMT to integrate the whole visible spectra, we obtain the *Figure 28*-a, demonstrating the linearity of the RL response between 1.1 mGy/s and 34 Gy/s as shown in *Figure 28*-b.

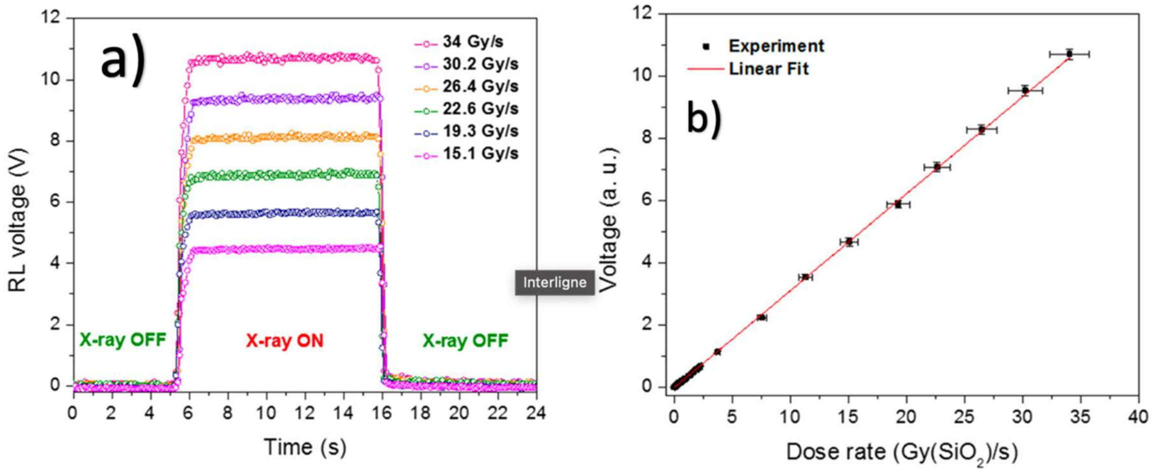

Figure 28 - a) RL emission of CuCe co-doped fibre under X-rays at different dose rates measured with a PMT, b) Linearity of the RL emission versus dose rate. Adapted from [57]

Additionnally, the time decay constants of the emission of this fibre have been measured under PL excitation as shown in in *Figure 29*. It shows that the lifetimes of the emission from Cerium ions in this fibre is of about 91 ns (compatible with the measurement performed on the singly Cerium-doped fibre in *[64]*. The Copper ions emission is described by a two-exponential model with 9.3 and 45 µs time decay constants, similarly to what was observed in the singly copper doped fibre, as presented in *[67]*.

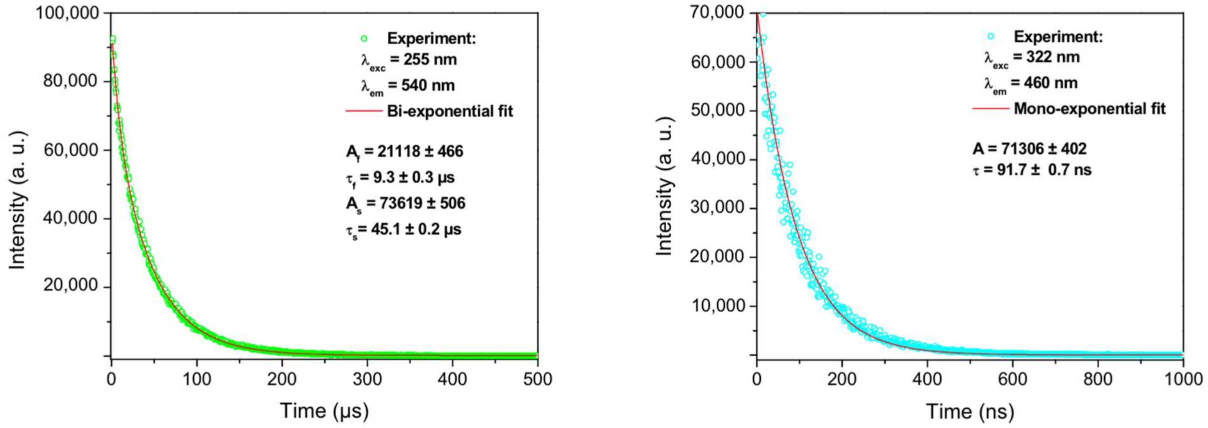

(a) (b)

Figure 29 - Emission decay attributed to a) Copper ions and b) Cerium ions in CuCe-codoped fibre under PL excitation. Adapted from [57].

4.2.4 Gd-doped

The Gd-doped fibre has been designed using the same sol-gel technique used for the other optical fibre sensors, to profit from its known high radiation detection efficiency (especially for neutrons). Before this design, Gd^{3+} ions have been mainly used as a co-dopant in some fibres to enhance the luminescence of rare-earth dopants. In this case, the choice was made to use the Gd as the sole dopant. This fibre was characterized under PL as shown in Figure 30, showing a sharp emission peak centered at 314 nm with an emission time decay of 1.5 ms. This sharp emission is attributed to the Gd^{3+} transition between $^6P_{7/2}$ and $^8S_{7/2}$ states [68].

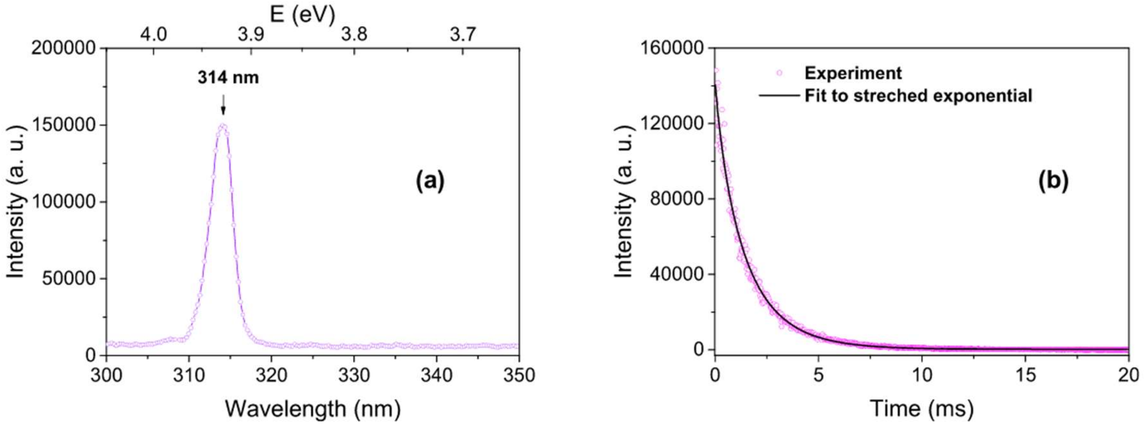

Figure 30 – a) Gd^{3+} emission spectrum in Gd-doped fibre measured under PL excitation at 275 nm. b) Emission time decay. Adapted from [69].

Additionnally, the fibre sensor response has been characterized under X-rays at the MOPERIX facility of Laboratoire Hubert Curien showing linear RL response between 125 µGy/s to at least 12.25 Gy/s as shown in Figure 31. These results show the potential of such doped fibres for a variety of applications such as a scintillator for ionizing radiations, and energetic particle beams.

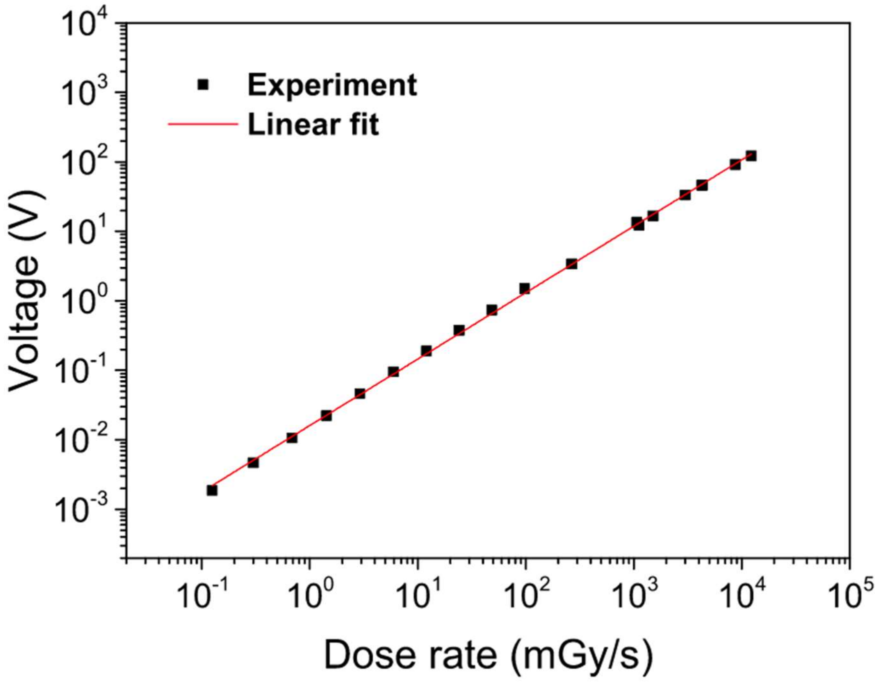

Figure 31 - RL emission linearity versus dose rate of Gd-doped optical fibre material under X-rays tested at the MOPERIX facility of Laboratoire Hubert Curien. Adapted from [69].

4.2.5 CeTb co-doped fibre

The first work introducing Cerium and Terbium co-doped silica based optical fibre, produced via the sol-gel technique to our knowledge is found in [70], where the authors produced co-doped glasses at different concentrations before characterizing them under photon excitation. The idea behind this co-doped composition is to profit from the efficient energy transfer from Ce^{3+} to Tb^{3+} ions, to induce a redshift of the emitted luminescence towards longer wavelengths, characterized by lower attenuation and greater sensitivity efficiencies of most detectors. The investigation of the authors, shows that there is an optimal concentration of Cerium and Terbium ions, due to a strong quenching of the luminescence with doping concentration higher than this optimum. As reported in Figure 32, the luminescence spectra under laser excitation at different wavelengths shows a serie of emission bands characteristics from Terbium ions.

The investigated fibre in this PhD is produced by the PhLAM group using the same sol-gel procedure described earlier, introducing both Cerium and Terbium ions in the silica glass.

The fibre was designed towards the end of the PhD project, therefore there was no previous characterization of the radiation response of this fibre.

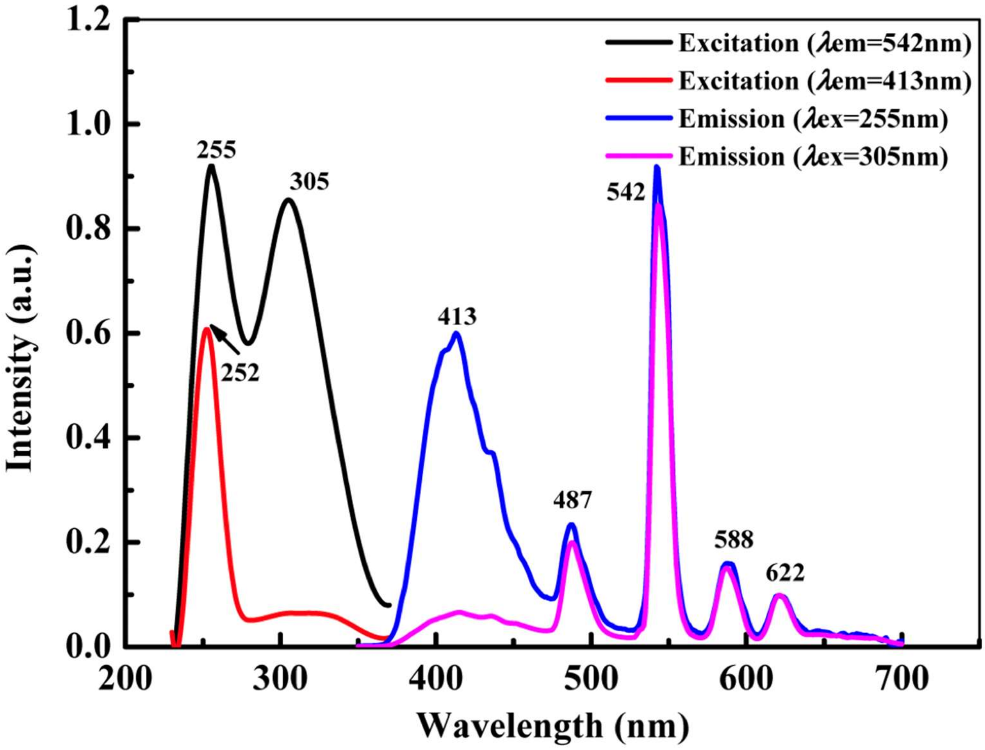

Figure 32 - PL excitation spectra of a Ce/Tb co-doped silica glass optical fibre. Adapted from [70].

4.2.6 N-doped fibre

This fibre differs from those presented earlier in this chapter by the manufacturing technique used for its fabrication. It has been extensively studied in [59], and was designed at first as a radiation hardened optical fibre in the infrared domain for harsh environment. During this study, the optical properties of the fibre have been presented focused on the impact of dopants on RIA notably. Further work [71] highlighted a RL emission present in this fibre, potentially interesting for dosimetry applications. The RL response has been characterized under X-rays at the MOPERIX facility of Laboratoire Hubert Curien, for 1 cm and 10 cm long samples, showing a good linearity from 1 mGy to 50 Gy/s as shown in Figure 33.

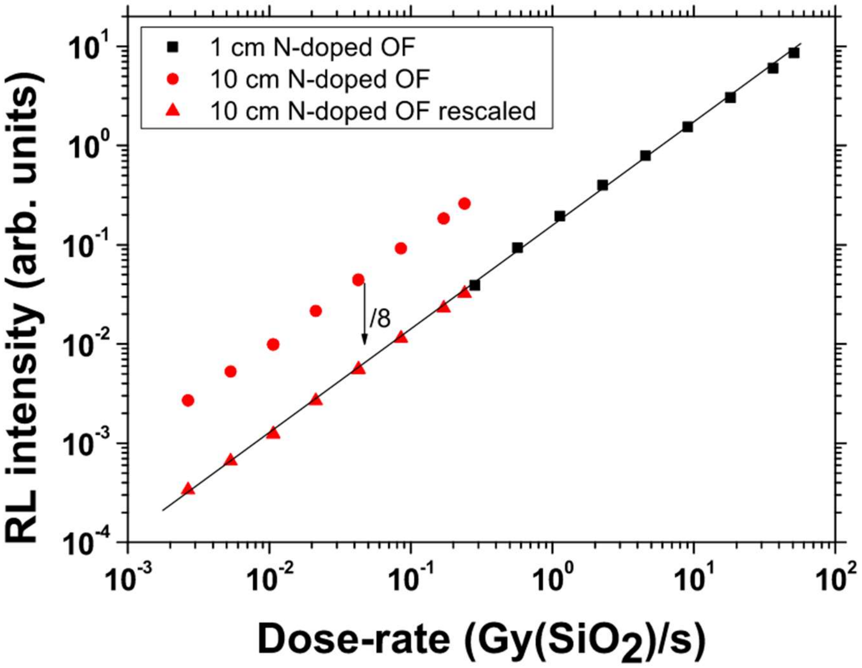

Figure 33 - RL response under X-rays measured on 1 and 10-cm long samples of nitrogen doped fibre. Adapted from [71].

Furthermore, as shown in Figure 34, the RL emission under gamma rays measured on a 2 m long sample was investigated at low dose rate showing linearity which was not maintained below 1 mGy/s due to some technical issue with ambient light pollution.

Finally, this fibre was characterized under proton beam at the TRIUMF facility in Vancouver, Canada, in a water phantom in order to evaluate its capability to reproduce the bragg peak of protons in water. In comparison, a markus chamber was tested at the same time since it is the reference dosimetry solution in such configuration, for medical application. As shown in Figure 35, the nitrogen-doped fibre highlighted a very good behavior, reproducing quite sucessfully the Bragg peak under 74-MeV proton beam. It has to be noted that this fibre produced better results than Cerium-doped and Copper-doped fibres, previously tested in this configuration [65]. Althought this result is promising, some small mismatches with markus chamber indicates that further improvements are needed in order to match the accuracy requested in radiotherapy applications [71], [72].

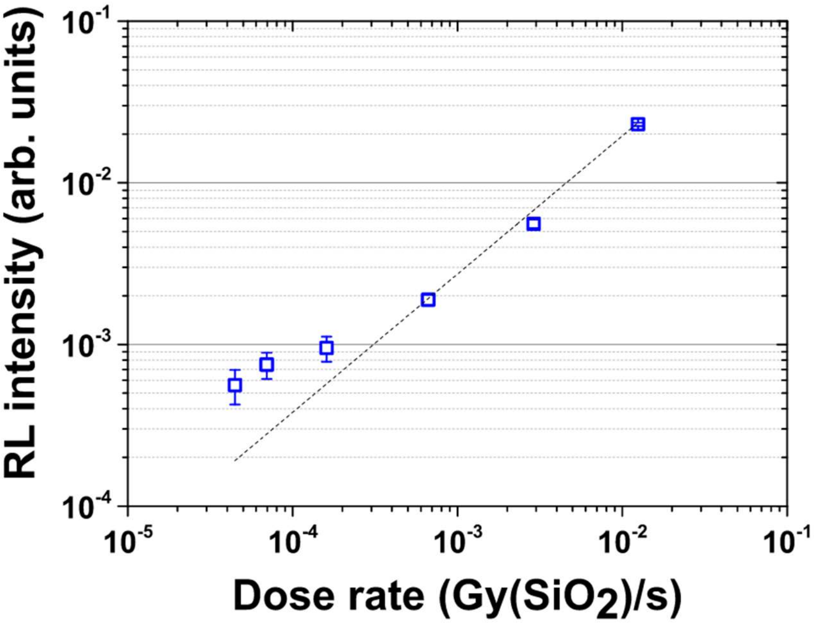

Figure 34 - RL emission under gamma rays measured at the Co60 facility at CERN on Nitrogen-doped optical fibre. Adapted from [71].

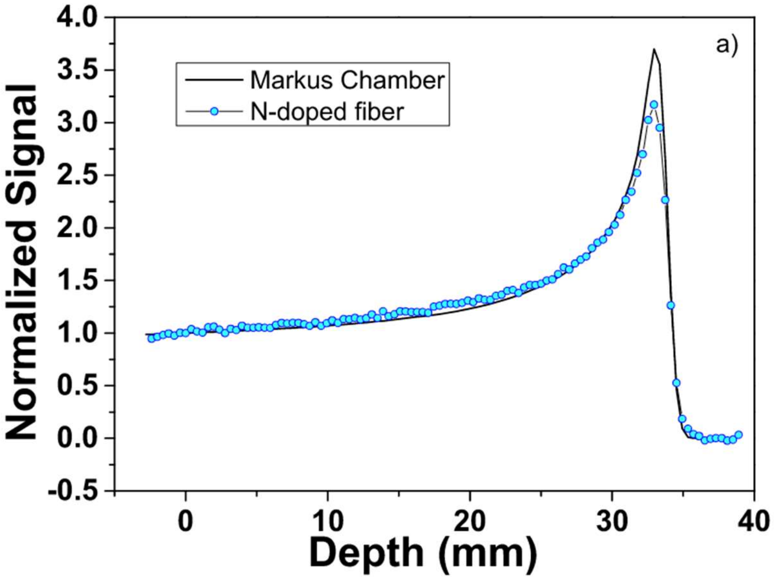

Figure 35 - RL response of nitrogen-doped fibre and markus chamber measurements in water phantom under 74-MeV protons reproducing the Bragg peak of protons in water. Adapted from [71].

4.3 EXPERIMENTAL SETUP AND TECHNIQUES – OF

In this chapter we present the experimental setups and techniques used to characterize the dosimetry potential of the fibres included in this PhD work.

4.3.1 RL setup

As described in the precedent chapter, the RL process takes place during the irradiation of an optical fibre, and can serve in certain conditions as a mean to monitor radiation dose rate (and giving access to the dose knowing the irradiation duration). For this purpose we need to measure the light emitted by the radiosensitive optical fiber by guiding it towards a detector deported in a radiation-free zone.

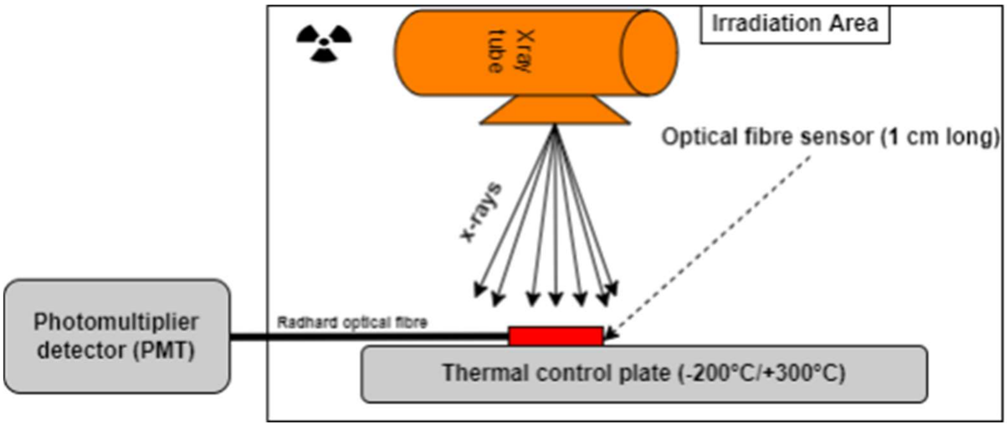

Figure 36 - Experimental setup used to characterize the RL response of optical fibres. The detector can either be a PMT or a spectrometer depending on the expected data.

Indeed, since the detector used during the characterization under irradiation is radiation sensivite, we need to deport the measurement outside the irradiation area. This is done via transport optical fibre, which should be a multimode radiation hardened optical fiber. In this work, we use as example a specialty multimode optical fiber radiation hardened un the NIR range from Draka, which expresses good radiation hardness in the visible. The sensor comprises a short length (less than five centimers) of doped optical fibre that is fusion spliced to this transport optical fibre. When the fusion splice is not possible, optical connections are ensured using optical glue and capillaries maintaining aligned the radioluminescent silica glass and the transport optical fibre. This latter technique is for instance used in this work to test the doped silica glass rods which are larger than standard multimode optical fibre diameters.

As shown in *Figure 36*, we use either a spectrometer or a PMT (PhotoMultiplier Tube) to measure the photons emitted from the optical fibre sensor under test during the irradiation. The advantage of the PMT is its extremely high sensitivity (able to perform single photon counting for the best references) thanks to important amplification factor. This is an interesting feature when dealing with low RL signal. Additionnally, PMTs are fast detectors which for the best detectors, allow time resolution of about 3 ns which enables characterizing fast RL processes. However, PMTs do not provide any spectral information, which is an important feature when one would like to understand the basics mechanism and point defects related to RL, as well as the different evolutions of the various involved emission bands with dose or dose rate. The PMT used during this PhD work was a Hamamatsu H9305-13 while for the spectrometers we mostly used the Ocean optics Jazz and QE65000 models. The PMT is fed by a power supply, with the possibility to modify its amplification factor by changing the voltage applied to an input. The output of the PMT is then connected to an oscilloscope to collect, display and save the raw data. For the spectrometers, the raw data are directly collected on the computer through the software provided by the manufacturer without any processing.

This setup can also be upgraded to evaluate the temperature effects on the RL response. For this purpose, we use a thermal plate which consists of a 30 × 20 cm² surface whose temperature can be changed across the – 120 to +300 ºC range using a combination of liquid nitrogen cooling and electrical heating. The set temperature is stabilized automatically by the controller of the device, and is expected to be accurate within 1° C depending on the location on the plate as well as the quality of the contact of the optical fibre with the plate. Additionnally, we prefer in this case to limit the error on the optical fibre temperature by waiting a sufficiently long time after reaching the set temperature, before starting the measurement. This step usually takes between 5 and 10 minutes. This is not mandatory since the optical fibre sensors usually have a fast temperature adaptation (for example during temperature measurement using FBGs sensors), but we choose to follow this step as an extra caution during the PhD work.

4.3.2 RIA setup

The RIA characterization setup used during the PhD work slightly differs from that used for RL. For this one, we added a stable light source which provides a known broad light spectrum across the UV, visible and infrared regions. This light signal is injected on one end of the optical fibre sensor under test, while the other end is connected to the spectrometer. The idea behing this measurement is to evaluate the RIA level across the optical region of interest. As described in the Figure 37, the setup can also be used in parralel to the RL setup to characterize at the same time and under the same conditions, similar optical fibre sensors. This technique is used in the rest of the PhD work.

While the temperature effects on the RIA can also be characterized using the thermal plate presented in the previous sub-chapter, we did not include this task in the study presented in this document as the number of irradiation weeks would have become excessive.

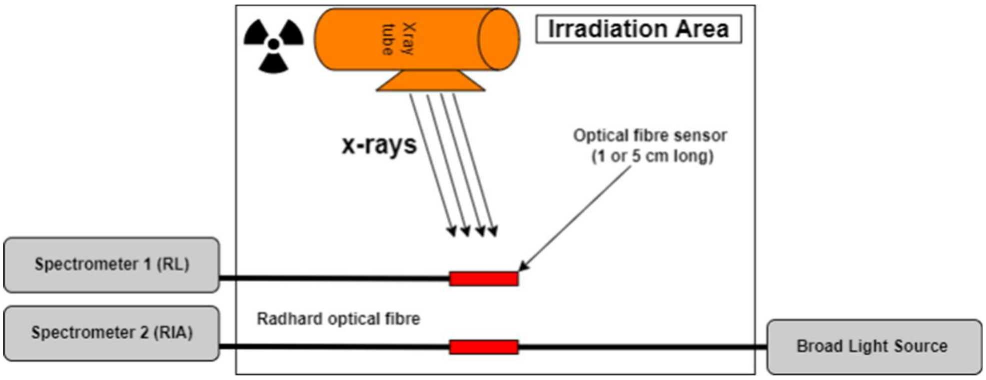

Figure 37 - Experimental setup used to perform RIA measurement on optical fibre sensors. In same figure is also present the RL setup, which was used at the same time during the PhD work to measure RL and RIA under the same exact experimental conditions.

4.3.3 OSL setup

In order to investigate the OSL response of an optical fibre, we need to irradiate it and after irradiation stops, to inject laser light at a specific wavelength, to trigger the release of the photon through recombination of the meta-stable defects. These photons are collected by the detector for integration. The integration of the photons counts can, in some conditions, provide a measurement of the dose deposited during the irradiation. This technique can be complementary to the RL, in the sense that the signal can be monitored at all times to provide RL measurement while the laser source is switched ON at regular interval to perform OSL measurement. For the OSL measurements in experimental conditions such as those of this PhD work, we usually switch ON the laser at a fixed time just after the end of the irradiation in order to avoid having the RL and OSL signals at the same time.

However, since we are injecting optical light through the optical fibre, we need to make sure that the measurement are not impacted the laser light. This is why we often use a filter placed in line between the optical fibre sensor and the detector with the role of cutting the excitation wavelength, while transmitting the OSL signal wavelengths.

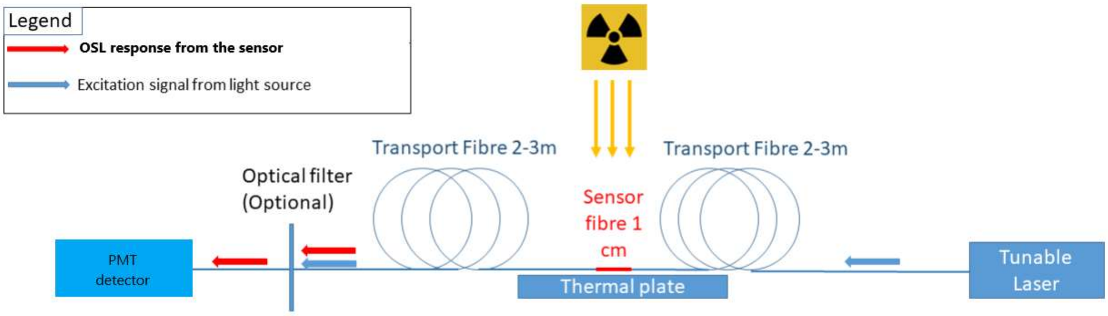

Figure 38 – Experimental setup used to characterize the OSL response of an optical fibre.

4.4 IRRADIATION SETUP

4.4.1 LABHX

Among all the radiation sources available in the market, the X-ray tubes are one of the most used facilities due to ease of use, relatively low cost, easily adjustable dose rate and small size. However, the main drawback of these devices is the effective range of the X-rays photons in the target material. The penetration range depends on the energy (and therefore directly on the tension applied to the tube), and the target material density and composition. This is a major issue for testing of electronics while it is less limiting for optical fibre testing. Indeed, with a 100 kV voltage applied to the tube, we obtain a 40 keV average energy fluence spectrum delivered on the optical fibre under test [73]. We can consider in this case that the dose deposited by the photons on the optical fibre is homogenous across the whole section of the fibre. This is not true for multiple layers of optical fibre, and therefore it limits the maximum length of optical fibres we can irradiated at the same time under an homogenous dose rate under X-rays.

Figure 39 - LABHX X-rays irradiation source located in the Laboratoire Hubert Curien of Saint-Etienne, France.

During this PhD work we used the LABHX facility of Laboratoire Hubert Curien of Saint-Etienne, France. This installation illustrated in Figure 39, provides an interesting platform to investigate the radiation effects on optical fibres, using an X-ray tube and movable plate. The current applied to the tube can be set from 0 to 30 mA, allowing the coverage of dose ranges of 100 µGy(SiO_2)/s up to at least 20 Gy/s.

4.4.2 Co^{60}

Gamma rays are the international standard for ionizing radiation testing for electronics testing for instance, as imposed by widely adopted standards [74]. Their advantages are the important penetration of the gammas across the testing material leading to an homogenous irradiation, even with bulky devices under test. The most used gamma rays source for radiation testing are Co^{60} radioactive sources. These sources are made of an artificial radioactive isotope which does not exist naturally on Earth. The Co^{60} is obtained by using neutrons to activate stable Co^{59} found easily on Earth. The radioactive decay of Co^{60} leads to the emission of two gamma photons of 1.17 and 1.33 MeV [75].

The room is equipped with a moving table allowing to change the distance between the source and the device under test, and therefore the effective dose rate. When testing an optical fibre sensor in this facility, we usually use a 5 meters long transport optical fibre, which connects the sensor to the detector placed outside the irradiation area, in the control room.

An important things to keep in mind in such testing, is that when using gammas on optical fibre, we need to use a screen layer of material to homogenize the radiation field on the fibre. Indeed, as shown in some studies, the effective dose rate can be inaccurate if this precaution is not followed, especially with extremely thin sensitive devices which are strongly affected by the thickness of material struck by incident photons prior to reach the active region [76].

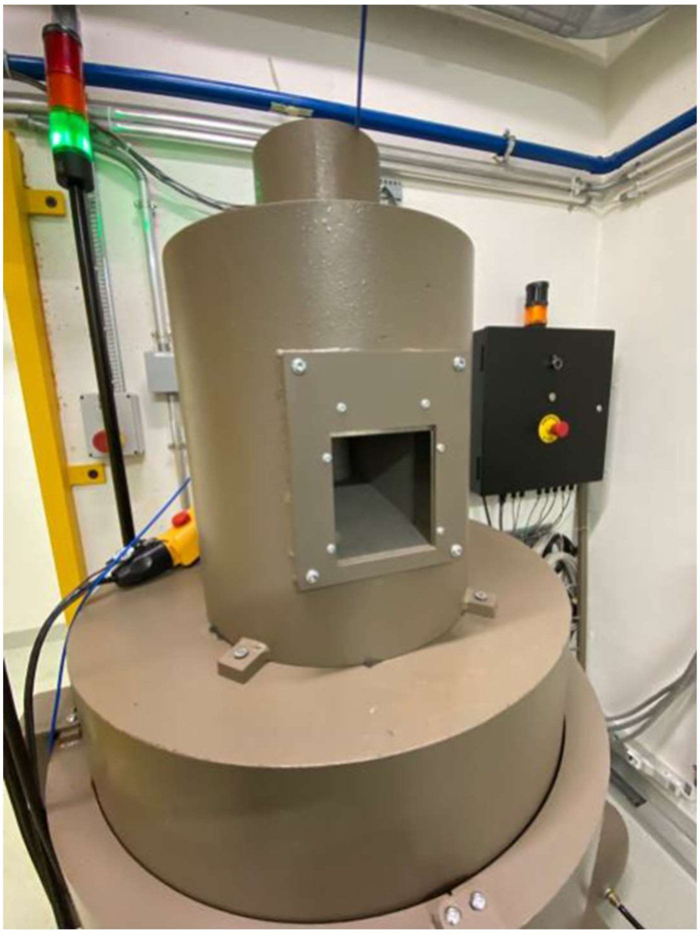

Figure 40 - Co^{60} source installation at CERN within the CC60 facility

At CERN, a facility called CC60 [77] provides access to gamma rays for radiation testing of electronics as well as radiation protection purposes. The maximum reachable dose rate was around 400 Gy/h at the time of writing of this PhD thesis, keeping in mind that the half-lifetime of the Co^{60} is 5.27 years [75].

4.4.3 CHARM

During the exploitation of the LHC [78] at CERN, an important rate of failure was observed in the electronics placed in the tunnels. Further investigation showed that it was due the intense radiation field generated by the accelerator beam interaction with the machine [79]. An important work was therefore planned and executed to improve the radiation hardness assurance of the electronics of the tunnels, through the framework of the R2E (Radiation To Electronics) project [80]. Part of this work relies on the adapted qualification and radiation testing of the electronic devices placed in the machine. To do so, it is important to perform the qualification testing in a radiation environment which is representative of the environment found in the accelerator. This environment is very specific due to the high energy particle spectra generated by the machine, and therefore not available in standard radiation testing facilities.

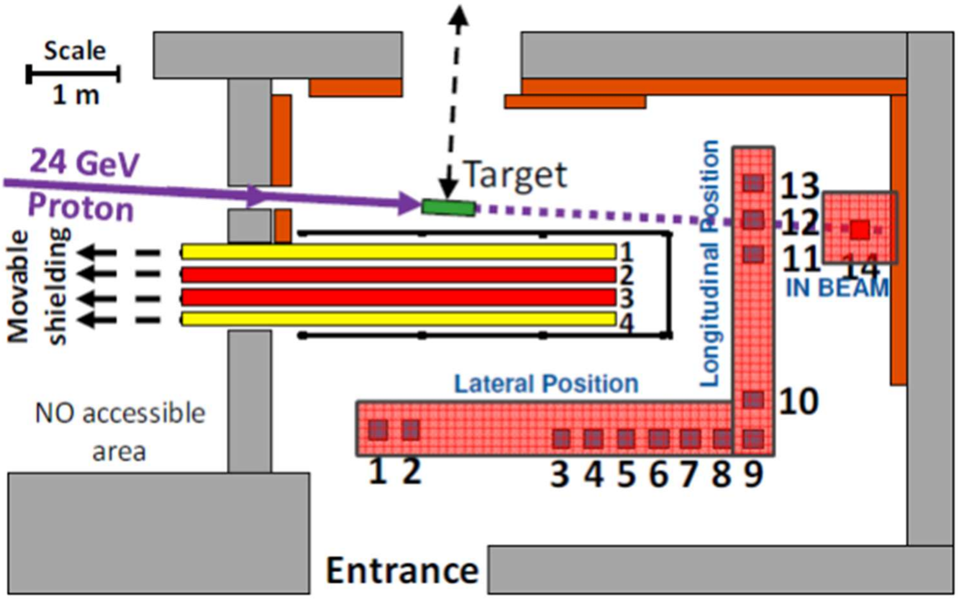

Figure 41 - Top view of the CHARM facility irradiation room, with numbered test positions [81],

This is the reason which the CHARM [44], [81] facility was developed, to obtain an accelerator-like environment facility able to reproduce the conditions supported by the electronics of the LHC. Additionnally, it has been shown in some studies that this facility can be used to estimate the SEEs expected in space during a mission, for low LET sensitivity threshold components [82] or can serve as a way to perform a screening of components at low cost [83] which becomes more and more interesting for the New Space market.

This facility uses the 24 GeV proton beam provided by the Proton Synchrotron (PS) accelerator of the CERN accelerator complex, to generate a shower of secondary particles via an interaction with a target made of copper or aluminium. The generated radiation field can be changed by placing slabs of concrete or iron in between of the target and the test position depending on the needed radiation spectrum. The obtained radiation field is a mix of different types of particules dominated by protons and/ or neutrons depending on the test position, the target material and the slabs in place.

5 STUDY OF THE RADIATION RESPONSES OF THE FIBRES UNDER INVESTIGATION

5.1 RADIATION INDUCED LUMINESCENCE

In this sub-chapter of the PhD work, we characterize the RL emission of the investigated fibres under X-rays at UJM, while monitoring the emission using a spectrometer. The idea is to to obtain online measurements, providing spectral measurements as well as kinetics versus dose, at different wavelengths of interest. When dealing with RL based dosimetry in this PhD, there was always the goal to maximize the RL signal to obtain the best SNR ratio achievable. Apart from playing with the design and composition of the sensor, this can be achieved by increasing the sensitive volume of the sensor and optimizing the detection chain of the system. This PhD work focused on the optimization of the sensitive volume.

To increase the sensitive volume of the sensor, one can increase the diameter of the fibre, or increase its length. These two options, have their drawbacks that need to be assessed. Indeed, increasing the volume of the sensor can reduce the ability to interconnect easily the sensor with standard optical fibre, or related opto-electronics detection system. This is a strong issue for deported measurements, when the detector is placed at a certain distance from the measurement point. Furthermore, the guiding properties of the sensor can be affected by this diameter increase, reducing the proportion of photons complying with TIR conditions, necessary for the collection of light towards the detection chain.

In the same time, increasing the length of the sensor can induce problems related to the self-absorption and RIA phenomena occurring in the optical fibre sensor. Indeed, the chemical dopants added in the sensor to generate and enhance the RL response of the fibre, induce often a strong increase of its intrinsic attenuation, leading to a non-linear evolution of the light collected at the output of the fibre per length unit of sensor. In top of that, the RIA during the irradiation can induce an additional loss of signal, with an effect increasing with the sensor length.

Due to the need in some potential application identified in the PhD project (mainly for use in accelerator environment), it has been decided to prioritize the ability to collect and transport efficiently the signal from the sensor towards a distant detection chain, and therefore the optimization will be done by adjusting the length of the radioluminescent fiber.

In order to assess, how the response of the sensor evolves with the length of the sensor, we performed the RL study on different lengths of fibre. We selected two lengths for the study : 1 and 5-cm. The number of lengths were restricted due to limited availability of fibre samples, irradiation time, and ability to provide an homogenous beam over a large sample while being able to reach high dose rates.

Additionnaly, as described in the previous chapters, some of the applications require the capability for the sensor to sustain large TID without overwhelming degradation of its response. For this purpose, we will extend the measurements towards high doses, as high as 600 kGy.

Finally, as introduced earlier in the document, the radiation effects on optical fibre response can be greatly affected by the dose rate of the irradiation. In order to evaluate how the dose rate can affect the evolution of the RL response of the investigated sensors, we will perform the measurements at different dose rates. The number of investigated dose rates was also limited due to limited availability of irradiation time and fibre sample length.

The final experimental plan choosen to perform all the tests on the investigated samples was defined as follows:

Table 5 - Experimental conditions of the spectral RL study on investigated fibres for different doses, lengths and dose rates.

Dose rate / Length of fibre	20 Gy/s	5 Gy/s	0.5 Gy/s
1 cm	1cm@20Gy/s	1cm@5Gy/s	
5 cm		5cm@5Gy/s	5cm@0.5Gy/s

The selected experimental conditions allow us comparing different sets of data, while changing only one parameter at a time. For instance, we can compare the 1cm@20Gy/s data with the 1cm@5Gy/s, and assume that any observed difference is related to the change in dose rate, since the same sensor length is maintained.

For all the datasets, we maintained a 8h 20 min long irradiation. All the irradiations were performed overnight using the irradiation time programmation capabilities of the LABHX facility. This leads to the final dose listed hereafter :

Table 6 - Final dose reached during the spectral RL study for each experimental conditions

Experimental conditions	Final dose
1cm@20Gy/s	600 kGy
1cm@5Gy/s	150 kGy
5cm@5Gy/s	150 kGy
5cm@0.5Gy/s	15 kGy

Furthermore, at the end of the irradiation period a recovery period was observed with no irradiation for a duration of one hour. After this recovery time, a short second irradiation of one hour was then performed on the sensor (with no change applied to the experimental bench, and without opening the door of the irradiator) under the same experimental conditions than the first irradiation.

5.1.1 RL study in Ce-doped fibre

5.1.1.1 RL Ce-doped fibre : 1cm@20Gy/s

For the first measurement, we used 1-cm long sample of Ce-doped fibre, which was exposed to a 20 Gy/s dose rate. As shown in Figure 43, the emission spectrum of this fibre sensor extends from 380 nm to 700 nm. The maximum amplitude of the radioluminescence band is found around 500 nm. When measuring the emission spectra at different deposited doses during the irradiation, we notice that the amplitude of the emission changes with dose. The emission amplitude is higher at the end of the irradiation with respect to the beginning of the irradiation. However, when normalizing the different spectra obtained at the different doses to their own amplitudes, we observe that there is a very limited change in the emission spectrum shape.

In order to better visualize the amplitude change during the irradiation, we selected a few wavelengths in the emission band, around the maximum amplitude, and plotted them versus dose during the irradiation. The obtained plot is presented in Figure 43 with in a) a linear scale view, and in b) a logarithmic scale for better visualization of the RL signal evolution across large dose range.

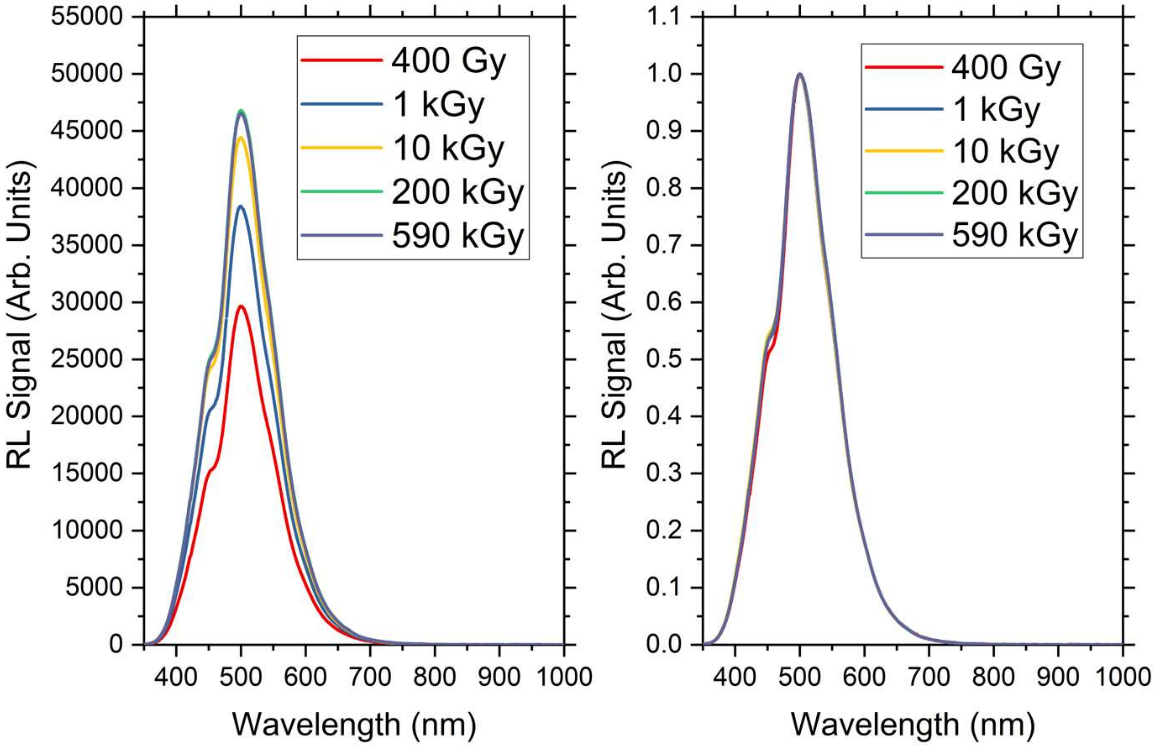

Figure 42- RL spectra measured on 1-cm Ce-doped fibre sample at 20 Gy/s, for different deposited doses. Left: Raw data, Right: Each curve is normalized to its own amplitude for shape comparison.

One of the observations we can make in this case is that the signal increases notably during the first part of the irradiation, until at least 100 kGy. Progressively, the signal increase rate reduces to finally reach a stable response from 100-200 kGy up to the end of the irradiation at 600 kGy. The signal is found stable within 0.5% from the stabilization to the end of the irradiation. This is a very interesting observation since this change in amplitude at the beginning of the irradiation was already documented in the past, and attributed to deep electrons traps as described in chapter 4.2.1. However, no previous work, to the best of our knowledge presented such data which shows that the signal becomes stable after a 100 kGy irradiation. Furthermore, the fact that the signal restarts at a similar level after a 5 hours long recovery time, tends to suggest that this obtained stability of the signal might rather be a long term effect than a transient effect. This paved the way to treatment of the optical fibre sensor before use, using pre-irradiation in order to stabilize the response of the sensor during the dosimetry application.

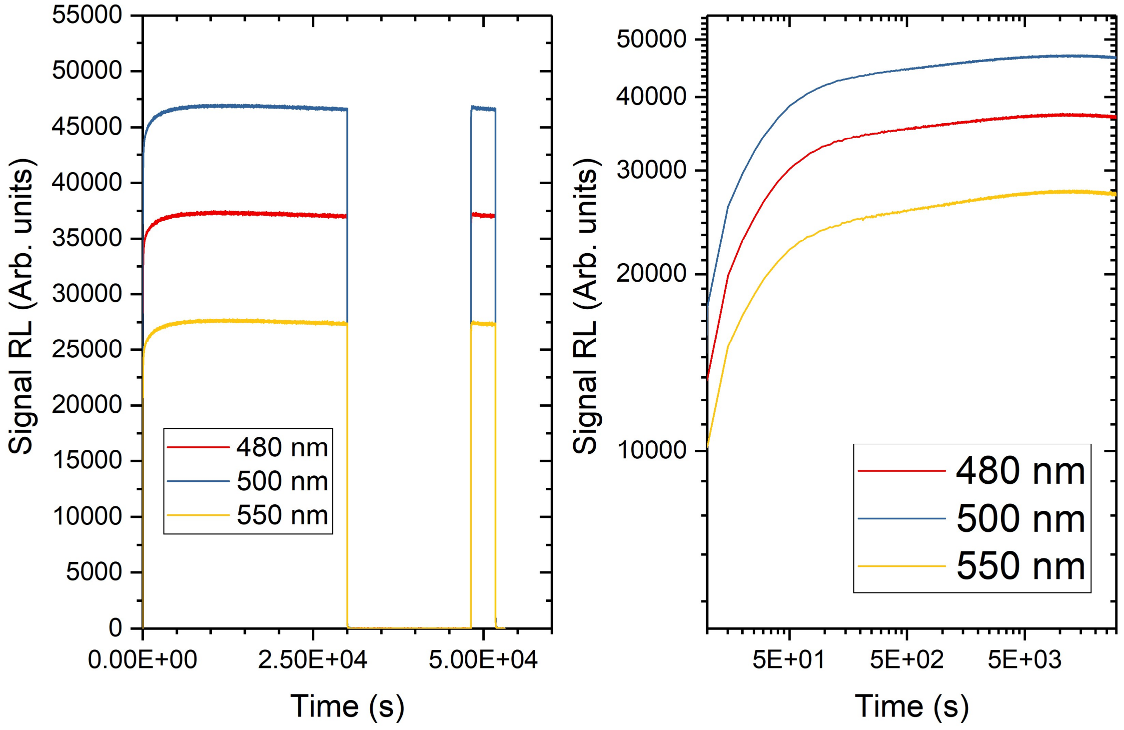

Figure 43 - Kinetics of the RL emission of 1-cm long Ce-doped fibre sample at 20 Gy/s, for a few selected wavelengths across the emission band. a) raw data in linear scale, b) logarithmic scale

5.1.1.2 RL Ce-doped fibre : 1cm@5Gy/s

For the second set of experiment, we performed the irradiation on 1-cm long Ce-doped fibre under a 5 Gy/s dose rate. As shown in Figure 45, and similarly to what was shown at higher dose rate, we observe a change in the amplitude of the emission band during the irradiation. The normalized emission spectra measured at the different doses reveal no evolution of the emission spectral shape.

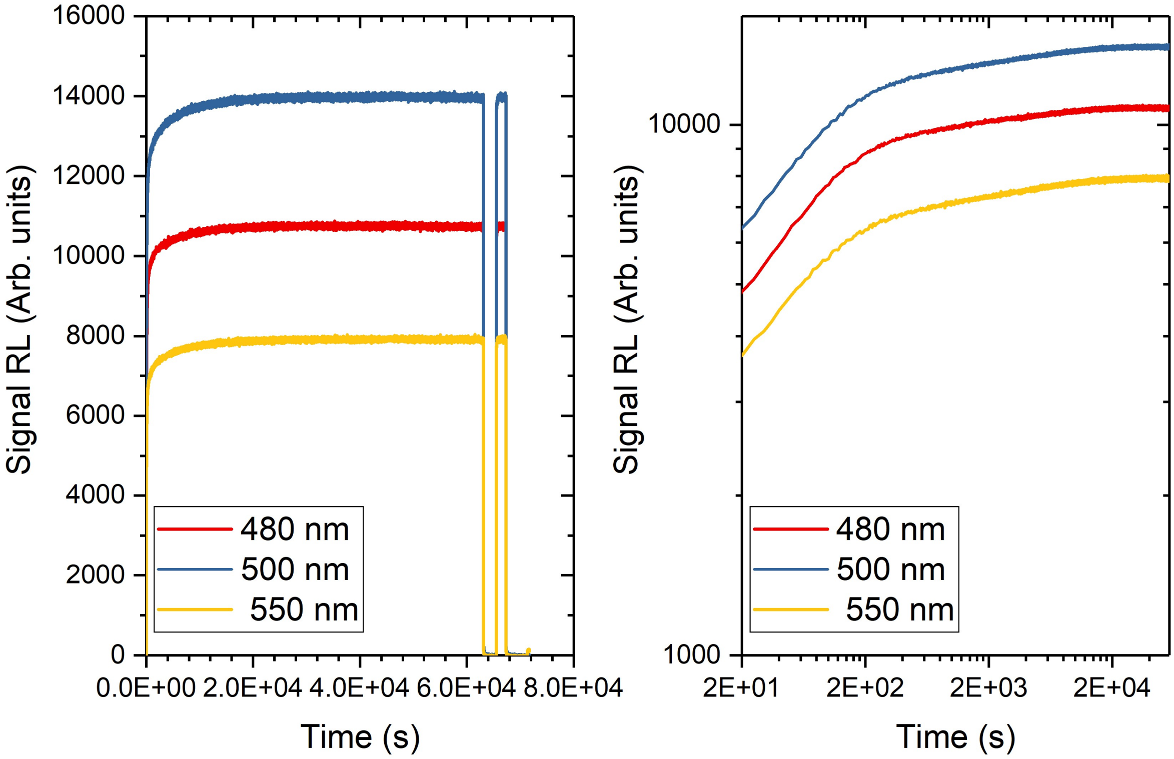

Figure 44 - Kinetics of the RL emission of 1-cm long Ce-doped fibre sample at 5 Gy/s, for few selected wavelengths across the emission band. a) raw data in linear scale, b) logarithmic scale

Furthermore, when following the kinetics of the emission at a few wavelengths during the irradiation we observe that the behavior is similar to that observed previously at higher dose rate. There is again a significant variation of the amplitude of the signal during the first part of the irradiation, before a stabilization of the signal after a 100 kGy irradiation, which restarts at the same level after a few hours recovery time. This observation further tends to suggest the possibility to use pre-irradiation to such level to induce a stabilization of the response of such sensor before use in dosimetry application.

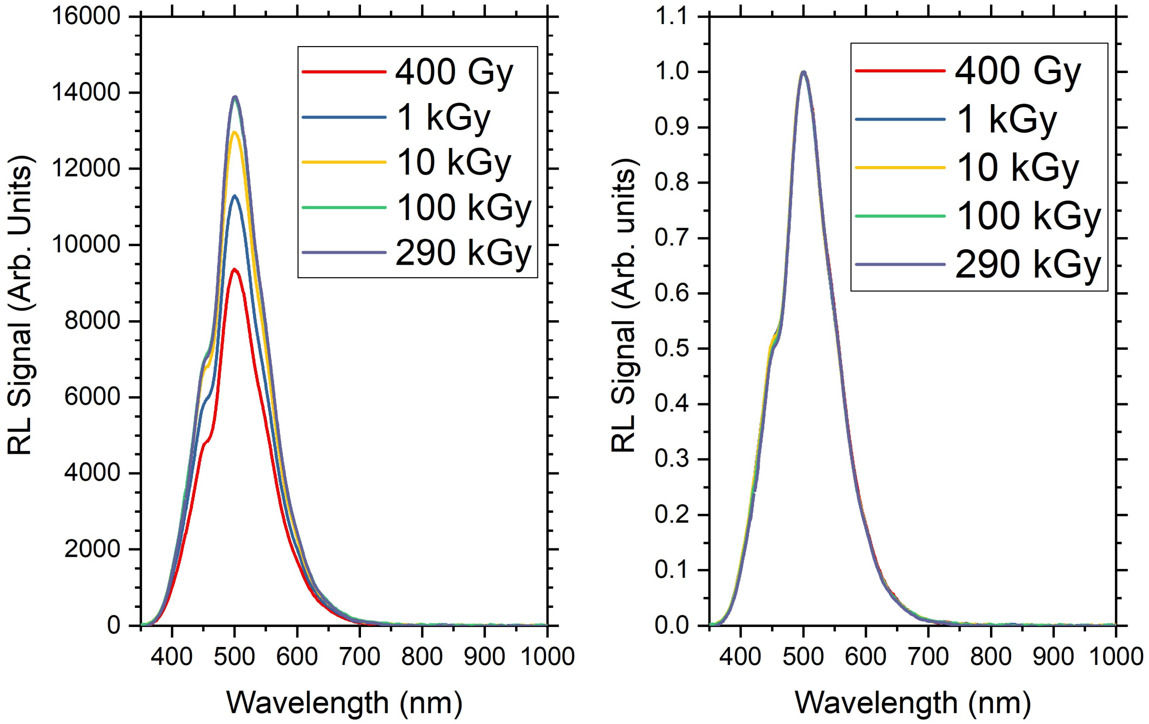

Figure 45 - RL spectra measured on 1-cm Ce-doped fibre sample at 5Gy/s, for different deposited doses. Left : Raw data, Right : Each curve is normalized to its own amplitude for shape comparison.

5.1.1.3 RL Ce-doped fibre : 5cm@5Gy/s

To continue to study of the Ce-doped fibre RL emission, we performed the same procedure in 5-cm long sample under a 5 Gy/s. As shown in Figure 47, the emission spectrum amplitude changes during irradiation. The normalization of the spectra obtained at different doses shows no significant change in the emission spectrum shape, similarly to what observed in previously presented data.

Additionnally, when focusing on the kinetics extracted at different wavelengths, a behavior similar to what observed in previous data is highlighted. The signal amplitude increases at the beginning of the irradiation before becoming much more stable at doses higher than 100 kGy. The level of stability observed at 150 kGy in this set of data is similar to that observed at higher dose rate, which tends to indicated that the pre-irradiation procedure suggested earlier could be performed at higher dose rate, allowing faster treatment, generating the same effect. However, it seems clear that the pre-irradiation procedure is much more effective if it is extended beyond 200 kGy.

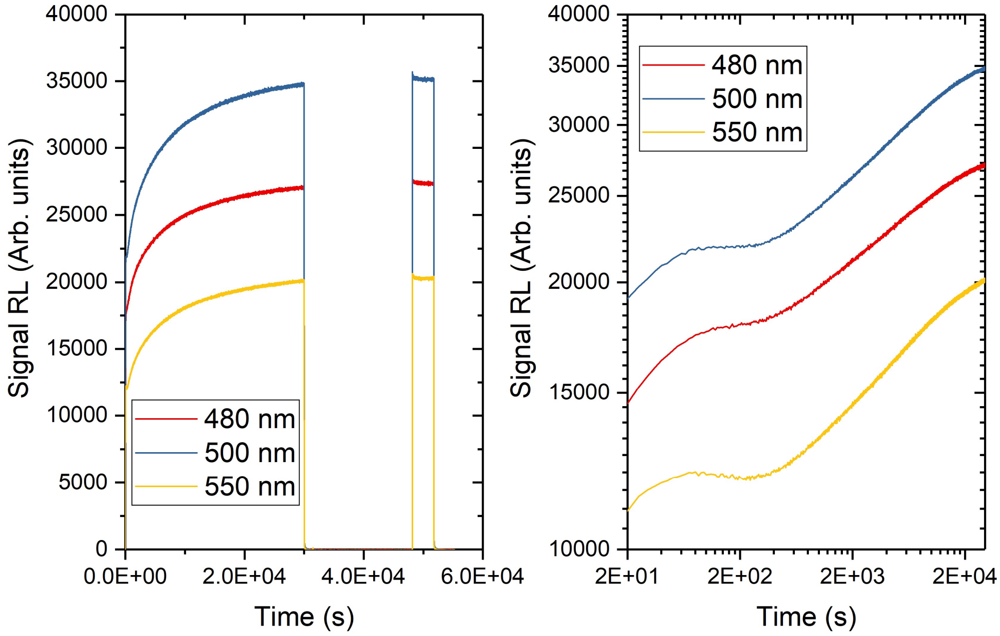

Figure 46 – Kinetics of the RL emission of 5-cm long Ce-doped fibre sample at 5 Gy/s, for a few selected wavelengths across the emission band. a) Raw data in linear scale, b) logarithmic scale

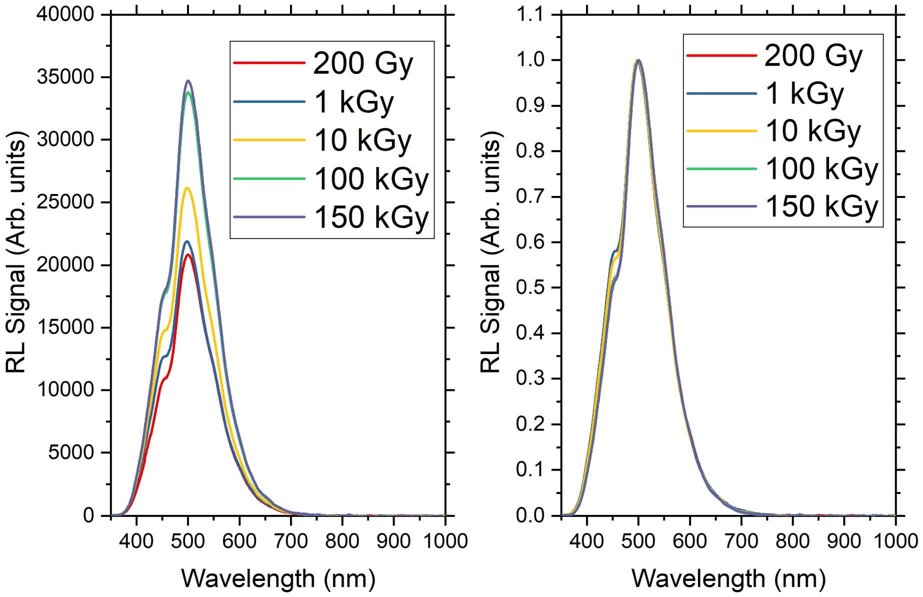

Figure 47 - RL spectra measured on 5-cm Ce-doped fibre sample at 5Gy/s, for different deposited doses. Left : Raw data, Right : Each curve is normalized to its own amplitude for shape comparison.

5.1.1.4 RL Ce-doped fibre : 5cm@0.5Gy/s

Finally, we performed again this test on a 5cm-long Ce-doped fibre sample under a 5 Gy/s dose rate. As shown in Figure 49, we observe that the amplitude of the signal changes again during the irradiation but we noticed no change in the shape of the emission when applying a normalization of the data.

When focusing on the kinetics extracted at different wavelengths, we note an increase of the signal until the end of the irradiation of 15 kGy. A comparable level is measured after the recovery time.

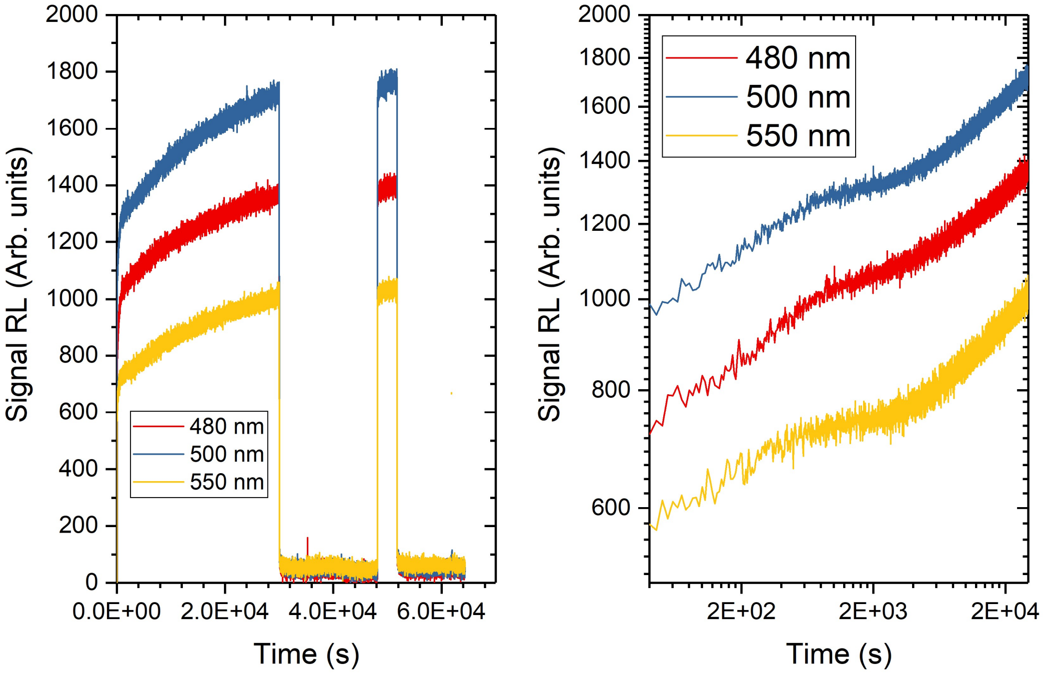

Figure 48 – Kinetics of the RL emission of 5-cm long Ce-doped fibre sample at 0.5 Gy/s, for a few selected wavelengths across the emission band. a) Raw data in linear scale, b) logarithmic scale

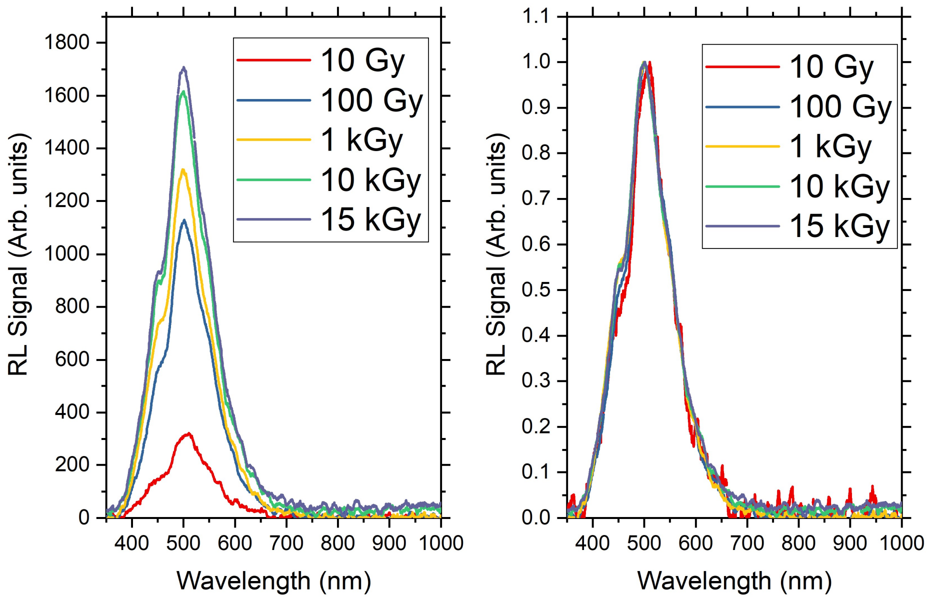

Figure 49 - RL spectra measured on 5-cm Ce-doped fibre sample at 0.5Gy/s, for different deposited doses. Left : Raw data, Right : Each curve is normalized to its own amplitude for shape comparison.

5.1.2 RL study in Cu-doped fibre

In this part of the thesis we characterize the Cu-doped fibre RL emission under X-rays, following the same procedure than for the Ce-doped fibre. The amplitude of this emission band changes during irradiation, but shows no significant shape change during the irradiation when applying a normalization in amplitude.

This narrower emission band is located between 430 and 700 nm, with a maximum amplitude found around 550 nm. The first comment one could have is that this feature should make it potentially more interesting for RL based dosimetry since a higher wavelength usually means better propagation in related transport optical fibre, since the attenuation usually decreases at increasing wavelengths. However, when focusing on the kinetics of the signal versus dose, we observe a behavior that differs strongly with that observed in Ce-doped fibre. Indeed, in all tested configurations, the signal increases strongly at the beginning of the irradiation until 2-3 kGy, before starting to decrease until the end of the irradiation.

The signal however does become more stable after a first irradiation phase of 100 kGy.

Even if the reached signal stability is not as good as that observed in Ce-doped fibre, a pre-irradiation procedure clearly improves the stability of the response with respect to that of a pristine sample. Furthermore, this improved stability is also maintained after a few hours of recovery time, which further suggests that a pre-irradiation could be beneficial for the application.

To summarize the result of the RL response testing for different lengths of Cu-doped fibre, and different dose rates, we observe that the amplitude of the signal changes during the irradiation while the emission shape does not change during the irradiation. Additionnally, the study of the kinetics of the signal at different wavelengths shows that the signal changes but becomes more stable after a 100 kGy dose, which strongly suggests that a pre-irradiation before using this type of fibre in dosimetry application would be very interesting. However, this better stability reached after pre-irradiation is not as good as that observed in Ce-doped fibre for which the signal becomes almost flat.

5.1.2.1 RL Cu-doped fibre : 1cm@20Gy/s

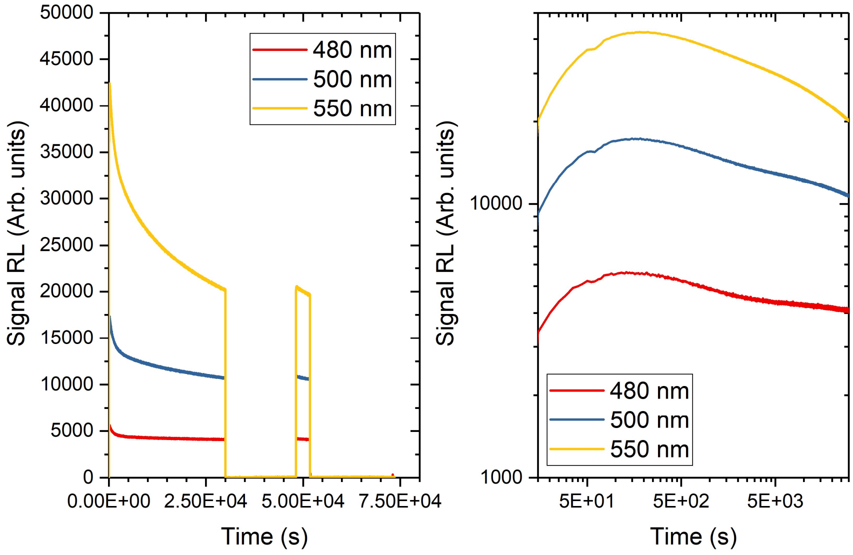

Figure 50 – Kinetics of the RL emission of 1-cm long Cu-doped fibre sample at 20 Gy/s, for a few selected wavelengths across the emission band. a) Raw data in linear scale, b) Logarithmic scale

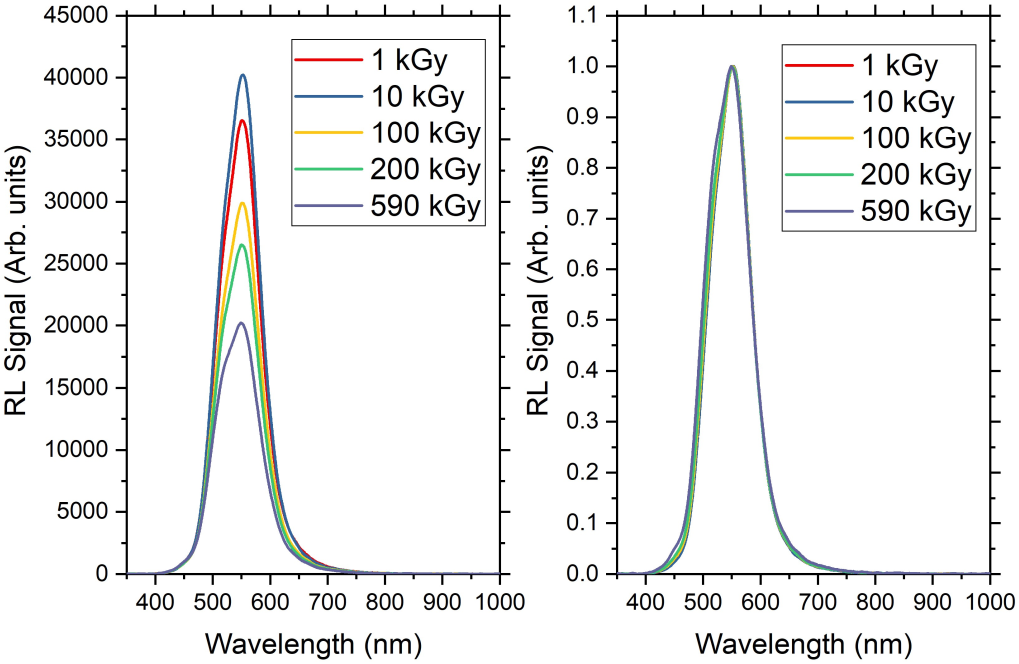

Figure 51 - RL spectra measured on 1-cm Cu-doped fibre sample at 20 Gy/s, for different deposited doses. Left : Raw data, Right : Each curve is normalized to its own amplitude for shape comparison.

5.1.2.2 RL Cu-doped fibre : 1cm@5Gy/s

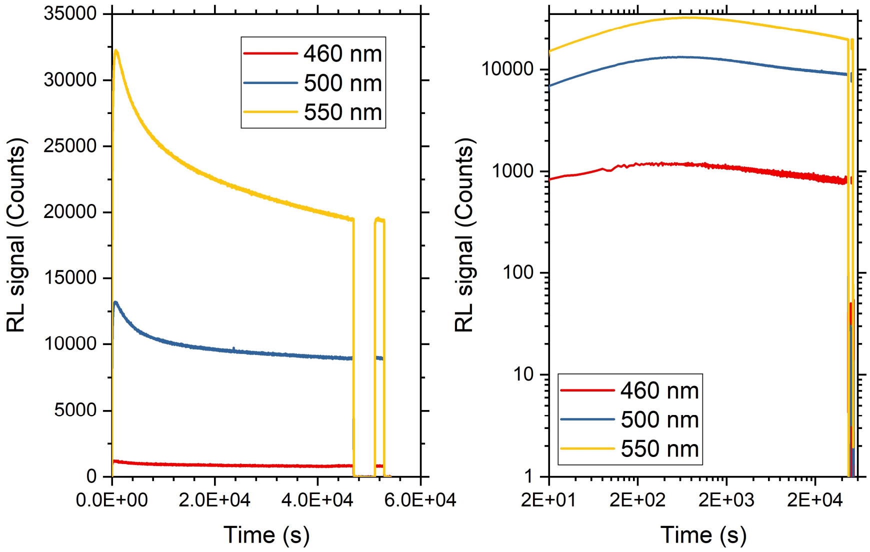

Figure 52 - Kinetics of the RL emission of 1-cm long Cu-doped fibre sample at 5 Gy/s, for a few selected wavelengths across the emission band. a) Raw data in linear scale, b) logarithmic scale

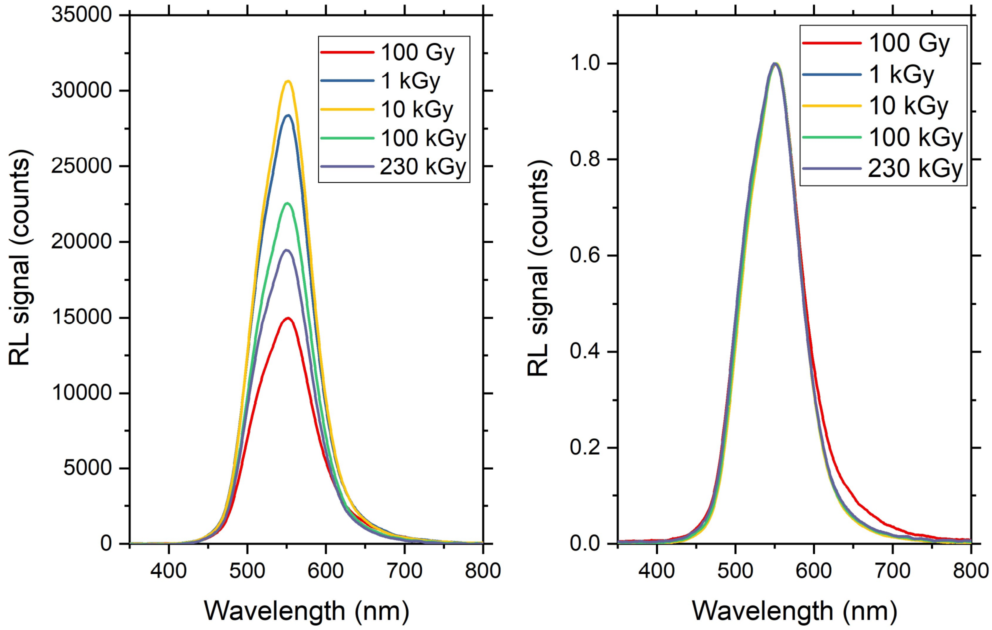

Figure 53 - RL spectra measured on 1-cm Cu-doped fibre sample at 5 Gy/s, for different deposited doses. Left: Raw data, Right: Each curve is normalized to its own amplitude for shape comparison.

5.1.2.3 RL Cu-doped fibre : 5cm@5Gy/s

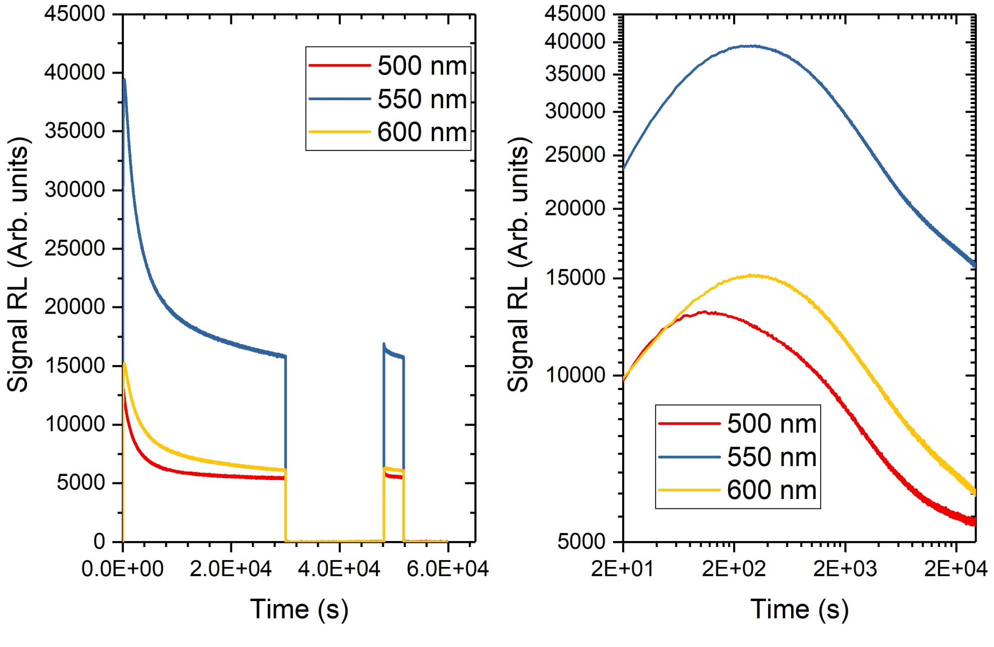

Figure 54 – Kinetics of the RL emission of 5-cm long Cu-doped fibre sample at 5 Gy/s, for a few selected wavelengths across the emission band. a) Raw data in linear scale, b) logarithmic scale

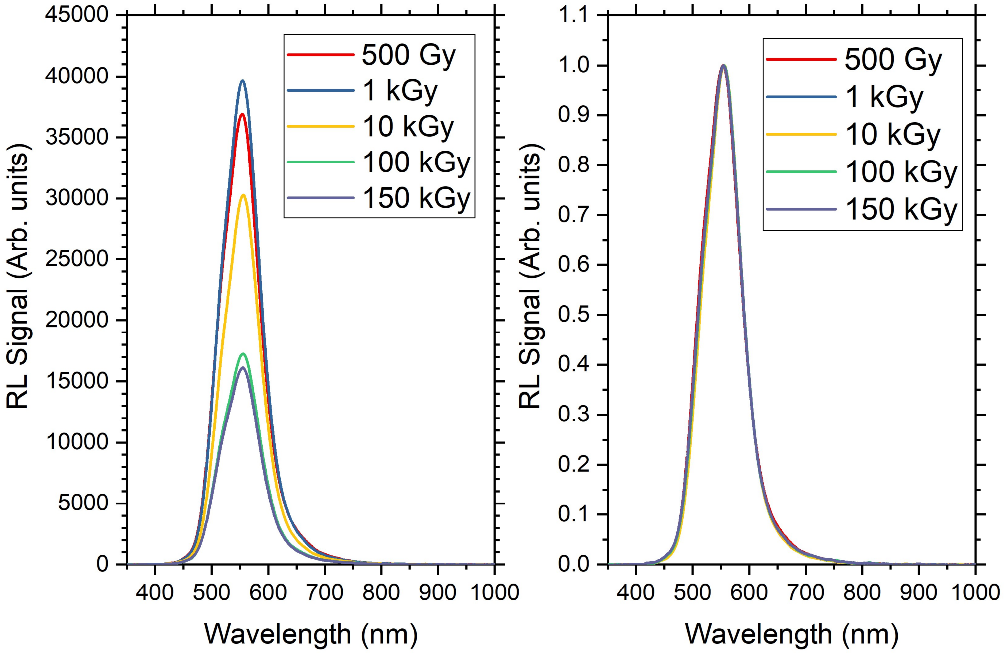

Figure 55 - RL spectra measured on 5-cm Cu-doped fibre sample at 5 Gy/s, for different deposited doses. Left: Raw data, Right: Each curve is normalized to its own amplitude for shape comparison.

5.1.2.4 RL Cu-doped fibre : 5cm@0.5Gy/s

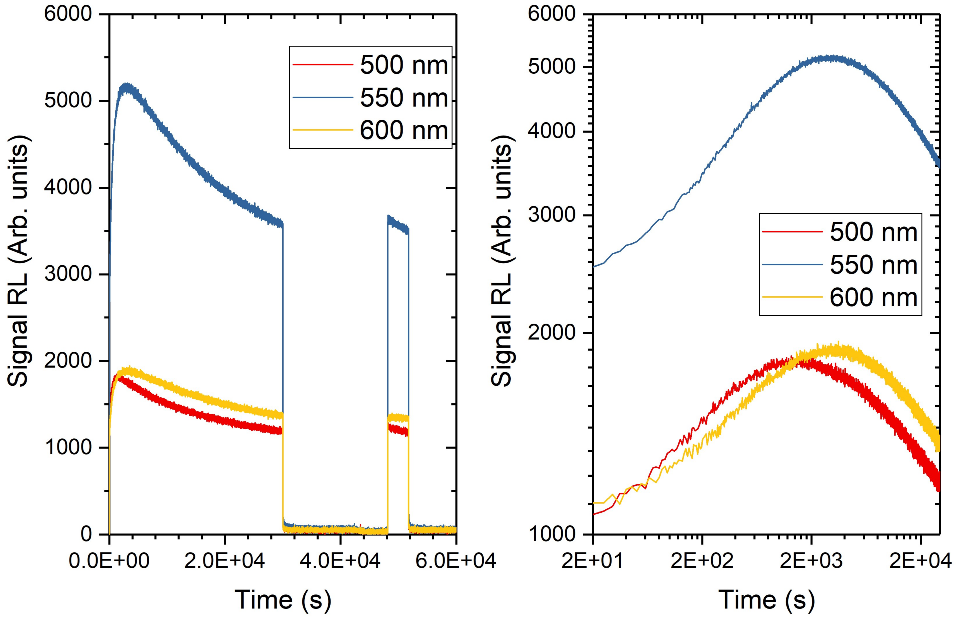

Figure 56 – Kinetics of the RL emission of 5-cm long Cu-doped fibre sample at 0.5 Gy/s, for a few selected wavelengths across the emission band. a) Raw data in linear scale, b) logarithmic scale

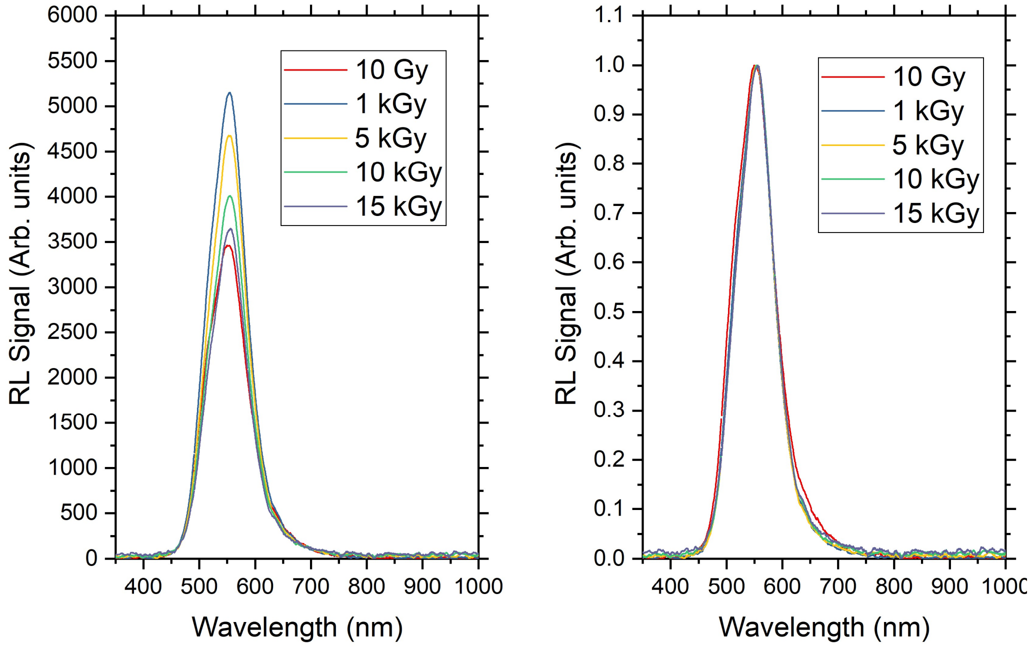

Figure 57 - RL spectra measured on 5-cm Cu-doped fibre sample at 0.5 Gy/s, for different deposited doses. Left : Raw data, Right : Each curve is normalized to its own amplitude for shape comparison.

5.1.3 RL study in CuCe-codoped fibre

In this part of the chapter, we will perform the same study presented on previous samples, on CuCe-codoped fibre. We observe in this fibre, a broad spectra extending from 380 nm to 700 nm combining the emission of Ce^{3+}- and Cu^{+}- ions present in this fibre. The spectra measured at different doses during the irradiation, show a change in amplitude versus dose. When normalizing these spectra to their own maximum amplitude we highlight a change in the shape of the emission band. This is easily explainable by the composition of the fibre. Indeed, we have shown earlier that the emissions from Ce- and Cu- ions evolve during the irradiation in different ways. Therefore, this observed change in shape is explained by the fact that combined emission spectra of CuCe-doped fibre represent the different evolution rates of both contributions of Ce- and Cu-ions.

The kinetics of the response of this fibre show trends similar to what observed in Cu-doped fibre. We observe an increase until 2 kGy before a decrease up to the end of the irradiation. We can easily determine that this behavior is dominated by the Cu- ions contribution since the Ce- ions showed an important stability at dose higher that 100 kGy whereas in this case, the stability is worse. However, the pre-irradiation induces again in this case an important improvement of the stability of the response of the sensor, which suggests again the need to pre-irradiate this type of fibre before use in dosimetry application.

5.1.3.1 RL CuCe- codoped fibre : 1cm@20Gy/s

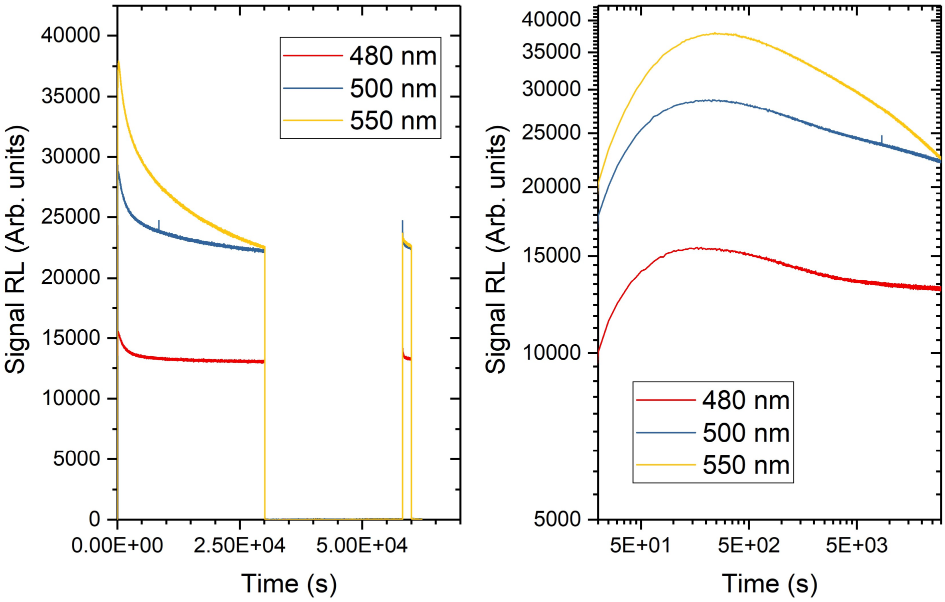

Figure 58 – Kinetics of the RL emission of 1-cm long CuCe-doped fibre sample at 20 Gy/s, for a few selected wavelengths across the emission band. a) Raw data in linear scale, b) logarithmic scale

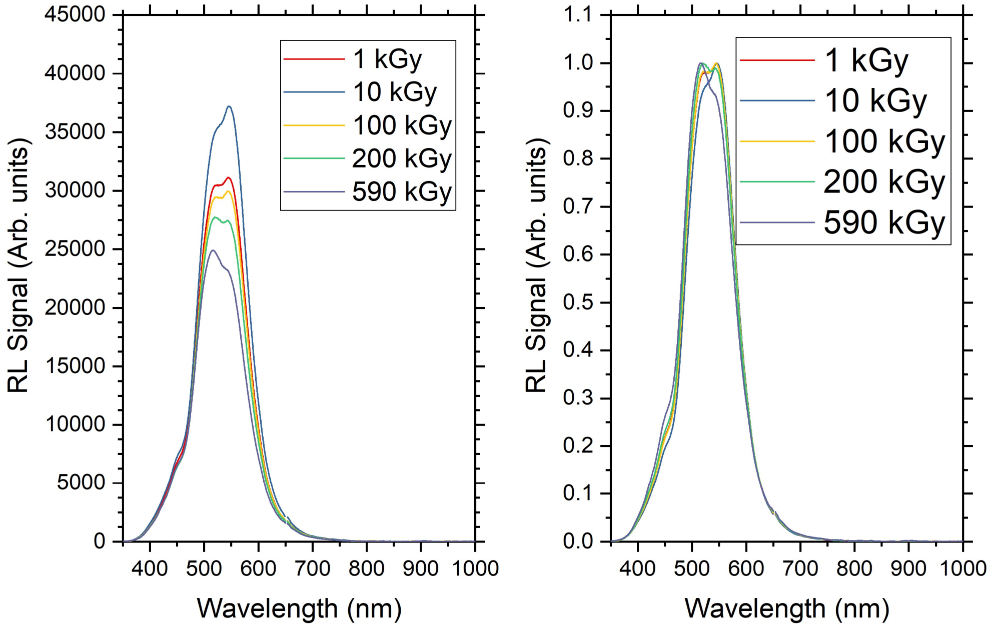

Figure 59 - RL spectra measured on 1-cm CuCe-doped fibre sample at 20Gy/s, for different deposited doses. Left : Raw data, Right : Each curve is normalized to its own amplitude for shape comparison.

5.1.3.2 RL CuCe- codoped fibre : 1cm@5Gy/s

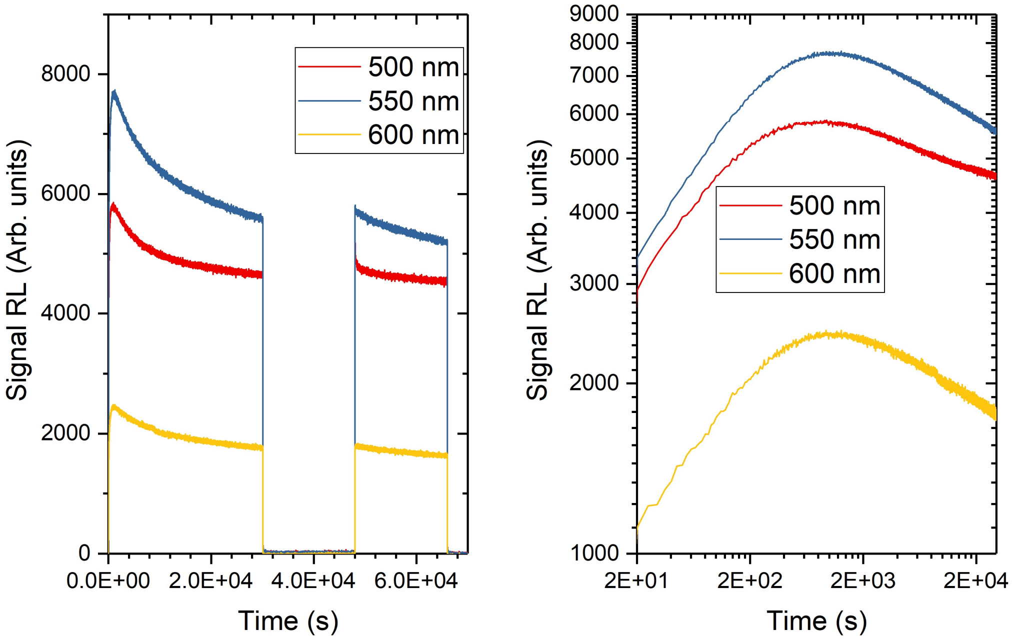

Figure 60 -Kinetics of the RL emission of 1-cm long CuCe-codoped fibre sample at 5 Gy/s, for a few selected wavelengths across the emission band. a) Raw data in linear scale, b) logarithmic scale

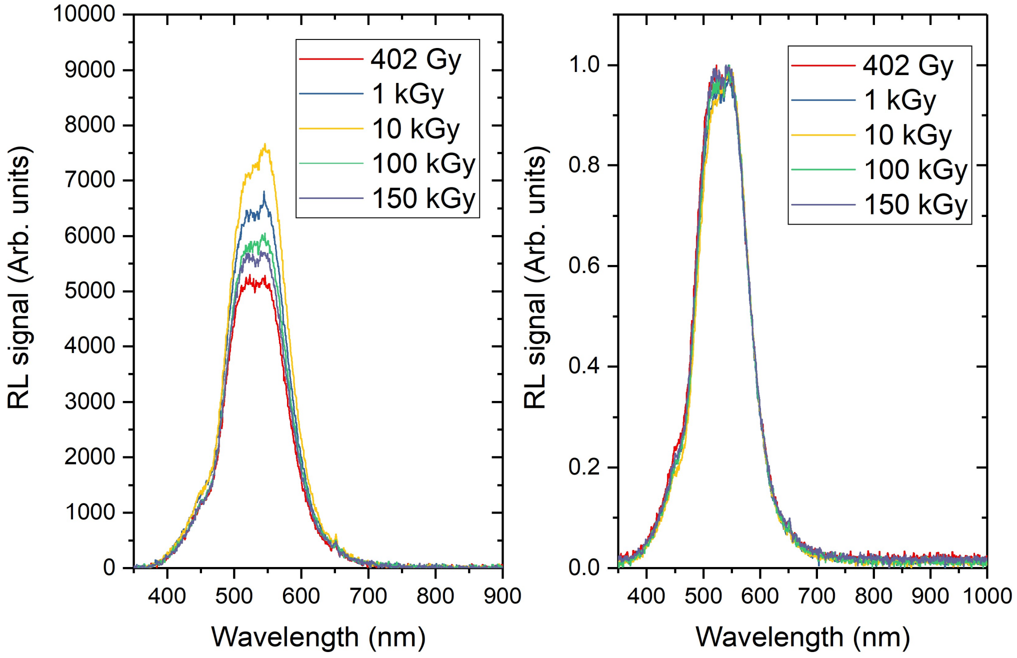

Figure 61 - RL spectra measured on 1-cm CuCe-doped fibre sample at 5 Gy/s, for different deposited doses. Left : Raw data, Right : Each curve is normalized to its own amplitude for shape comparison.

5.1.3.3 RL CuCe- codoped fibre : 5cm@5Gy/s

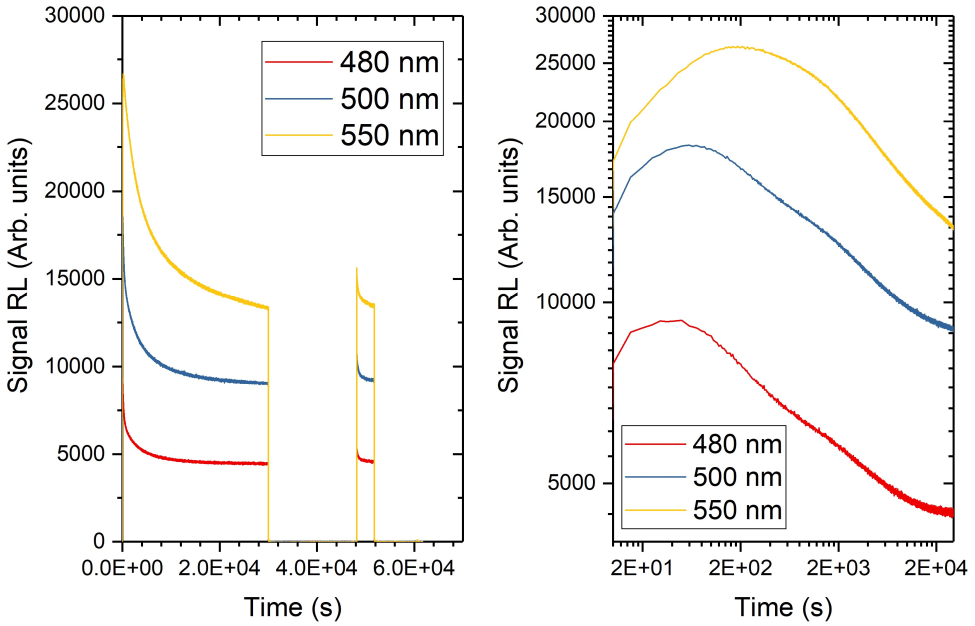

Figure 62 – Kinetics of the RL emission of 5-cm long CuCe-codoped fibre sample at 5 Gy/s, for a few selected wavelengths across the emission band. a) Raw data in linear scale, b) logarithmic scale

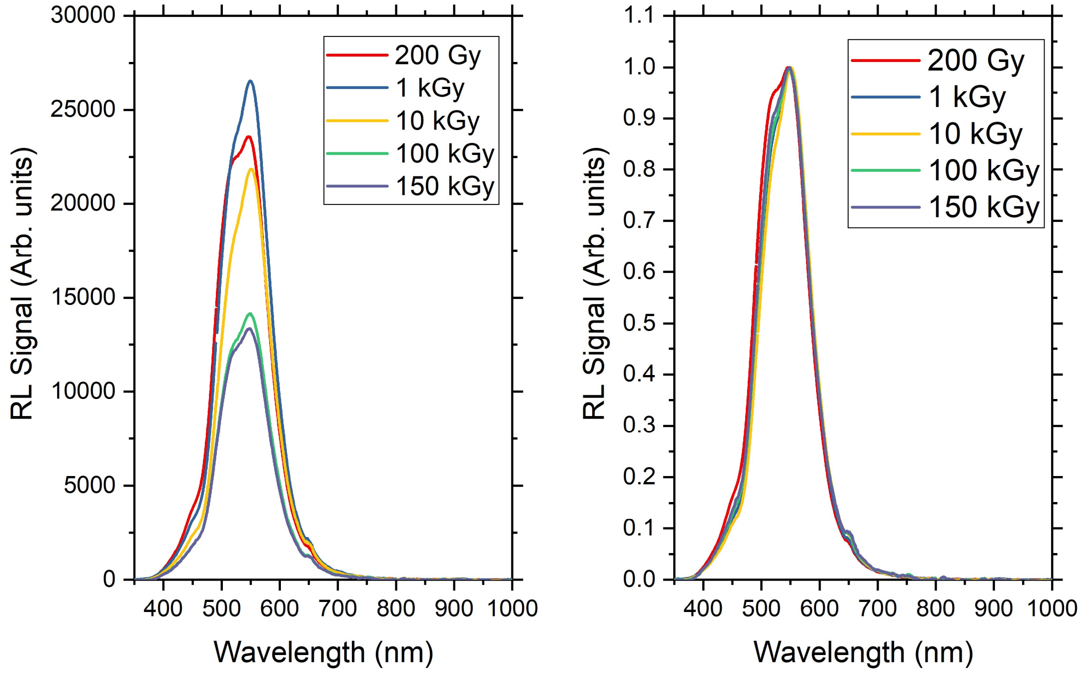

Figure 63 - RL spectra measured on 5-cm CuCe-doped fibre sample at 5 Gy/s, for different deposited doses. Left : Raw data, Right : Each curve is normalized to its own amplitude for shape comparison.

5.1.3.4 RL CuCe- codoped fibre : 5cm@0.5Gy/s

Unfortunately, in this experimental dataset, the second irradiation did not happen because of a technical issue with the automatization of the irradiation sequence, which did not restart as planned.

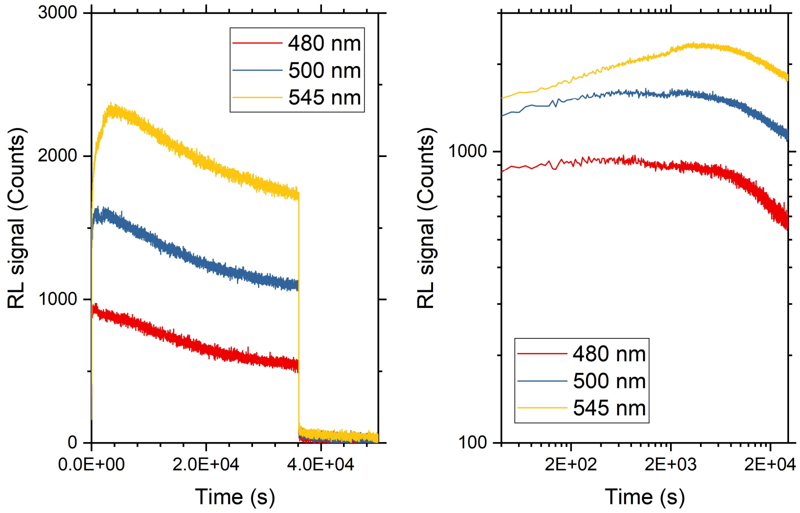

Figure 64 – Kinetics of the RL emission of 5-cm long CuCe-codoped fibre sample at 0.5 Gy/s, for a few selected wavelengths across the emission band. a) Raw data in linear scale, b) logarithmic scale

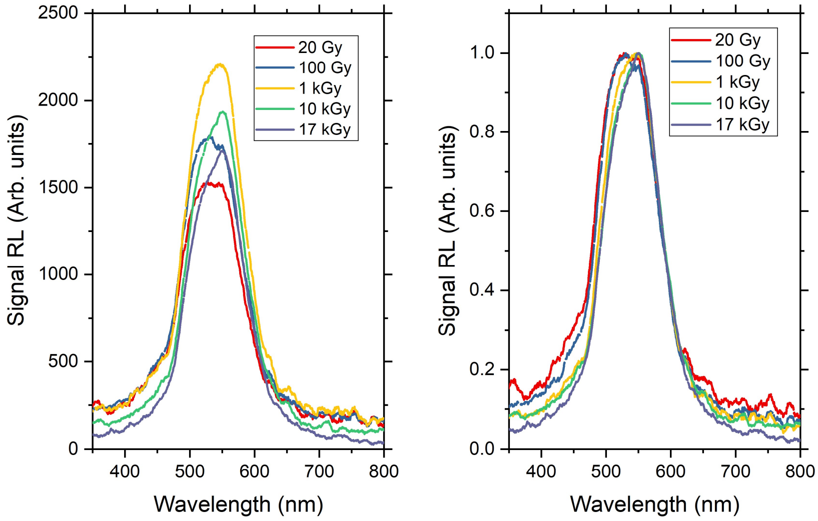

Figure 65 - RL spectra measured on 5-cm CuCe-codoped fibre sample at 0.5 Gy/s, for different deposited doses. Left : Raw data, Right : Each curve is normalized to its own amplitude for shape comparison.

5.1.4 RL study in Gd-doped fibre

In this part of the study, we now focus on the Gd-doped fibre, which differs from the previously presented sensors in the sense that its radio-emission occurs in the UV-region, instead of the visible domain.

The emission spectra is a sharp and narrow band located around 314 nm. This band amplitude changes during the irradiation, but no significant change in its shape is observed when applying a normalization of the spectra at their own maximum amplitude. However, we have to note here that given the very narrow width of the emission band, it is very difficult to highlight changes in shape in such measurement because it would require a better spectral resolution than the 1.7 nm achieved by the used spectrometer.

When focusing on the kinetics extracted in this very sharp emission band, we observe an increase at the beginning until 2-3 kGy which is followed by a decrease until the end of the irradiation. We also observe a fast and sharp increase, with a limited amplitude, of the signal at the start of the second irradiation. During this second irradiation, the evolution of the signal seems to follow a similar decreasing trends as observed in the first irradiation.

As observed in other fibre types, we can see that a pre-irradiation up to 100 kGy at least, reduces significantly the variation of the emission of the sensor. This means that we can also suggest in this case, a pre-irradiation of the sensor before its use in dosimetry application.

However, the observed improved stability is not as good as that observed in the Ce-doped fibre experiments.

5.1.4.1 RL Gd-doped fibre : 1cm@20Gy/s

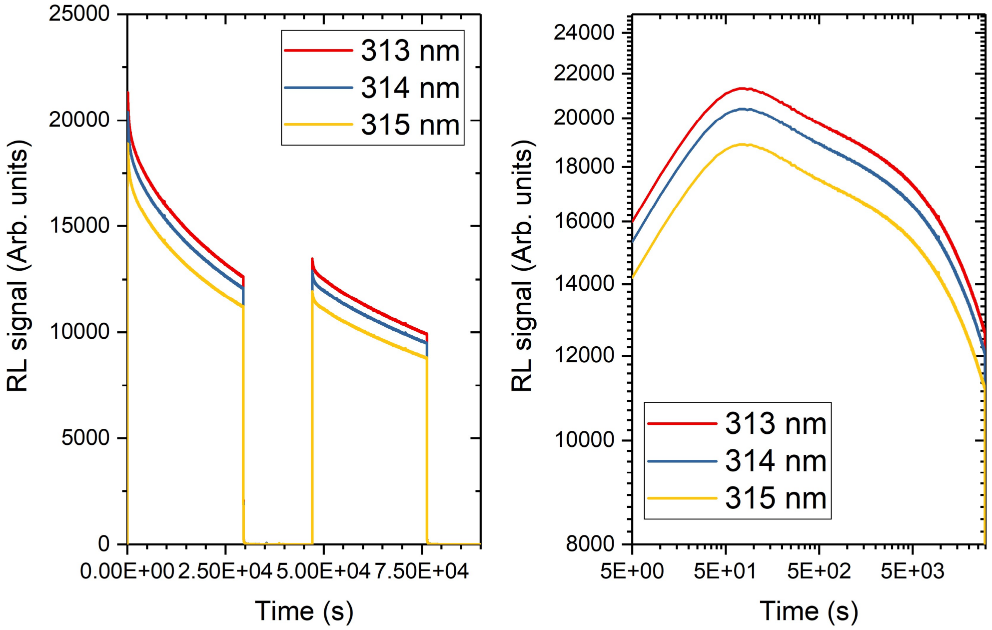

Figure 66 – Kinetics of the RL emission of 1-cm long Gd-doped fibre sample at 20 Gy/s, for a few selected wavelengths across the emission band. a) Raw data in linear scale, b) logarithmic scale

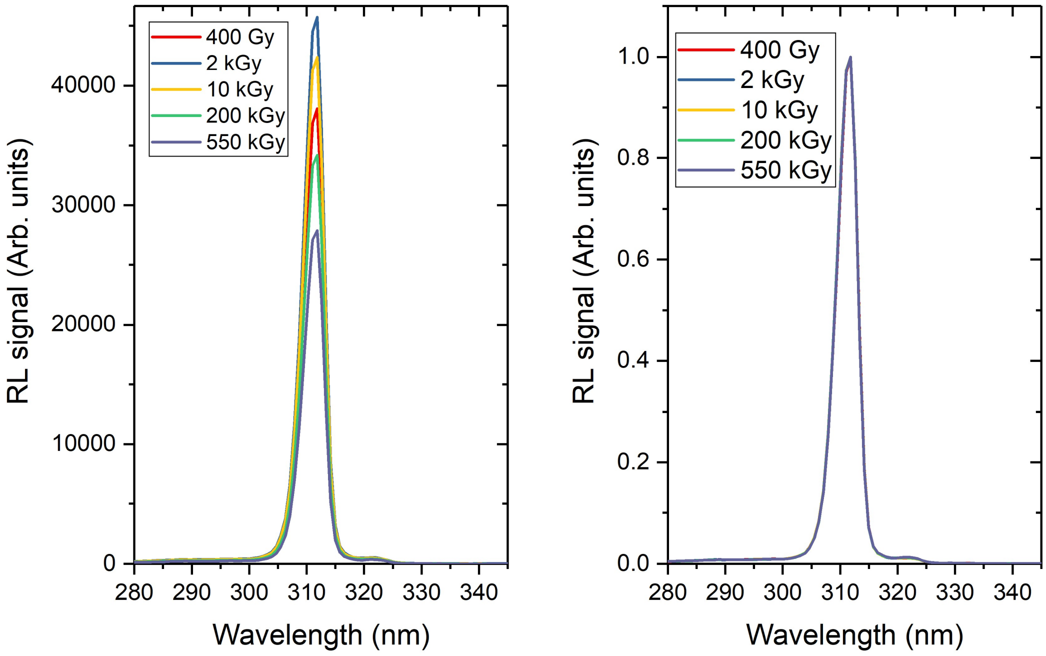

Figure 67 - RL spectra measured on 1-cm Gd-doped fibre sample at 20 Gy/s, for different deposited doses. Left : Raw data, Right : Each curve is normalized to its own amplitude for shape comparison.

5.1.4.2 RL Gd -doped fibre : 1cm@5Gy/s

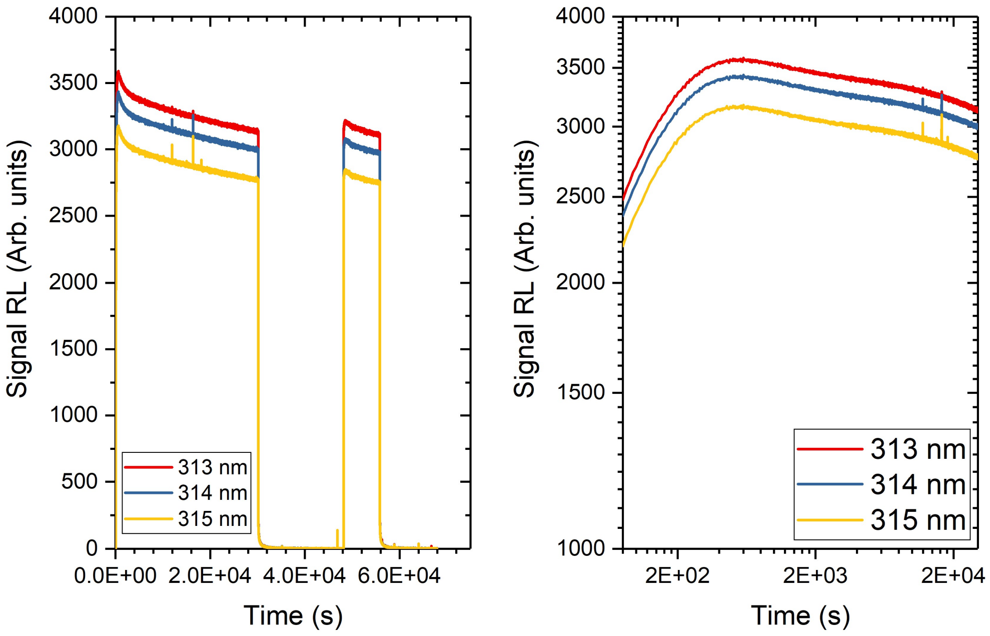

Figure 68 – Kinetics of the RL emission of 1-cm long Gd-doped fibre sample at 5 Gy/s, for a few selected wavelength across the emission band. a) Raw data in linear scale, b) Logarithmic scale.

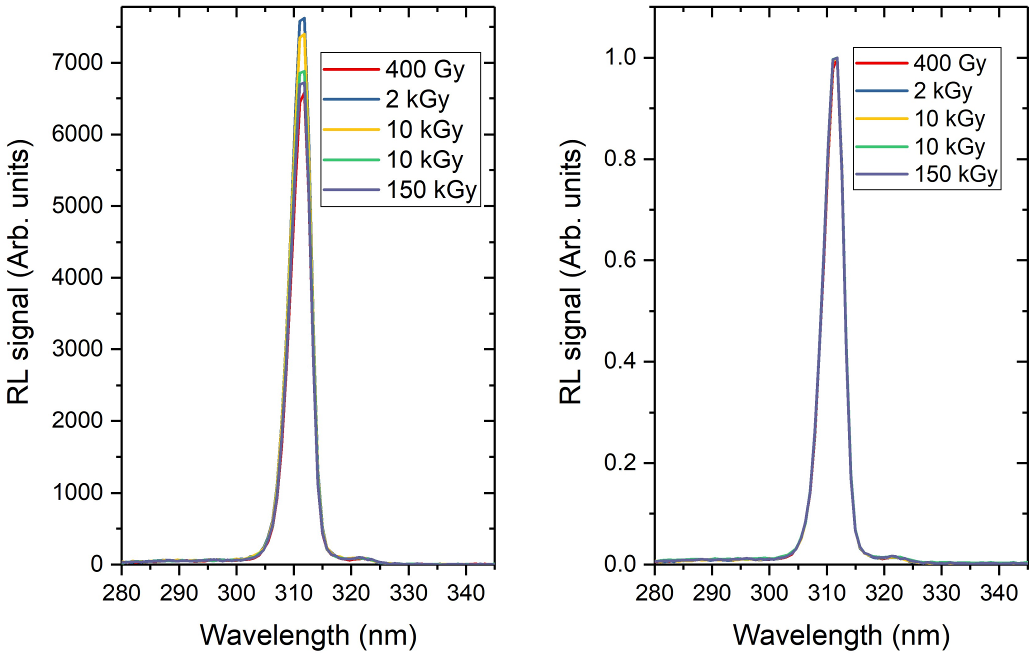

Figure 69 - RL spectra measured on a 1-cm Gd-doped fibre sample at 5 Gy/s, for different deposited doses. Left : Raw data, Right : Each curve is normalized to its own amplitude for shape comparison.

5.1.4.3 RL Gd -doped fibre : 5cm@5Gy/s

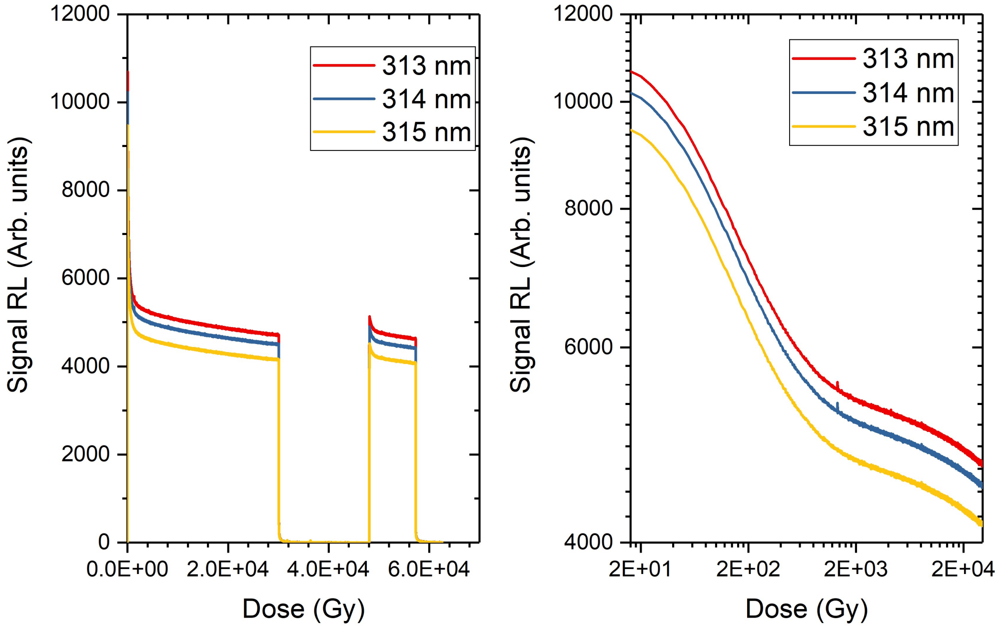

Figure 70 – Kinetics of the RL emission of 5-cm long Gd-doped fibre sample at 5 Gy/s, for a few selected wavelength across the emission band. a) Raw data in linear scale, b) Logarithmic scale.

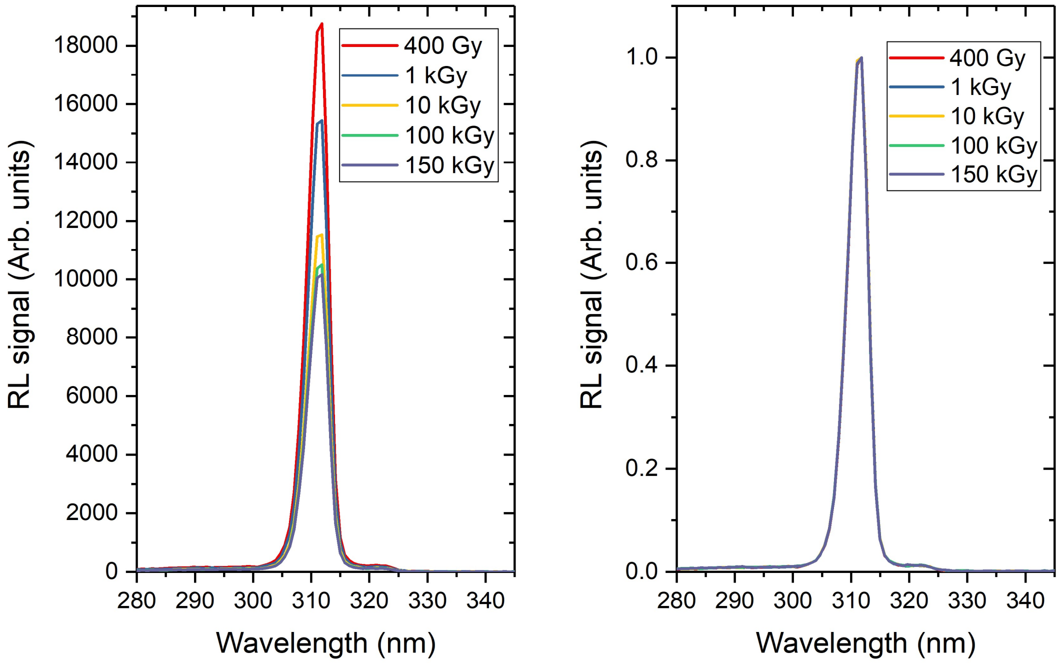

Figure 71 - RL spectra measured on a 5-cm Gd-doped fibre sample at 5 Gy/s, for different deposited doses. Left : Raw data, Right : Each curve is normalized to its own amplitude for shape comparison.

5.1.4.4 RL Gd -doped fibre : 5cm@0.5Gy/s

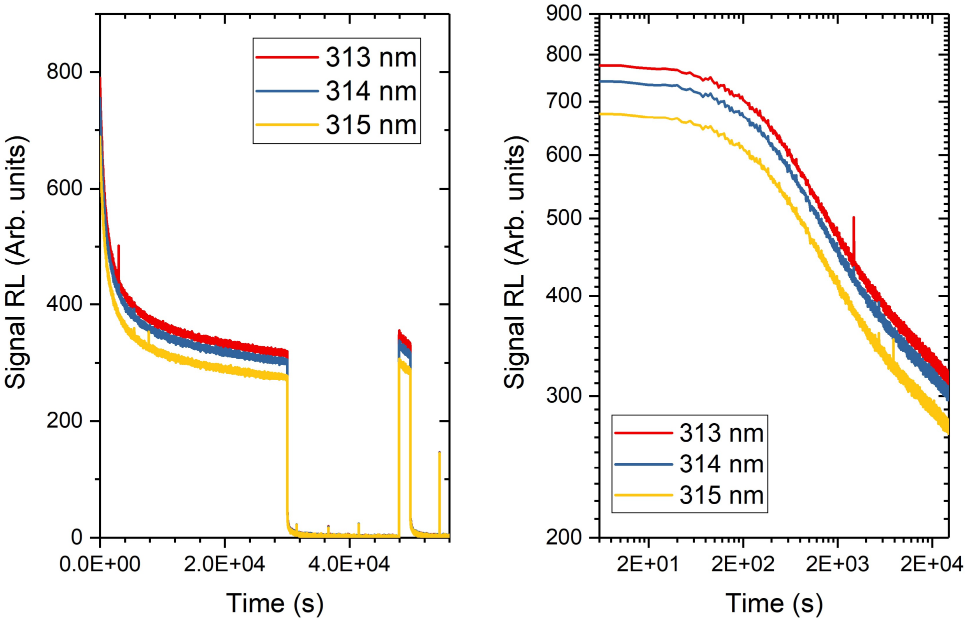

Figure 72 – Kinetics of the RL emission of 5-cm long Gd-doped fibre sample at 0.5 Gy/s, for a few selected wavelength across the emission band. a) Raw data in linear scale, b) logarithmic scale.

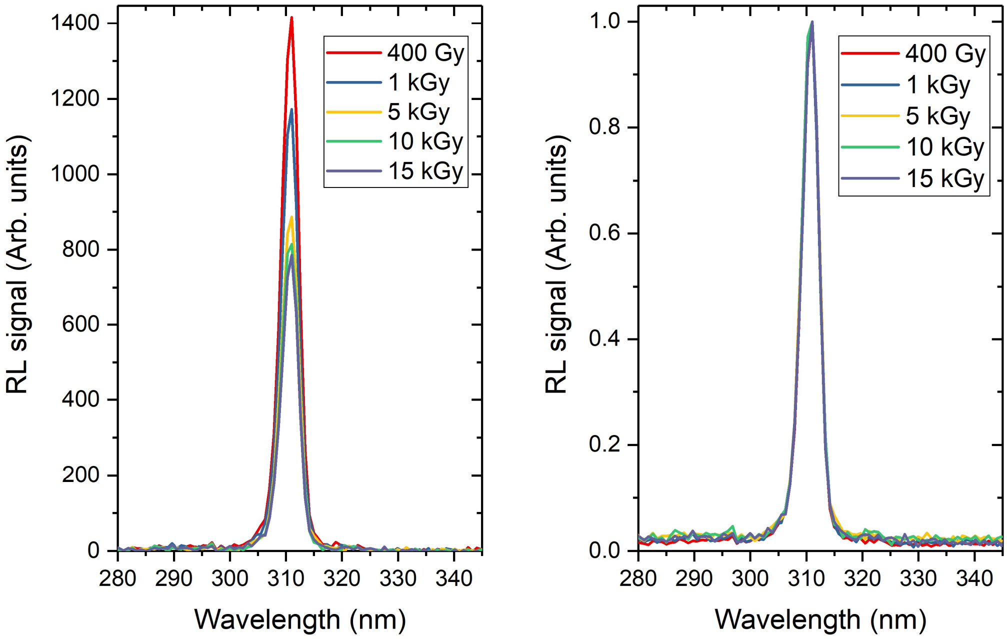

Figure 73 - RL spectra measured on a 5-cm Gd-doped fibre sample at 0.5 Gy/s, for different deposited doses. Left : Raw data, Right : Each curve is normalized to its own amplitude for shape comparison.

5.1.5 RL study in N-doped fibre

For the study of the N-doped fibre, we had access to very limited fiber lengths for testing. For this reason, we did not perform RL study on this fibre.

5.1.6 RL study in CeTb-codoped fibre

5.1.6.1 RL CeTb-codoped fibre : 1cm@20Gy/s

In this fibre, we observe a very complex RL emission under irradiation as shown in Figure 75. We observe a multitude of peaks across the 370 nm to 700 nm range. We also observe that the emission amplitude changes during irradiation . The response measured at different doses, shows a change in the shape of the emission, on the different peaks. We cannot at this point explain this change but we can imagine that the energy exchanges between Tb- and Ce- ions, introduced in the chapter 4.2.5 are affected during the irradiation. Further work needs to be carried out to understand this effect.

Additionnaly, we have selected different wavelengths located around the maximum amplitude of the peaks observed in the RL signal emission spectrum, and we plotted their amplitudes measured during irradiation. As shown in Figure 74, we observe an increase of the signal during the irradiation before a stabilization of the the response after 100 kGy. The stabilization is more efficient on certain wavelengths with respect to that related to other bands in the spectra. This feature is maintained after several hours time which in this case again suggests that a pre-irradiation should be done before using such fibre for dosimetry application.

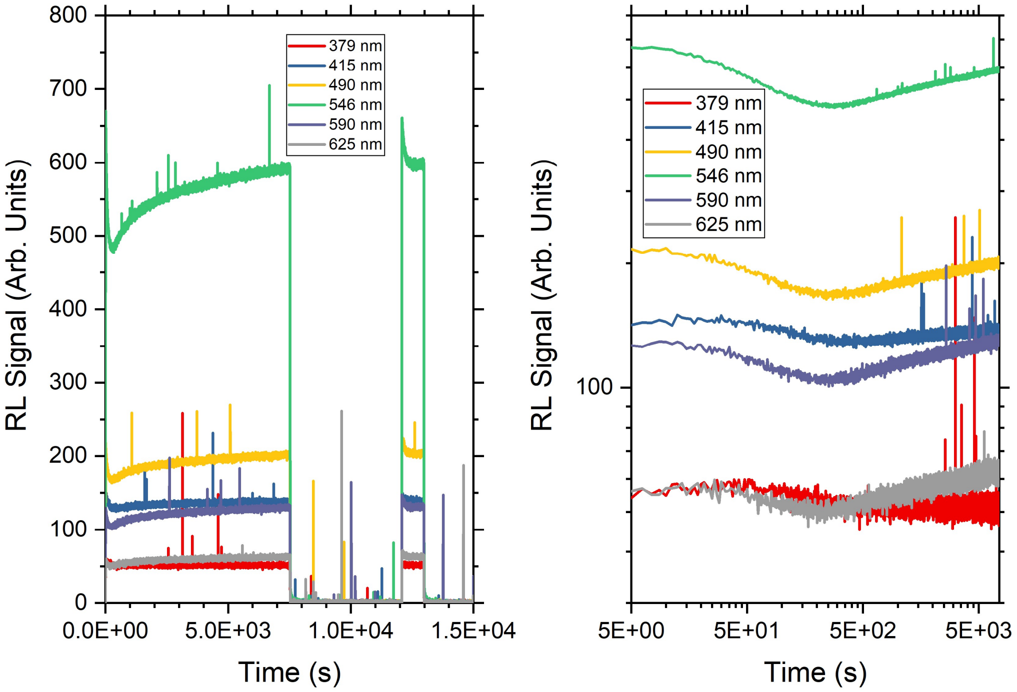

Figure 74 – Kinetics of the RL emission of 1-cm long CeTb-codoped fibre sample at 20 Gy/s, for a few selected wavelength across the emission band. a) Raw data in linear scale, b) logarithmic scale

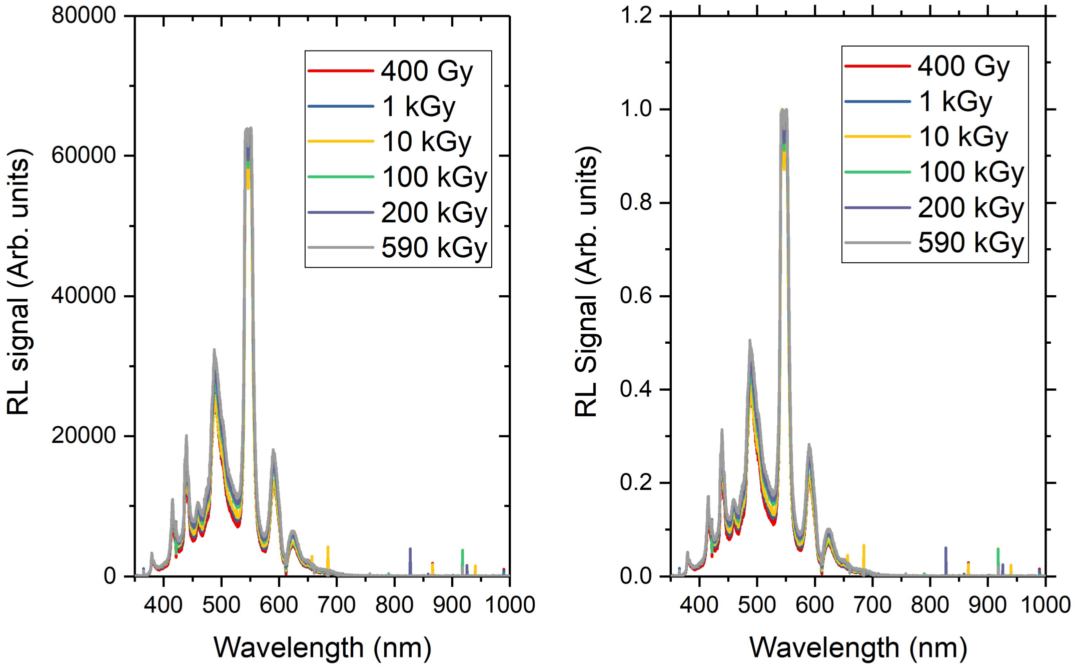

Figure 75 - RL spectra measured on 1-cm CeTb-doped fibre sample at 20 Gy/s, for different deposited doses. Left: Raw data, Right: Each curve is normalized to its own amplitude for shape comparison.

5.1.6.2 RL CeTb - codoped fibre : 1cm@5Gy/s

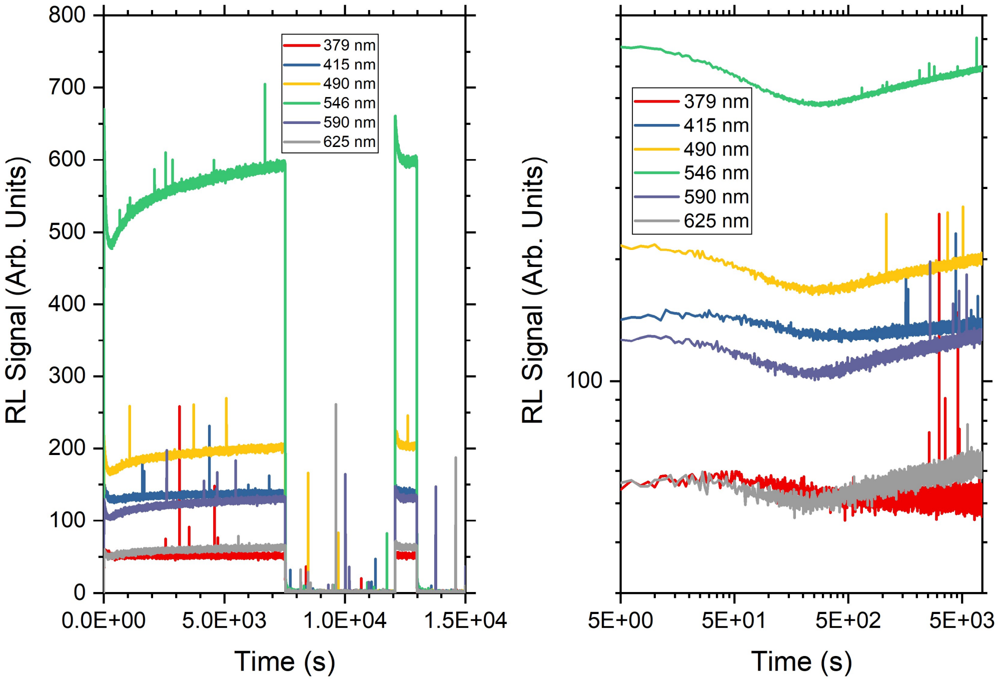

Figure 76 – Kinetics of the RL emission of 1-cm long CeTb-codoped fibre sample at 5 Gy/s, for a few selected wavelength across the emission band. a) Raw data in linear scale, b) logarithmic scale

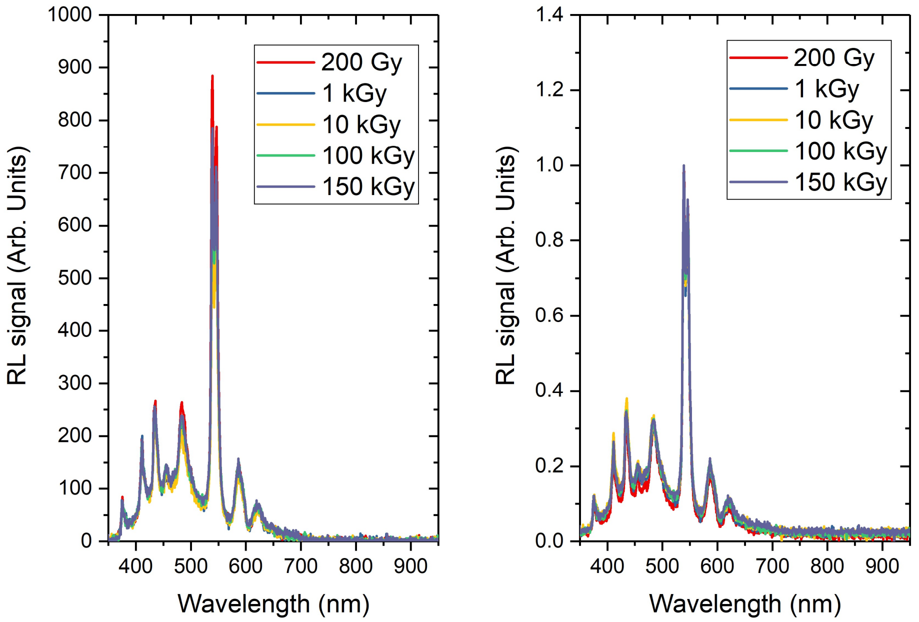

Figure 77 - RL spectra measured on 1-cm CeTb-doped fibre sample at 5 Gy/s, for different deposited doses. Left : Raw data, Right : Each curve is normalized to its own amplitude for shape comparison.

5.1.6.3 RL CeTb – codoped fibre : 5cm@5Gy/s

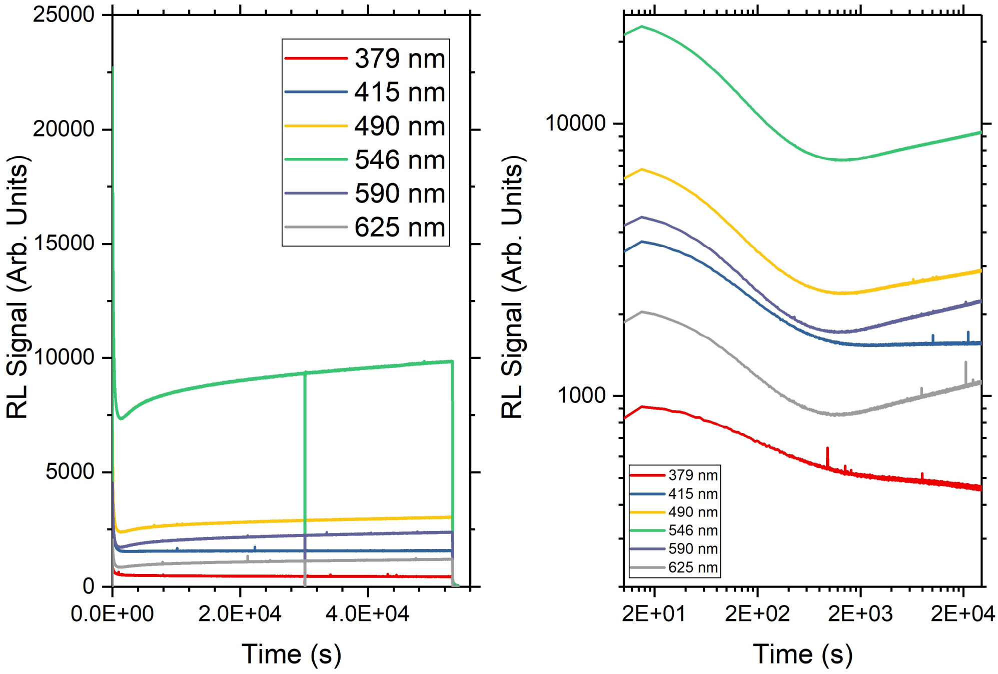

Figure 78 – Kinetics of the RL emission of 5-cm long CeTb-codoped fibre sample at 5 Gy/s, for a few selected wavelength across the emission band. a) Raw data in linear scale, b) logarithmic scale

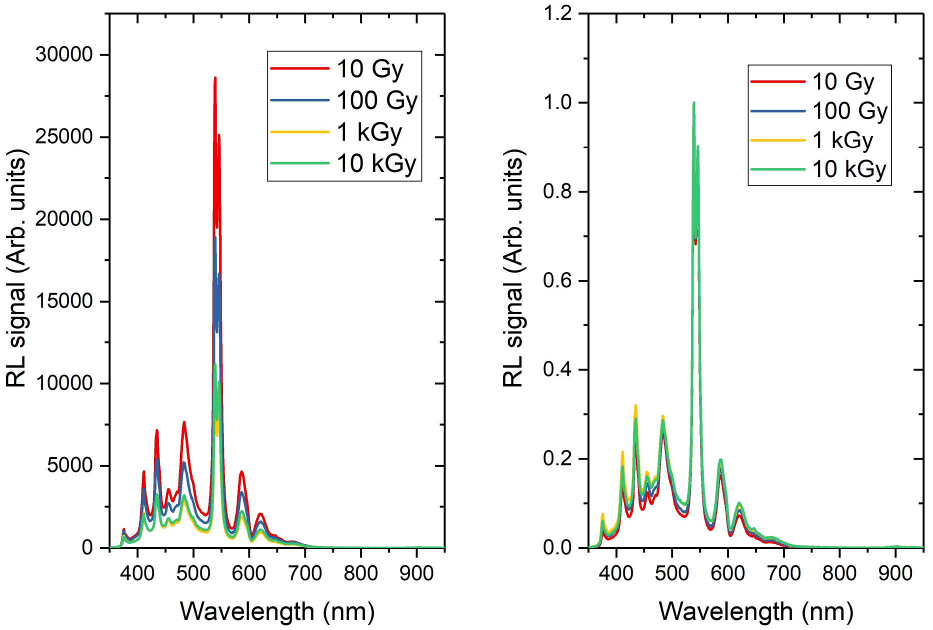

Figure 79 - RL spectra measured on 5-cm CeTb-doped fibre sample at 5 Gy/s, for different deposited doses. Left: Raw data, Right: Each curve is normalized to its own amplitude for shape comparison.

5.1.6.4 RL CeTb – codoped fibre : 5cm@0.5Gy/s

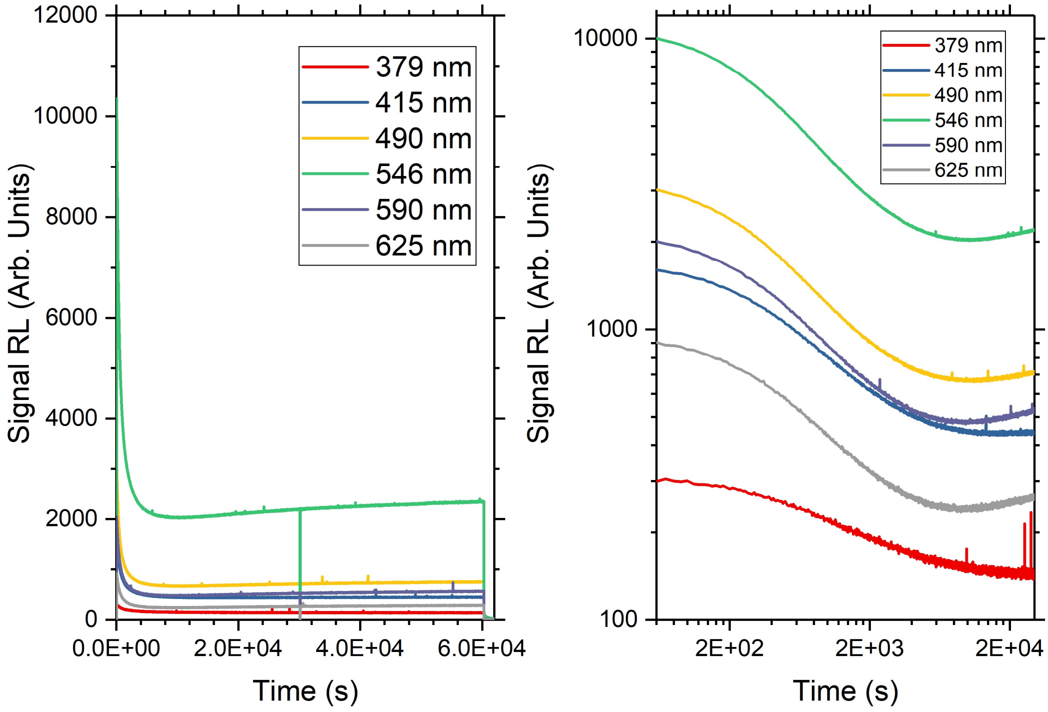

Figure 80 – Kinetics of the RL emission of 5-cm long CeTb-codoped fibre sample at 0.5 Gy/s, for a few selected wavelength across the emission band. a) Raw data in linear scale, b) logarithmic scale

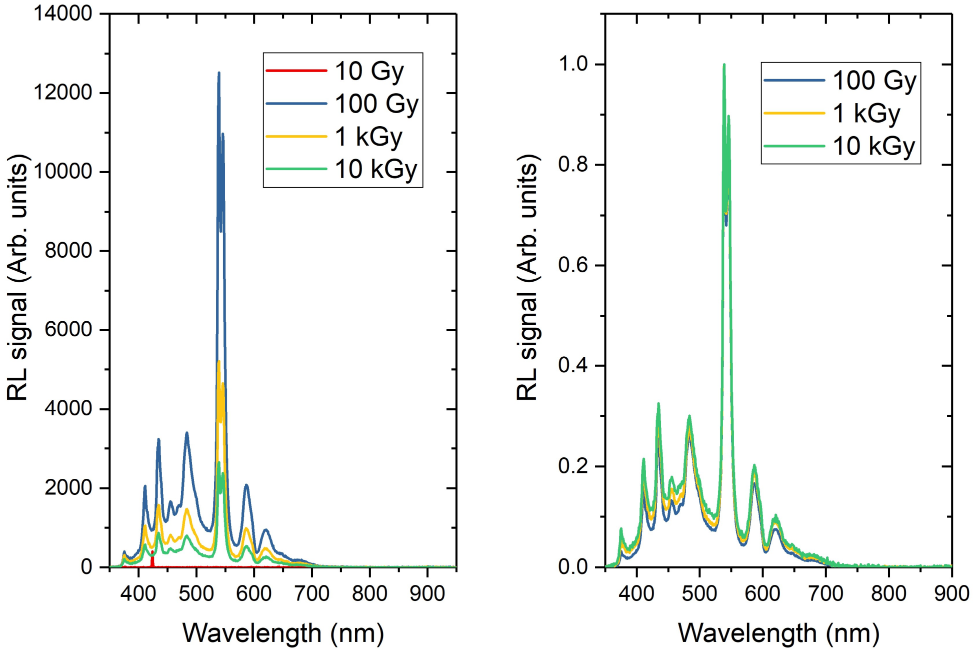

Figure 81 - RL spectra measured on 5-cm CeTb-doped fibre sample at 5 Gy/s, for different deposited doses. Left: Raw data, Right: Each curve is normalized to its own amplitude for shape comparison.

5.2 RADIATION INDUCED ATTENUATION

The RIA is one of the major effects occurring in optical fibres under irradiation, happening at the same time than other effects such as RL.The photons emitted through RL can be absorbed, not only due to intrinsic attenuation, but also by the new absorbing color centers created during the irradiation. This combination of effects leads to a subsequent competition between the RL and RIA phenomena. Consequently, the RIA contribution needs to be assessed to fully understand the physics behind the measured RL response of the sensor, even if in the end, only the RL emission is exploited for the dosimetry measurements.

However, measuring RIA in an optical fibre in the wavelength domain of the RL emission is a real challenge. Indeed, when measuring RIA, we need to inject light in the core of the fibre, and measure it from the other side of the fibre, after a certain length of the fibre under test. The change of light intensity during the irradiation is related to the RIA, but not only. A fraction of the light measured at the output of the fibre under test can also be composed of the RL emitted photons in our radioluminescent fibers. This can lead to an underestimation of the RIA contribution. Since there is no way to stop the RL from happening during the RIA measurement, it is important to be able to decorrelate as much as possible the two phenomena.

To do so, the easiest way is to to ensure the fact that the RL light emission is negligible with respect to the light injected for the RIA measurement. Therefore, there is a need to find the right tradeoff between having enough light to have a good SNR during the RIA measurement, and at the same time not too much not to impact notably induce other side effects such as photobleaching. This effect occurs in fibres under irradiation when light is injected in the core of the fibre, and bleaches the color centres defects created by radiation, leading to a decrease of the measured RIA. Several attempts were needed to empirically find the right injected light power to keep the RL photons effects on the RIA measurement negligible. A way to verify this assumption, is to perform a RIA measurement, and stop the light at a time where the RIA amplitude is the highest (worst case scenario), and evaluate the remaining light measured at this time, which comes only from the RL. If this light intensity is negligible with respect to that present just before stopping the light source, therefore, we can consider that RL contribution is negligible in the RIA measurement.

In order to be later able to understand the interplay between RL and RIA during an irradiation, we need to perform both measurements in the same conditions. Since it is not possible to measure simultaneously the RL and the RIA in the same fibre sample, we need to find a way to have the same experimental conditions. For this reason, we performed all the RL and RIA measurements irradiations at the same time, on two different samples coming from the same few centimeters of a spool to limit the variability from sample to sample as well as obtaining the same dose rate, dose, and temperature conditions. Dedicated study of the repeatability are needed for the final application, and are investigated within another PhD work hosted by the Laboratoire Hubert Curien. For this RIA measurement, we will therefore fix the same set of experimental conditions as described in table 4 during the RL measurement.

The obtained data represent tens of thousands of individual files containing each spectrometer acquisition. These Giga-Bits of data are saved on a computer during the acquisition. After the experiment, we used a serie of python scripts developed during the course of the PhD thesis allowing an efficient repetitive analysis of these dataset in order to extract easily handlable data for plotting the presesented results.

5.2.1 RIA study in Ce-doped fibre

We start the analysis of the RIA measurements on the Ce-doped fibre with the same experimental conditions used in the RL study.

5.2.1.1 RIA Ce-doped fibre : 1cm@20Gy/s

We begin with the measurements performed on 1-cm long Ce-doped fibre irradiation at 20 Gy/s. As shown in Figure 82, we observe a strong RIA for the fibre with levels reaching values above 180 dB/m (1.8 dB/cm). As expected, the RIA levels generally decrease at increasing wavelengths. Another observation we made is that the levels of RIA changes during the irradiation. When extracting the RIA kinetics at a few selected wavelengths, we obtain the kinetics shown in Figure 83. We observe an increase of the RIA in the first part of the irradiation until a maximum located at 2-3 kGy, which is compatible with the dose level at which we observed the maximum RL signal in this fibre. When the irradiation is stopped at 600 kGy, we note a fast recovery followed by a slower recovery to much lower RIA levels. Then, when the second irradiation took place, we note a very fast increase of the RIA levels to similar values observed during the first irradiation.

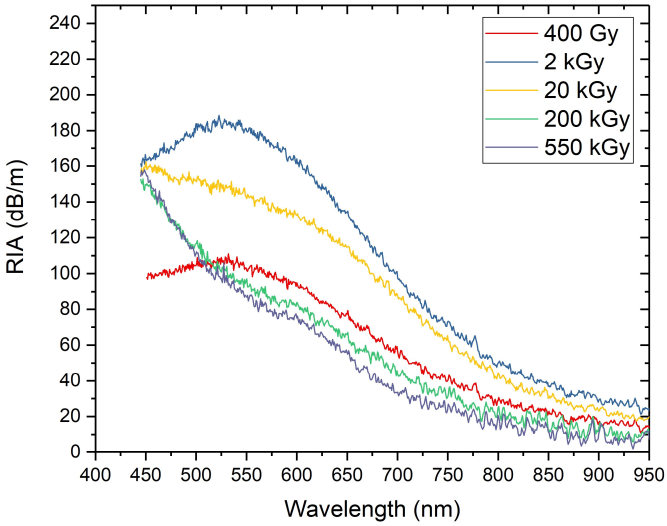

Figure 82 – RIA spectra measured on a 1-cm long Ce-doped fibre sample at 20 Gy/s at different deposited doses.

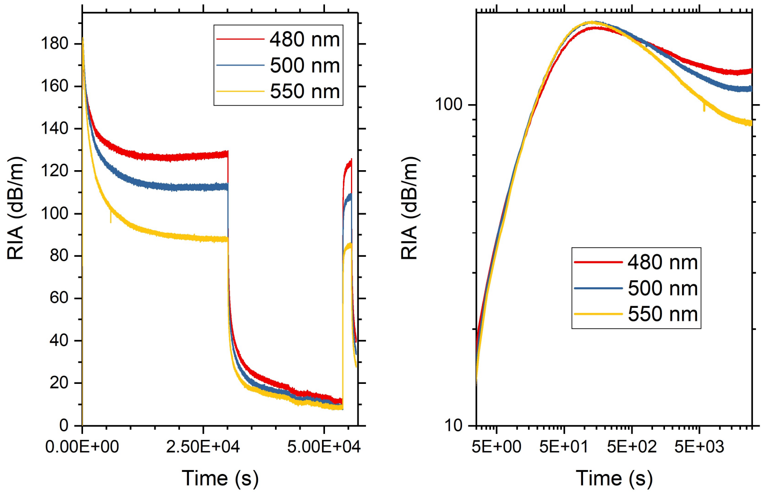

Figure 83 – RIA kinetics at a few selected wavelengths measured on a 1-cm long Ce-doped fibre at 20 Gy/s/ a) Linear scale, b) Logarithmic scale.

5.2.1.2 RIA Ce -doped fibre : 1cm@5Gy/s

Here, we tested the RIA response of a 1-cm long Ce-doped fibre under a 5 Gy/s, and obtained the RIA spectra shown in Figure 84. We observe again strong RIA levels above 140 dB/m, slightly lower than that observed at higher dose rate. The amplitude of the RIA spectra changes depending on the dose.

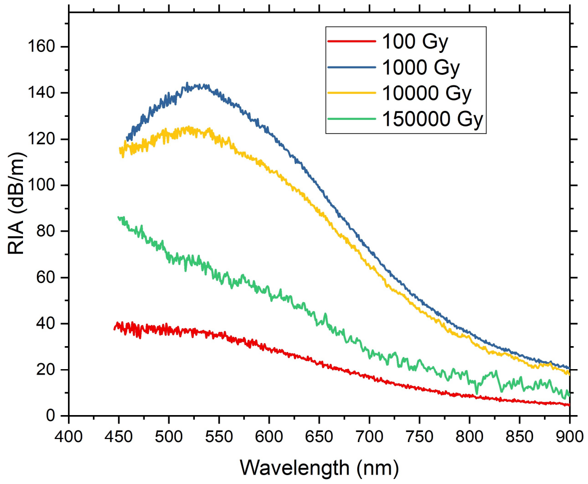

Figure 84 - RIA spectra measured on a 1-cm long Ce-doped fibre sample at 5 Gy/s at different deposited doses.

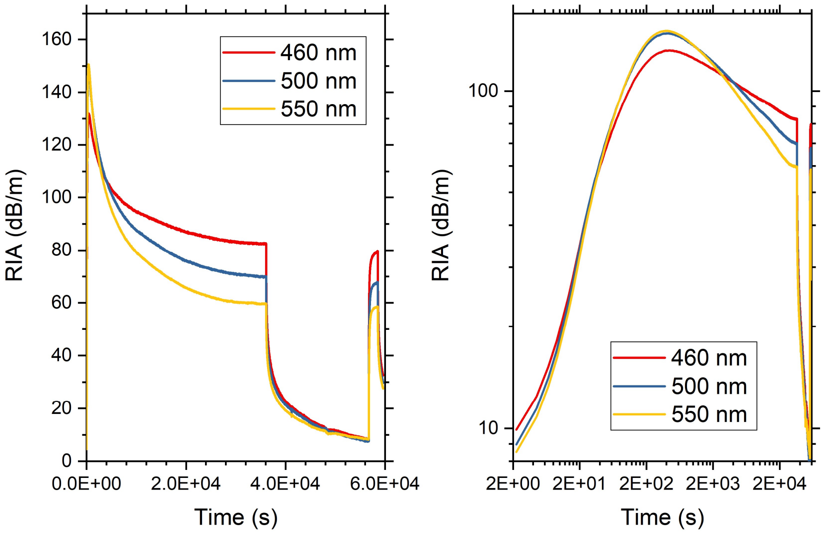

Figure 85 – RIA kinetics at a few selected wavelengths measured on a 1-cm long Ce-doped fibre at 5 Gy/s/ a) Linear scale, b) Logarythmic scale.

When focusing on the RIA kinetics extracted from the spectra different wavelengths, we not a similar trend with respect to that observed at 20 Gy/s. We note an increase of the RIA levels until 2-3 kGy, before a decrease until the end of the irradiation. Again, the RIA levels comes back to a similar level when restarting the irradiation after several hours recovery.

5.2.1.3 RIA Ce -doped fibre : 5cm@5Gy/s

In this part, we performed the same test on 5-cm long Ce-doped fibre under 5 Gy/s. We obtained the RIA spectra measured at different doses shown in Figure 86. We observe important RIA levels compatible with that observed in chapter 5.2.1.2. Additionnaly, we note a change in the amplitude of the RIA spectrum during the irradiation.

In the kinetics extracted from the measured spectra, at different wavelengths we observe very similar trends with respect to that observed in chapter 5.2.1.2. Indeed, the RIA increases until a maximum value around 140 dB/m reached at a 2-3 kGy dose before a decrease until the end of the irradiation. Furthermore, the RIA recovery trend between the first and the second irradiation are similar as well. The RIA levels during the second irradiation are close to that observed during the last first irradiation.

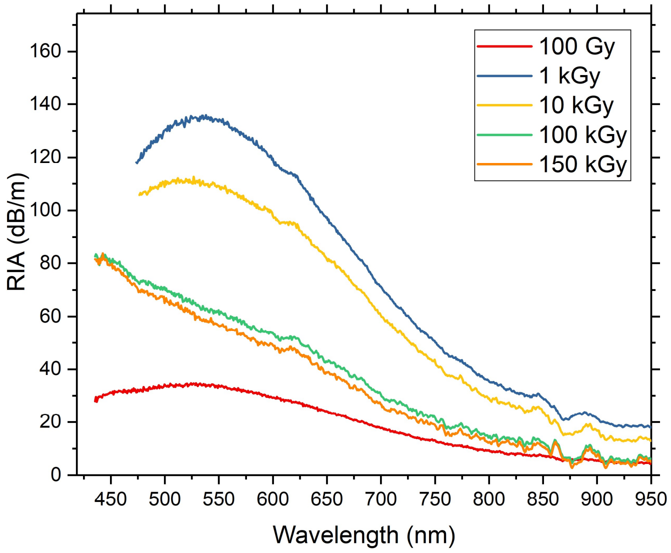

Figure 86 - RIA spectra measured on a 5-cm long Ce-doped fibre sample at 5 Gy/s at different deposited doses.

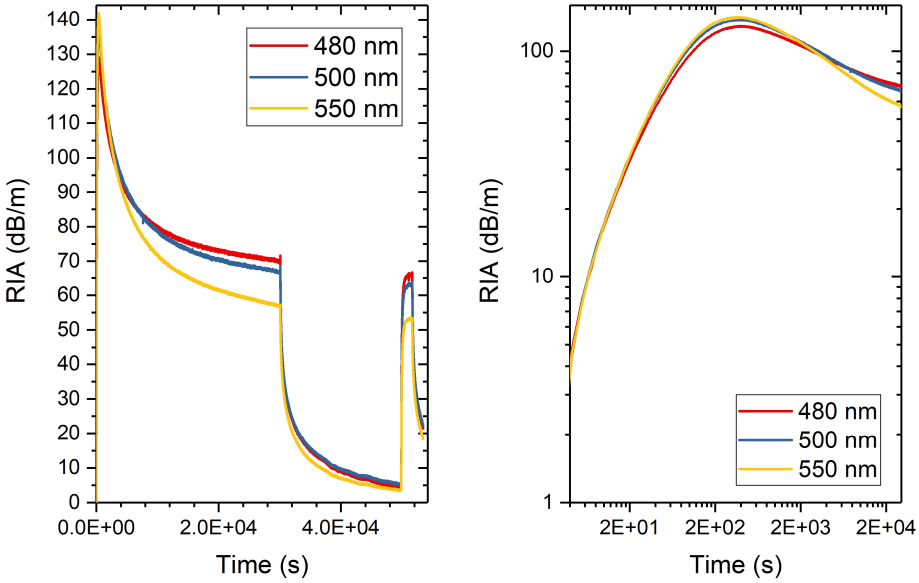

Figure 87 – RIA kinetics at a few selected wavelengths measured on a 5-cm long Ce-doped fibre at 5 Gy/s/ a) Linear scale, b) Logarithmic scale.

5.2.1.4 RIA Ce -doped fibre : 5cm@0.5Gy/s

In this part, we measure the RIA response of 5-cm long Ce-doped fibre under 0.5 Gy/s. The obtained RIA spectra measured at different doses are shown in Figure 88 showing RIA levels reaching up to 110 dB/m. The spectra also changes during the irradiation.

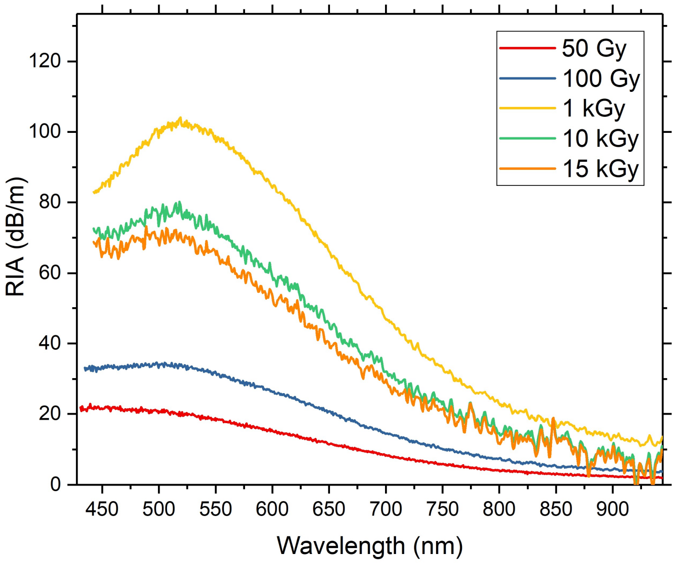

Figure 88 - RIA spectra measured on a 5-cm long Ce-doped fibre sample at 0.5 Gy/s at different deposited doses.

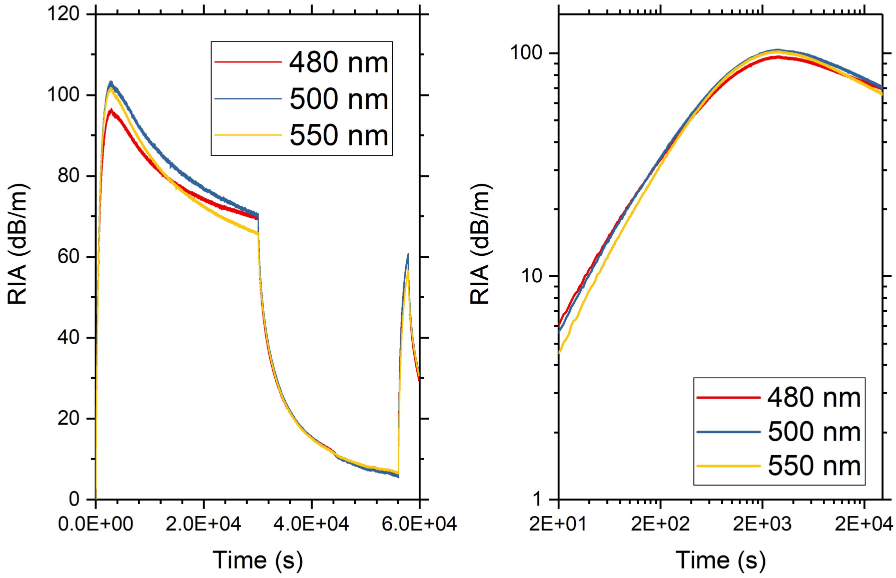

Figure 89 – RIA kinetics at a few selected wavelengths measured on a 5-cm long Ce-doped fibre at 0.5 Gy/s/ a) Linear scale, b) Logarythmic scale.

The RIA levels are lower than those observed at higher dose rates in this fibre. On the RIA kinetics side, we note that the RIA increases until a 2 kGy dose before decreasing until the end of the irradiation. After the recovery time, we note that the RIA levels come back to levels slightly lower than those measured during the first irradiation, but during this short irradiation, the RIA does not reach a plateau, as for the other irradiation conditions.

5.2.2 RIA study in Cu-doped fibre

We continue the analysis of the RIA measurements with those performed on Cu-doped fibre.

5.2.2.1 RIA Cu-doped fibre : 1cm@20Gy/s

During this irradiation, we obtained the RIA spectra at different doses shown in Figure 91. We observe very important RIA levels with amplitude reaching up to 500 dB/m. This value is more important than that observed previously in Ce-doped fibre. The RIA amplitude changes during the irradiation, and it is decreasing at larger wavelengths.

When extracting the RIA kinetics, we notice an increase of the RIA levels until 100 kGy, before a decrease until the end of the irradiation. The maximum amplitude of the RIA is reached at higher dose than in Ce-doped fibre. During the recovery time, we note an anneling effect less pronounced than the one observed in Ce-doped fibre. At the start of the second irradiation, we observe a return to similar levels to that measured at the end of the first irradiation.

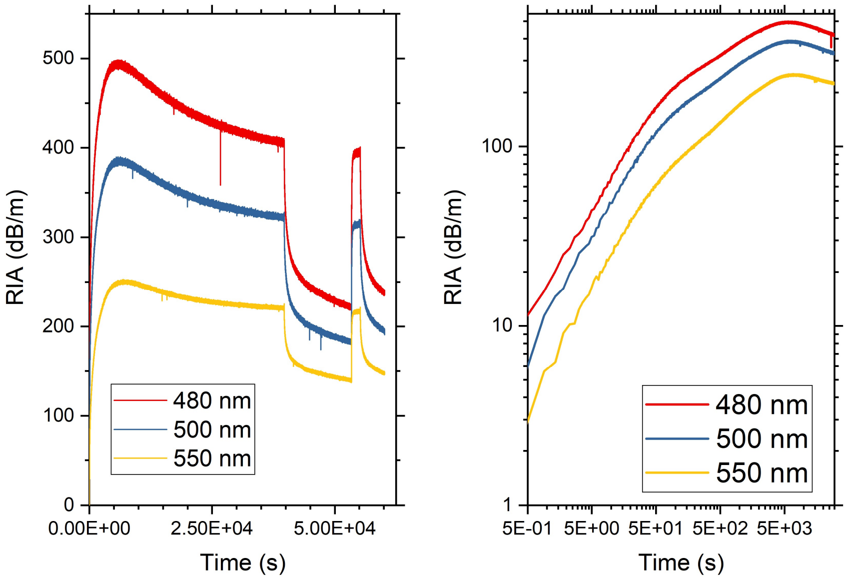

Figure 90 – RIA kinetics at a few selected wavelengths measured on a 1-cm long Cu-doped fibre at 20 Gy/s/ a) Linear scale, b) Logarythmic scale.

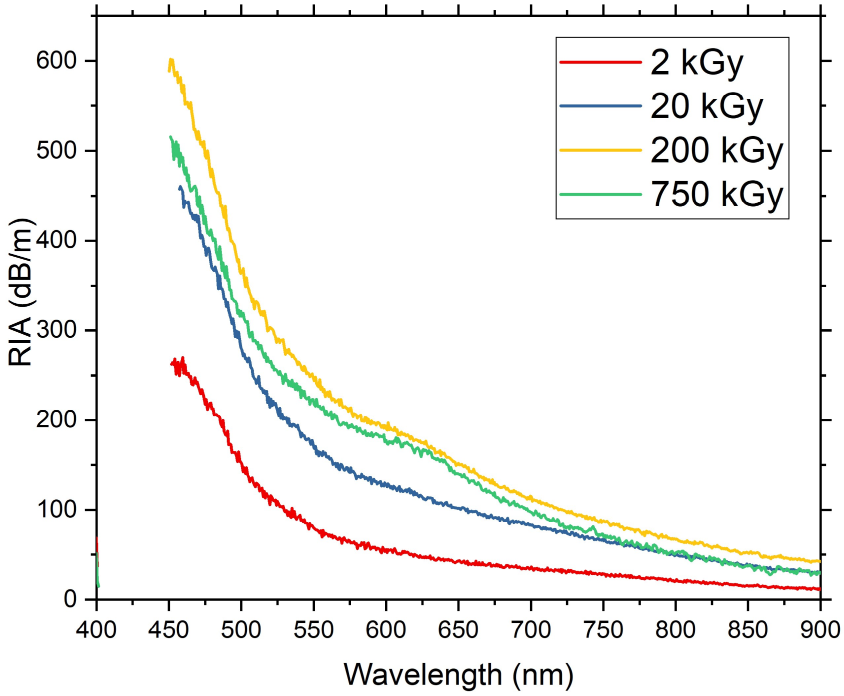

Figure 91 – RIA spectra measured on a 1-cm long Cu-doped fibre sample at 20 Gy/s at different deposited doses.

5.2.2.2 RIA Cu-doped fibre : 1cm@5Gy/s

Here, we performed an irradiation on 1-cm long fibre of Cu-doped fibre under a 5 Gy/s. We observe important RIA levels, slightly lower than those observed at 20 Gy/s. The RIA still changes during the irradiation.

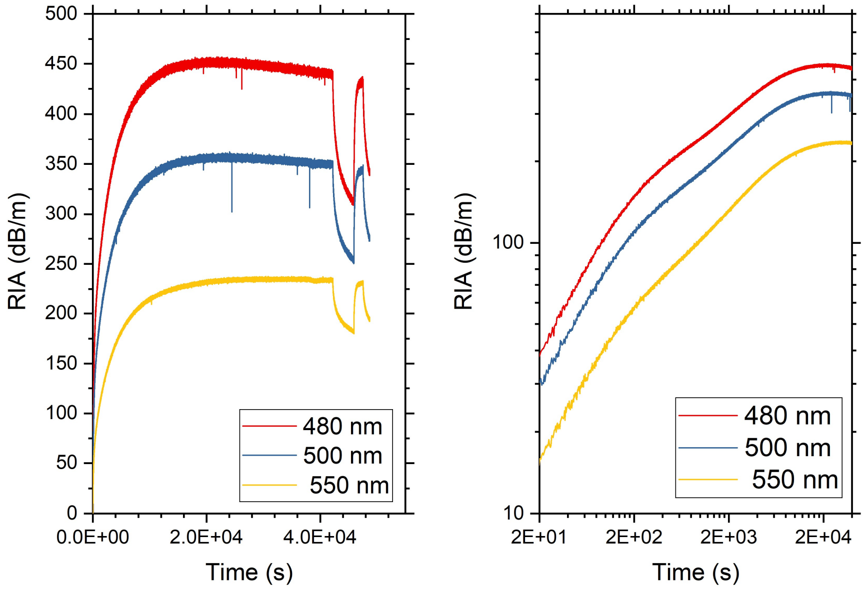

Figure 92 – RIA kinetics at a few selected wavelengths measured on a 1-cm long Cu-doped fibre at 5 Gy/s/ a) Linear scale, b) Logarythmic scale.

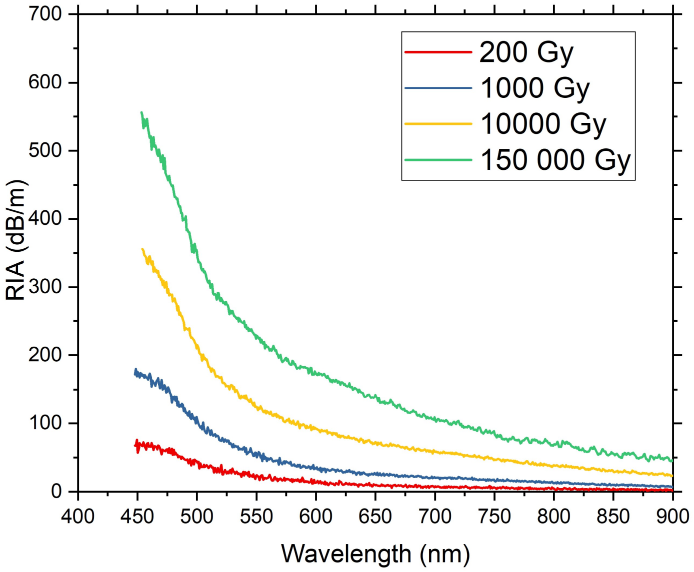

Figure 93 - RIA spectra measured on a 1-cm long Ce-doped fibre sample at 5 Gy/s at different deposited doses.

When focusing on the kinetics of the RIA shown in Figure 92, we observe an increase of the RIA levels until 100 kGy before a stabilization of the RIA levels until the end of the irradiation.

5.2.2.3 RIA Cu-doped fibre : 5cm@5Gy/s

When performing the same test on 5-cm long Cu-doped fibre under a 5 Gy/s irradiation, we measure the RIA spectra shown in Figure 95. The RIA reaches levels as high as 400 dB/m which are lower than those observed at higher dose rate in the 1-cm long sample.

When focusing on the kinetics of the RIA shown in Figure 94, we note an increase of the RIA before a stabilization around 100 kGy. The observed trends is close to that observed in 1-cm long fibre tested at 5 Gy/s. During the recovery time without irradiation, we note that the annealing is limited, and that the RIA levels after the restart of the irradiation are compatible with those measured during the first irradiation.

We observe at the end of the irradiation, a peak in the RIA measurement. This is due to the fact that when the irradiation stops, the RL signal stops within few hundreds of μs whereas the RIA recovery takes more time. Thus, the peak is linked to the impact of RL signal on the RIA measurement, which is in this case more important than in other datasets.

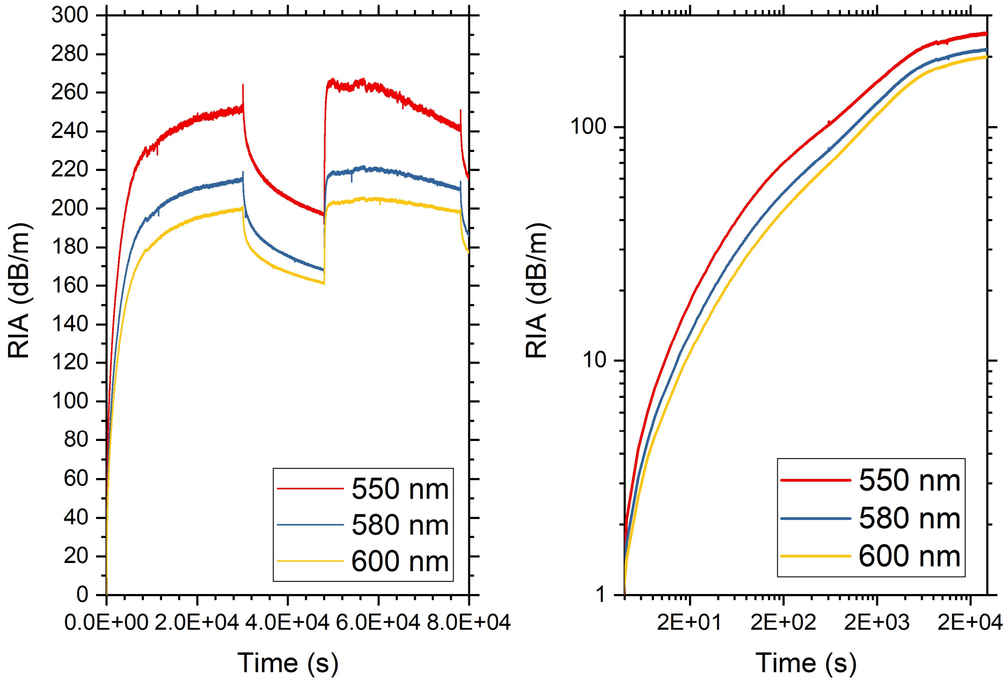

Figure 94 – RIA kinetics at a few selected wavelengths measured on a 5-cm long Cu-doped fibre at 5 Gy/s/ a) Linear scale, b) Logarithmic scale.

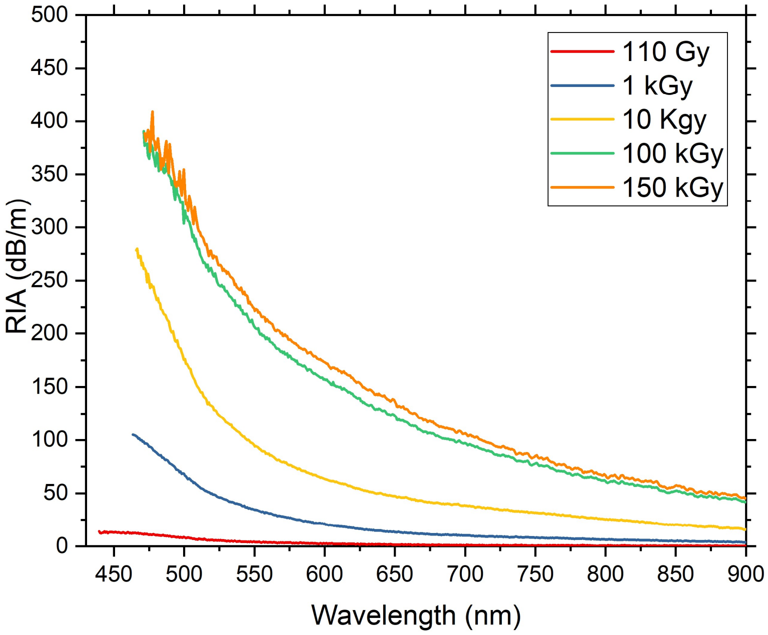

Figure 95 - RIA spectra measured on a 5-cm long Cu-doped fibre sample at 5 Gy/s at different deposited doses.

5.2.2.4 RIA Cu-doped fibre : 5cm@0.5Gy/s

In this part of the study, we perform the same RIA study on a 5-cm long Cu-doped fibre during a 0.5 Gy/s irradiation. We noted RIA levels as high as 400 dB/m, changing during the irradiation as shown in Figure 97.

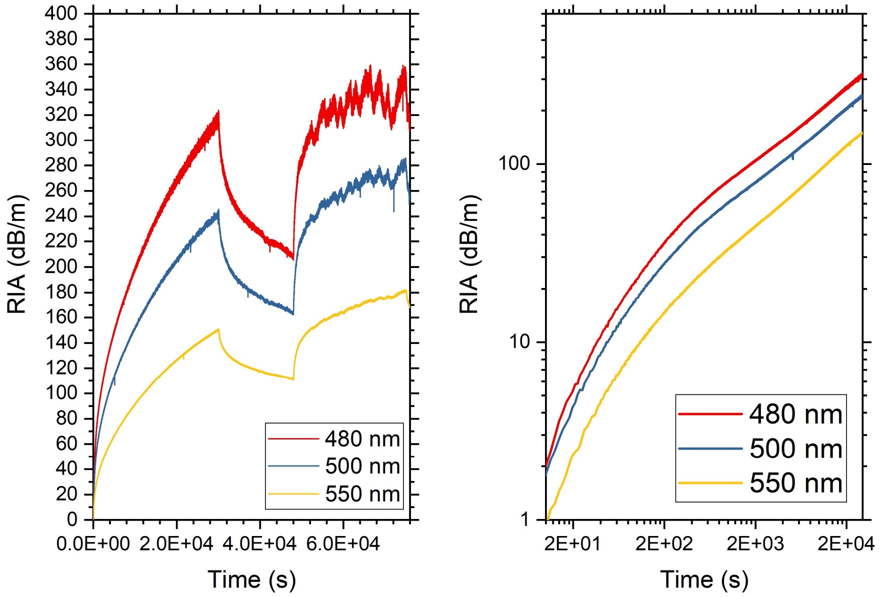

Figure 96 – RIA kinetics at a few selected wavelengths measured on a 5-cm long Cu-doped fibre at 0.5 Gy/s/ a) Linear scale, b) Logarithmic scale.

When focusing on the kinetics of the RIA presented in Figure 96, we observe an increase of the RIA during the irradiation, and a limited annealing effect during the recovery. The RIA levels during the second irradiation are similar to those of the first irradiation. We note also that there are some fluctuations of the signal during the irradiation which are most likely linked to the experimental bench and the very high RIA levels.

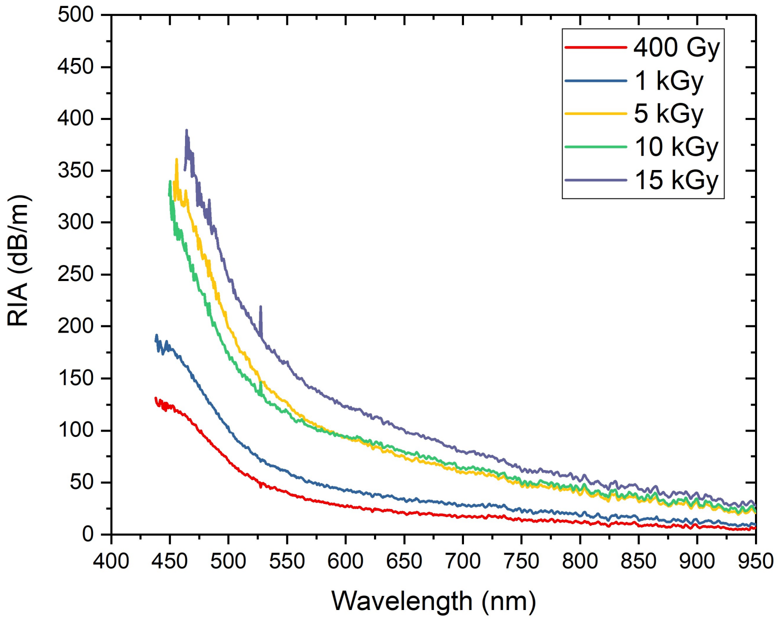

Figure 97 – RIA spectra measured on a 5-cm long Cu-doped fibre sample at 0.5 Gy/s at different deposited doses.

5.2.3 RIA study in CuCe-codoped fibre

In this part of the study we now introduce the RIA measurements performed in the CuCe-codoped optical fibre.

5.2.3.1 RIA CuCe-codoped fibre : 1cm@20Gy/s

We start with the irradiation on 1-cm long CuCe-codoped fibre under a 20 Gy/s dose rate. The RIA spectra measured during the irradiation are shown in Figure 99. We observe strong RIA levels reaching 600 dB/m, with amplitude changing during the irradiation. These levels are compatible with those observed in Cu-doped fibre.

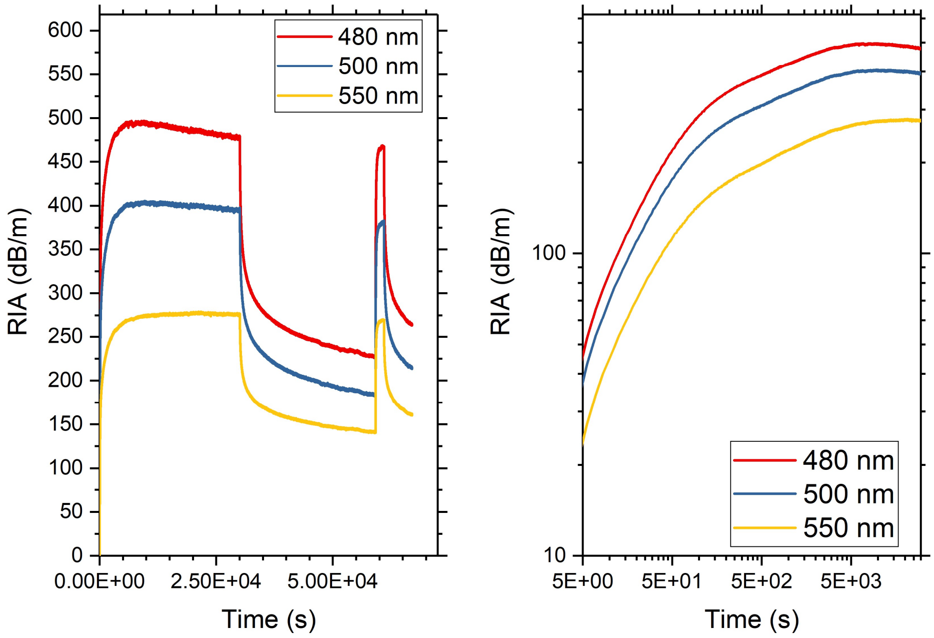

Figure 98 - RIA kinetics at a few selected wavelengths measured on a 1-cm long CuCe-codoped fibre at 20 Gy/s/ a) Linear scale, b) Logarithmic scale.

When focusing on the kinetics of the RIA, we note an increase of the RIA until 100 kGy before a stabilization of the signal until the end of the irradiation. We then observe a pronounced annealing during the recovery time. During the second irradiation, we note that the RIA levels are compatible with those measured during the first irradiation.

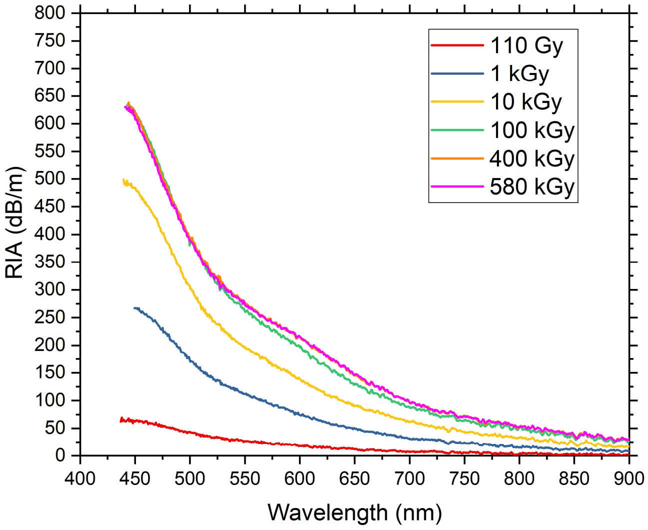

Figure 99 - RIA spectra measured on a 1-cm long CuCe-codoped fibre sample at 5 Gy/s at different deposited doses.

5.2.3.2 RIA CuCe-codoped fibre : 1cm@5Gy/s

In this case, we introduce the RIA measurements performed on 1-cm long CuCe-codoped fibre under a 5 Gy/s dose rate. We note important RIA levels reaching close to 600 dB/m, with amplitude changing during the irradiation as shown on the RIA spectra in Figure 101.

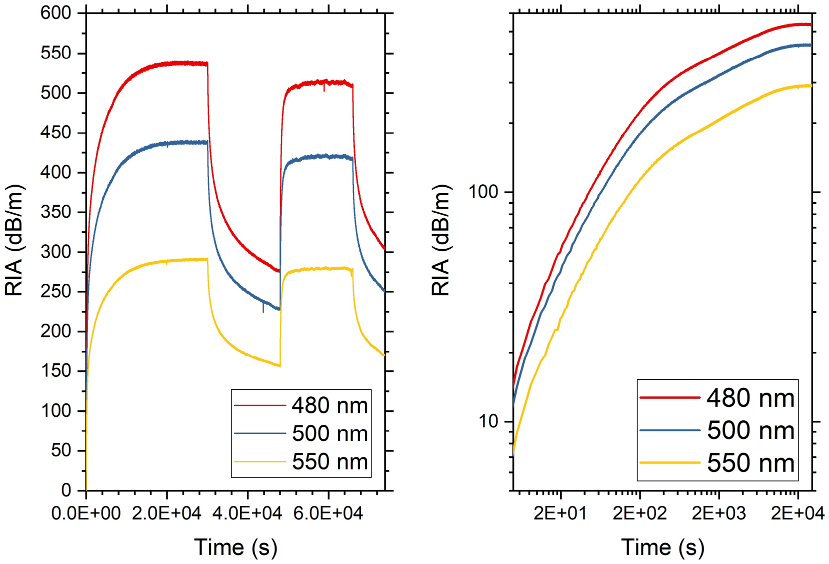

Figure 100 – RIA kinetics at a few selected wavelengths measured on a 1-cm long CuCe-codoped fibre at 5 Gy/s/ a) Linear scale, b) Logarithmic scale.

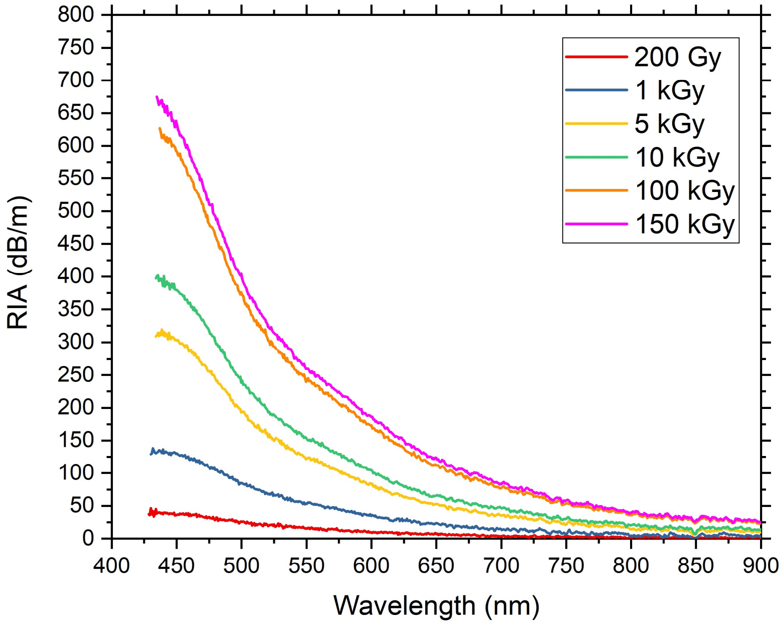

Figure 101 - RIA spectra measured on a 1-cm long CuCe-codoped fibre sample at 5 Gy/s at different deposited doses.

When focusing on the kinetics extracted from the spectra, we obtain the RIA kinetics presented in Figure 100. We observe an increase of the RIA until 100 kGy before a stabilization until the end of the irradiation. After the several hours recovery time, the restart of the irradiation brings the RIA levels back close to those of the first irradiation.

5.2.3.3 RIA CuCe-codoped: 5cm@5Gy/s

We present now the RIA measurement performed on 5-cm long CuCe-codoped fibre irradiated at 5 Gy/s. The obtained RIA spectra are shown in Figure 103, where we observe a strong RIA with levels as high as 300 dB/m at 550 nm. These levels are compatible with those obtained on 1-cm long samples at the same dose rate. The RIA changes during the irradiation.

When extracting the RIA kinetics from the spectra, we obtain the results shown in Figure 102 where we observe an increase of the RIA until 100 kGy before a stabilization until the end of the irradiation. After several hours of recovery time, we note that the RIA levels are brought back to levels similar to those measured during the first irradiation. We also observe a fast and sharp peak appearing at the stop of the first and second irradiations, which highlights the limited impact of the RL signal during the measurement. When we stop the irradiation, the RL signal disappears extremely fast resulting in a sharp increase of the measured RIA. The amplitude of this peak shows that the impact of the RL contribution is more present in this measurement than in others, however still with a minor contribution. Reducing further the light injection would potentially result in more noisy data or limited achievable dose range before saturation of the spectrometer dynamic range.

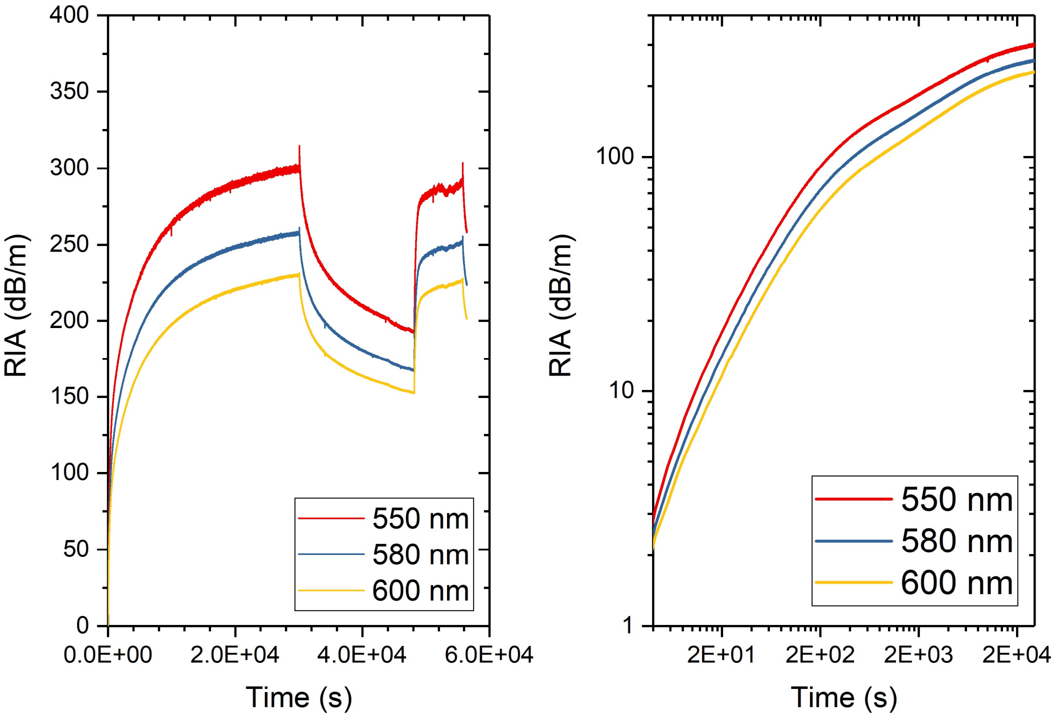

Figure 102 - RIA kinetics at a few selected wavelengths measured on a 5-cm long CuCe-codoped fibre at 5 Gy/s/ a) Linear scale, b) Logarithmic scale.

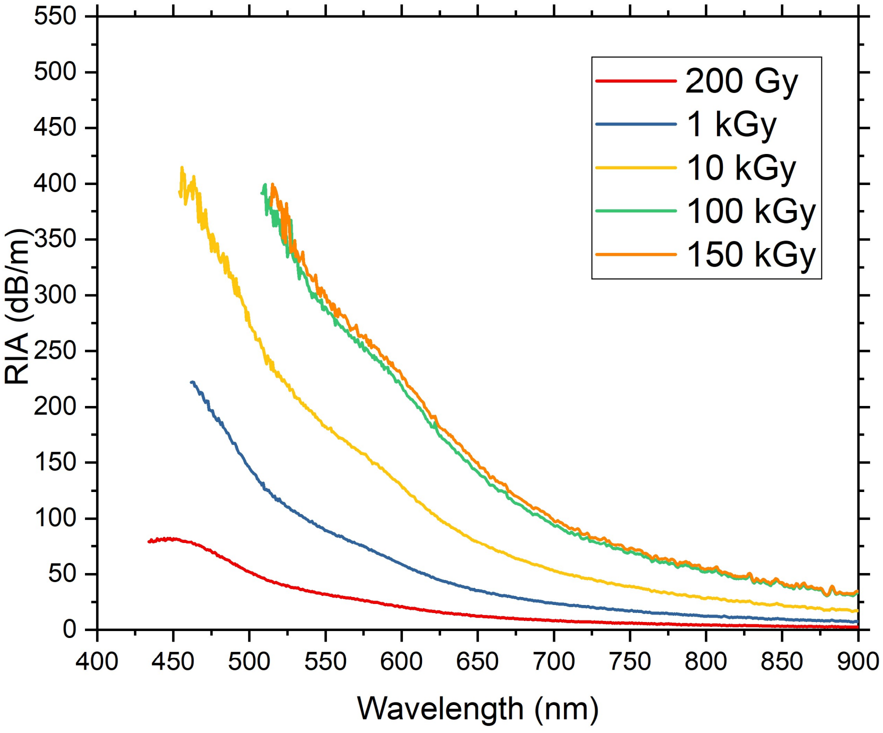

Figure 103 - RIA spectra measured on a 5-cm long CuCe-codoped fibre sample at 5 Gy/s at different deposited doses.

5.2.3.4 RIA CuCe-codoped: 5cm@0.5Gy/s

We finally analyse the RIA measurements on a 5-cm long CuCe-codoped fibre under a 0.5 Gy/s irradiation.

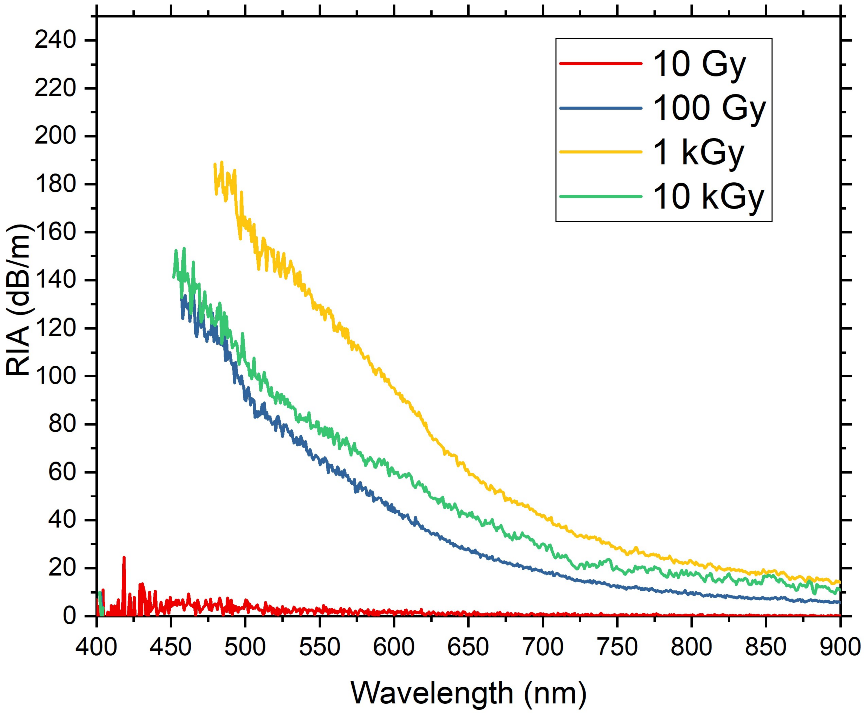

Figure 104 - RIA spectra measured on a 5-cm long CuCe-codoped fibre sample at 0.5 Gy/s at different deposited doses.

In Figure 104, we observe important RIA levels up to 180 dB/m at 500 nm. The RIA amplitude changes during the irradiation. When extracting the kinetics of the RIA, we observe an increase from the beginning to the end of the irradiation. Unfortunately, the second irradiation was not performed due to a technical issue with the programming of the irradiation. We therefore observe a long recovery after the 15 kGy irradiation.

At the end of the irradiation, we note that there is a small spike in the signal which is again the abrupt stop of the RL contribution in the signal when the irradiation ends. The impact on the RIA measurement is limited and cannot easily be more reduced without impacting the quality of the data.

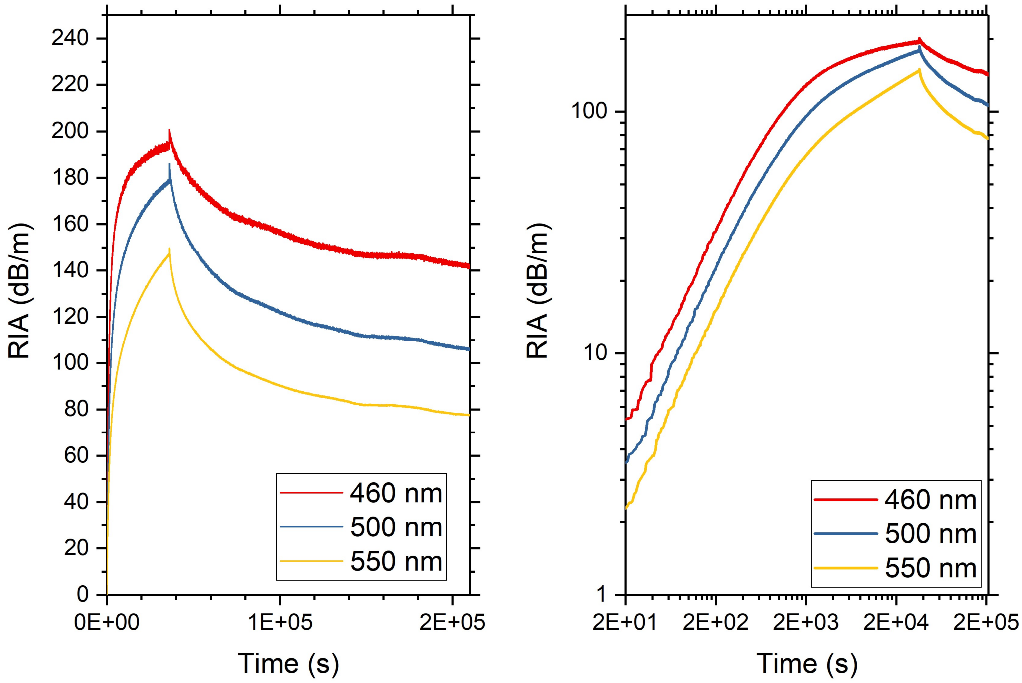

Figure 105 – RIA kinetics at a few selected wavelengths measured on a 5-cm long CuCe-codoped fibre at 0.5 Gy/s a) Linear scale, b) Logarithmic scale.

5.2.4 RIA study in Gd-doped fibre

In this part, we focus our RIA study on the Gd-doped fibre. This study is very challenging because the RIA in the UV-spectral region where the emission of the fibre takes place, is known to be very important. Therefore, we need to inject enough light to obtain a good measurement without saturating the dynamic of our sensor, but in the mean time keep under control the light injection to limit photobleaching.

As shown in the next figures, we observe in the results that the limited injected power in the UV is not high enough with respect to the RL emission of the Gd-centers located at 314 nm. This is highlighted by the negative peak appearing in the RIA spectra aroung 314 nm, explained by the fact that the increase of the RL signal during the irradiation induces a reduction of the measured RIA. To overcome this effect and being able to trace a kinetics of the RIA during the irradiation, around the RL emission spectral range, we decided to select a range close to 314 nm but outside the visible negative peak. The proximity with the emission spectral range should allow obtaining a measurement close the searched value,without impact of the sharp and narrow emission band.

By doing so, we observe an increase of the RIA until the end of the irradiation reaching strong RIA levels as high as 800 dB/m. At the stop of the irradiation, we note a slow recovery. After the restart of the irradiation, the RIA level is compatible with that observed during the first irradiation. The strong RIA is more important that that observed in other fibres, but remains logical owing the spectral location of the measurement.

5.2.4.1 RIA Gd-doped fibre : 1cm@20Gy/s

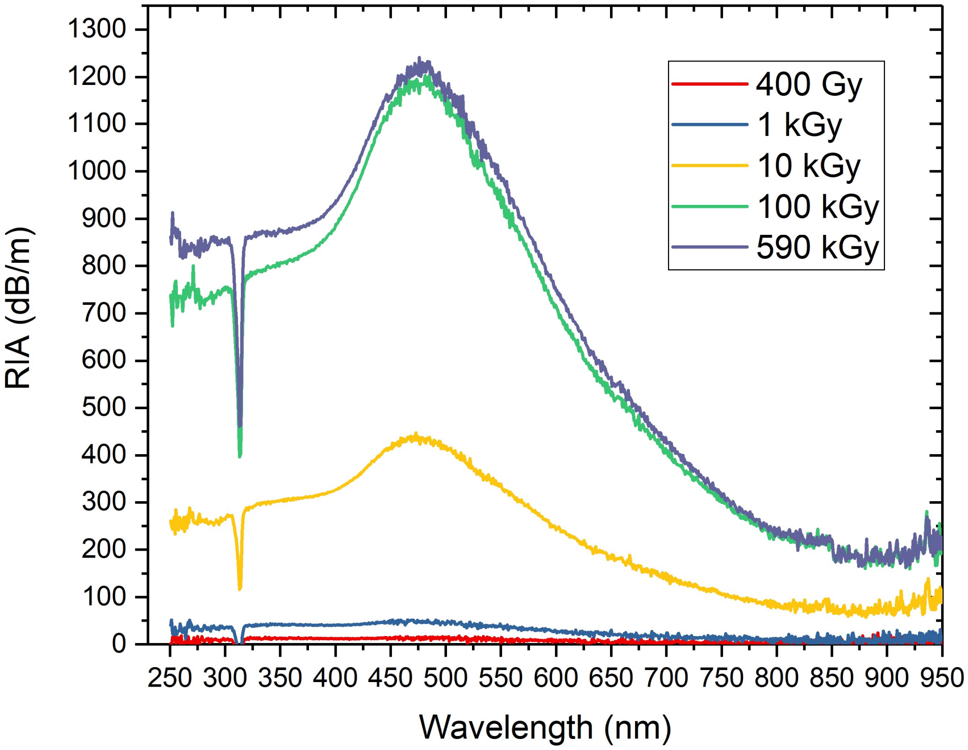

Figure 106 – RIA spectra measured on a 1-cm long Gd-doped fibre sample at 20 Gy/s at different deposited doses.

.

5.2.4.2 RIA Gd -doped fibre : 1cm@5Gy/s

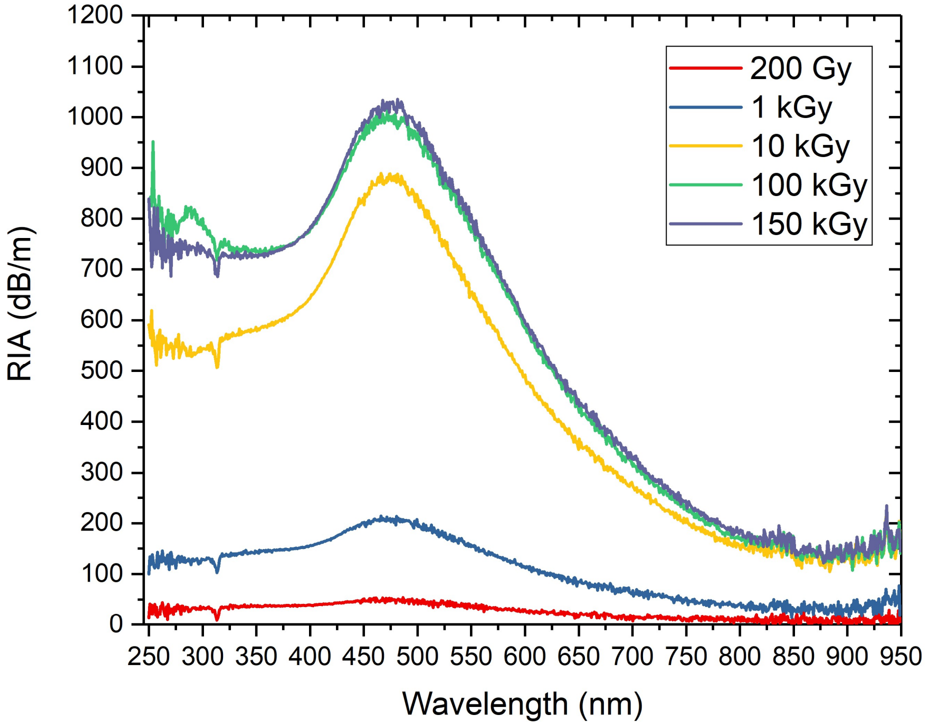

Figure 107 – RIA spectra measured on a 1-cm long Gd-doped fibre sample at 5 Gy/s at different deposited doses.

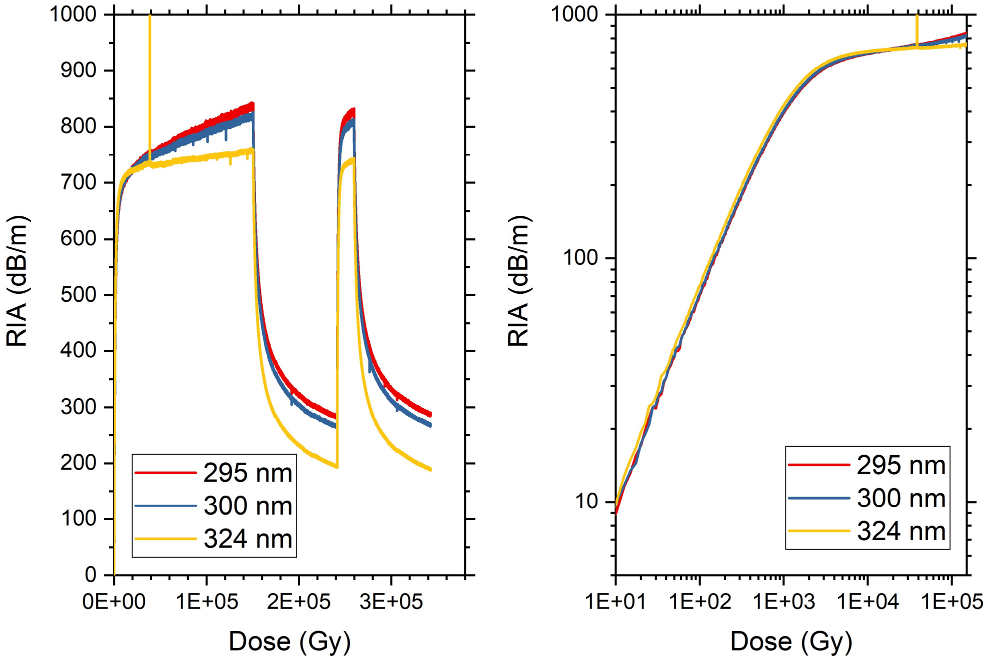

Figure 108 - RIA kinetics at a few selected wavelengths measured on a 1-cm long Gd-doped fibre at 5 Gy/s. a) Linear scale, b) Logarithmic scale.

5.2.4.3 RIA Gd -doped fibre : 5cm@5Gy/s

In this case, the RIA spectra measured are too noisy to be exploitable, therefore no kinetics are presented for this dataset.

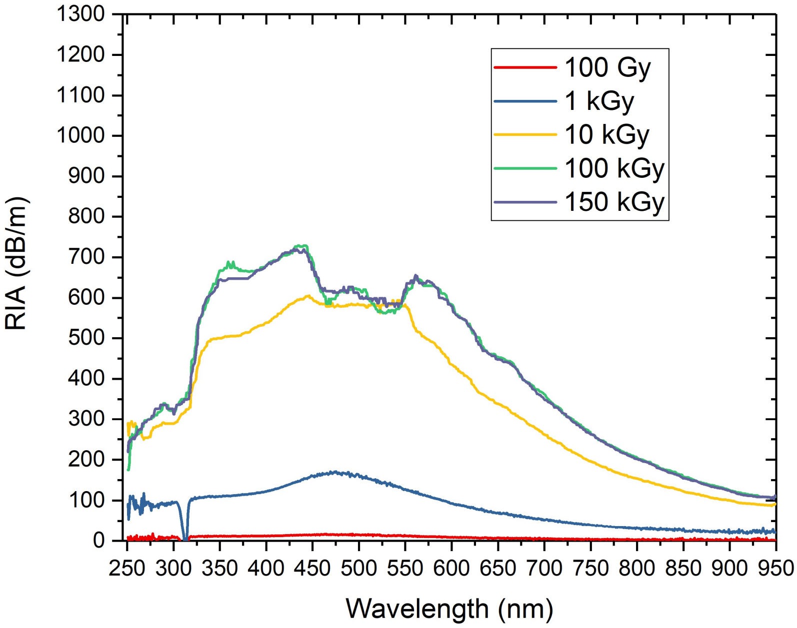

Figure 109 - RIA spectra measured on a 5-cm long Gd-doped fibre sample at 5 Gy/s at different deposited doses.

5.2.4.4 RIA Gd -doped fibre : 5cm@0.5Gy/s

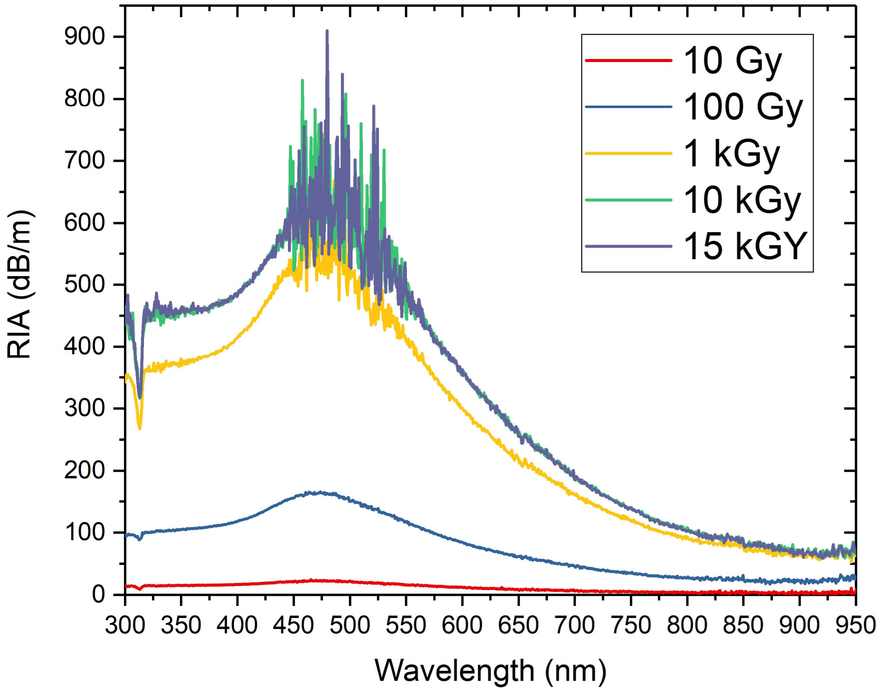

Figure 110 – RIA spectra measured on a 5-cm long Gd-doped fibre sample at 0.5 Gy/s at different deposited doses.

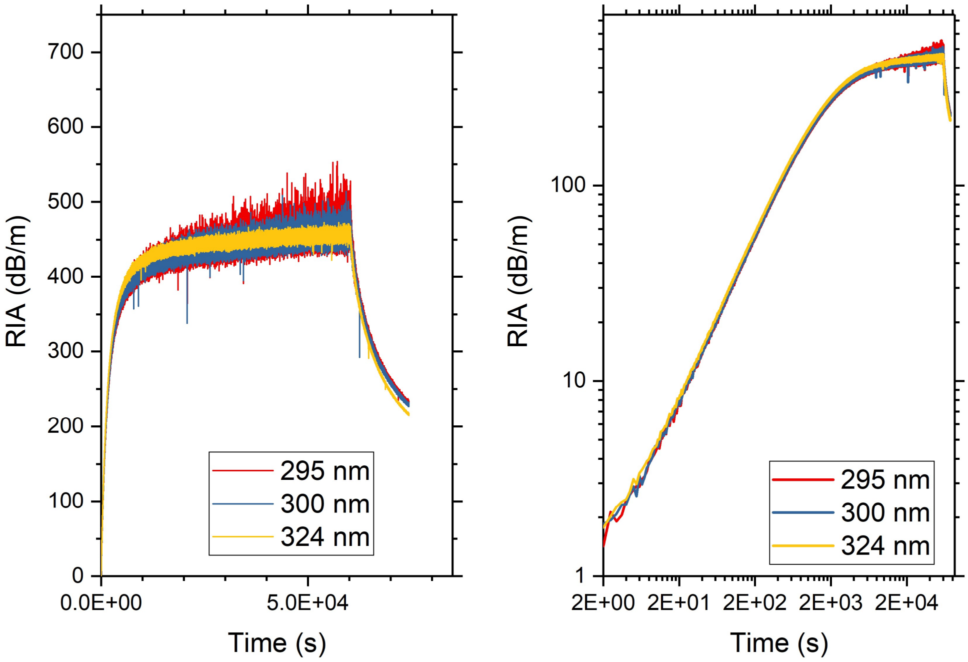

Figure 111 - RIA kinetics at a few selected wavelengths measured on a 5-cm long Gd-doped fibre at 0.5 Gy/s a) Linear scale, b) Logarithmic scale.

5.2.5 RIA study in N-doped fibre

Due to limited quantities of N-doped fibre available, since this fibre is not manufactured anymore, we could not perform the RIA measurements.

5.2.6 RIA study in CeTb-codoped fibre

Hereafter, we show the RIA measurements performed on the CeTb-codoped fibre. We show the spectra as well as the kinetics of the RIA at few selected wavelengths, choosen at the peaks observed in the complex RL emission spectra. The spectra shows a strong RIA reaching up to 600 dB/m, changing with dose. On the kinetics side we observe an increase of the RIA up to few kGys before a stabilization until the end of the irradiation on some selected wavelengths, whereas for some other the RIA slowly decrease. At the second irradiation, we note RIA levels similar to those observed during the first irradiation. In the two last datasets, we could not obtain the expected second irradiation due to a technical issue with the programmation of the irradiator

5.2.6.1 RIA CeTb-codoped fibre : 1cm@20Gy/s

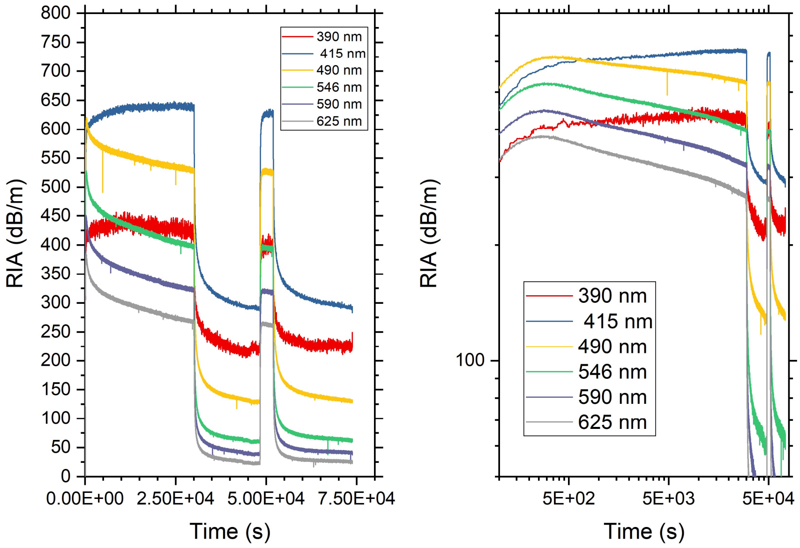

Figure 112 – RIA kinetics at a few selected wavelengths measured on a 1-cm long CeTb-codoped fibre at 20 Gy/s a) Linear scale, b) Logarithmic scale.

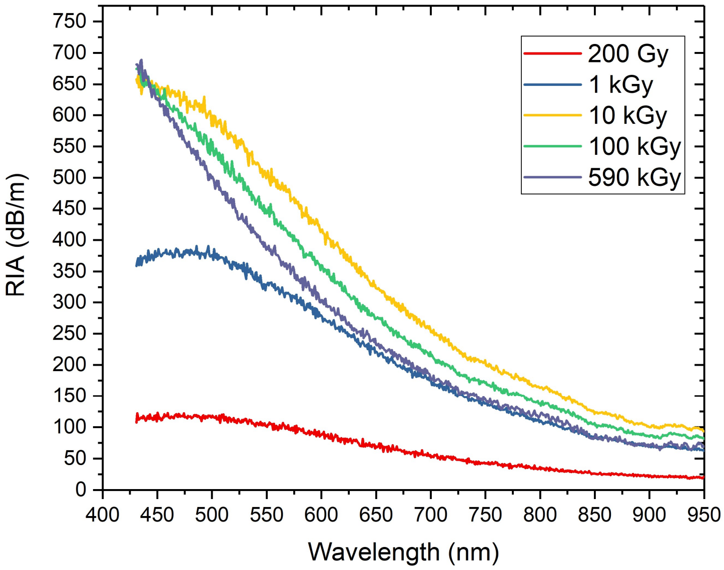

Figure 113 - RIA spectra measured on a 1-cm long CeTb-codoped fibre sample at 20 Gy/s at different deposited doses.

5.2.6.2 RIA CeTb-codoped fibre : 1cm@5Gy/s

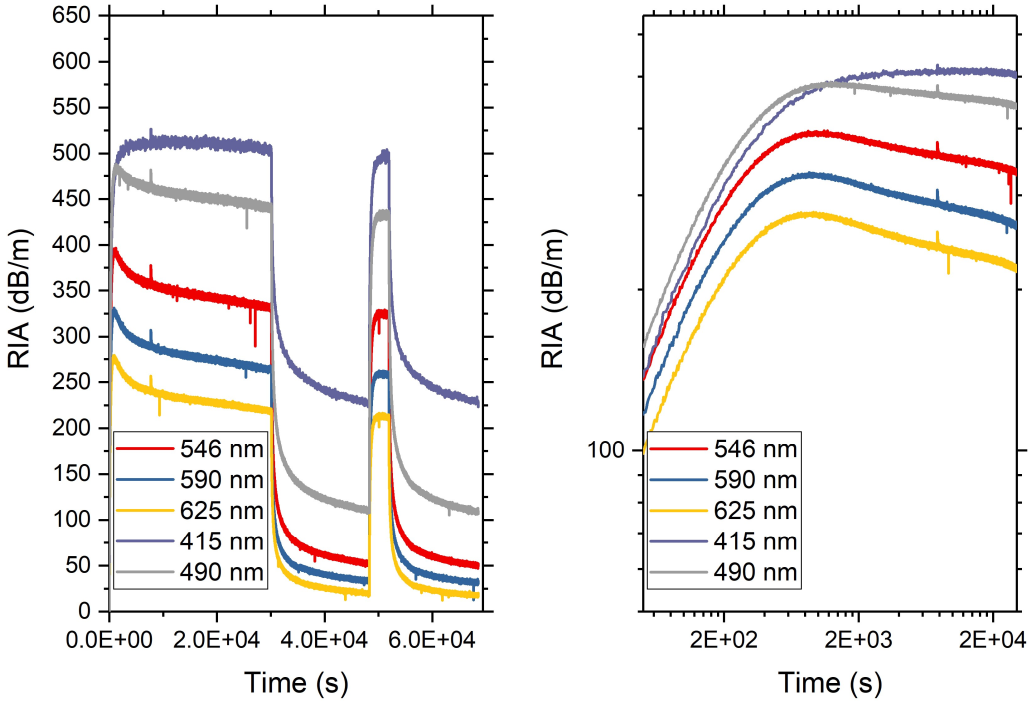

Figure 114 – RIA kinetics at a few selected wavelengths measured on a 1-cm long CeTb-codoped fibre at 5 Gy/s a) Linear scale, b) Logarithmic scale.

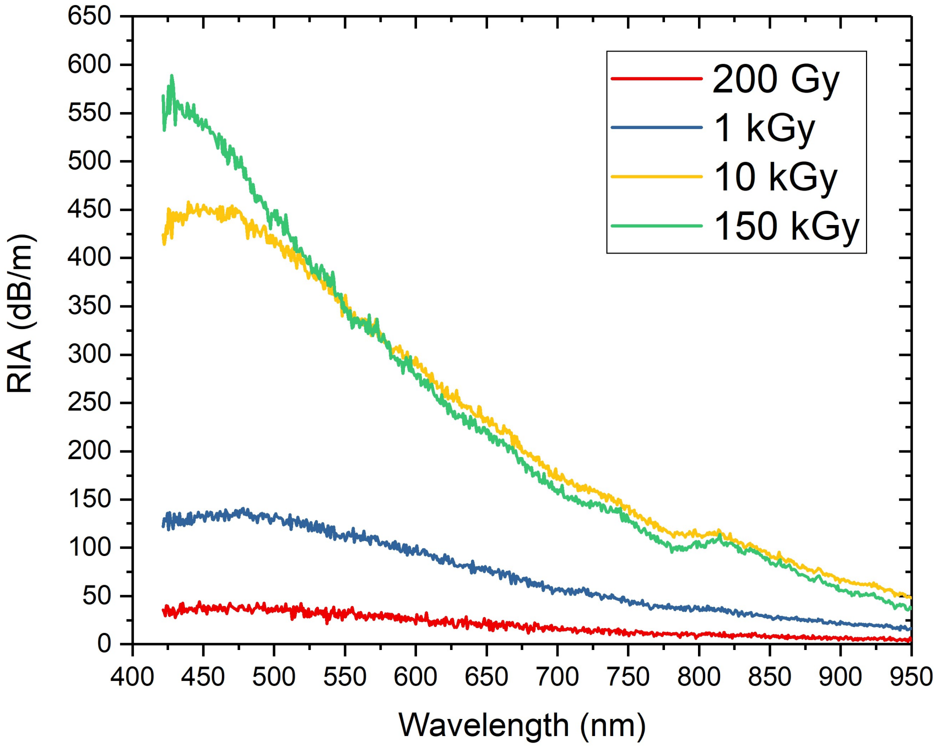

Figure 115 - RIA spectra measured on a 1-cm long CeTb-codoped fibre sample at 5 Gy/s at different deposited doses.

5.2.6.3 RIA CeTb-codoped fibre : 5cm@5Gy/s

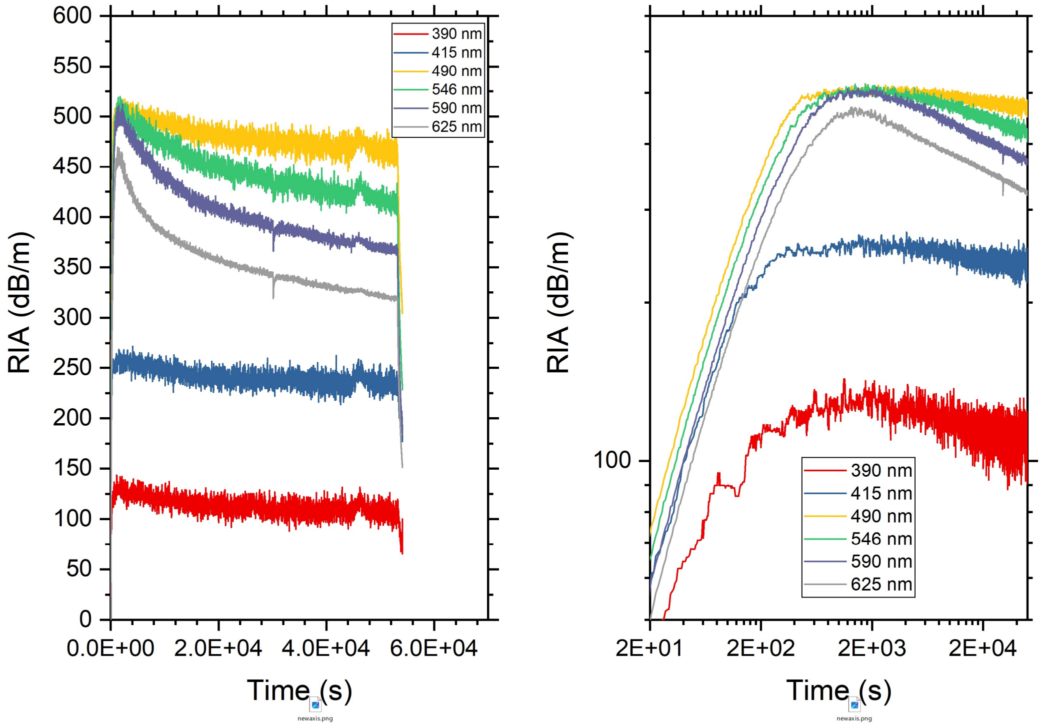

Figure 116 – RIA kinetics at a few selected wavelengths measured on a 5-cm long CeTb-codoped fibre at 5 Gy/s a) Linear scale, b) Logarithmic scale.

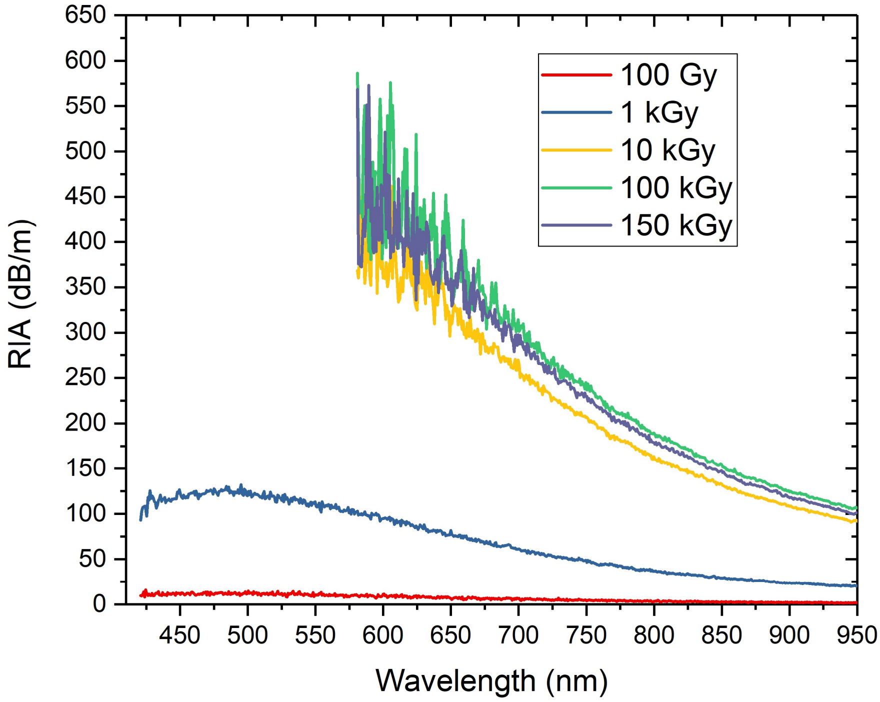

Figure 117 - RIA spectra measured on a 5-cm long CeTb-codoped fibre sample at 5 Gy/s at different deposited doses.

5.2.6.4 RIA CeTb-codoped fibre : 5cm@0.5Gy/s

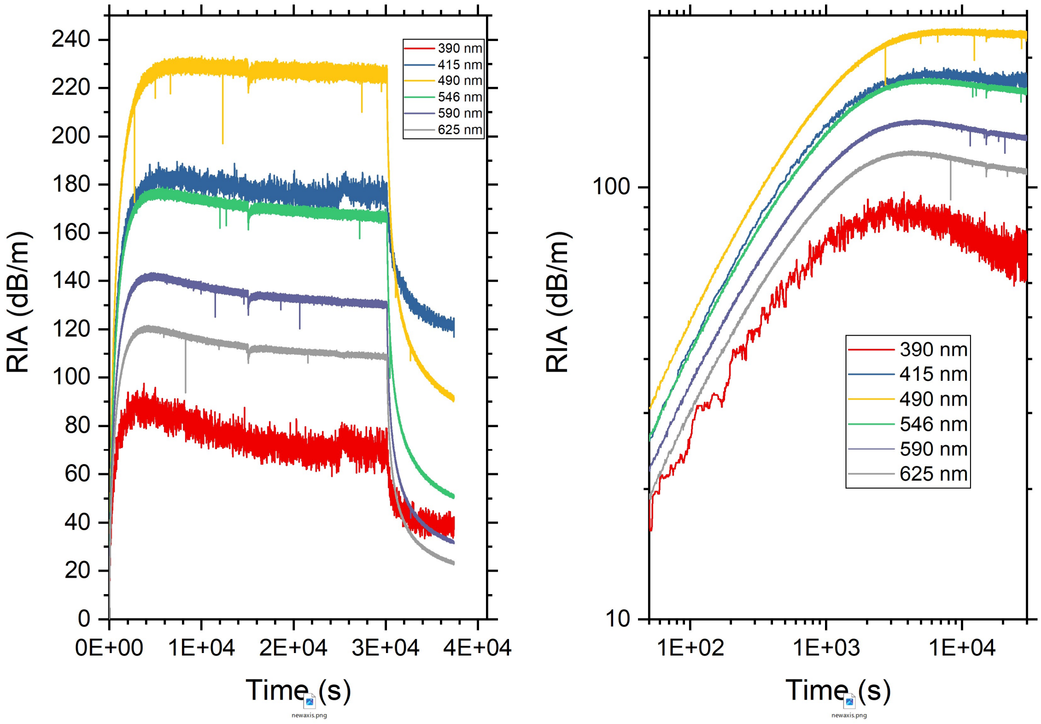

Figure 118 – RIA kinetics at a few selected wavelengths measured on a 5-cm long CeTb-codoped fibre at 0.5 Gy/s a) Linear scale, b) Logarithmic scale.

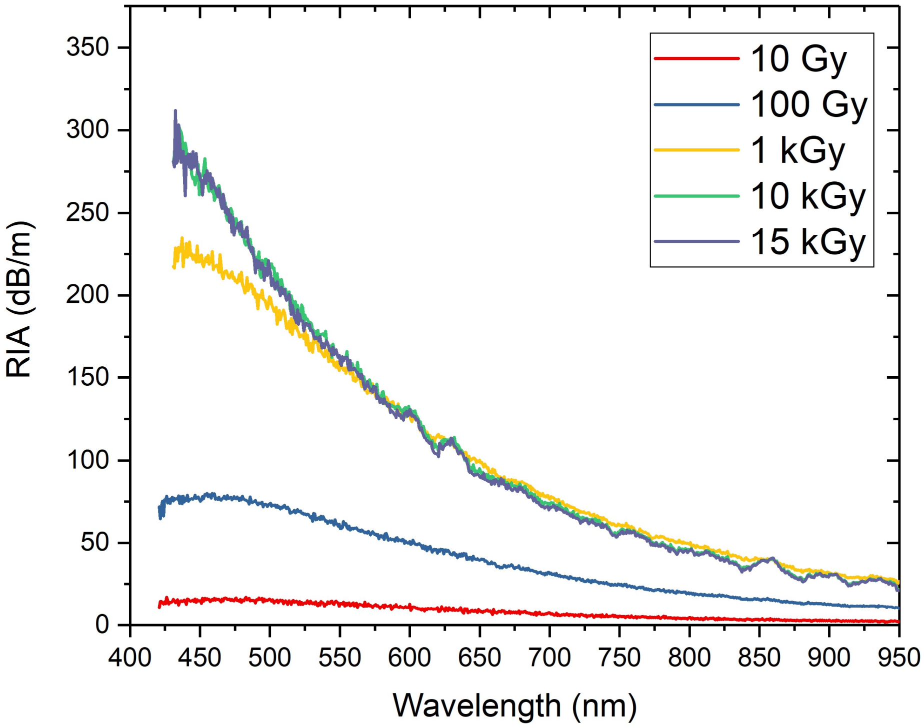

Figure 119 - RIA spectra measured on a 5-cm long CeTb-codoped fibre sample at 0.5 Gy/s at different deposited doses.

5.3 TEMPERATURE DEPENDENCE OF THE RL EMISSION

In the framework of this PhD project, the intended application environments are accelerator complexes and space applications. In the accelerator applications, the temperature remains usually around the ambient temperature, at least for the CERN accelerator complex. On the contrary, the temperature in a spacecraft depends on many parameters such as the position in the orbit, the orientation of the satellite, the altitude, the position in the spacecraft, as well as the thermal regulation capabilities of the satellite.

As described ealier, temperature is one of the environmental parameters that can affect the fibre radiation response. The temperature effects therefore need to be carefully evaluated to limit unwanted variation of the response of the sensor. At the beginning of the PhD, no work existed to the best of our best knowledge on the temperature effects regarding the thermal dependence of the selected fibre responses. We had then to define an experimental procedure to assess it, which was based on the use of a thermal control plate using a combination of liquid nitrogen and a resistor, to control the temperature of the fibre under test. The plate is placed in the irradiator, and the samples are fixed on top of it. The available temperature range achievable with the experimental bench described earlier is -120 °C to +300°C. However, we limited the investigated temperature range in this study to -120 °C to +80°C due to maximum temperature recommended for the coating material of the investigated fibres.

5.3.1 Experimental procedure

During this characterization, we decided to use short sample of sensors (rods or fibre) which were roughly 1-cm long. Before starting the test, a calibration of the dose rate in the test position was performed. We decided to fix the dose rate at 200 mGy/s in order to obtain sufficient signal, while depositing a small dose on the sample. The samples were coupled to a transport optical fibre, and placed inside the LABHX xray irradiator on top of the thermal plate. The other side of the transport optical fibre was connected to a PMT, to provide the RL signal measurement. For each measurement we performed a 10s long irradiation, which results in a 2 Gy deposited dose. Once the whole setup was ready, we performed the first acquisition at room temperature (around 22°C). Afterwards, we changed several times the temperature of the thermal plate to cover the range investigated and performed a measurement at each temperature step. The steps of temperature used for the fibre (not the rods, where more point were used) testing and their order are presented in Figure 120. For the rods we used 3 times more temperature steps covering the same range.

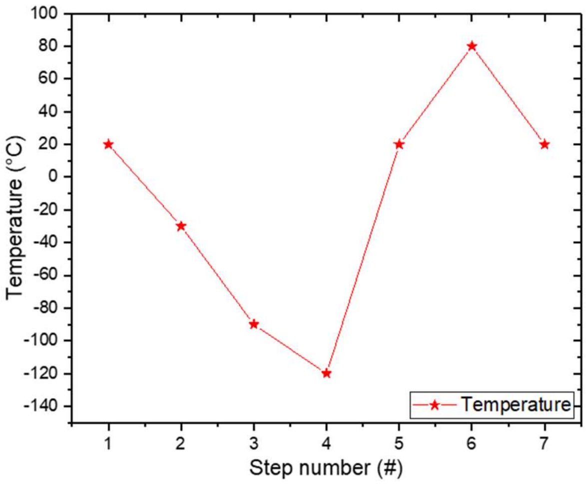

Figure 120 - Illustration of the temperature steps used during the evaluation of the temperature dependence of the RL response of the sensors.

At each measurement, we determine the response of the sensor by extracting the difference between the RL amplitude during the irradiation versus the background signal measured before the irradiation. In addition, we have also performed the same measurement using a spectrometer in order to evaluate how the emission spectra of the sensors are affected by temperature. An illustration of a typical RL measurement is shown in Figure 121, as well as a reminder of the architecture of the used experimental bench.

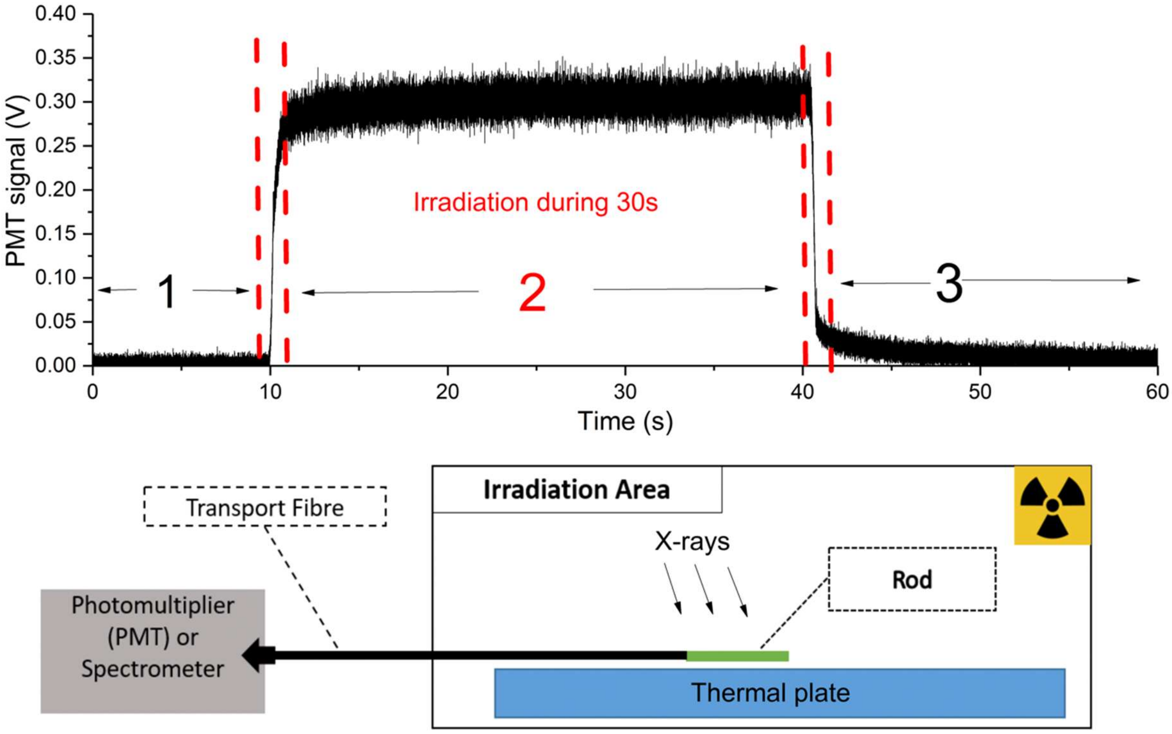

Figure 121 - a) An example of a typical RL measurement showing area (1) before irradiation, area (2) during irradiation at constant dose rate, and area (3) after irradiation. (b) Schematics of the experimental setup of the MOPERIX facility for temperature effects measurements, and related acquisition equipment.

In Figure 121-b, we can see that a portion of the transport optical fibre is inside the irradiation area. To avoid RIA related problems in this part of the optical link, we cover this fibre with 3 mm thick lead plates, absorbing the vast majority of the X-rays. Additionnally, we use pure silica fibres for the rods, and radiation hardened MMF for the optical fibres samples, to further reduce RIA related effects. Now that we have introduced the experimental plan and the setup, we continue with the presentation of the temperature dependence of the response of the rods.

5.3.2 Temperature dependance in rods

During this experiment on the rods, we only had Ce-, Cu-doped and CuCe-codoped samples available. Furthermore, for technical reasons, the measurement on the Cu-doped rod was not possible above 20°C. As shown by the results presented in Figure 122, we observed a significant temperature dependence of the RL response of all the investigated samples, over the investigated range of temperature. The RL response of the sensors increases with increasing temperature. We observe for instance a reduction of 60% in amplitude on the signal measured at -120°C from the sensors with respect to that measured at 20°C.

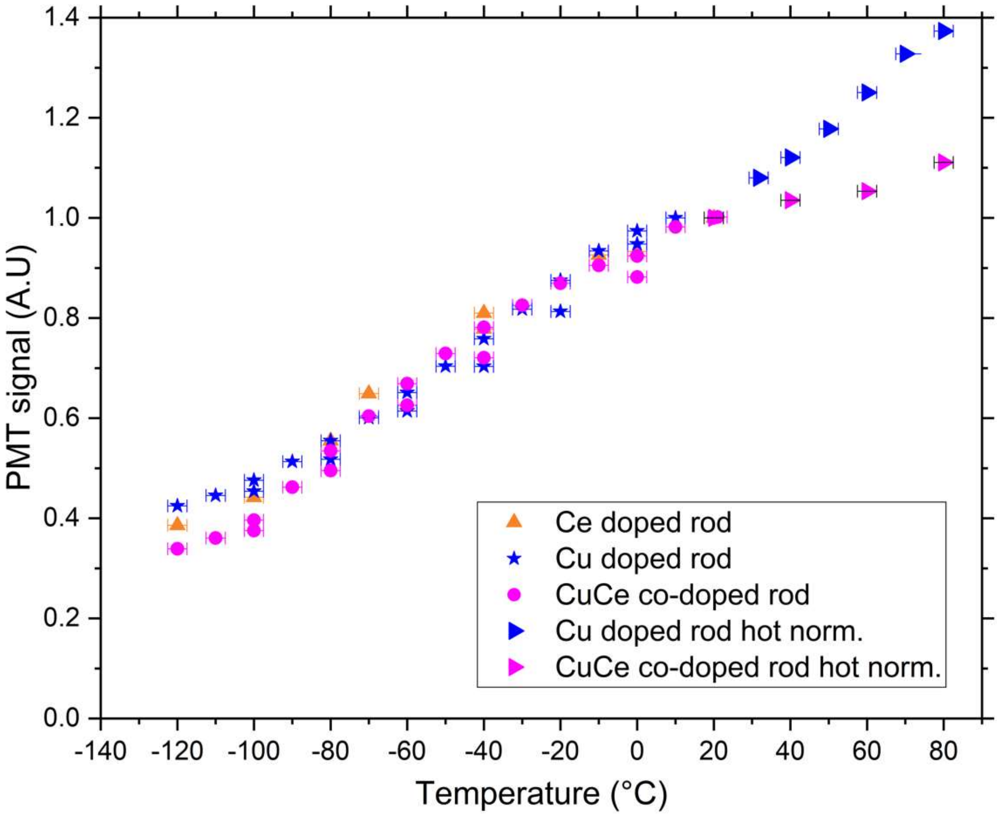

Figure 122 - Rods RL response measured by the PMT under fixed dose rate (184 mGy/s) for temperature ranging from 20 °C to -120 °C and from -120°C to 20°C. Right oriented triangular dots show the normalized measurements from 20°C to 80°C. Error bars on the signal (y-axis) are compatible with the size of the dots.

Even though this temperature dependence is significant, these sensors are still interesting for dosimetry applications if a monitoring of the temperature during the irradiation is performed, as well as an adapted temperature calibration before its use. Also, if the sensors are used in an environment where temperature variations are limited to a few degrees, the temperature calibration seems not mandatory.

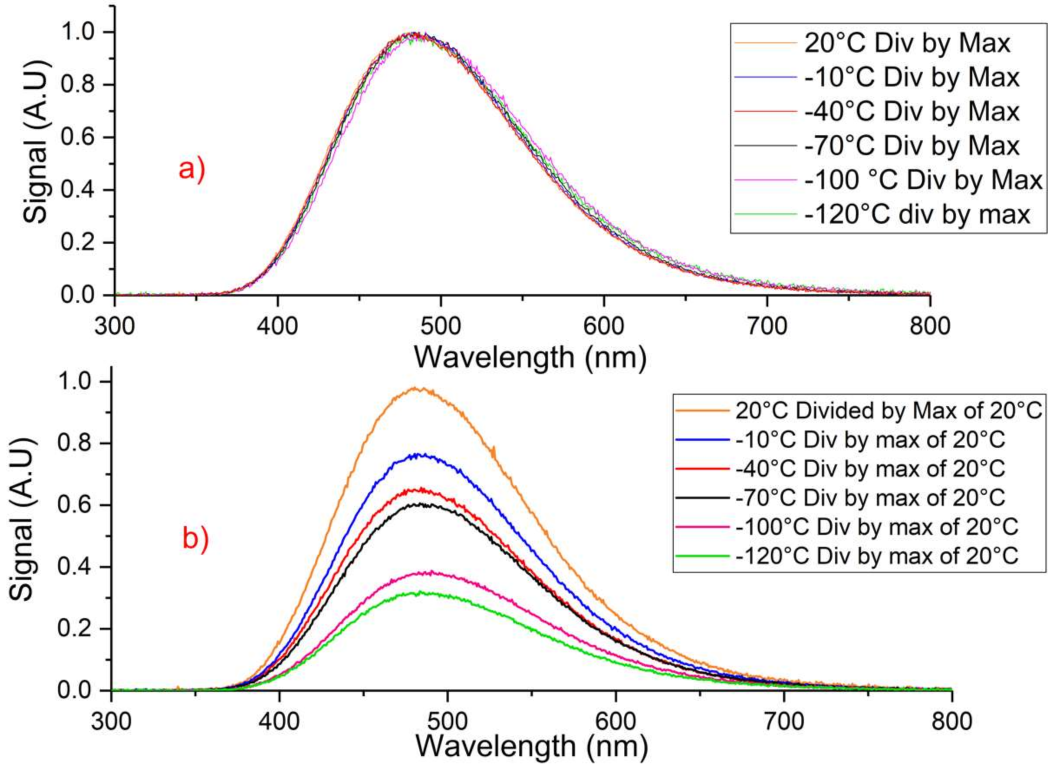

Figure 123 - Ce-doped rod spectral RL response for temperature ranging from 20°C to -120°C. a) Top – Each curve is normalized to its maximum peak value b) Bottom – Each curve is normalized to the maximum peak value at 20°C.

Continuing the study with the spectral measurement obtained with a spectrometer, we can observe how the temperature affects the emission spectra of the fibre. As shown in Figure 123, we can notice that only the amplitude of the emission band of the Ce-doped rod changes during the test. Indeed, as shown specifically in Figure 123-a, we notice that when normalizing each obtained curve to its own maximum amplitude, we do not observe any significant shape change.

For the Cu-doped rods, the observation we can make is the same, as shown in the data presented in Figure 124. The overall shape of the Cu-doped rod emission is not significantly affected by the temperature. Only a minor change in the spectra around 440 nm is observed, highlighted in the inset of the Figure 124-a. In this region, the relative amplitude seems to increase when lowering the temperature. This emerging band can be attributed to the emission from Cu^+ ions in eight-coordinated cubic sites, that might exist in silica glass, as reported by Debnath and Das in [84].

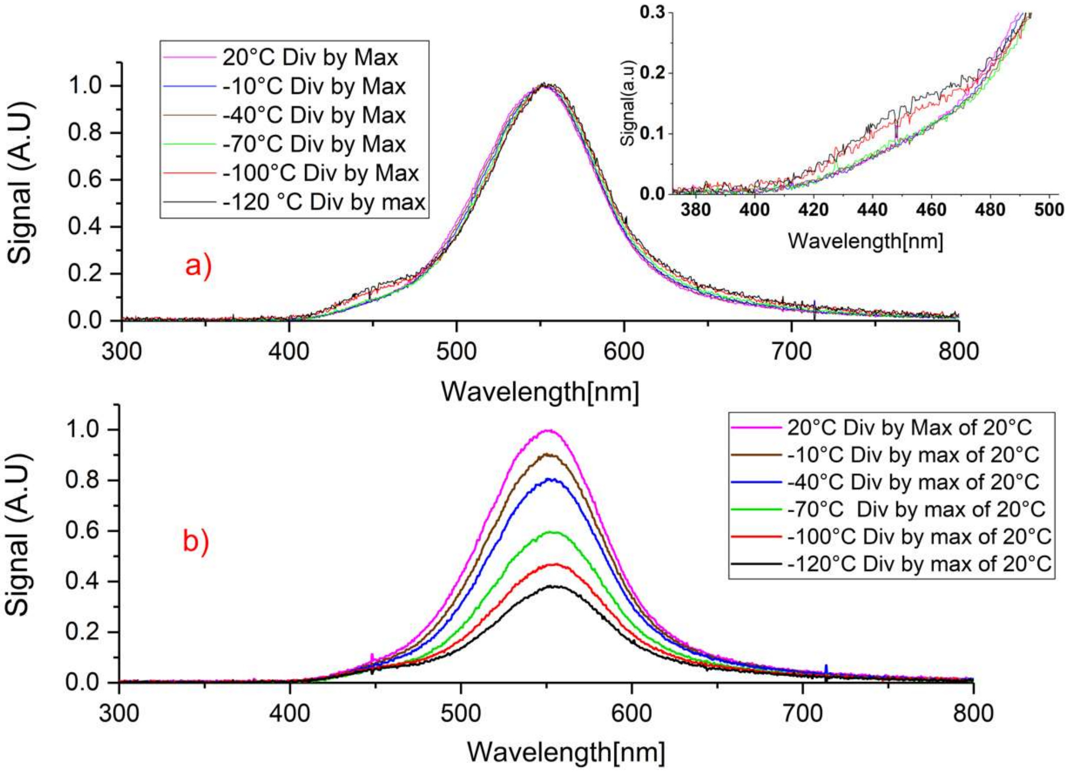

Figure 124 – Cu-doped rod spectral RL response for temperature ranging from 20°C to -120°C. a) Top – Each curve is normalized to its maximum peak value b) Bottom – Each curve is normalized to the maximum peak value at 20°C.

Finally, we can analyse the temperature effects on the emission spectra of the CuCe-codoped rod, which are shown in Figure 125. As observed in the other doped rod sensor, there is no important change in the RL emission shape at the different investigated temperatures. The only small observed change is located around 650 nm. This small band, has not been reported in previous studies performed on this rod found in [57]. After a more detailed analysis of this small band, we did not manage to attribute this effect to a specific defect, but we tend to exclude a parasitic origin that would be otherwise present in the other samples since there are produced using the same method.

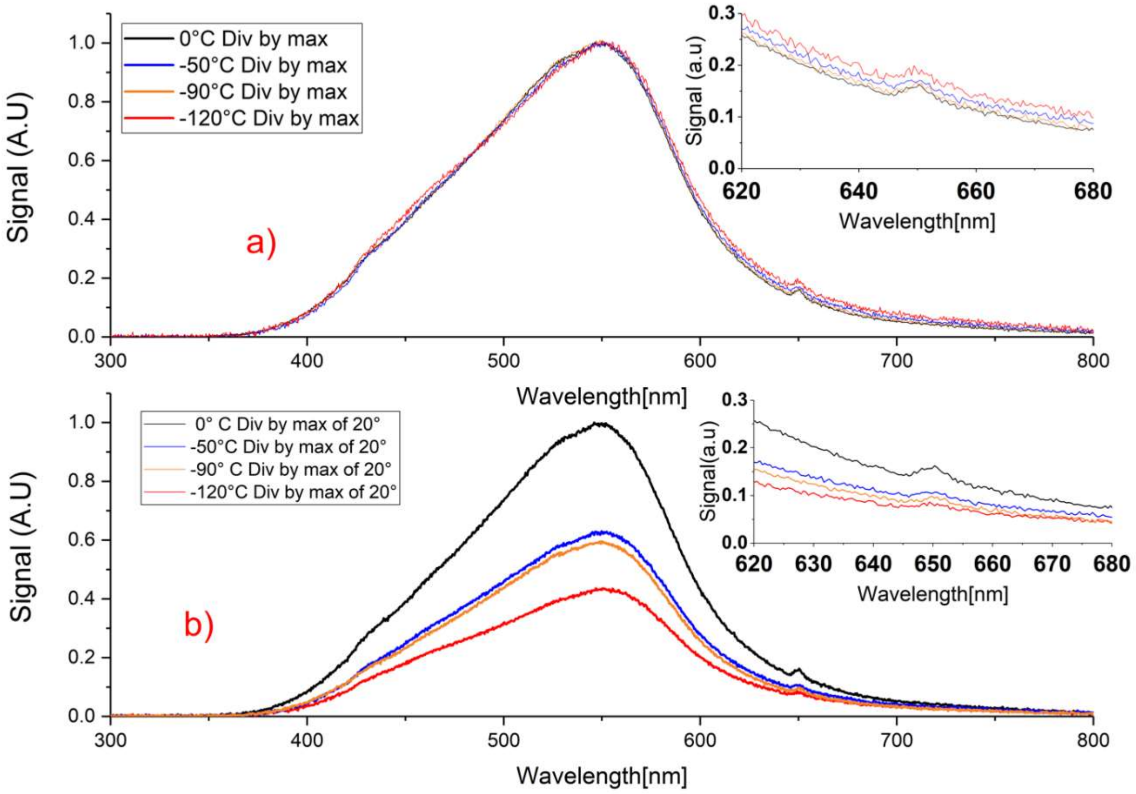

Figure 125 - CuCe co-doped rod spectral RL response for temperature ranging from 0°C to -120°C. a) Top – Each curve is normalized to its maximum peak value. b) Bottom – Each curve is normalized to the maximum peak value at 20°C.

Finally, we evaluated the linearity of the responses of the different sensors at the different temperatures. It is an important question that arised from the study, since we need to ensure that the temperature has no impact on the linearity of the sensors response. For this purpose, we performed measurements at different dose rates from 20 to 180 mGy/s, at each temperature steps.

The obtained results are shown in Figure 126 and proves that the RL signal linearity is kept over the temperature and dose range investigated. This had never been verified before to our best knowledge. The linear fitting coefficients of the different curves are then reported in Table 7.

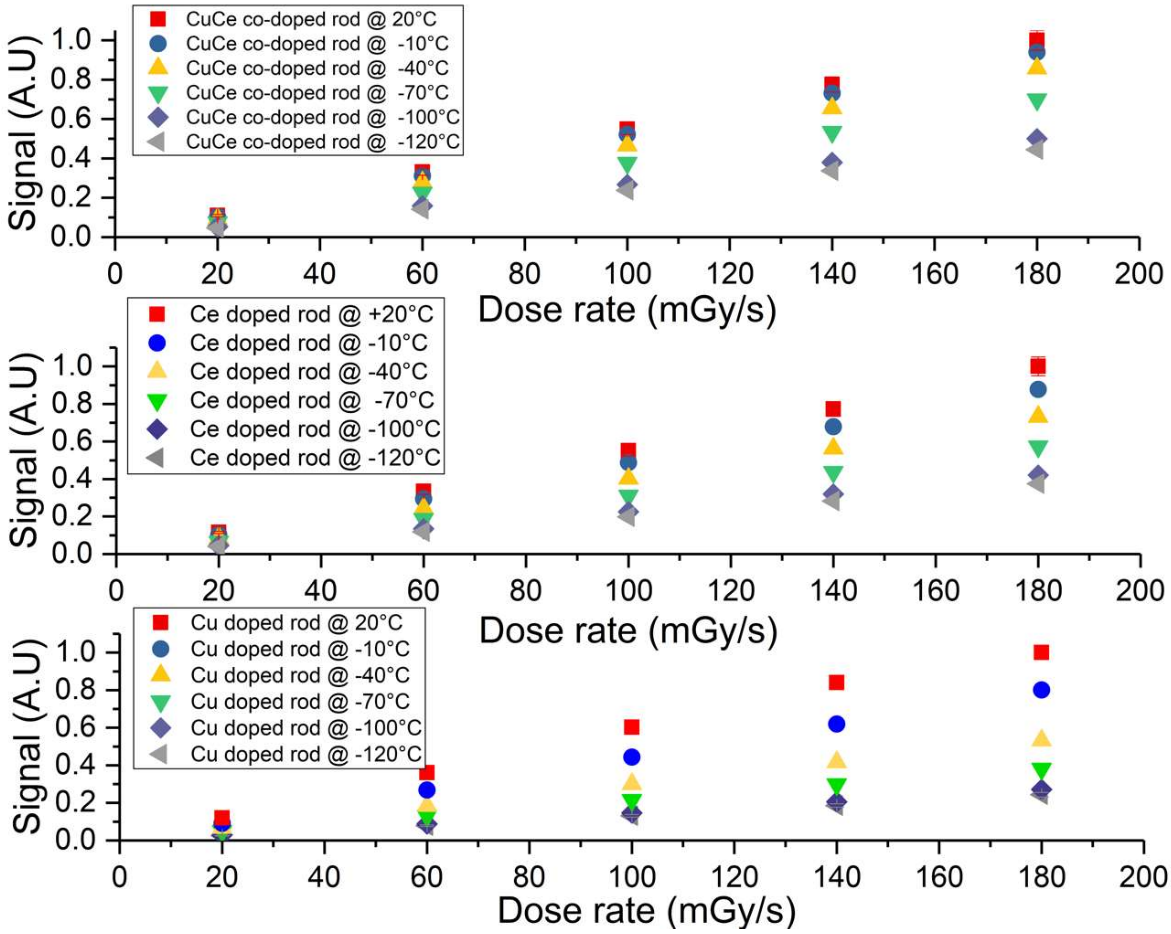

Figure 126 - Assessment of the linearity of Cu-, Ce-doped rods, and CuCe-codoped rods at the different investigated temperature ranges.

Table 7 - Linear fitting coefficients applied to the RL measurement curves presented in Figure 126.

Rod type	T° (°C)	Slope	Adj. R-Square
CuCe	20	$(5.53\pm 0.018)\times10^{-3}$	0.99996
	-10	$(5.23\pm 0.002)\times10^{-3}$	1
	-40	$(4.77\pm 0.04)\times10^{-3}$	0.99964
	-70	$(3.89\pm 0.04)\times10^{-3}$	0.99953
	-100	$(2.79\pm 0.04)\times10^{-3}$	0.9992
	-120	$(2.48\pm 0.04)\times10^{-3}$	0.99919
Ce	20	$(5.49\pm 0.018)\times10^{-3}$	0.99996
	-10	$(4.84\pm 0.017)\times10^{-3}$	0.99995
	-40	$(4.04\pm0.03)\times10^{-3}$	0.99978
	-70	$(3.17\pm 0.04)\times10^{-3}$	0.99934
	-100	$(2.34\pm 0.04)\times10^{-3}$	0.99885
	-120	$(2.08\pm 0.04)\times10^{-3}$	0.99848
Cu	20	$(5.6\pm 0.2)\times10^{-3}$	0.993
	-10	$(4.43\pm 0.016)\times10^{-3}$	0.99995
	-40	$(2.9\pm 0.005)\times10^{-3}$	0.99999
	-70	$(2.08\pm 0.005)\times10^{-3}$	0.99997
	-100	$(1.5\pm 0.02)\times10^{-3}$	0.99929
	-120	$(1.34\pm 0.01)\times10^{-3}$	0.9998

5.3.3 Temperature dependence in fibres

We decided to start a complete characterization of these fibres, including the temperature dependence. Our interrogation at that time was the following : Does the fibre sensors have the same behaviours than the rod in terms of temperature dependence ?

Indeed, they are produced from the same material. However, additional steps in the manufacturing process are needed to obtain the final fibre with regards to the rods. We therefore asked ourselves if these additional steps, in particular the high temperature drawing, could induce a change in this behavior. For this purpose, we submitted the optical fibres to same experimental testing presented earlier, that we have applied to the rod.

However, one small change in the experimental plan was added. We decided to include both pristine and pre-irradiated fibres in the study, because of the outcomes of the dose study presented in chapter 5.1. The pre-irradiation was performed up to 250 kGy under X-rays, at least 24 hours before the test. Indeed, during this study we have shown that the RL response of the fibres changes with the deposited dose, but that this change can be significantly reduced or stopped after a 100-200 kGy pre-irradiation. We therefore strongly recommended that the fibres needed to be pre-irradiated before use in dosimetry application. Thus, it is important to evaluate if this additional step of pre-irradiation, can induce any change in the temperature dependence of the response of such sensors.

5.3.3.1 Temperature dependence of RL emission in Ce-doped fibres

We started with the study of the 1-cm long Ce-doped fibre response at different temperatures. As shown in Figure 127, we observed a significant temperature dependence of the RL response of both pristine and pre-irradiated sensors. The amplitude of this temperature dependence is close to what was observed in the rods. However, we note an interesting difference between the pristine and pre-irradiated samples responses. We note that the temperature dependence of the pre-irradiated fibre is lower than that of the pristine fibre. We can therefore imagine that the temperature response of the fibre can somehow be affected by a pre-irradiation phase up to 250 kGy.

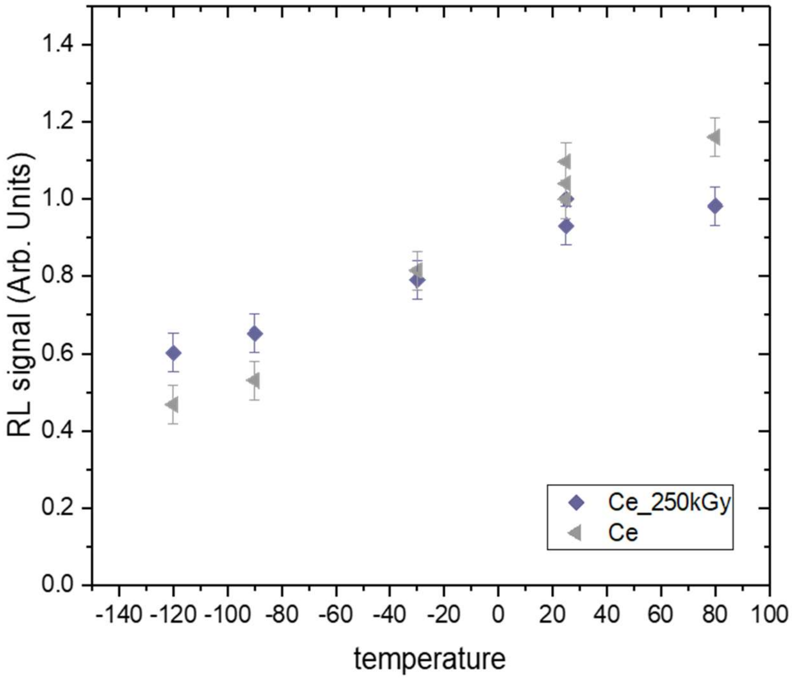

Figure 127 - Temperature dependence of the RL emission of Pristine and Pre-irradiated 1-cm long Ce-doped fibres under 200 mGy/s X-rays dose rate.

Furthermore, this information suggests as well that the temperature calibration recommended earlier in the use of such sensor, should be performed after the pre-irradiation phase since it affects the temperature dependence.

5.3.3.2 Temperature dependence of RL emission in Cu-doped fibres

We continue the study with 1-cm long Cu-doped fibre sample. As shown in Figure 128, we observe again a significant temperature dependence on the RL response of the sensors. The pristine sample response is close to that observed in the rods. Furthermore, we observe again an impact of the pre-irradiation on the temperature dependence response of the sensor. The temperature dependence is reduced after a pre-irradiation. We can therefore make the same recommandations we made for Ce-doped fibre, concerning the temperature calibration.

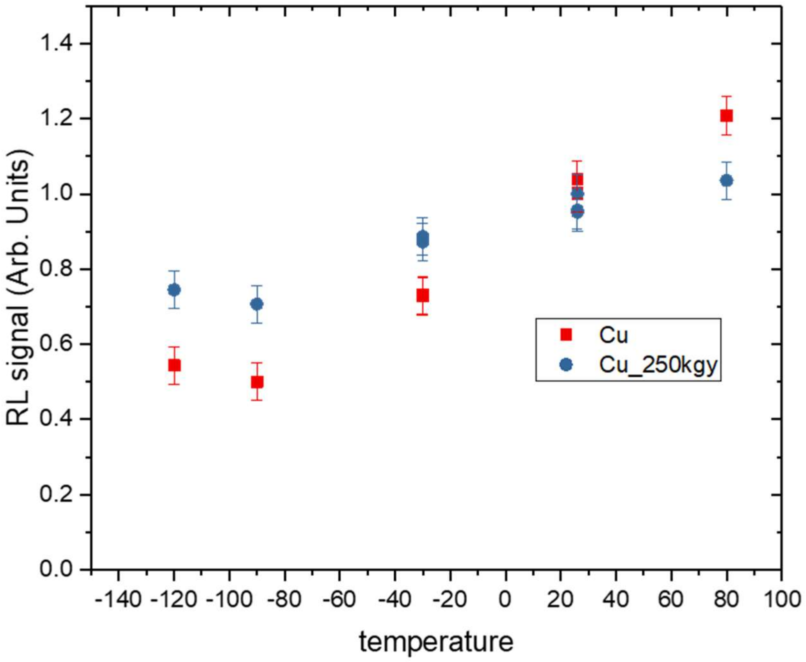

Figure 128 - Temperature dependence of the RL emission of Pristine and Pre-irradiated 1-cm long Cu-doped fibres under 200 mGy/s Xrays dose rate.

5.3.3.3 Temperature dependence of RL emission in CuCe-codoped fibres

In this part, we performed the same test on the 1-cm CuCe-codoped pristine and pre-irradiation fibres. The results given in Figure 129, show that the RL temperature dependence in this fibre is slightly affected by the pre-irradiation. The temperature dependence is also reduced by the pre-treatment. We can therefore, also recommend to perform the temperature calibration of such sensors after the pre-irradiation step.

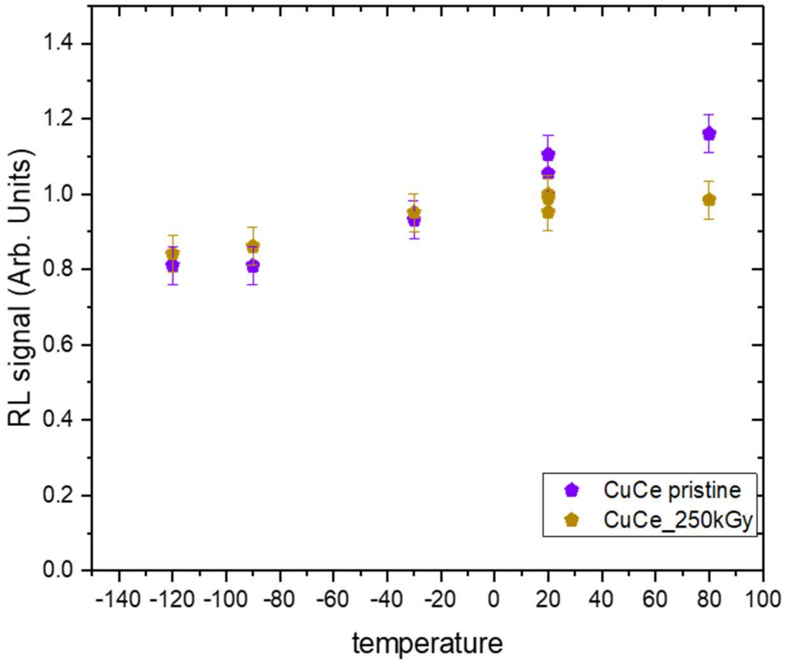

Figure 129 - Temperature dependence of the RL emission of Pristine and Pre-irradiated 1-cm long CuCe-codoped fibres under 200 mGy/s X-rays dose rate.

5.3.3.4 Temperature dependence of RL emission in Gd-doped fibres

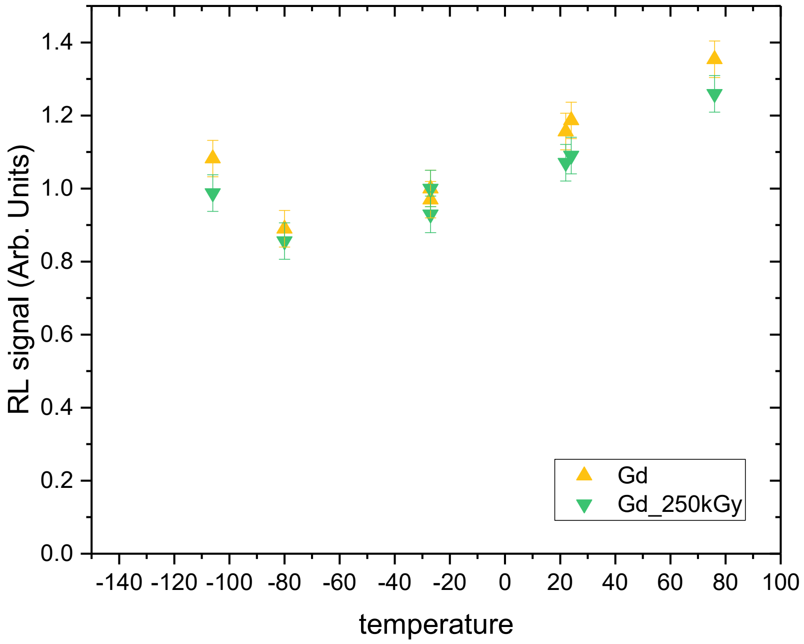

Figure 130 - Temperature dependence of the RL emission of Pristine and Pre-irradiatid 1-cm long Gd-doped fibres under 200 mGy/s X-rays dose rate.

We also performed the test on Gd-doped fibres. We observed a temperature dependence, with lower amplitude than those observed in other fibres. Furthermore, the measurements did not show any particular effect of the pre-irradiation on the temperature dependence. Another interesting observation is that the RL response at lowest tested temperature increase is characterized by a change in the linearity of the temperature dependence in the rest of the investigated range. Indeed, from -80°C to -120 °C, we note an increase of the RL response.

5.3.3.5 Temperature dependence of RL emission in CeTb-doped fibres

We observe in this fibre a temperature dependence which is comparable with that measured on Ce-doped fibre in terms of amplitude and trend versus temperature. We also do not notice a significant difference between pre-irradiated fibre response and that of pristine fibres.

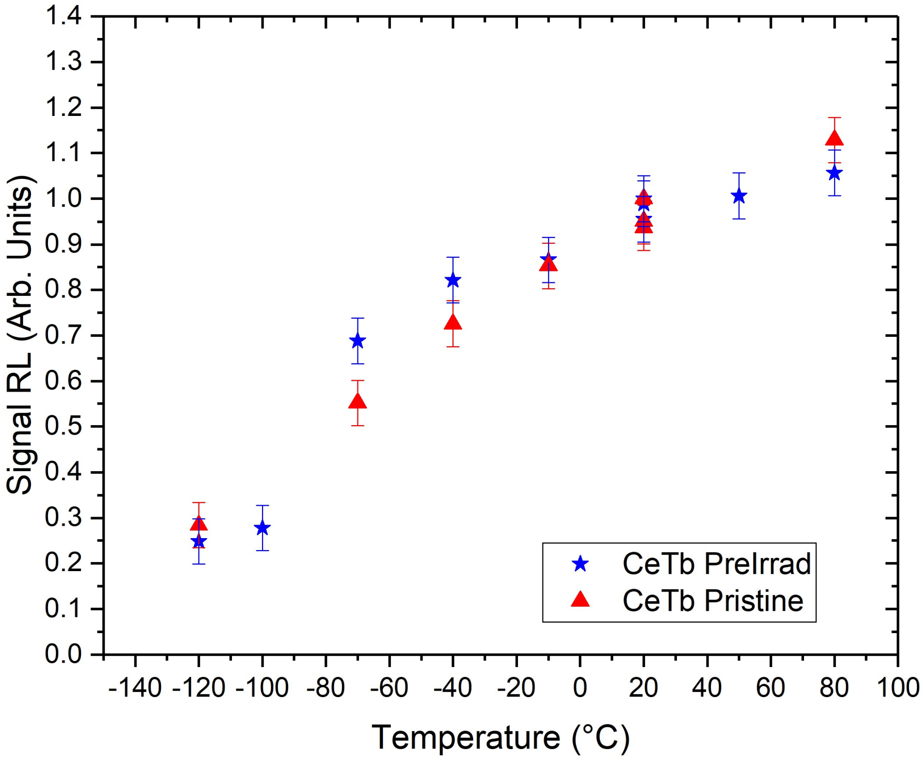

Figure 131 - Temperature dependence of the RL response of 1-cm long Pristine and Pre-irradiated CeTb-codoped fibre under 200 mGy/s X-rays dose rate

5.3.3.6 Temperature dependence of RL emission in N-doped fibres

For this specific fibre, we observed a very different behavior with respect to that measured on the other fibres of the study. Indeed, we note an increase of the RL response of the fibre at decreasing temperatures. This effect is significant and reaches a factor 2.3 at -120°C, with respect to that measured at 20°C.

In addition, we noted a significant difference on the responses before and after the pre-irradiation. The temperature dependence is notably lower at the lowest investigated temperatures in pre-irradiated fibres than it is in pristines.

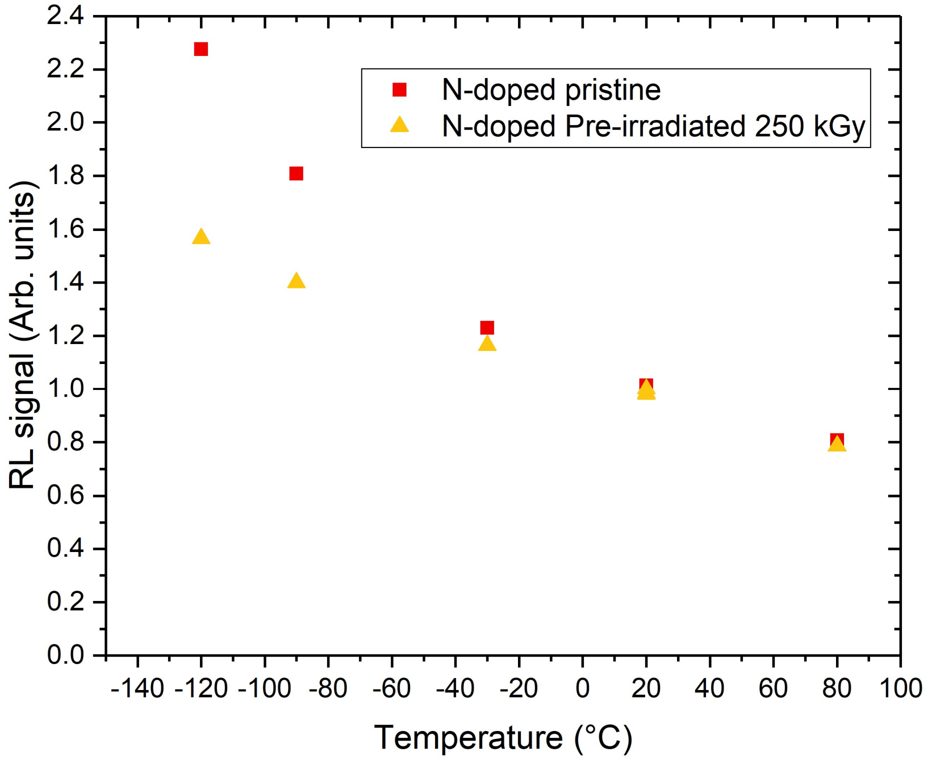

Figure 132 - Temperature dependence of the RL response of 1-cm long Pristine and Pre-irradiated N-doped fibre under 200 mGy/s X-rays dose rate

6 EXPERIMENTAL WORK TOWARDS A FIRST APPLICATION ORIENTED UTILIZATION

In the previous chapter, we characterized how the temperature affects the RIL response of our sensors. This can be an issue for space-oriented applications since this can affect the precision of the measurement. The amplitude of this dependence remains manageable and can be easily corrected by using temperature monitoring of the sensor, coupled with a prior adapted temperature dependance calibration. This solution remains simple but comes at the cost of increased complexity of the system, which can limit its use in certain case where mass, energy , cost and volume are limited – which is often the case in a satellite. Therefore, in this part of the work, we introduce an experimental attempt to reduce this effect.

6.1 TEMPERATURE DEPENDENCE COMPENSATION

6.1.1 Optically Stimulated Radiation Induced Luminescence (OSRIL)

During his PhD work at Laboratoire Hubert Curien, few years prior to this PhD thesis, Dr. Diego Di Francesca performed experimental measurements of the OSRIL response of a Nitrogen-doped optical fibre. The excitation wavelength was set at 1064 nm. The obtained result is shown in Figure 133. The result differs from usual OSL measurements because in this case, the laser excitation was trigerred during the irradiation, whereas in OSL measurements the triggering occurs after the irradiation. This unusual way of performing an OSL-like test highlighted an interesting behavior : When the radiation starts, we observe an increase of the signal due to the RL emission (about 0.3 V in negative amplitude), then the laser excitation starts and we observe a characteristic OSL peak, followed by another flat response during the rest of the irradiation (still with the laser ON). The interesting thing to note is that this level is higher in amplitude, than the RL response itself of about 12%. The laser is stopped after the irradiation stop, to highlight the minimal impact of the laser contribution in the signal measurement. This behavior is interesting because it shows that we could potentially increase the efficiency of the RL response of an RL sensor by applying a laser excitation.

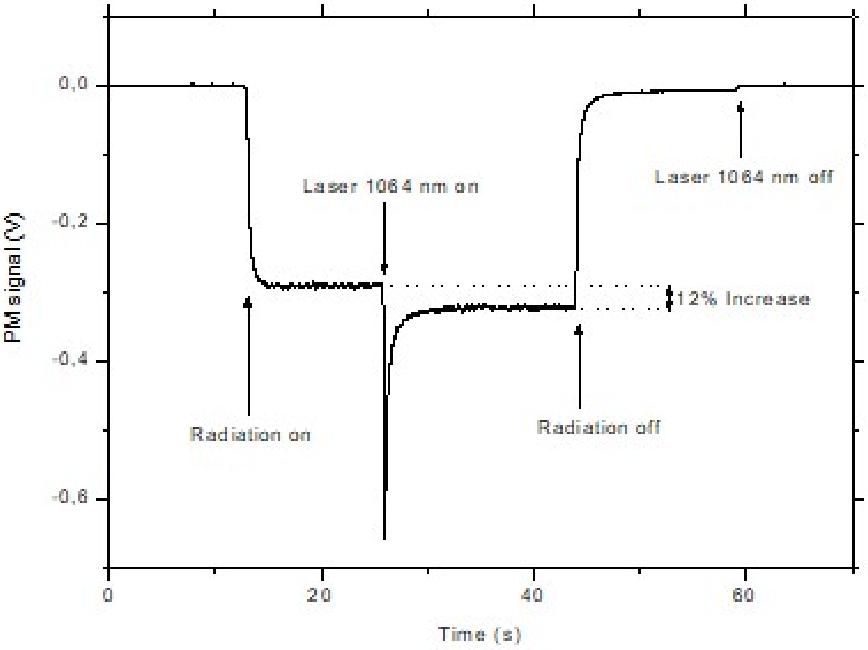

Figure 133 – OSRIL measurement performed on N-doped fibre under 1064 nm excitation. Figure kindly provided by D. Di Francesca.

Later on, during the course of this PhD work, we have highlighted the temperature dependence of the RIL of different optical fibre sensors. We have therefore made the hypothesis that the RIL process could be somehow phonon-assisted. Meaning that at lower temperature for instance, the reduction of the RIL signal is due to reduced actions of phonons in the RIL process.

At this point, an innovative potential way of compensating the “lack” of phonon-assistance at lower temperatures was suggested. The idea is to compensate the missing action of the phonons using a laser excitation. The initial hypothesis developed at this point was that the phonon-assistance was involved in this excitation-process of the RIL. We did not to this day proved or disproved completely this hypothesis. However, we decided to investigate this idea by performing OSRIL measurements at different temperatures in the same way we did in the previous part of the thesis. We started the experiment by designing an experimental bench described earlier, allowing to inject light in a RIL sensor while measuring on the other side the RIL emission, taking care of limiting the impact of the laser on the PMT measurement. To do so, we have searched for optical filters allowing to filter as efficiently as possible the laser wavelength while preserving as much as possible the signal transmission in the RIL emission range. We found a filter from Thorlabs providing interesting characteristics Including a transmission above 65% in the RIL emission range of Ce-doped fibre, with an optical density of 6 elsewhere. The transmission properties of the filter is shared in Figure 134.

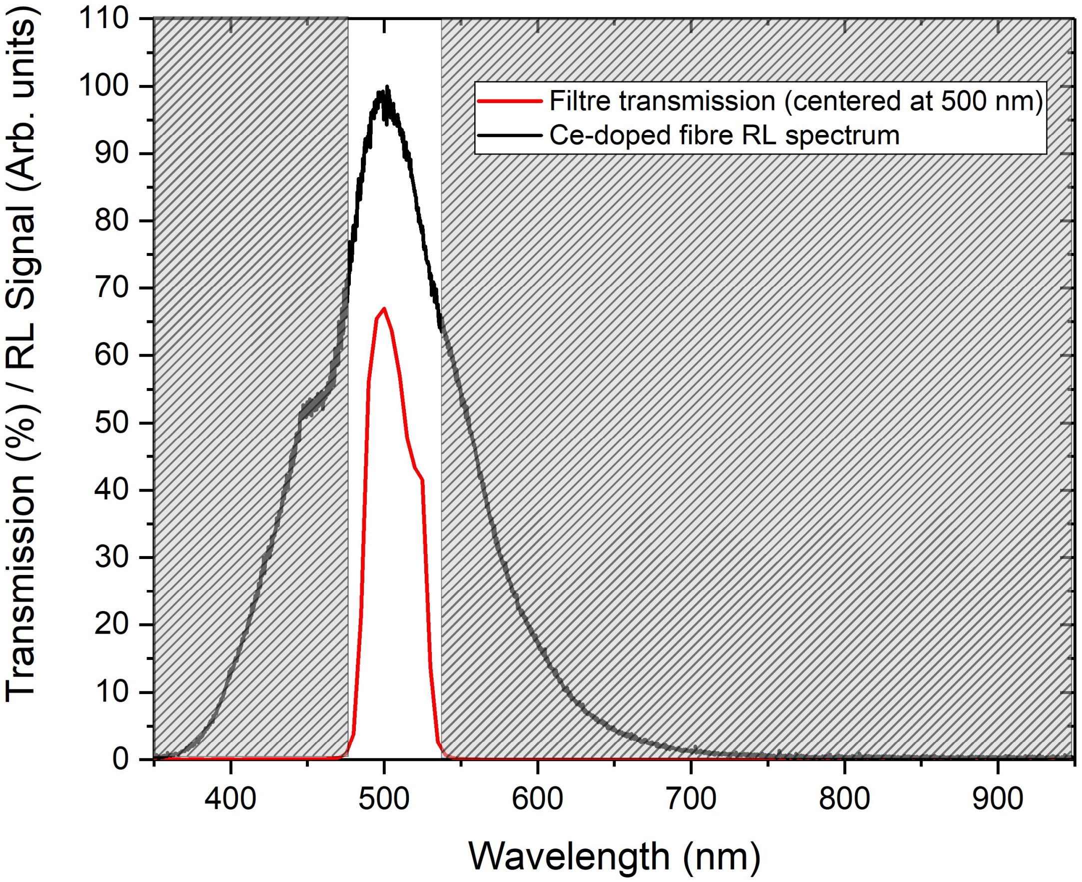

Figure 134 – Transmission spectrum of the 500 nm centered filtre with a ±40 nm window from Thorlabs. In black is plotted the Ce-doped RL emission spectrum to highlight the transmitted portion. The dashed grid represents the attenuated portions.

The transmission window of the filtre allow the preservation of an important portion of the emission spectrum of the Ce-doped fibre whereas the rest is strongly attenuated.

6.1.2 Results of the experimental testing of the OSRIL technique

We then performed the OSRIL measurement using a 1064 nm laser excitation, using a 200 mGy/s X-ray irradiation in the LABHX facility of Laboratoire Hubert Curien, at different temperatures. We performed the test in the following way described in *Figure 135*.

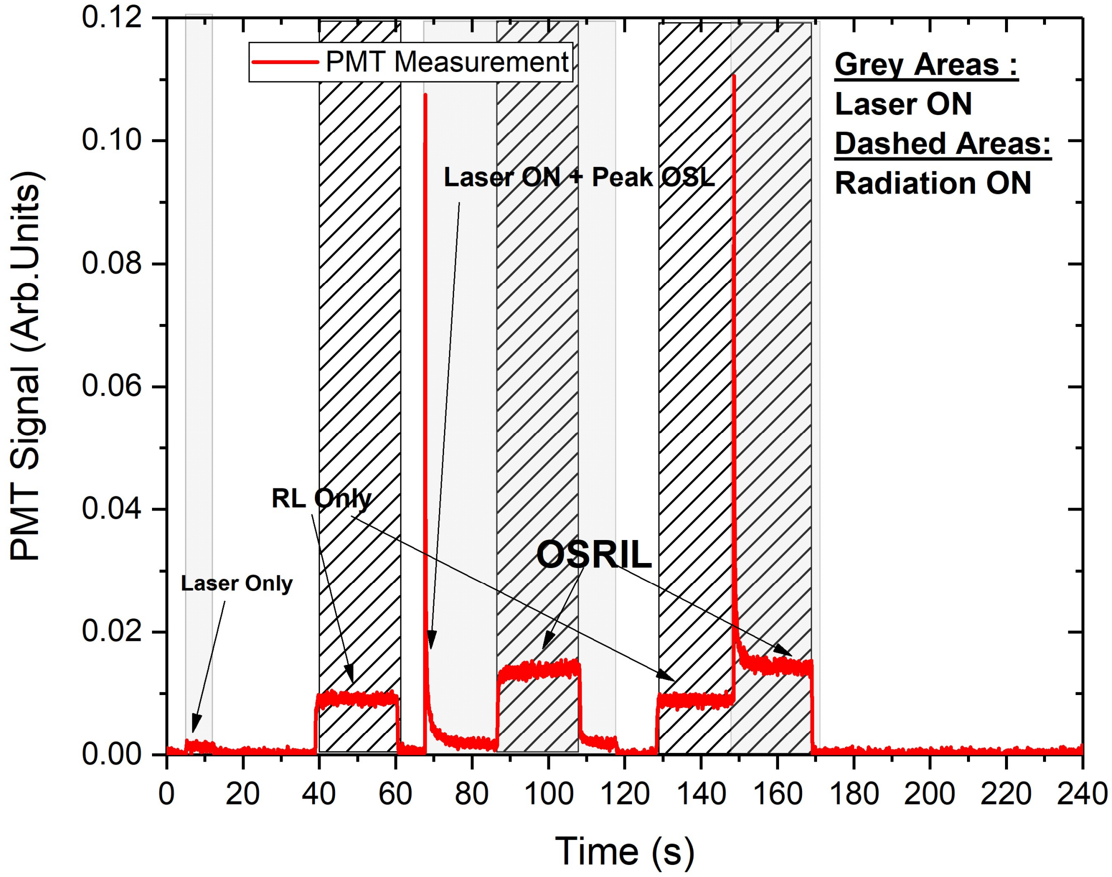

Figure 135 - Exemple of OSRIL experiment measurement on the Ce-doped sample

The measurement is performed at each temperature step in the investigated temperature range, and is composed of the following sequence : We start the measurement, then we start by switching ON the laser only for few seconds. This part indicates how much laser signal remains after the filtre, in this case the laser is still visible but the attenuation is already very efficient. Then we switch OFF the laser and start the irradiation for few seconds to measure the RL signal. Then after stopping the irradiation, we start again the laser and observe a strong OSL signal emission. We leave the laser ON and after few seconds we restart the irradiation in order to measure the OSRIL signal. We stop the laser after stopping the radiation before testing again the OSRIL signal but this time switching ON the laser during the irradiation in order to compare the levels of the OSRIL in both cases. The levels are in this cases comparable, after waiting sufficient time for the OSL peak to decay. The OSRIL data is obtained by substracting the mean levels in laser ON only portion and background noise to the OSRIL mean signal.

The result, shown in *Figure 136* highlights an interesting effect. We note that the OSRIL response differs at lowest temperature and is higher by 35 % with respect to the RL response.

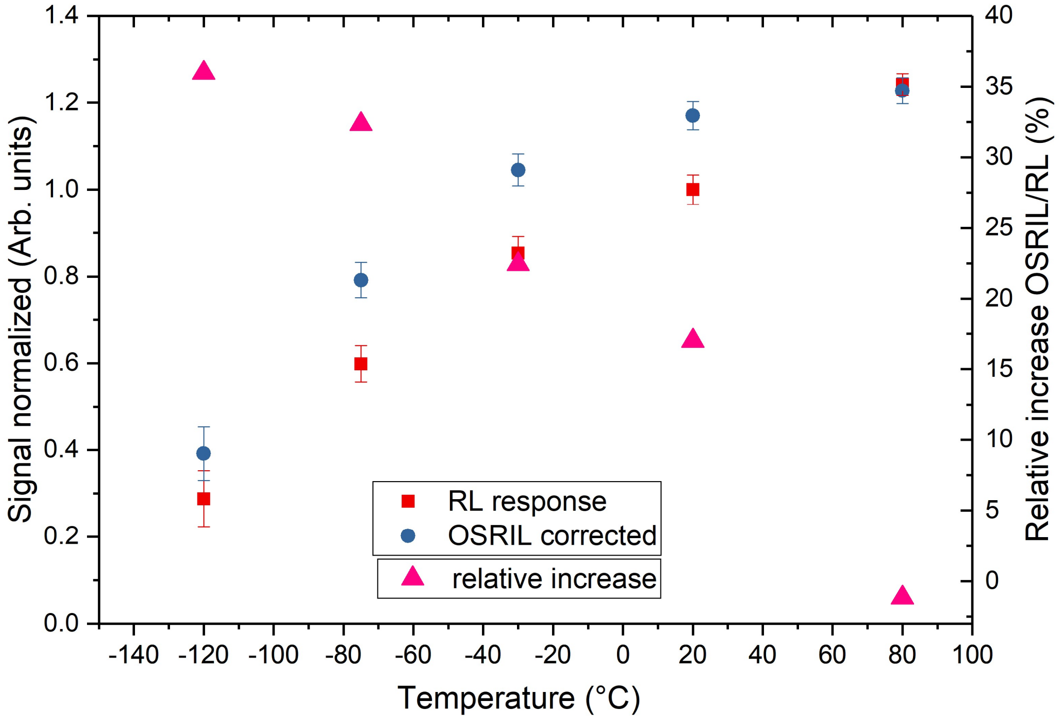

Figure 136 - OSRIL vs RL response of Ce-doped fibre at different temperature using a 1064 nm laser excitation.

In other words, it seems that the laser excitation could potentially reduce to a certain extent the temperature dependence of the sensor. However, the effect is limited and would need to be improved in order to have be effective in a final application. Our hypothesis was that reducing the excitation wavelength could potentially increase the effectiveness of the OSRIL due to the higher photon energy. In order to verify this point, we performed a second test using a 786 nm laser excitation keeping in mind that we cannot go below the RL emission range, to avoid PL excitation, and that we need to remain far away enough from RL emission to be able to filter excitation while preserving the RL.

To do so, we included another filtre in the study from Edmunds Optics providing interesting transmission features, cutting very efficiently the wavelegnths above 525 nm until 800 nm while transmitting around 90% of the RL signal up to 525 nm.

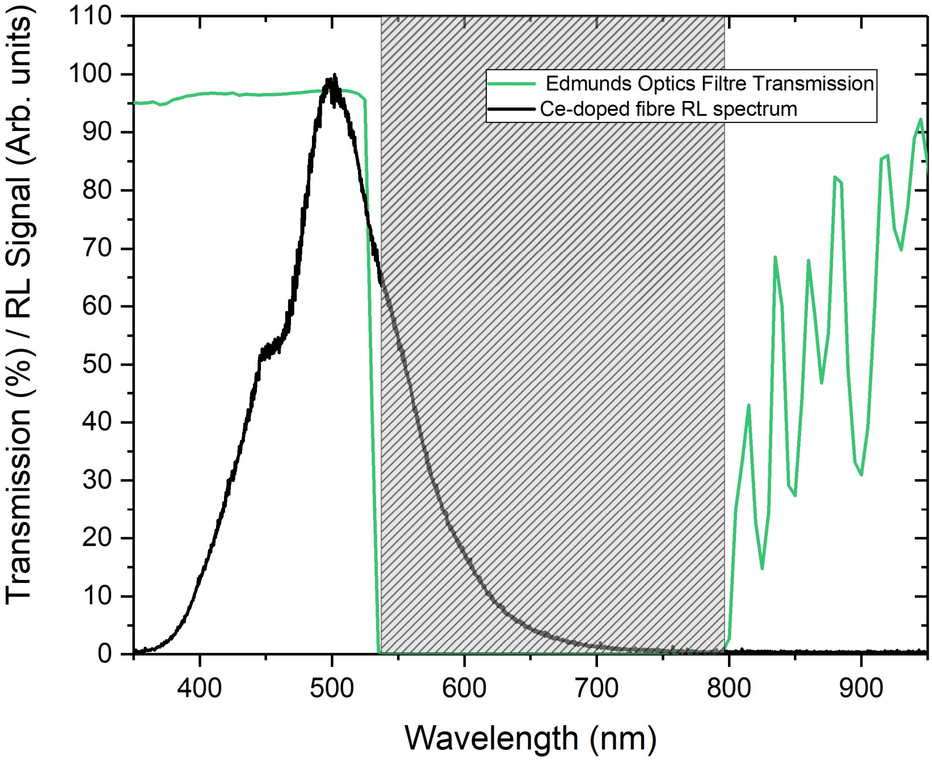

Figure 137 - Transmission Spectrum of the 525 nm Low-pass filtre from Edmunds Optics along with the Ce-doped RL signal to highlight the transmitted portion.

However, we directly noticed that the excitation laser signal was not correctly filtered and was impacting significantly the measurement of the OSRIL/RL. We therefore could not perform successfully this test, which will require in the future some further work. An optimization of the bench architecture as well as a change of filters can improve the results by increasing the attenuation of the laser signal incoming on the PMT. This work is planned for a future study.

6.1.3 Complementary response of N-doped fibre and Cu-doped fibre to reduce temperature dependence

Noticing that the N-doped fibre RL response increases at decreasing temperatures, we imagined a simple way to potentially use this feature to reduce the temperature dependence of the investigated dosimeter. Since all other investigated fibres responses decreases with increasing temperature, we could read on the same detector, the signal coming from a N-doped fibre as well as from another investigated fibre in order that the combination of both signals, produces a temperature dependence free response. To do so, we have searched empirically the best fitting parameters of the linear combination of N-fibre response and Cu-doped fibre, leading to the flattest achievable response. As shown in Figure 138, the best parameters were found to be 0.3 times the signal from Cu-doped fibre and 0.7 times the signal from N-doped fibre. The result expresses a contained temperature dependence with a maximum 5% effect on the signal at the lowest tested temperature.

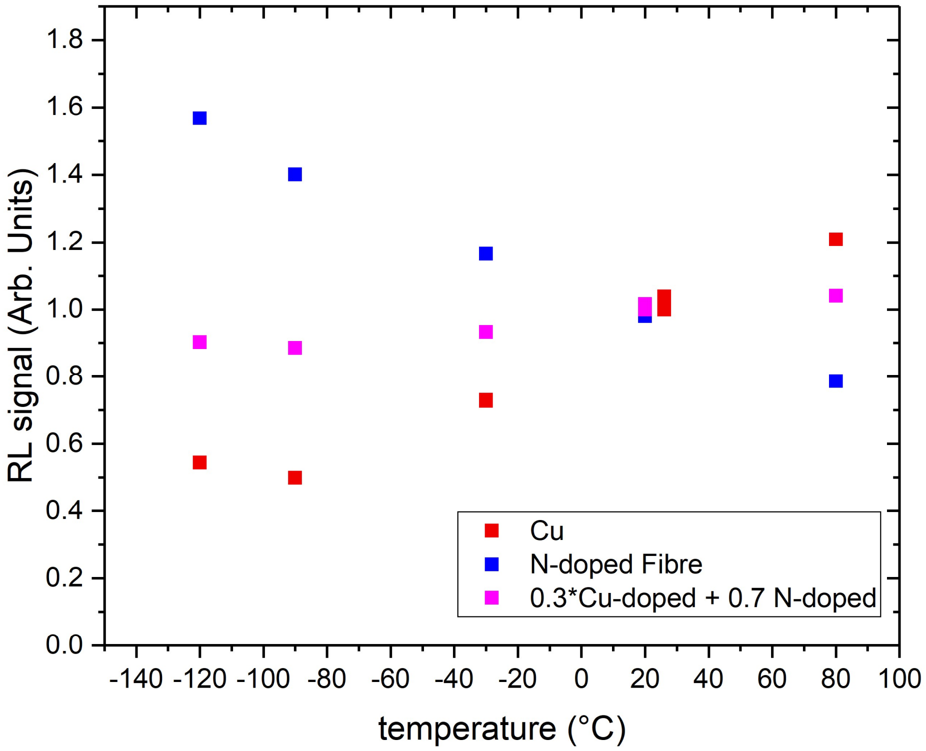

Figure 138 - Combination of N-doped and Cu-doped fibre responses with linear combination coefficients

Therefore, we decided to test this effect experimentally by measuring the response of a 3 mm long Cu-doped fibre and 7 mm long N-doped fibre, on the same PMT, at different temperatures. Unfortunately, the result was not satisfactory in the sense that we observed no effect on the temperature dependence. The response was extremely close that of N-doped fibre. We have to note that this task is not easy owing the short length of fibres that are involded, as well as uncertainties linked to the light coupling with the PMT which can differ slightly.

6.2 FIRST ONLINE MEASUREMENT OF RADIATION FIELD USING OPTICAL FIBRE RL EMISSION IN THE MIXED-FIELD CHARM FACILITY AT CERN

In this PhD work, we have up to this point presented experimental measurements in very-well controlled conditions that allow focusing on specific characteristics of the sensors response. This is important to be able to draw conclusions on the sensors characterization.

Nevertheless, these experimental conditions differ from the conditions that the sensors will experience in the final applications. One of the main differences between the X-ray testing and the accelerator or space application domain is the diversity of particle types. Indeed, these environments are characterized by their field composed of a mix of particules of different types and having different energies.

Even though the investigated fibres have in some case proven that their responses are not energy or type of particle dependent, it was important for us to attempt a first application like experimental radiation detection measurement in a representative environment. For such purpose, the CERN accelerator complex offers an unique irradiation facility providing a mixed radiation field which is representative of the accelerator environment, and space domain up to a LET threshold around 15 Mev.cm^2/g. Additionnally, since the beam is pulsed, it can give an information about how accurately the sensor is able to provide an information on the temporal structure of the accelerator beam.

In the rest of the chapter, we will introduce the experimental plan developed for this test as well as presenting the challenges we faced during the preparation of the experimental bench. Finally, we will present the obtained results and their comparison with dosimetry provided by the facility.

6.2.1 Experimental plan and challenges of the measurement

A first attempt of measurement in this facility using rod sensor was performed in 2018. In this test, we connected a 1 cm long rod of Gd-doped sensor to a PMT detector (Hamamatsu H9305-13), placed in a small shielded area inside the irradiation area of CHARM. A coaxial cable was then used to send the signal collected towards the control room, outside the facility. Several runs were performed over the course of two weeks of irradiation. In the end, we discovered that the measurement was not possible in this configuration since the PMT was very sensitive to the charged particles crossing its sensitive area, and therefore our signal was completely polluted by ambient radiation impinging on the PMT.

At the time of this first test, the only sensors available were the rods, which are 500 µm diameter glassy sensor. This size is not compatible with a fusion splice with a standard MMF. Therefore, at that time is was impossible to extract the optical RL signal from the irradiation room. However, since the standard sized optical fibres sensors were developed during the period covering this PhD work, we had the opportunity to prepare and plan a new campaign in this facility. This time, the plan was to send the optical RL signal to the control room using the optical fibre patch panels, towards our PMT. In this configuration, we can avoid parasitic signals from particles crossing the sensitive areas of our PMT. The configuration is introduced and detailed in the next part of the document.

6.2.2 Experimental measurements

Several challenges had to be overcomed for this experiment, the first one being the preparation of the optical fibre sensor and their related transport fibres. The transport fibres needed to be at least 7m long in order to connect the sensor placed in position 5 in the CHARM irradiation room, to the patch panel interconnexion. Since this transport fibre would be under irradiation, we decided to select a radiation hardened MMF. Additionnally, we decided to set the sensor length at 5-cm in order to maximize our chances to detect light while maintaining a good spatial resolution.

Also, since the RL signal occurs in the Visible domain we have used a PMT (Hamamatsu H7421-40) sensitive in this spectral region. This PMT is so sensitive that it is able to perform single-photon counting. Therefore, any spurious light coming from the environment, will pollute the measurement. For this reason we need to ensure the light tightness of the sensor, transport optical fibre and interconnexions to the PMT. We therefore selected an adapted custom cable coated with light tight material, which allowed us to observe no spurious light during preparation testing.

The sensor was placed in the irradiation room and connected via the transport cable to the panel panel towards the control room where the PMT was placed as shown in Figure 139.

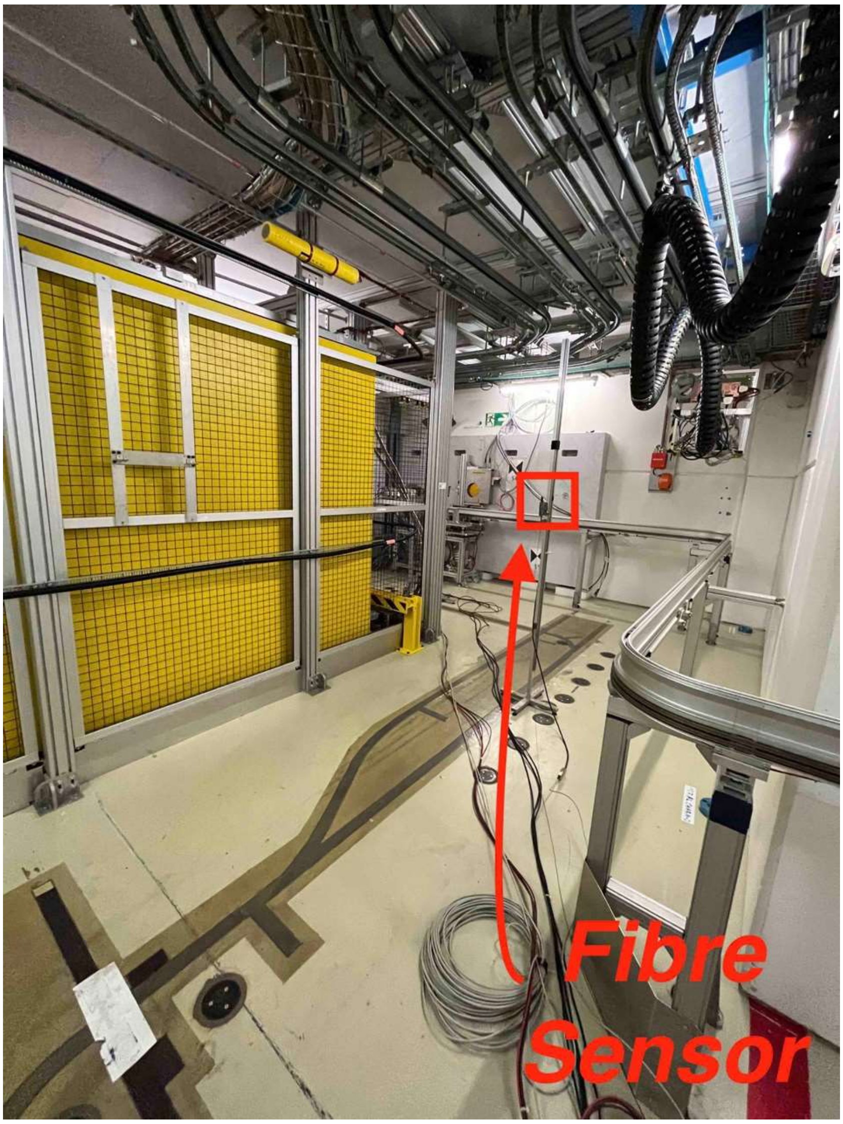

Figure 139 - Picture of the installation of the fibre sensor inside the irradiation room of the CHARM facility

We then started a one-week long irradiation using the Cp-OOOO configuration were all slabs are removed in between the target and the test positions. Several acquistions were performed during this time. The measurements were performed using two configurations : Either 20 ms integration time with a 30 min duration, or 500 ms integration time with a 10 hours long acquisition time. These conditions are explained by the fact that the buffer size of the acquisition system is limited to 100 000 points.

Figure 140 and Figure 142 shows respectively an exemple of measurement with small and larger integration time, performed during this test.

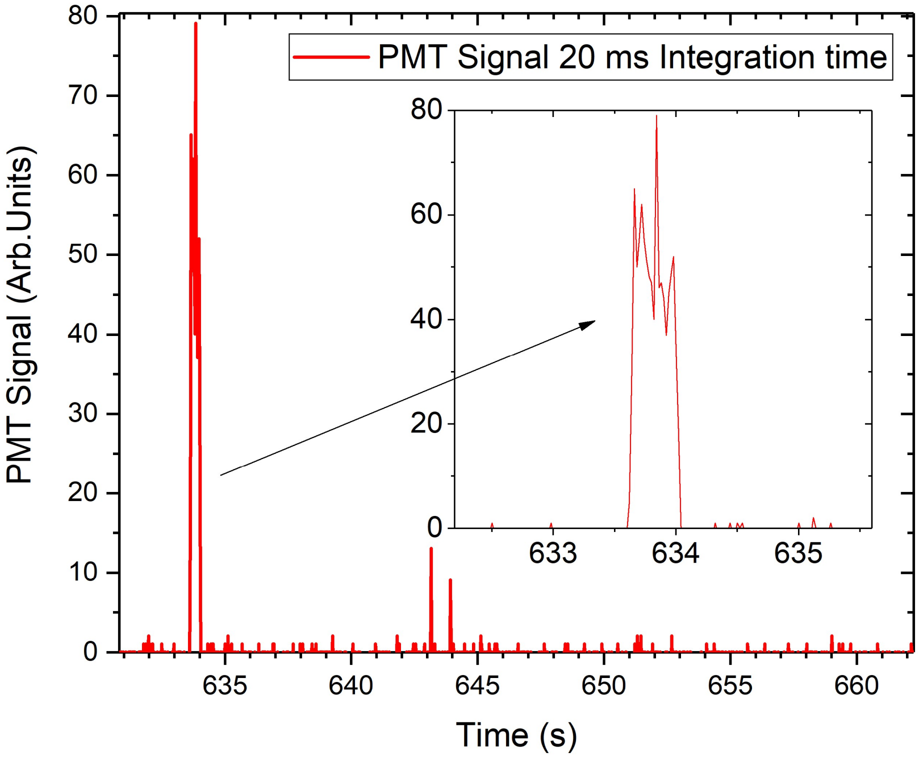

Figure 140 – Exemple of Short Integration time RL measurement performed in the CHARM facility

We observe that the small integration time configuration is able to somehow follow the temporal structure of the beam. To support this point, a measurement of the time structure of the primary proton beam feeding the CHARM facility, using a secondary emission chamber is shown in Figure 141. This figure provides an important information that we used when we planned the experiment: The length of the spills provided by the accelerator, which are around 450 ms long. On the other hand, the long integration time does not describe precisely the temporal structure of the beam but provide an accurate integration of the sensors response over a long period of time. The used PMT features a double counter which means that there is no dead time between two integration periods, which is primordial feature when integrating over a long period of time.

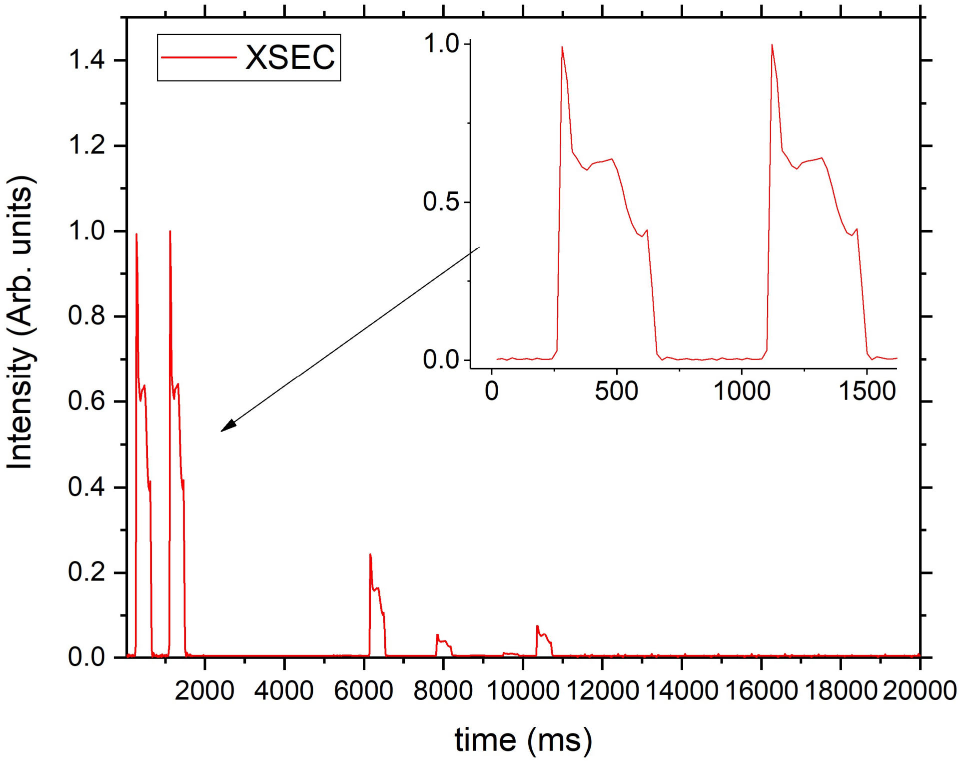

Figure 141 – Primary proton beam from CERN's Proton Syncrotron Accelerator feeding the CHARM facility measured using a secondary emission chamber placed upstream in the beamline.

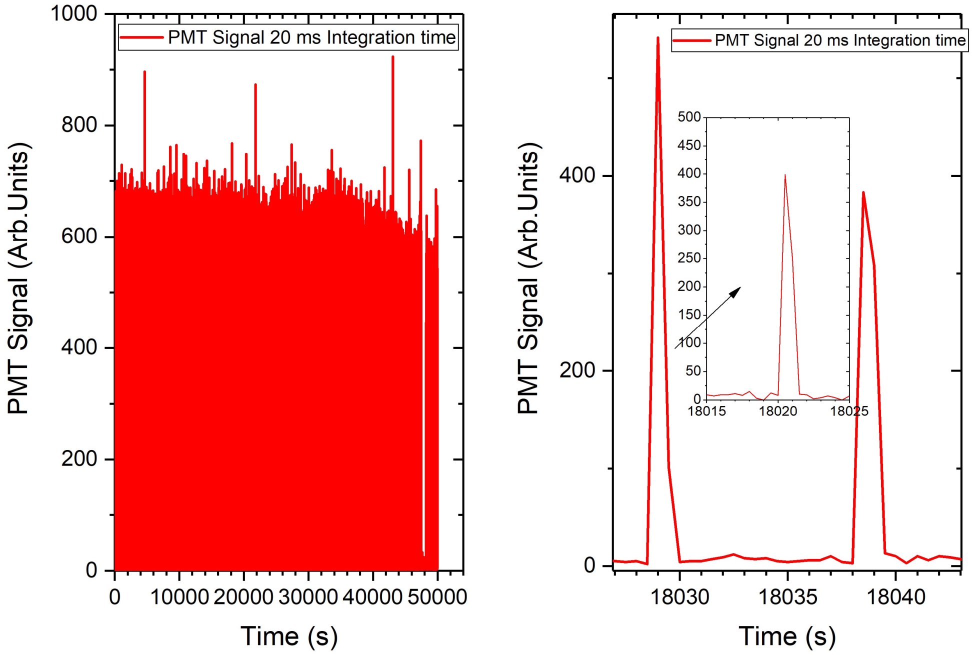

Figure 142 – Exemple of Large Integration time RL measurement performed in the CHARM facility

We performed different measurements at different times during one-week irradiation which resulted in an estimated 160 Gy TID (data from facility).

6.2.3 Comparison of measurements with the facility dosimetry

During this experiment, we performed several runs using alternatively short and long integration time. The measurements were not performed all day long because the used software requires a manual input to save the files at the end of the measurements. The obtained files were stored on a computer along with the timestamps of the start of the measurement allowing to correlate each data point to a corresponding timestamp in post-processing. We therefore obtained measurements with a time scale with an estimated one-second precision.

We also obtained the dosimetry data provided by the facility, containing along with other parameters, the TID measured by the FGDOS placed in proximity to our optical fibre sensor, and the Proton On Target (POT) counts versus time. The POTs are usually used to estimate the reached fluence of given type of particles and dose, at a given position using conversion factors obtained via a combination of FLUKA simulation and experimental measurements.

The obtained data (both from our sensor and the facility) were then put in the same time scale and plotted together. In order to assess the ability of our sensor to follow the dose deposited during the irradiation, we have normalized the signal of the OF sensor and substracted a constant value to both TID (FGDOS) and POT signals to force them at zero at the beginning of the fibre measurement. Then, we scaled down using an empirically defined factor our optical fibre measurement to find the best fit between OF sensor, TID and POT data. This method was needed since our experimental bench is as of today only capable of providing qualitative measurement, therefore this method replaces the usual pre-calibration (which was not possible here) of the sensor in this case.

6.2.3.1 RUN 1

In this first Run, we used the long integration setting and let it run all night. The result are plotted in Figure 143 and shows a very good agreement between the RL signal, the TID and

POT signals. The trend is mainly monotonical however a small change in the slope around 07/07/2022 5:00 is present. This part is very well described by the fibre sensor, which shows that in this case the sensor provides a good dose measurement over 17 Gy, across several hours.

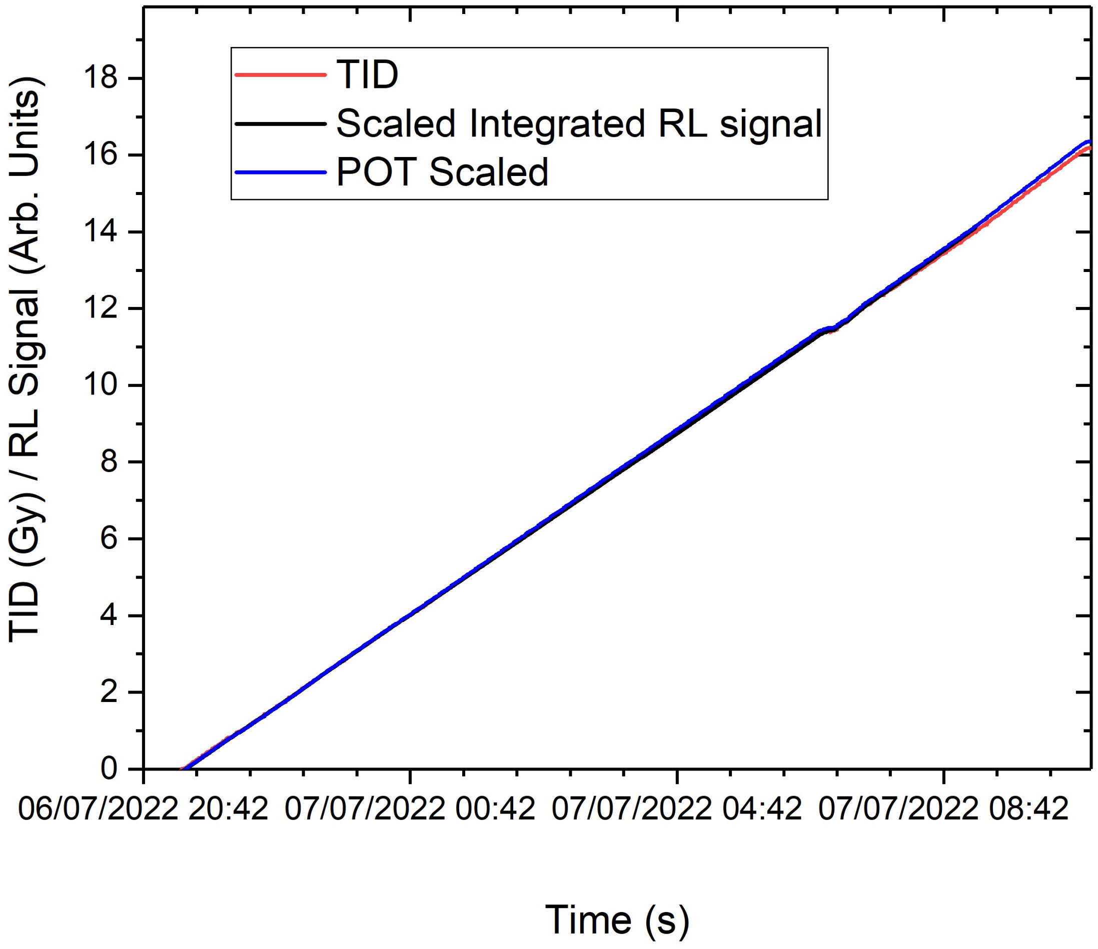

Figure 143 -RL measurement performed during the RUN 1 at the CHARM facility along with TID and POTs provided by the facility. The Long Integration time (500 ms) was used in this case.

6.2.3.2 RUN 2

In this second Run, we used the short integration time setting. The result is plotted in *Figure 144* and shows a different result with respect to Run 1. The general trend of the TID and POT signal are well described by the OF sensor however, many small variation are not correctly described. Nevertheless, the measurement can be considered close enough to describe correctly the dose deposited in during this Run.

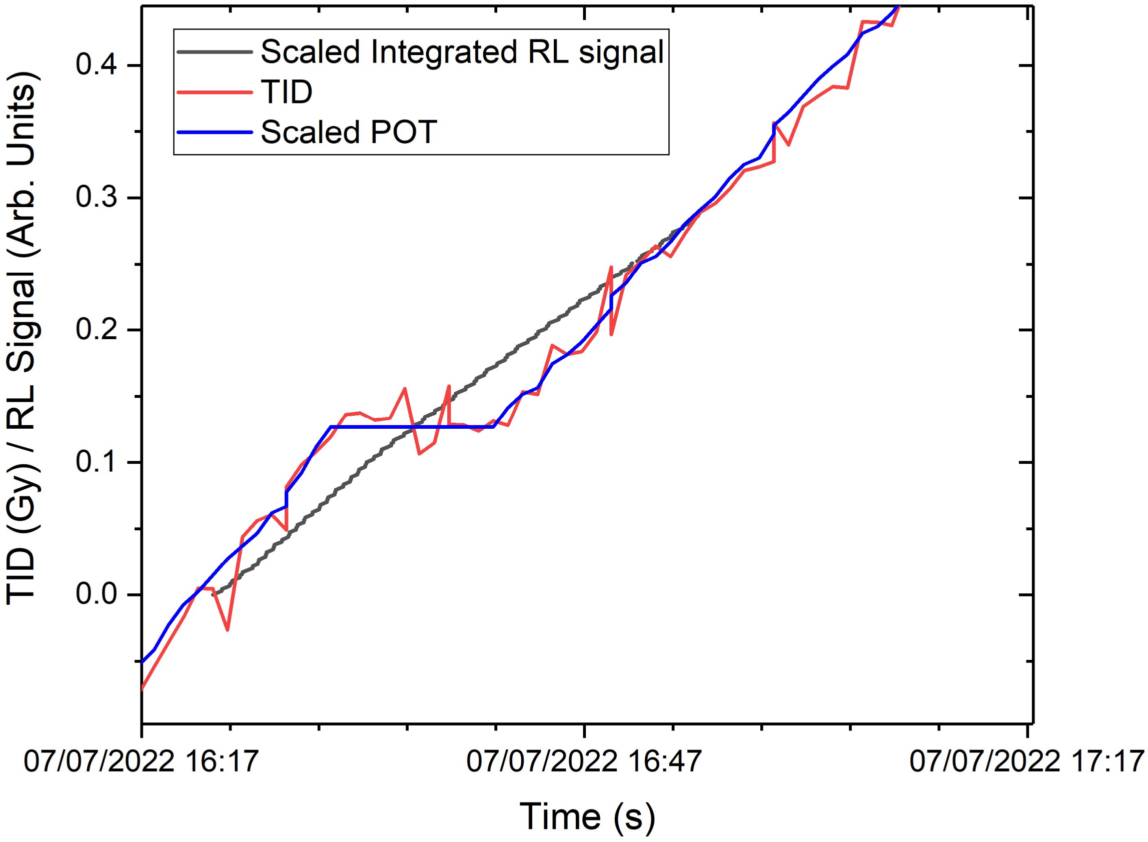

Figure 144 - RL measurement performed during the RUN 2 at the CHARM facility along with TID and POTs provided by the facility. The Short Integration time (20 ms) was used in this case.

6.2.3.3 RUN 3

In this Run, we used the long integration time setting. The RL measurement describes correctly the long term trend of the TID measurement but do not match perfectly the small variations. However, the result is considered as satisfactory in this case.

On the POT measurement side, we note a strange behavior where the POT have a different shape than the two other quantities. This behavior might be due to some beamline instrumentation considerations that we are not aware of. For instance, the POT measurement seems uncorrect because an increase of TID should come with an increase in POT, which is not the case here.

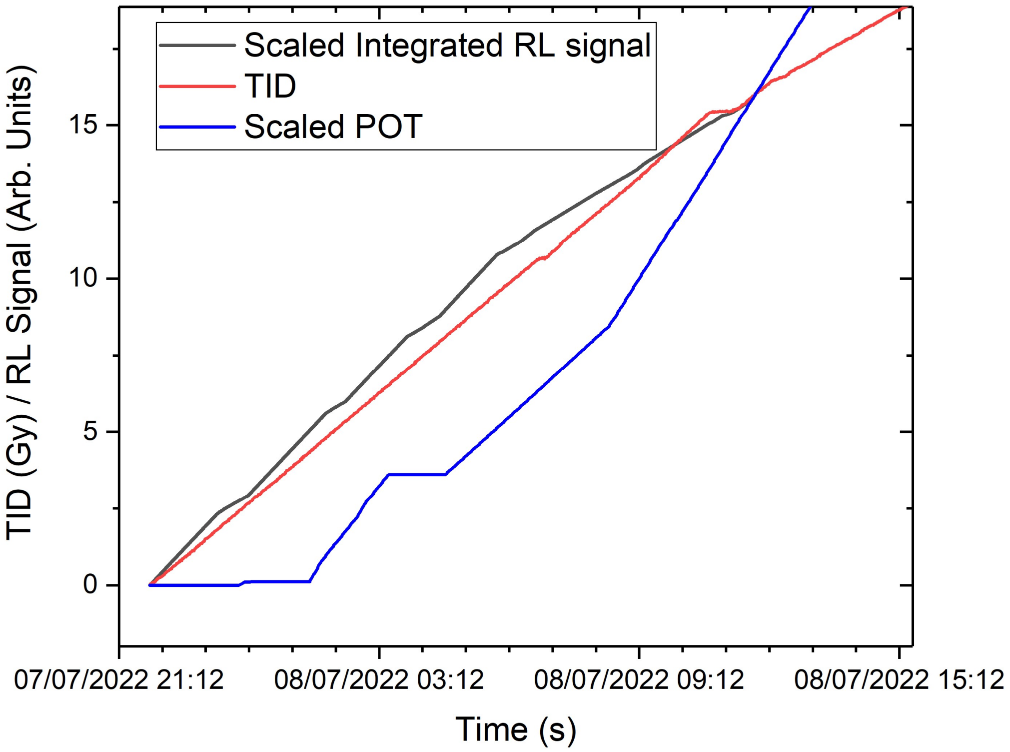

Figure 145 - RL measurement performed during the RUN 3 at the CHARM facility along with TID and POTs provided by the facility. The Long Integration time (500 ms) was used in this case.

6.2.3.4 RUN 4

In this Run, we used the long integration time configuration and obtained the following results. We observe a good description of the evolution of the TID with the RL signal, but the POT signal do not have the same evolution than the other quantities. The RL signal remains within a factor two with respect to the TID measurement which can be considered as satisfactory in such mixed-field environment.

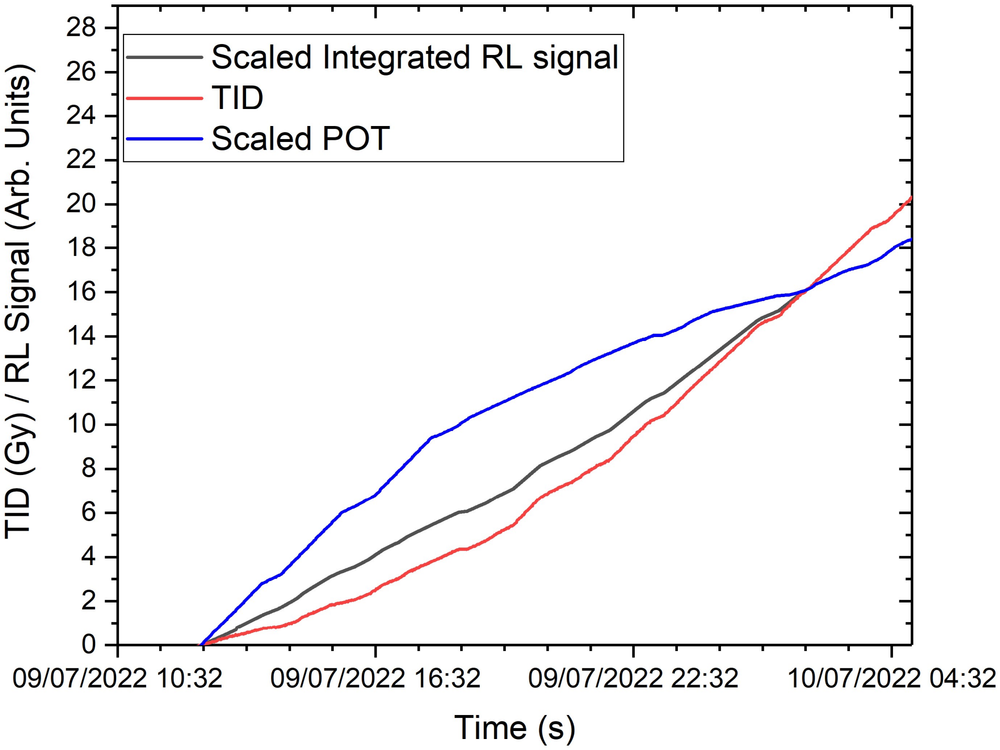

Figure 146 - RL measurement performed during the RUN 4 at the CHARM facility along with TID and POTs provided by the facility. The Long Integration time (500 ms) was used in this case.

6.2.3.5 RUN 5

In this Run, we used the long integration time configuration and obtained the following results. We observe a good description of the evolution of the TID with the RL signal, but similarly as in Run 4, the POT signal do not have the same evolution than the other quantities. The RL signal remains within a factor two with respect to the TID measurement which can be considered as satisfactory in such mixed-field environment.

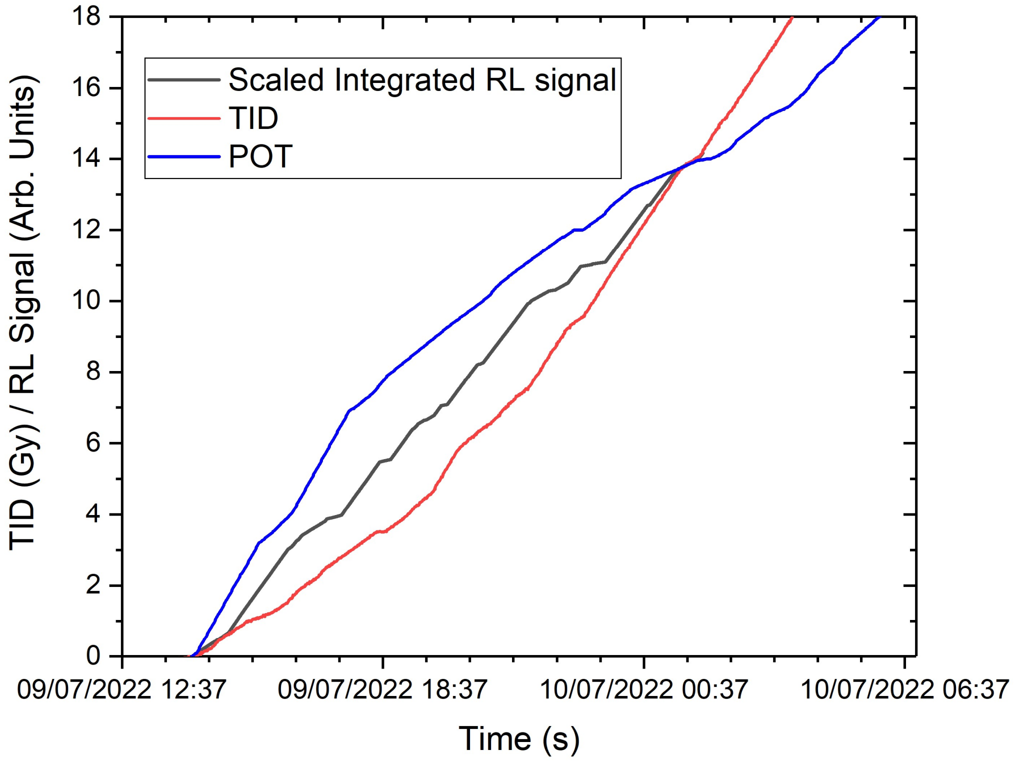

Figure 147 - RL measurement performed during the RUN 5 at the CHARM facility along with TID and POTs provided by the facility. The Long Integration time (500 ms) was used in this case.

6.2.3.6 RUN 6

Here, we used again the long integration time settings during the Run and obtained the following results. We noted a very good agreement between the RL signal and the TID. The POT signal diverges from both RL and TID signals towards the end of the measurement. The measurement is considered as very satisfactory.

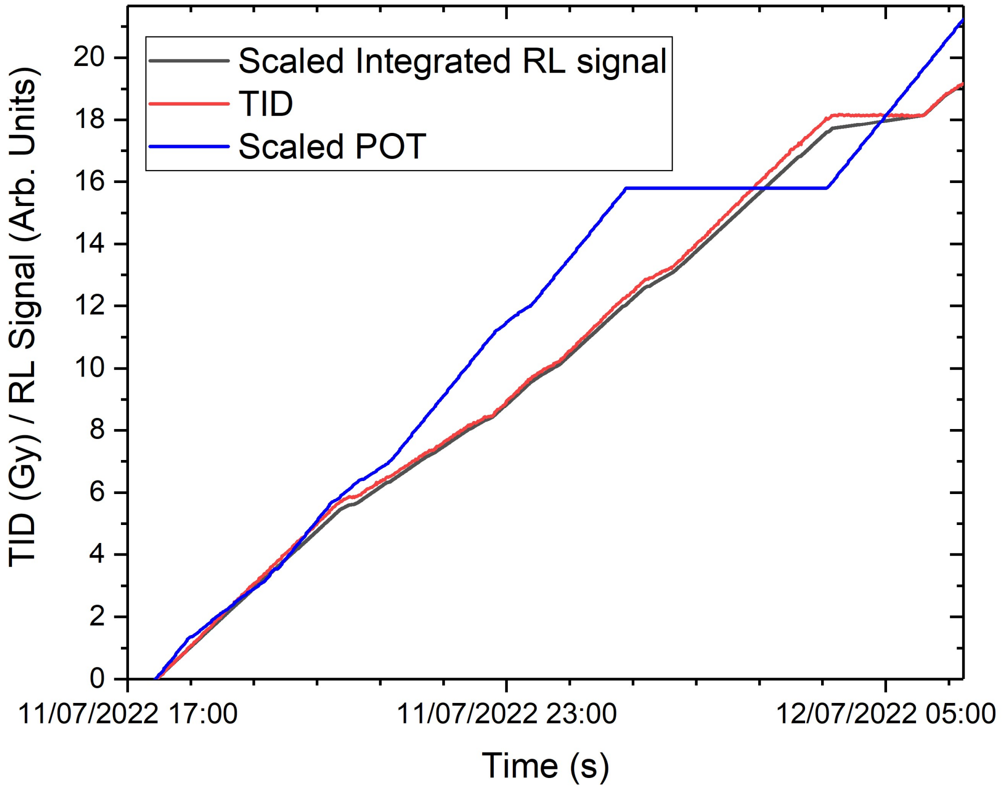

Figure 148 - RL measurement performed during the RUN 6 at the CHARM facility along with TID and POTs provided by the facility. The Long Integration time (500 ms) was used in this case.

6.2.3.7 RUN 7

In this Run, the RL signal follows accurately the TID and POT signals over the 0.8 Gy irradiation. The small variations of the TID are not described by the RL signal however, we can still consider the measurement successful.

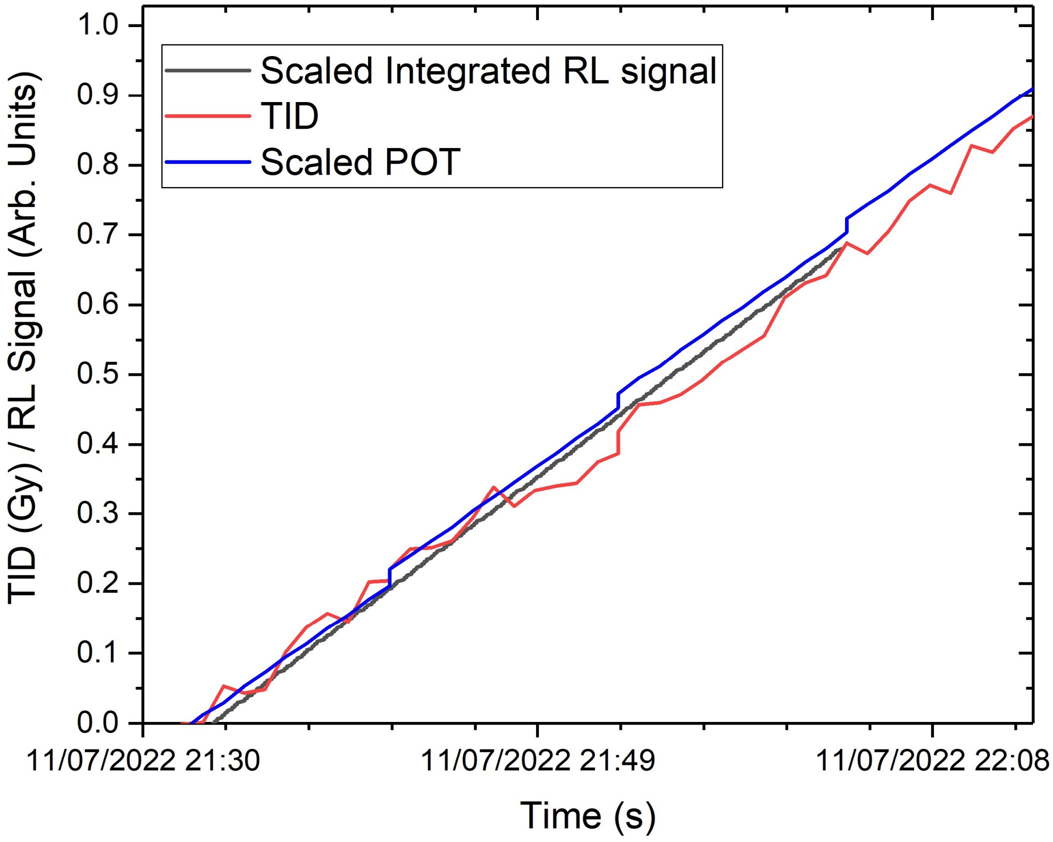

Figure 149 - RL measurement performed during the RUN 7 at the CHARM facility along with TID and POTs provided by the facility. The Short Integration time (20 ms) was used in this case.

6.2.3.8 RUN 8

This last Run covers the end of the irradiation campaign. We used in this case the long integration time setting, and the result presented hereafter shows a good agreement of the RL and TID signals until a point where the TID becomes flat whereas the RL signal and POT keeps increasing. Further work might be needed to understand this second phase of the measurement. The measurement can be considered successful at least in the first phase whereas the second phase needs to be investigated.

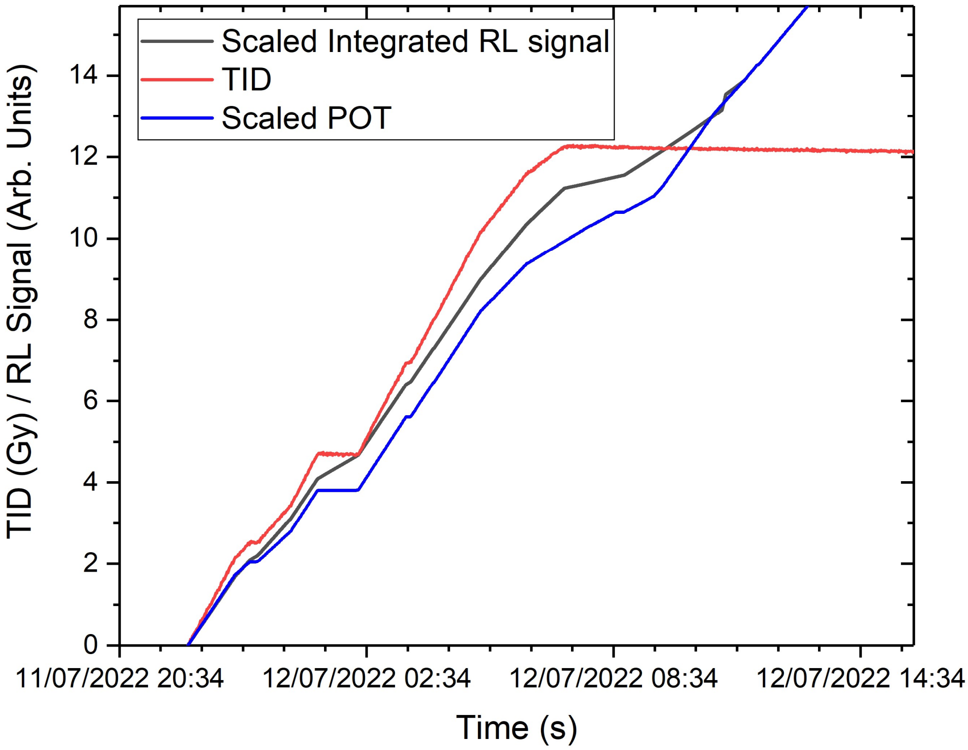

Figure 150 - RL measurement performed during the RUN 6 at the CHARM facility along with TID and POTs provided by the facility. The Long Integration time (500 ms) was used in this case.

7 DISCUSSION

7.1 COMPETITION BETWEEN RL AND RIA CONTRIBUTIONS IN THE INVESTIGATED FIBRES

As introduced earlier, the response of an RL based optical fibre dosimeter sensor relies on an internal competition between the RL phenomena emitting photons, and the RIA absorbing part of these photons before they reach the output of the fibre. When we characterized the RL signal of the investigated fibres, we observed significant variations of the signal with dose, whereas the RIA measurements showed an important RIA amplitude, with levels reaching several hundred of dB/m. Even through the length of the RL based sensor is kept short, we can still wonder to which extend this RIA plays a role in the measured output signal. To answer this question, we directly compare the RL and RIA measurements performed on the fibres under test, which as a reminder, were obtained under the same experimental irradiation conditions. For this purpose, we present the results of the RL and RIA measurements performed in the following way: panel (a) in top part of the figure - we directly compare the measurements of RL and RIA performed on 1-cm long samples, at 5 and 20 Gy/s. In panel (b) in the bottom part of the figure, we show the measurements performed on 5-cm long samples at 5 and 0.5 Gy/s. We found that this way of presenting the data was the most adapted in order to compare the trends followed by RL and RIA signals during irradiation.

We normalize the RL signal to its amplitude at 10 kGy (arbitrary choice), to be able to compare the dynamics across different experiments. In the same figure, we plot on a second y-axis, the RIA measurement (same sample length), under the same irradiation condition. The RL and RIA are both spectral measurements thus, to plot the evolution of the RL and RIA, we choose to plot the signal averaged around the wavelength of the maximum amplitude of the RL emission band of each fibre.

Before starting to present the analysis on different fibres, we have to remind the reader that the RIA affecting the fibres are present in the same UV-Vis spectral region as the RL emission. This is highlighted by the Figure 151, which displays the RL and RIA spectra of some of the investigated fibres.

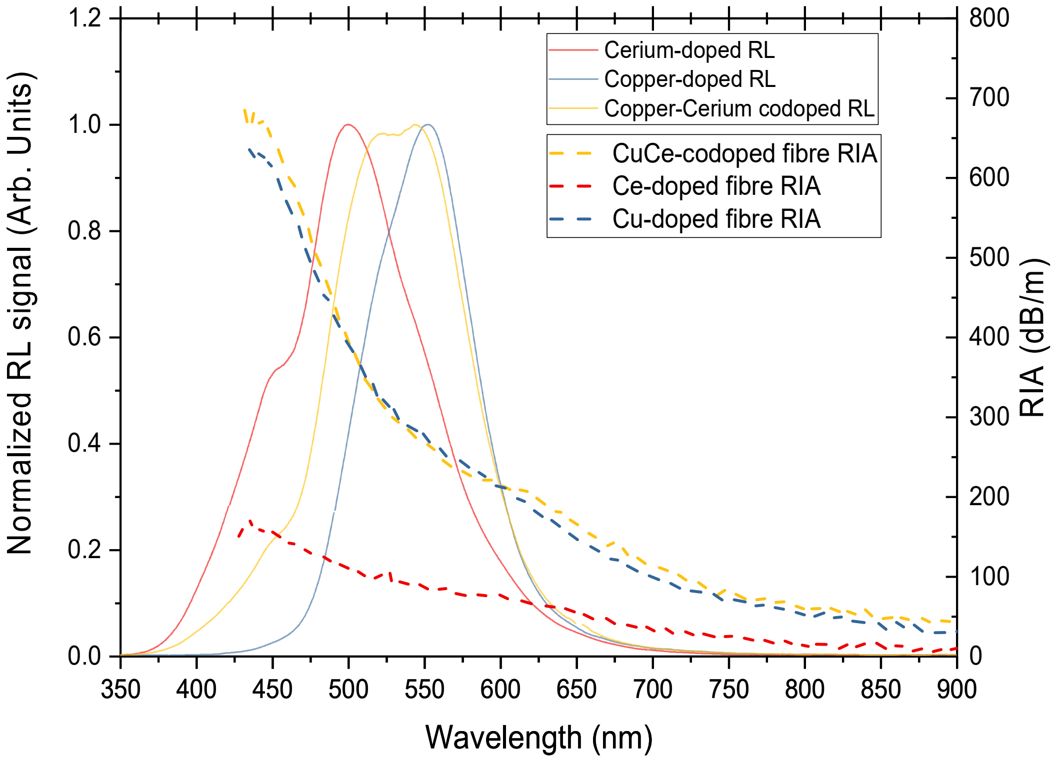

Figure 151 - RIA spectral responses and RL spectra measured on 1-cm long Ce-doped, Cu-doped and CuCe-codoped samples at a TID of 600 kGy under a dose rate of 20 Gy/s

7.1.1 Ce-doped fibre RL/RIA comparison

We start with the Ce-doped fibre, for which the results of the combined RL and RIA study are shown in Figure 152. In the case of 1-cm long measurements, we can observe that the RL signal increases significantly until a TID of a few kGy, then reaches a saturation value above 100 kGy. The saturation/stabilization of the RL signal maintains itself within 0.2 % from 100 kGy until at least 600 kGy. In parallel to the RL, we observe an increase of the RIA, until a maximum value located around a TID of 2 kGy. After that, the RIA (in dB/m) decreases slowly and stabilizes after 100 kGy within 1.5 %. For 5-cm long samples reported in (b), the RL signal increases at the beginning of the irradiation, then decreases to a flex point at 2 kGy, before increasing again until the end of the irradiation.

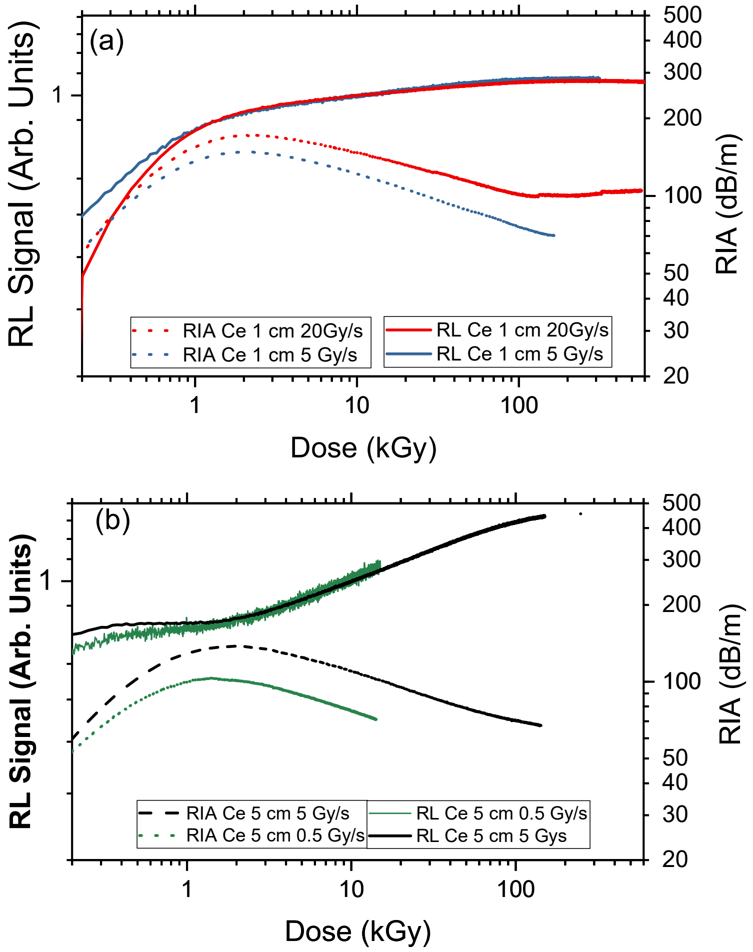

Figure 152 - RL and RIA measurements at 500 nm versus dose (at two different dose rates) on Ce-doped optical fibre for (a) 1 cm-long and (b) 5-cm long samples. RL data are normalized to the response at 10 kGy. Both RIA and RL are plotted in logarithmic scales.

A conclusion that can be made from this comparison of RL and RIA dynamics is that the RIA levels observed in the 1-cm experiment cannot explain by themselves the RL variation. We can deduce that in such short sample, the RIA is not dominating the RL response. In the case of 5-cm long sample, the RL is more correlated to the RIA evolution which means that for such length, the RIA may play a significant role on the RL signal output of the fibre. This is explained by the fact that the average distance travelled by the light in long samples is longer than that in short samples. Therefore, the impact of the RIA on the signal is more important.

7.1.2 Cu-doped fibre RL/RIA comparison

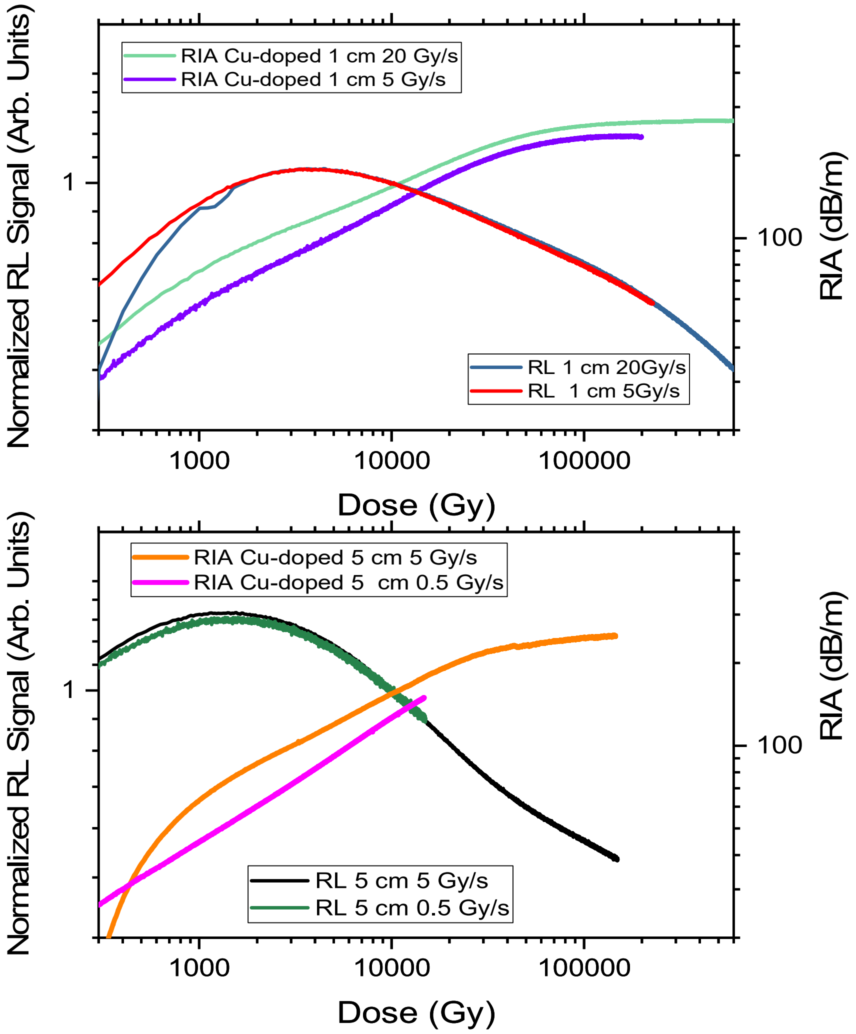

Figure 153 - RL and RIA measurements at 550 nm versus dose on Cu-doped optical fibre for (a) 1 cm-long and (b) 5-cm long samples. RL data are normalized to the response at 10 kGy. Both RIA and RL are presented in logarithmic scales.

In the case of Cu-doped fibre, the RL and RIA data are measured at 550 nm and shown in Figure 153. In 1-cm long sample testing reported in Figure 153(a), we observe an increase of the RL signal until 3 kGy, then a decrease until the end of the irradiation. During the same irradiation, the RIA increases monotonically before becoming more stable towards the end of the irradiation within 2.3% RIA variation between 150 kGy and 600 kGy.

For 5-cm long samples, the dynamics of the RL is very similar. On the RIA side, we also observe a saturation tendency at 100 kGy. One can also note the higher RIA levels observed in the Cu-doped fibre with respect to the Ce-doped fibre, with maximum RIA levels in the order of 180 and 250 dB/m respectively.

In the same way as shown for Ce-doped fibre, we note that RIA impact on RL response is dominant only for the longest sample.

7.1.3 CuCe-codoped fibre RL/RIA comparison

The same comparison is performed on the CuCe co-doped fibre. The obtained data shown in Figure 154 are measured around 525 nm. In this fibre, the radiation response is analogous to that of the Cu-doped fibre.

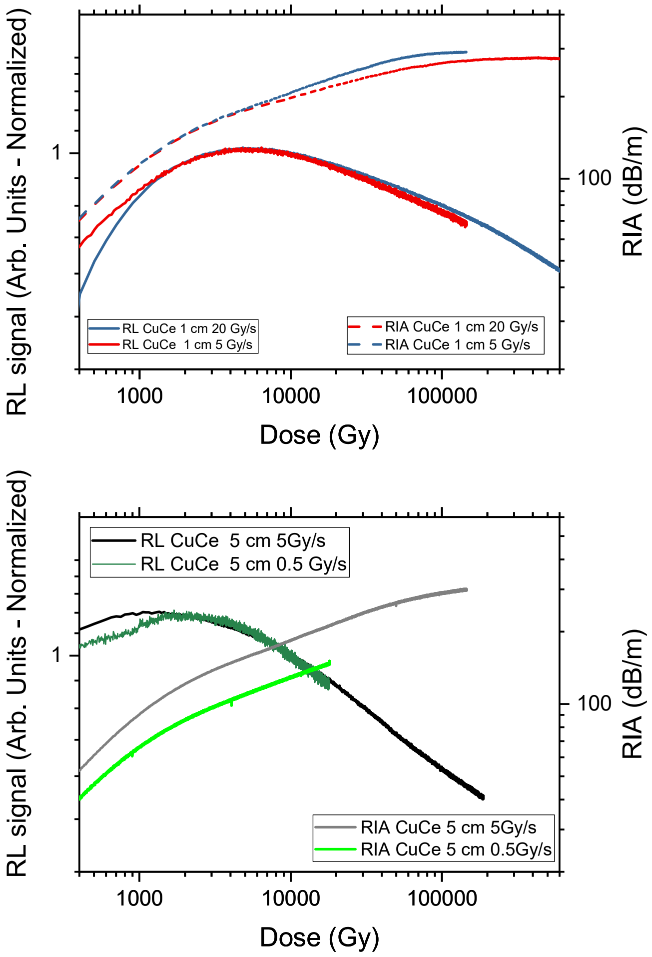

Figure 154 - RL and RIA measurement at 525 nm plotted versus dose on CuCe-codoped optical fibre for (a) 1 cm-long and (b) 5-cm long samples. RL data are normalized to the response at 10 kGy. Both RIA and RL presented in logarithmic scale.

First, the RIA levels follow a similar trend and reach comparable amplitudes for both short and long sample lengths, with respect to that of Cu-doped fibre. Second, the RL signal also follows a similar trend as Cu-doped fibre. It is certainly explained by the presence of Cu ions which have a predominant effect on the overall response of the fibre due to their strong RIA contribution.

7.1.4 Gd-doped fibre RL/RIA comparison

Whereas the OFs doped with Ce, Cu or a combination of both compounds emit light in the visible domain, the Gd doped fibre emits light around 314 nm.

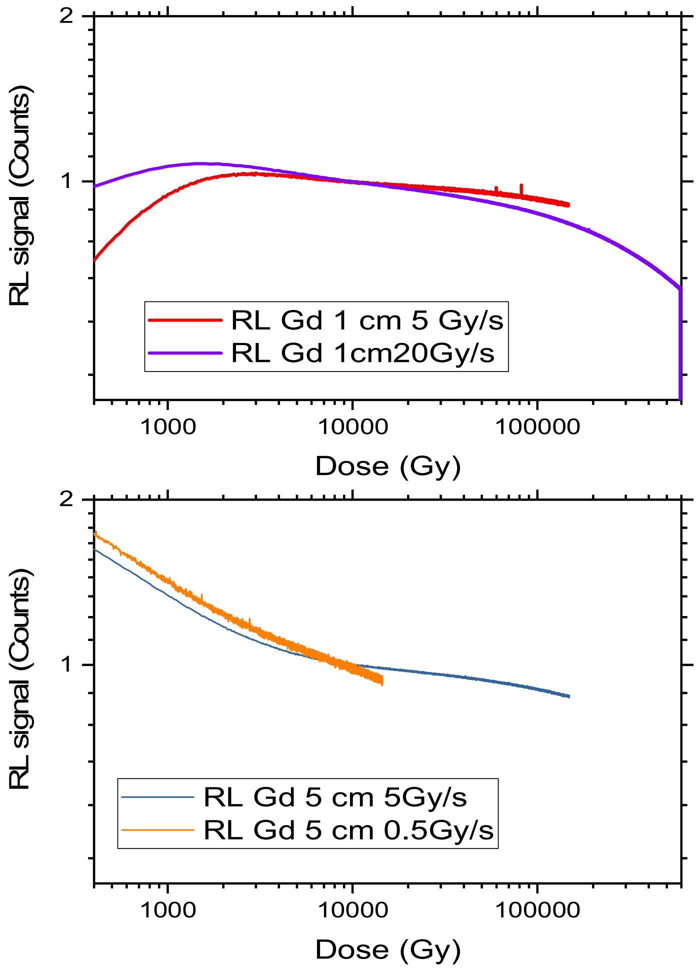

Figure 155 - RL and RIA measurements at 314 nm versus dose on Gd-doped optical fibre for (a) 1 cm-long and (b) 5-cm long sample. RL data are normalized to the response at 10 kGy.

The RL signal data shown in Figure 155 are measured at this wavelength. In the 1-cm long samples, it can be observed that the RL signal increases until 2 kGy and decreases slowly afterwards. In between 2 and 100 kGy the signal changes by less than 10 %.

However, in the 5-cm long samples, we observed a different behavior. In the first part of the irradiation, the signal decreases strongly until 5 kGy before reducing much slower until 150 kGy. This could be explained by strong RIA effects in the UV region, more effective in this case because of the longer length of the sample.

7.2 DISCUSSION ON THE TEMPERATURE DEPENDENCE OF RL RESPONSES OF THE FIBRES.

Experimental measurements on the temperature dependence on the RL response of the investigated fibres have shown a non-negligible temperature dependence in the -120°C / 80°C range. As stated before hand, this dependence is still however compatible with a use in dosimetry application with prior calibration and temperature monitoring if the temperature is susceptible to vary during the measurement. It is also important to note that such temperature effects can also be found in standard radiation monitoring used in various fields such as RadFETs. Indeed, as shown in Figure 156 we can observe a strong effect of the temperature reaching around 0.3 %/K in this case. This value is in the same order of magnitude with respect to that observed in the investigated fibres.

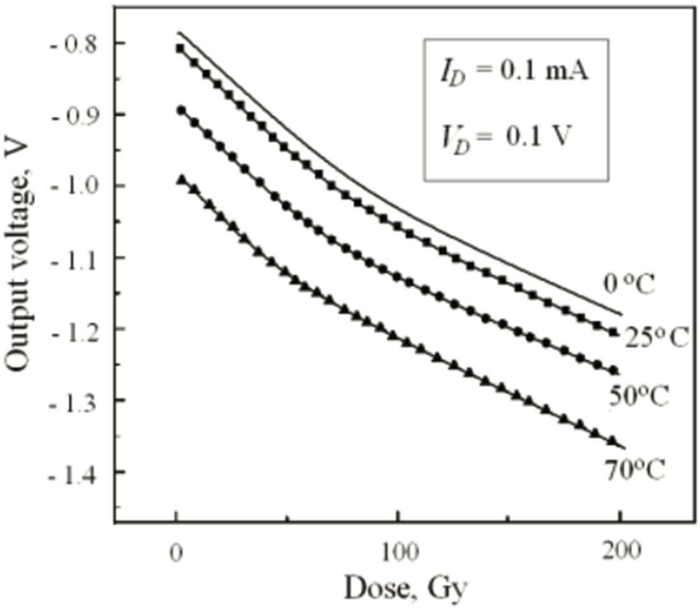

Figure 156 - Evolution of the output response of a RadFET sensor during irradiation at different temperatures, adapted from [85]

7.3 DISCUSSION ON THE CHARM EXPERIMENTAL RESULTS.

This first application-oriented experimental measurement within this PhD work showed that the RL could be an interesting technique for in-situ measurement of TID during mixed-field testing. Indeed, we have shown earlier that the RL response follows closely the measurement extracted from an FGDOS dosimeter placed in the same position during a one-week testing.

However, further work and testing needs to be carried out in order to fully assess the quality of the measurement. For instance, we did not in this test perform a measurement of the Cerenkov contribution which can in certain conditions degrade the measurement quality. Also, the optimal configuration (length of fibre for instance, integration time, automation of the data processing …) needs to be searched in order to exploit the capabilities of the system to its maximum potential.

In addition, some work is needed on the calibration of the sensor to obtain a quantitative measurement. The variability of the response of the sensors from part to part can induce an error on the final measured dose. This is for instance already on-going work within the PhD work of Fiametta Fricano from the Laboratory Hubert Curien, who is performing this type of study on the Ce-doped fibre for intended medical applications. Complementary optimization and calibration is also needed on the bending effects on the transport fibre which can also induce error on the measurement.

Additionnally, further work needs to be performed on the detection chain in order to be able to deploy such technology in space where the detection chain is also subject to radiation, which can induce degration or noise in the detector. This aspect will be further explored in a future dedicated PhD thesis.

8 CONCLUSIONS

Over the course of this PhD work, we have presented the diverse radiation effects induced in optical fibres, and explained how we can make use of the macroscopic effects to provide dosimetry measurements. Our study focused on RL based dosimetry and aimed at providing a consolidated characterization of the responses under irradiation of different optical fibre sensor candidates.

We have identified interesting radiation detection capabilities exhibited by the investigated sensors which can be potentially used in dosimetry application in space and accelerator applications. This technology profits from the reduced size of the sensor which can be benefical for applications where the measurement needs to be performed in precise locations. Additionnally, the response of such sensors has proven to be linear over a large range of dose rate, and to provide an online real-time monitoring of this parameter which is not always achievable with widely used dosimetry solutions (such as RadFETs). Althought the reading of the sensor needs to be perform continuously to collect all the emitted photons, and therefore retrieve the information on the dose/dose-rate, this solution presents many advantages for both accelerator and space applications.

Additionnaly, we show that the RL efficiency of the sensors vary during the irradiation, with the dose. These variations are very important at the beginning of the irradiation before being more contained at higher doses. After 100-200 kGy irradiation, the variation of the RL response becomes much more stable in all the investigated fibres, and almost null in the Ce-doped fibre. This effect remains effective after several hours recovery time. This effect is expected to be related to deep traps present in the optical fibre material that are filled at lower doses, which effect was previously described in the scientific literature.

Eventually, we showed that a temperature dependence of the sensors response is observed over the -120°C to +80°C range. This effect have not been to our best knowledge investigated earlier on this type of radiosensitive fibres and our observation is compatible with a reduction of the RL response at lower temperature that could be related to a RL phonon-assisted process whose efficiency decreases at lower temperatures. This temperature depedence is not a problem for CERN's accelerator applications since this parameter is usually very stable in the targeted environments. However, the temperature can induce perturbations of the dosimetry performances in space. This can be solved by monitoring online the temperature fluctuations together with the dose rate, coupled with an adapted temperature calibration before use. It is important to note here that the observed dependence is comparable to that observed in RadFET sensors, which are widely used in dosimetry application for both space and accelerator sectors. Addtionnally, we have performed an experimental attempt to reduce this temperature dependence by using an innovative solution that we named OSRIL (Optically Stimulated Radiation Induced Luminescence). This technique employs a laser injection in the optical fibre sensor in order to potentially replace totally or partially the phonons contribution to the RL process at lower temperatures, and therefore reduces its temperature dependence. A first attempt has shown an increase in the RL response of roughly 30% at -120°C using a 1064 nm excitation (200 µW). This is still not enough to fully cancel the dependence but is an indication that OSRIL could potentially be developed to obtain a RL dosimeter which does not require a temperature compensation, and therefore can simplify the final dosimeter calibration.

Finally, we have performed a first application-oriented experiment in the CHARM facility at CERN. During this testing, we performed RL measurement on a Ce-doped fibre placed inside the irradiation room while the PMT detector remained in the control room. The obtained results have shown a good description of the TID levels deposited during the irradiation in comparison with a FGDOS sensor provided by the facility. This encouraging result paves the way to RL based dosimetry in mono-energetic and mixed field facilities beams. However, further work is still required in order to fully reach the potential of this solution by working on the calibration of optimized optical fibres and detection chain.

Here are listed below the perspectives studies that would be required in the future to progress towards an operational system :

- Accelerators :
    - If the detector needs to be deported in a shielded area far way from the sensor, a careful evaluation of the RIA effects on the transport cable, as well as the ambient light tightness should be carried out. Both effects can have an impact on the measurement.
    - The transport cable and sensor should be robust and withstand handling for installation and maintenance activities taking place in the tunnels.
    - The transport cable should be able to limit bending effects, which can have an impact on the measurement.
    - The Cerenkov effect should be kept under control (or mitigated) using for instance an additional transport fibre with no sensor, to have a control line enabling substraction of the Cerenkov contribution to the response of the sensor.
- Space :
    - The temperature effects should be compensated using adapted temperature calibration and monitoring.
    - The detector used in the system should be insensitive to magnetic effects and robust to survive the vibration and chocks due to the rocket launch.
    - The detector should be radiation qualified in order to assess the TID/SEEs effects.
    - A focus on the noise and performance degration of the detector is important during the qualification process. Indeed, we have identified in the past strong impact on the PMT signal due to particles directly impinging on the sensitive area of the detector.
    - The OSRIL technique should be further investigated in order to determine if this solution could be employed in missions where the temperature variation are important and where the temperature monitoring is difficult.

9 LIST OF SCIENTIFIC CONTRIBUTIONS

9.1 LIST OF CONTRIBUTION DURING THE PHD :

- N. Kerboub *et al.*, « Radiation Induced Attenuation and Luminescence study in Radioluminescent Optical Fibres », *IEEE Trans. Nucl. Sci.*, p. 1-1, 2023, doi: 10.1109/TNS.2023.3246239. [ORAL].

- N. Kerboub *et al.*, « Temperature Effect on the Radioluminescence of Cu-, Ce-, and CuCe-Doped Silica-Based Fiber Materials », *IEEE Trans. Nucl. Sci.*, vol. 68, nº 8, p. 1782-1787, août 2021, doi: 10.1109/TNS.2021.3075481. [ORAL].

- N. Kerboub *et al.*, « Temperature Effect on the Radioluminescence of Differently doped Silica-based Optical Fibres », p. RADECS 2023 conference [POSTER]. Submitted to IEEE TNS journal.

9.2 PARTICIPATION TO INTERNATIONAL CONFERENCES DURING THE PHD:

- RADECS 2020 [ORAL presentation – Online]
- RADECS 2021 [No contribution presented] Vienna, Austria
- RADOPT 2022 Conference [ORAL presentation], Saint-Etienne, France
- RADECS 2022 [ORAL presentation], Venice, Italy
- RADECS 2023 [POSTER presentation], Toulouse, France

9.3 COMPLETE LIST OF SCIENTIFIC ARTICLES (BEFORE AND DURING PHD) :

- [1]
- N. Kerboub *et al.*, « Comparison Between In-flight SEL Measurement and Ground Estimation Using Different Facilities », *IEEE Trans. Nucl. Sci.*, vol. 66, nº 7, p. 1541-1547, juill. 2019, doi: 10.1109/TNS.2019.2915019.
- [2]
- R. G. Alia *et al.*, « Direct Ionization Impact on Accelerator Mixed-Field Soft-Error Rate », *IEEE Trans. Nucl. Sci.*, vol. 67, nº 1, p. 345-352, janv. 2020, doi: 10.1109/TNS.2019.2951307.
- [3]

- H. El hamzaoui *et al.*, « Gd $^{3+}$ -doped sol-gel silica glass for remote ionizing radiation dosimetry », *OSA Continuum*, vol. 2, n° 3, p. 715-721, mars 2019, doi: 10.1364/OSAC.2.000715.
- [4]
- V. Wyrwoll *et al.*, « Heavy Ion Nuclear Reaction Impact on SEE Testing: From Standard to Ultra-high Energies », *IEEE Trans. Nucl. Sci.*, vol. 67, n° 7, p. 1590-1598, juill. 2020, doi: 10.1109/TNS.2020.2973591.
- [5]
- N. Kerboub *et al.*, « Radiation Induced Attenuation and Luminescence study in Radioluminescent Optical Fibres », *IEEE Trans. Nucl. Sci.*, p. 1-1, 2023, doi: 10.1109/TNS.2023.3246239.
- [6]
- P. Fernandez-Martinez *et al.*, « SEE Tests With Ultra Energetic Xe Ion Beam in the CHARM Facility at CERN », *IEEE Trans. Nucl. Sci.*, vol. 66, n° 7, p. 1523-1531, juill. 2019, doi: 10.1109/TNS.2019.2907112.
- [7]
- M. Kastriotou *et al.*, « Single Event Effect Testing With Ultrahigh Energy Heavy Ion Beams », *IEEE Trans. Nucl. Sci.*, vol. 67, n° 1, p. 63-70, janv. 2020, doi: 10.1109/TNS.2019.2961801.
- [8]
- N. Kerboub *et al.*, « Temperature Effect on the Radioluminescence of Cu-, Ce-, and CuCe-Doped Silica-Based Fiber Materials », *IEEE Trans. Nucl. Sci.*, vol. 68, n° 8, p. 1782-1787, août 2021, doi: 10.1109/TNS.2021.3075481.
- [9]
- R. G. Alia *et al.*, « Ultraenergetic Heavy-Ion Beams in the CERN Accelerator Complex for Radiation Effects Testing », *IEEE Trans. Nucl. Sci.*, vol. 66, n° 1, p. 458-465, janv. 2019, doi: 10.1109/TNS.2018.2883501.
- [10]
- S. Girard *et al.*, « X-Rays, γ -Rays, and Proton Beam Monitoring With Multimode Nitrogen-Doped Optical Fiber », *IEEE Trans. Nucl. Sci.*, vol. 66, n° 1, p. 306-311, janv. 2019, doi: 10.1109/TNS.2018.2879791.
- [11]
- Coronetti *et al.*, « Mixed-Field Radiation Qualification of a COTS Space On-Board Computer along with its CMOS Camera Payload », in *2019 19th European Conference on Radiation and Its Effects on Components and Systems (RADECS)*, Montpellier, France: IEEE, sept. 2019, p. 1-8. doi: 10.1109/RADECS47380.2019.9745699.
- [12]
- Coronetti *et al.*, « Radiation Hardness Assurance Through System-Level Testing: Risk Acceptance, Facility Requirements, Test Methodology, and Data Exploitation », *IEEE Trans. Nucl. Sci.*, vol. 68, n° 5, p. 958-969, mai 2021, doi: 10.1109/TNS.2021.3061197.
- [13]
- N. Kerboub *et al.*, « Temperature Effect on the Radioluminescence of Differently doped Silica-based Optical Fibres », p. RADECS 2023 conference [POSTER]. Submitted to IEEE TNS journal.

10 BIBLIOGRAPHY

[1] A. Chappe, *Histoire de la télégraphie*. Ch. Richelet, 1840. [Online]. Available: https://books.google.fr/books?hl=fr&lr=&id=lBAzAQAAMAAJ&oi=fnd&pg=PP9&dq=chappe+t%C3%A9l%C3%A9graphe&ots=z1uKrVDmvx&sig=3NeU4ud-Y6r1RNu44UnINdJIjw4&redir_esc=y#v=onepage&q=chappe%20t%C3%A9l%C3%A9graphe&f=false

[2] A. A. Huurdeman, *The worldwide history of telecommunications*. New York: J. Wiley, 2003.

[3] J. Tebo, “The early history of telecommunications: The first hundred years,” *Commun. Soc.*, vol. 14, no. 4, pp. 12–21, Jul. 1976, doi: 10.1109/MCOMD.1976.1089239.

[4] “Telstar,” *Wikipedia*. Jan. 08, 2023. Accessed: Jan. 31, 2023. [Online]. Available: https://en.wikipedia.org/w/index.php?title=Telstar&oldid=1132309999

[5] “Courier 1B,” *Wikipedia*. Jul. 08, 2022. Accessed: Jan. 31, 2023. [Online]. Available: https://en.wikipedia.org/w/index.php?title=Courier_1B&oldid=1097040925

[6] “Sputnik 1,” *Wikipedia*. Jan. 24, 2023. Accessed: Jan. 31, 2023. [Online]. Available: https://en.wikipedia.org/w/index.php?title=Sputnik_1&oldid=1135459585

[7] “List of communications satellite firsts,” *Wikipedia*. Jan. 10, 2023. Accessed: Jan. 31, 2023. [Online]. Available: https://en.wikipedia.org/w/index.php?title=List_of_communications_satellite_firsts&oldid=1132841657

[8] K. C. Kao and G. A. Hockham, “Dielectric-fibre surface waveguides for optical frequencies,” *Proc. Inst. Electr. Eng.*, vol. 113, no. 7, pp. 1151–1158, Jul. 1966, doi: 10.1049/piee.1966.0189.

[9] A. J. Rogers, “Distributed optical-fibre sensors for the measurement of pressure, strain and temperature,” *Phys. Rep.*, vol. 169, no. 2, pp. 99–143, Oct. 1988, doi: 10.1016/0370-1573(88)90110-X.

[10] H. C. Lefèvre, “The fiber-optic gyroscope, a century after Sagnac’s experiment: The ultimate rotation-sensing technology?,” *Comptes Rendus Phys.*, vol. 15, no. 10, pp. 851–858, Dec. 2014, doi: 10.1016/j.crhy.2014.10.007.

[11] W. R. Habel and K. Krebber, “Fiber-optic sensor applications in civil and geotechnical engineering,” *Photonic Sens.*, vol. 1, no. 3, pp. 268–280, Sep. 2011, doi: 10.1007/s13320-011-0011-x.

[12] A. H. Hartog, *An Introduction to Distributed Optical Fibre Sensors*, 1st ed. CRC Press, 2017. doi: 10.1201/9781315119014.

[13] “File:OF-MCVD.” [Online]. Available: https://commons.wikimedia.org/wiki/File:OF-MCVD.svg

[14] N. Grote and H. Venghaus, Eds., *Fibre Optic Communication: Key Devices*, 2nd ed. 2017. in Springer Series in Optical Sciences, no. 161. Cham: Springer International Publishing : Imprint: Springer, 2017. doi: 10.1007/978-3-319-42367-8.

[15] H. E. Hamzaoui, M. Bouazaoui, and B. Capoen, “Sol–gel materials for optical fibers,” in *Sol-Gel Derived Optical and Photonic Materials*, Elsevier, 2020, pp. 315–346. doi:

10.1016/B978-0-12-818019-8.00014-4.

[16] “Drawing Tower image.” [Online]. Available: https://www.thorlabs.com/NewGroupPage9_PF.cfm?ObjectGroup_ID=6832

[17] T. Wijnands, K. Aikawa, J. Kuhnhenn, D. Ricci, and U. Weinand, “Radiation Tolerant Optical Fibers: From Sample Testing to Large Series Production,” *J. Light. Technol.*, vol. 29, no. 22, pp. 3393–3400, Nov. 2011, doi: 10.1109/JLT.2011.2168512.

[18] M. G. Stabin, Ed., “Interaction of Radiation with Matter,” in *Radiation Protection and Dosimetry*, New York, NY: Springer New York, 2003, pp. 43–66. doi: 10.1007/978-0-387-49983-3_4.

[19] J. A. Van Allen, G. H. Ludwig, E. C. Ray, and C. E. McILWAIN, “Observation of High Intensity Radiation by Satellites 1958 Alpha and Gamma,” *J. Jet Propuls.*, vol. 28, no. 9, pp. 588–592, Sep. 1958, doi: 10.2514/8.7396.

[20] A. Samaras, A. Varotsou, N. Chatry, E. Lorfevre, F. Bezerra, and R. Ecoffet, “CARMEN1 and CARMEN2 Experiment: Comparison between In-Flight Measured SEE Rates and Predictions,” in *2015 15th European Conference on Radiation and Its Effects on Components and Systems (RADECS)*, Moscow, Russia: IEEE, Sep. 2015, pp. 1–6. doi: 10.1109/RADECS.2015.7365590.

[21] R. Harboe-Sorensen *et al.*, “The Technology Demonstration Module On-Board PROBA-II,” *IEEE Trans. Nucl. Sci.*, vol. 58, no. 3, pp. 1001–1007, Jun. 2011, doi: 10.1109/TNS.2010.2095468.

[22] D. Boscher *et al.*, “In Flight Measurements of Radiation Environment on Board the French Satellite JASON-2,” *IEEE Trans. Nucl. Sci.*, vol. 58, no. 3, pp. 916–922, Jun. 2011, doi: 10.1109/TNS.2011.2106513.

[23] R. G. Bingham, W. C. Erickson, R. L. Howard, J. Lezniak, D. Sawyer, and W. R. Webber, “Two Satellite-Borne Cosmic Radiation Detectors,” *IEEE Trans. Nucl. Sci.*, vol. 13, no. 1, pp. 478–485, 1966, doi: 10.1109/TNS.1966.4324005.

[24] C. Josias, “Radiation Instrumentation Electronics for the Pioneers III and IV Space Probes,” *Proc. IRE*, vol. 48, no. 4, pp. 735–743, Apr. 1960, doi: 10.1109/JRPROC.1960.287476.

[25] Sé. Bourdarie and M. Xapsos, “The Near-Earth Space Radiation Environment,” *IEEE Trans. Nucl. Sci.*, vol. 55, no. 4, Art. no. 4, Aug. 2008, doi: 10.1109/TNS.2008.2001409.

[26] S. Girard *et al.*, “Recent advances in radiation-hardened fiber-based technologies for space applications,” *J. Opt.*, vol. 20, no. 9, Art. no. 9, Sep. 2018, doi: 10.1088/2040-8986/aad271.

[27] A. Infantino *et al.*, “Dose gradient assessment at the new CERN CHARM irradiation facility,” *Radiat. Phys. Chem.*, vol. 155, pp. 225–232, Feb. 2019, doi: 10.1016/j.radphyschem.2018.09.001.

[28] D. L. Griscom, “Nature Of Defects And Defect Generation In Optical Glasses,” presented at the 1985 Albuquerque Conferences on Optics, P. W. Levy, Ed., Albuquerque, Dec. 1985, p. 38. doi: 10.1117/12.975358.

[29] S. Girard *et al.*, “Radiation Effects on Silica-Based Optical Fibers: Recent Advances and Future Challenges,” *IEEE Trans. Nucl. Sci.*, vol. 60, no. 3, Art. no. 3, Jun. 2013, doi: 10.1109/TNS.2012.2235464.

[30] G. Pacchioni, L. Skuja, and D. L. Griscom, Eds., *Defects in SiO2 and Related Dielectrics: Science and Technology*. Dordrecht: Springer Netherlands, 2000. doi: 10.1007/978-94-010-0944-7.

[31] D. L. Griscom, “γ-Ray-induced visible/infrared optical absorption bands in pure and F-doped silica-core fibers: are they due to self-trapped holes?,” *J. Non-Cryst. Solids*, vol. 349, pp. 139–147, Dec. 2004, doi: 10.1016/j.jnoncrysol.2004.08.221.

[32] D. L. Griscom, “Self-trapped holes in pure-silica glass: A history of their discovery and characterization and an example of their critical significance to industry,” *J. Non-Cryst. Solids*, vol. 352, no. 23–25, pp. 2601–2617, Jul. 2006, doi: 10.1016/j.jnoncrysol.2006.03.033.

[33] Y. Sasajima and K. Tanimura, “Optical transitions of self-trapped holes in amorphous SiO 2,” *Phys. Rev. B*, vol. 68, no. 1, p. 014204, Jul. 2003, doi: 10.1103/PhysRevB.68.014204.

[34] S. Girard *et al.*, “Overview of radiation induced point defects in silica-based optical fibers,” *Rev. Phys.*, vol. 4, p. 100032, Nov. 2019, doi: 10.1016/j.revip.2019.100032.

[35] S. Girard *et al.*, “Recent advances in radiation-hardened fiber-based technologies for space applications,” *J. Opt.*, vol. 20, no. 9, Art. no. 9, Sep. 2018, doi: 10.1088/2040-8986/aad271.

[36] M. Brameld *et al.*, “Evaluation of Coherent Terahertz Radiation Generated from Tilted Electron Beams Aiming for Higher Light Intensity,” *Proc. 9th Int Part. Accel. Conf*, vol. IPAC2018, p. 3 pages, 1.224 MB, 2018, doi: 10.18429/JACOW-IPAC2018-THPMK145.

[37] D. Söderström *et al.*, “Properties of Gd-Doped Sol-Gel Silica Glass Radioluminescence under Electron Beams,” *Sensors*, vol. 22, no. 23, p. 9248, Nov. 2022, doi: 10.3390/s22239248.

[38] W. Primak, “Fast-Neutron-Induced Changes in Quartz and Vitreous Silica,” *Phys. Rev.*, vol. 110, no. 6, pp. 1240–1254, Jun. 1958, doi: 10.1103/PhysRev.110.1240.

[39] B. Brichard, P. Borgermans, A. F. Fernandez, K. Lammens, and A. Decreton, “Radiation effect in silica optical fiber exposed to intense mixed neutron-gamma radiation field,” *IEEE Trans. Nucl. Sci.*, vol. 48, no. 6, pp. 2069–2073, Dec. 2001, doi: 10.1109/23.983174.

[40] “IHEP and CERN collaborate well on beam-loss monitors,” *CERN Courier*, Sep. 19, 2007. https://cerncourier.com/a/ihep-and-cern-collaborate-well-on-beam-loss-monitors/ (accessed May 02, 2023).

[41] A. Holmes-Siedle and L. Adams, “RADFET: A review of the use of metal-oxide-silicon devices as integrating dosimeters,” *Int. J. Radiat. Appl. Instrum. Part C Radiat. Phys. Chem.*, vol. 28, no. 2, pp. 235–244, Jan. 1986, doi: 10.1016/1359-0197(86)90134-7.

[42] G. Spiezia *et al.*, “The LHC Radiation Monitoring System - RadMon”.

[43] R. Secondo *et al.*, “System Level Radiation Characterization of a 1U CubeSat Based on CERN Radiation Monitoring Technology,” *IEEE Trans. Nucl. Sci.*, vol. 65, no. 8, pp. 1694–1699, Aug. 2018, doi: 10.1109/TNS.2018.2797319.

[44] “About CHARM | CHARM.” https://charm.web.cern.ch/ (accessed Feb. 07, 2023).

[45] H. Henschel, M. Körfer, J. Kuhnhenn, U. Weinand, and F. Wulf, “Fibre optic radiation sensor systems for particle accelerators,” *Nucl. Instrum. Methods Phys. Res. Sect. Accel. Spectrometers Detect. Assoc. Equip.*, vol. 526, no. 3, pp. 537–550, Jul. 2004, doi: 10.1016/j.nima.2004.02.030.

[46] D. Di Francesca *et al.*, “Distributed Optical Fiber Radiation Sensing in the Proton Synchrotron Booster at CERN,” *IEEE Trans. Nucl. Sci.*, vol. 65, no. 8, pp. 1639–1644, Aug. 2018, doi: 10.1109/TNS.2018.2818760.

[47] M. Kastriotou, “Optimisation of Storage Rings and RF Accelerators via Advanced

Optical-Fibre Based Detectors," Liverpool U., 2019. Accessed: May 02, 2023. [Online]. Available: https://cds.cern.ch/record/2674434

[48] J. Wolfenden *et al.*, "Cherenkov Radiation in Optical Fibres as a Versatile Machine Protection System in Particle Accelerators," *Sensors*, vol. 23, no. 4, Art. no. 4, Jan. 2023, doi: 10.3390/s23042248.

[49] U. de Lille, "PhLAM: UMR8523 - Laboratoire de Physique des Lasers, Atomes et Molécules," Dec. 14, 2022. https://phlam.univ-lille.fr/ (accessed Jan. 31, 2023).

[50] "Accueil - Fibertech Université de Lille." https://fibertech.univ-lille.fr/fr (accessed Jan. 31, 2023).

[51] "Centre national de la recherche scientifique (CNRS)," Jan. 09, 2023. https://www.cnrs.fr/fr (accessed Jan. 31, 2023).

[52] K. Kajihara, "Recent advances in sol–gel synthesis of monolithic silica and silica-based glasses," *J. Asian Ceram. Soc.*, vol. 1, no. 2, pp. 121–133, Jun. 2013, doi: 10.1016/j.jascer.2013.04.002.

[53] H. El Hamzaoui *et al.*, "From porous silica xerogels to bulk optical glasses: The control of densification," *Mater. Chem. Phys.*, vol. 121, no. 1–2, pp. 83–88, May 2010, doi: 10.1016/j.matchemphys.2009.12.043.

[54] H. El Hamzaoui *et al.*, "Cerium-activated sol–gel silica glasses for radiation dosimetry in harsh environment," *Mater. Res. Express*, vol. 3, no. 4, Art. no. 4, Apr. 2016, doi: 10.1088/2053-1591/3/4/046201.

[55] H. E. Hamzaoui *et al.*, "Effects of densification atmosphere on optical properties of ionic copper-activated sol–gel silica glass: towards an efficient radiation dosimeter," *Mater. Res. Express*, vol. 1, no. 2, Art. no. 2, Jun. 2014, doi: 10.1088/2053-1591/1/2/026203.

[56] E. Mones *et al.*, "Ce-doped optical fibre as radioluminescent dosimeter in radiotherapy," *Radiat. Meas.*, vol. 43, no. 2–6, Art. no. 2–6, Feb. 2008, doi: 10.1016/j.radmeas.2008.01.031.

[57] J. Bahout *et al.*, "Cu/Ce-co-Doped Silica Glass as Radioluminescent Material for Ionizing Radiation Dosimetry," *Materials*, vol. 13, no. 11, Art. no. 11, Jun. 2020, doi: 10.3390/ma13112611.

[58] H. El hamzaoui *et al.*, "Gd $^{3+}$ -doped sol-gel silica glass for remote ionizing radiation dosimetry," *OSA Contin.*, vol. 2, no. 3, Art. no. 3, Mar. 2019, doi: 10.1364/OSAC.2.000715.

[59] D. D. Francesca, "Roles of dopants, interstitial O2 and temperature in the effects of irradiation on silica-based optical fibers," phdthesis, Université Jean Monnet - Saint-Etienne ; Università degli studi (Palerme, Italie), 2015. Accessed: Nov. 21, 2022. [Online]. Available: https://tel.archives-ouvertes.fr/tel-01432889

[60] N. Chiodini *et al.*, "High-efficiency SiO2:Ce3+ glass scintillators," *Appl. Phys. Lett.*, vol. 81, no. 23, Art. no. 23, Dec. 2002, doi: 10.1063/1.1524294.

[61] A. Vedda *et al.*, "Ce3+-doped fibers for remote radiation dosimetry," *Appl. Phys. Lett.*, vol. 85, no. 26, Art. no. 26, Dec. 2004, doi: 10.1063/1.1840127.

[62] I. Veronese *et al.*, "Feasibility study for the use of cerium-doped silica fibres in proton therapy," *Radiat. Meas.*, vol. 45, no. 3–6, Art. no. 3–6, Mar. 2010, doi: 10.1016/j.radmeas.2009.10.100.

[63] I. Veronese *et al.*, "Phosphorescence of SiO2 optical fibres doped with Ce3+ ions," *Phys. Status Solidi C*, vol. 4, no. 3, Art. no. 3, Mar. 2007, doi: 10.1002/pssc.200673758.

[64] J. Bahout *et al.*, “Remote Measurements of X-rays Dose Rate using a Cerium-doped Air-clad Optical Fiber,” *IEEE Trans. Nucl. Sci.*, pp. 1658–1662, 2020, doi: 10.1109/TNS.2020.2972043.

[65] S. Girard *et al.*, “Potential of Copper- and Cerium-Doped Optical Fiber Materials for Proton Beam Monitoring,” *IEEE Trans. Nucl. Sci.*, vol. 64, no. 1, Art. no. 1, Jan. 2017, doi: 10.1109/TNS.2016.2606622.

[66] N. Al Helou *et al.*, “Optical responses of a copper-activated sol-gel silica glass under low-dose and low-dose rate X-ray exposures,” *OSA Contin.*, vol. 2, no. 3, Art. no. 3, Mar. 2019, doi: 10.1364/OSAC.2.000563.

[67] N. Al Helou *et al.*, “Effects of ionizing radiations on the optical properties of ionic copper-activated sol-gel silica glasses,” *Opt. Mater.*, vol. 75, pp. 116–121, Jan. 2018, doi: 10.1016/j.optmat.2017.09.049.

[68] J. He, Y. Wang, S. Steigenberger, A. Macpherson, N. Chiodini, and G. Brambilla, “Intense ultraviolet photoluminescence at 314 nm in Gd3+-doped silica,” in *Conference on Lasers and Electro-Optics*, San Jose, California: OSA, 2016, p. JTh2A.86. doi: 10.1364/CLEO_AT.2016.JTh2A.86.

[69] H. El hamzaoui *et al.*, “Gd $^{3+}$ -doped sol-gel silica glass for remote ionizing radiation dosimetry,” *OSA Contin.*, vol. 2, no. 3, Art. no. 3, Mar. 2019, doi: 10.1364/OSAC.2.000715.

[70] D. Jiang *et al.*, “Luminescence and energy transfer characteristics in silica optical fiber materials with cerium and terbium co-doping,” *Opt. Mater. Express*, vol. 8, no. 6, p. 1593, Jun. 2018, doi: 10.1364/OME.8.001593.

[71] S. Girard *et al.*, “X-Rays, γ -Rays, and Proton Beam Monitoring With Multimode Nitrogen-Doped Optical Fiber,” *IEEE Trans. Nucl. Sci.*, vol. 66, no. 1, Art. no. 1, Jan. 2019, doi: 10.1109/TNS.2018.2879791.

[72] C. Hoehr *et al.*, “Novel Gd3+-doped silica-based optical fiber material for dosimetry in proton therapy,” *Sci. Rep.*, vol. 9, no. 1, Art. no. 1, Dec. 2019, doi: 10.1038/s41598-019-52608-5.

[73] A. Meyer, D. Lambert, A. Morana, P. Paillet, A. Boukenter, and S. Girard, “Simulation and Optimization of Optical Fiber Irradiation with X-rays at Different Energies,” *Radiation*, vol. 3, no. 1, Art. no. 1, Mar. 2023, doi: 10.3390/radiation3010006.

[74] “TOTAL DOSE STEADY-STATE IRRADIATION TEST METHOD ESCC Basic Specification No. 22900.” http://escies.org/escc-specs/published/22900.pdf (accessed Feb. 07, 2023).

[75] C. Medico-Sanitaire and V. Chambrette, “FICHE RADIONUCLEIDE CO60 IRSN”, [Online]. Available: https://www.irsn.fr/FR/Larecherche/publications-documentation/fiches-radionucleides/Documents/sante/Co60SAN.pdf

[76] M. Gaillardin *et al.*, “Investigations on Ionizing Dose Deposition in Thin-Layered Devices: Sample-to-Sample Variability and Electronic Equilibrium Dependence,” *IEEE Trans. Nucl. Sci.*, pp. 1–1, 2023, doi: 10.1109/TNS.2023.3239950.

[77] F. Pozzi *et al.*, “CERN IRRADIATION FACILITIES,” *Radiat. Prot. Dosimetry*, vol. 180, no. 1–4, pp. 120–124, Aug. 2018, doi: 10.1093/rpd/ncx187.

[78] L. Evans and P. Bryant, “LHC Machine,” *J. Instrum.*, vol. 3, no. 08, Art. no. 08, Aug. 2008, doi: 10.1088/1748-0221/3/08/S08001.

[79] R. Garcia Alia *et al.*, “LHC and HL-LHC: Present and Future Radiation Environment in the High-Luminosity Collision Points and RHA Implications,” *IEEE Trans. Nucl. Sci.*, vol.

65, no. 1, Art. no. 1, Jan. 2018, doi: 10.1109/TNS.2017.2776107.

[80] “Home | r2e.web.cern.ch.” https://r2e.web.cern.ch/ (accessed Feb. 07, 2023).

[81] J. Mekki, M. Brugger, R. G. Alia, A. Thornton, N. C. D. S. Mota, and S. Danzeca, “CHARM: A Mixed Field Facility at CERN for Radiation Tests in Ground, Atmospheric, Space and Accelerator Representative Environments,” *IEEE Trans. Nucl. Sci.*, vol. 63, no. 4, pp. 2106–2114, Aug. 2016, doi: 10.1109/TNS.2016.2528289.

[82] N. Kerboub *et al.*, “Comparison Between In-flight SEL Measurement and Ground Estimation Using Different Facilities,” *IEEE Trans. Nucl. Sci.*, vol. 66, no. 7, Art. no. 7, Jul. 2019, doi: 10.1109/TNS.2019.2915019.

[83] R. García Alía *et al.*, “Simplified SEE Sensitivity Screening for COTS Components in Space,” *IEEE Trans. Nucl. Sci.*, vol. 64, no. 2, pp. 882–890, Feb. 2017, doi: 10.1109/TNS.2017.2653863.

[84] R. Debnath and S. K. Das, “Site-dependent luminescence of Cu+ ions in silica glass,” *Chem. Phys. Lett.*, vol. 155, no. 1, Art. no. 1, Feb. 1989, doi: 10.1016/S0009-2614(89)87359-2.

[85] V. Felitsyn, B. Podlepetsky, A. Bakerenkov, A. Rodin, and Yu. Sukhoroslova, “Temperature influence on the TID effects in RadFETs,” in *2017 IEEE 30th International Conference on Microelectronics (MIEL)*, Nis: IEEE, Oct. 2017, pp. 167–169. doi: 10.1109/MIEL.2017.8190094.